UNIVERSITY OF CAMBRIDGE

Enhancing the functionality of photovoltaic and photonic biointerfaces through structuration

A dissertation submitted for the degree of
Doctor of Philosophy in Physics by

Tobias Wenzel

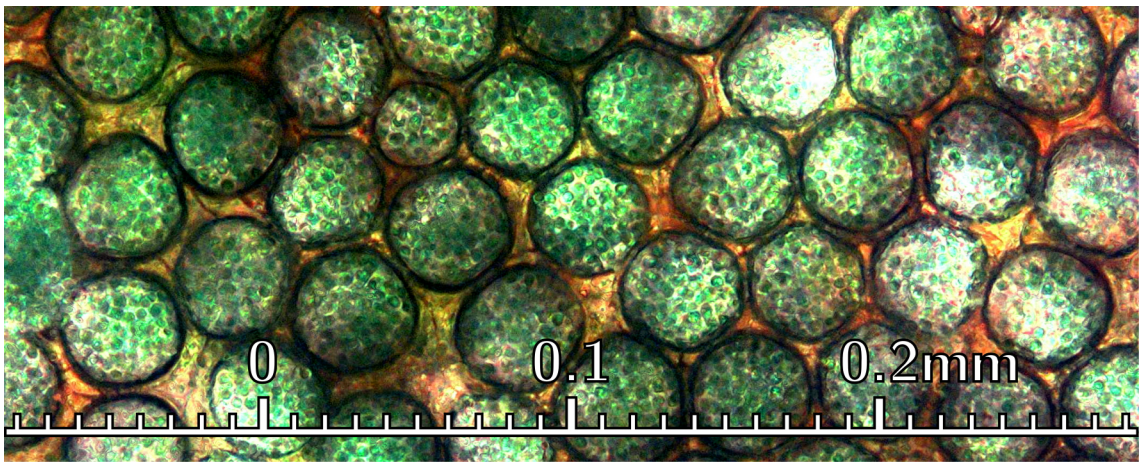

October 2017

University of Cambridge
Cavendish Laboratory
Trinity Hall

Abstract

Enhancing the functionality of photovoltaic and photonic biointerfaces through structuration – Tobias Wenzel

This two-part thesis focuses on biointerfaces of two different biological systems. It specifically examines the interplay of structure and functionality in these biointerfaces. Part one studies photo-bio-electrochemically active bacteria and the strong dependence of their electrical current generation on electrode structure and pigment organisation. Part two uncovers surprising design principles of photonic structures on flower petals and presents research tools to study disordered optical systems.

Biophotovoltaics (BPV) is a newly described biophysical effect in which a biofilm of photosynthetic microorganisms associated with an anode produces electrical current that can be harvested and passed through an external circuit. In this thesis-part, an experimental set-up is presented to quantitatively measure photo-electric activity of cyanobacteria in BPVs. Using this set-up, a systematic study of anode morphologies reveals that large electrode surface areas enhance photocurrents by two orders of magnitude, identifying structuration as key design criterion for bioelectrochemical interfaces. Electrodes with micrometer-sized pores allow enhanced direct contact area with bacteria, but with tested cyanobacteria this did not result in a photocurrent increase, disproving recent speculations in the literature. Furthermore, a theoretic-mathematical framework is presented to estimate light-energy utilisation in biofilms. It is detailed how pigment concentration and distribution affects the light-level dependent saturation of electron harvesting biofilms. This study brings the theory together with experiments, such as genetic modification and photo-current measurements.

Part two of this thesis approaches the interaction of light and biointerface structuration from a different angle. In a significant extension of the candidate's MPhil project, it was discovered that the disorder in natural photonic structures can be an advantage rather than a limitation in biology. With biological image analysis, optics simulations and nano-manufacturing a new photonic effect is uncovered which is iridescent but surprisingly constant in chroma. In collaboration with plant scientists, it is shown that many flowers have co-evolved disordered surface structuration that generates this bee-visible colouration.

Keywords

Microstructuration, biointerfaces, energy biophysics, bio-electrochemistry, nanotechnology, biomimicry, photonics, bioengineering, light-matter interaction.

Declaration

This dissertation is the result of my own work and includes nothing which is the outcome of work done in collaboration except as specified in the text.

It is not substantially the same as any that I have submitted, or, is being concurrently submitted for a degree or diploma or other qualification at the University of Cambridge or any other University or similar institution except as specified in the text. I further state that no substantial part of my dissertation has already been submitted, or, is being concurrently submitted for any such degree, diploma or other qualification at the University of Cambridge or any other University of similar institution except as specified in the text.

This thesis does not exceed the word limit of 60000 words set by the Physics and Chemistry Degree Committee, including abstract, tables, footnotes and appendices.

Cambridge, October 27^{th} 2017

Tobias Wenzel

Overview

The two parts of this thesis are loosely connected by the themes of structuration and functionality of biointerfaces. Every chapter, apart from introductions and conclusions, contains a large amount of custom techniques and measurement data because the development of methodologies was an important aspect of the research projects.

Part I Structure-function interplay of biophotovoltaic interfaces

Chapter 1 introduces biophotovoltaic (BPV) research and reviews the mechanisms of electricity generation from living photosynthetic microorganisms. In particular, it focuses on known and speculative pathways for electroactivity in the model cyanobacterium *Synechocystis*, the key organism for experimental work in this thesis part.

Chapter 2 describes the theory and methodologies for the structuration of transparent electrodes. The developed procedures for the fabrication of indium tin oxide electrodes with pores on different length scales are described, along with the characterisation of these electrodes using a range of methods.

Chapter 3 introduces bioelectrochemical techniques and the custom set up developed for BPV measurements in this thesis. Specifically, a white light source for photobioenergy measurements and a set of 3d-printed temperature controlled BPV devices are characterised. The chapter contains important quality control measurements on cell culture media and temperature dependence, which are currently absent from the literature.

Chapter 4 builds on the methodological framework developed in chapter 2 & 3 and presents key research results. The systematic study of electrode structuration on BPV current generation showed that large electrode surface areas in BPV devices can increase photocurrents by up to two orders of magnitude and speed up their response time. Pores larger than microorganisms have the potential to enhance direct electron transfer modes, but an absence of enhancement in cyanobacteria creates doubt in recently published hypotheses of their direct electron transfer capabilities.

Chapter 5 details a bio-optical model of saturation-limited electron (and energy) generation in photosynthetic biofilms, on the example of *Synechocystis* cyanobacteria. By considering recent characterisations of *Synechocystis*, known bottlenecks in the electron transfer chain and realistic assumptions for the energy input, an estimation for (saturated) photo-electron generation is made. Finally, experimental BPV results are presented for antenna mutant strains and discussed in comparison to the model predictions.

Chapter 6 contains the part one overall conclusions.

Part II **Function of variation in optical structures of biological systems**

Chapter 7 introduces structural colour (photonic light-biointerface interactions) in animals and on flowers. In particular, floral surface striations are discussed and evidence is given for their presence in many plant species.

Chapter 8 describes the finding of a new photonic effect, caused by the disorder in quasi-ordered surface striations. The chapter details the custom tools developed to study this disordered system, including its quantitative analysis, simulation and manufacturing. The characteristics of the optical effect are discussed with the help of simulation results and analysis of experimental implementations.

Chapter 9 shows that the photonic effect of disordered surface striations has a biological functionality. Detailed optical analyses of 11 flower species reveal that the directional photonic effect of disordered striations causes a hue-change of flower petals towards blue and UV shades. Furthermore, controlled bumblebee experiments with artificial flowers show that pollinators can see the new optical effect and that they can recognise it quickly.

Chapter 10 contains the part two overall conclusions.

Contents

Acknowledgements 5
List of publications 7
List of abbreviations 8

I Structure-function interplay of biophotovoltaic interfaces 10

1 Introduction to microbial photovoltaic current generation 11
1.1 My motivation for biophotovoltaic research 11
1.2 Electroactivity in biological organisms 13
1.2.1 Extracellular electron transfer 15
1.3 Summary of processes in biophotovoltaics 17
1.4 Bioelectrosynthesis – the reverse process 18

2 Translucent structured electrode design and testing 19
2.1 Significance and contributions 19
2.2 Electrode design and structuration 20
2.2.1 Transparent electrodes 20
2.2.2 Electrode structuration on different length scales 21
Porous ITO nanoparticle films 23
Templated inverse opal structuration 24
2.2.3 Hybrid structures 27
2.3 Characterisation of electrodes 28
2.3.1 Biocompatibility of electrodes 28
2.3.2 Resistance characterisation of electrodes 29
Sample preparation 29
Resistance measurements 29
2.3.3 Characterisation of optical electrode properties 31
2.3.4 Characterisation of microscopic electrode structuration 32
2.4 Discussion 35

3 Biophotovoltaic techniques for quantitative bioenergy measurements 36
3.1 Significance and contributions . . . 36
3.2 BPV energetics . . . 37
3.3 BPV experimental techniques . . . 38
3.3.1 Cell culture and quantification . . . 38
3.3.2 Conducting bioelectrochemical measurements . . . 40
Losses . . . 43
3.4 Custom solar simulator for bioenergy measurements . . . 44
3.4.1 Design and construction of an LED light source . . . 45
3.4.2 Light calibration and testing . . . 47
3.5 Custom biophotovoltaic devices . . . 48
3.5.1 Design of biophotovoltaic devices . . . 49
3.6 Quality control . . . 50
3.6.1 Testing temperature dependence . . . 50
3.6.2 Background measurements of cell culture medium . . . 52
3.7 Discussion . . . 54

4 Porous electrodes enhance biophotovoltaic current generation 56
4.1 Significance and contributions . . . 56
4.2 Introduction . . . 57
4.3 Experimental . . . 58
4.3.1 Bacteria growth and quantification . . . 58
4.3.2 BPV operation and measurements . . . 59
4.4 Results . . . 60
4.4.1 Electrode design and characterisation . . . 60
4.4.2 Photocurrent ratios . . . 61
4.4.3 Light response characteristics . . . 63
4.4.4 Redox reactions at the bio-anode . . . 65
4.5 Discussion . . . 68

5 Structural parameters of photosynthetic energy flux saturation 71
5.1 Significance and contributions . . . 71
5.2 Modelling photosynthetic energy flux saturation . . . 72
5.2.1 Defining variable solar energy input . . . 73
5.2.2 Photosynthetic absorption limitations . . . 75
Light penetration through cell layers (self-shading) . . . 76
Scattering in biofilms . . . 77
5.2.3 Photosynthetic energy conversion losses . . . 79

Charge separation . . . 79
Electron generation . . . 80
5.2.4 Photosynthetic electron transport dynamics . . . 81
Kinetic limitations of electron generation (saturation) . . . 81
Fast light adaptation and quenching . . . 83
5.2.5 Carbon fixation and respiration . . . 84
Electron usage for carbon fixation . . . 84
Respiration and basal metabolism . . . 85
5.3 The role of pigment distribution . . . 86
5.3.1 Motivation for pigment reduction . . . 86
5.3.2 Cyanobacterial antenna mutant BPVs . . . 87
5.3.3 Experimental results . . . 89
5.3.4 Energy flux saturation in theory and practice . . . 90
5.4 Discussion . . . 92

6 Conclusions **95**

References I **97**

II Function of variation in optical structures of biological systems **109**

7 Photonic surface structures in flowers **110**
7.1 Introduction . . . 110
7.2 Disorder is intrinsic in natural photonic structures . . . 111
7.3 Surface striations are widely distributed in flowers . . . 111

8 Analysis and fabrication of disordered photonic striations **113**
8.1 Significance and contributions . . . 113
8.2 Physics of grating interference . . . 114
8.3 Floral surface striations and their analysis . . . 115
8.4 Simulating disordered photonic striations . . . 117
8.4.1 Approach . . . 117
8.4.2 Modelling the angle-dependent scattering of floral striations . . . 120
8.5 Manufacture of disordered grating structures . . . 123
8.5.1 Approach . . . 124
8.5.2 Height limitations of thin-film processing . . . 127
8.5.3 Material stability at the nano-scale . . . 128
8.5.4 Role of polarisation . . . 129

8.6 Discussion 130

9 Disorder in floral photonic structures is functionally significant 132
9.1 Significance and contributions 132
9.2 Measuring photonic surface scattering effects 133
9.2.1 Bee vision in context 135
9.2.2 Visual differences for bees 137
9.3 Techniques of bee experiments 139
9.3.1 Artificial flower design 139
9.3.2 Bumblebee experiments 140
9.3.3 Differential conditioning experiments 140
9.3.4 Foraging speed experiments 141
9.4 Results 142
9.4.1 Floral surface striation parameters and optical signatures 142
9.4.2 Separation of surface structure and background pigmentation . . 146
9.4.3 Bee recognition and foraging tests 148
9.5 Discussion 151

10 Conclusions 153

References II 155

Acknowledgements

I am very grateful to my supervisor Ullrich Steiner for welcoming me into his group and being my mentor. The years in his group have been a truly unique opportunity to explore my own ideas with a large amount of freedom while being well supported and advised whenever needed. This was true even after the group moved to Switzerland at the end of my first year and the presence of my colleagues in Cambridge decreased. I have learned about a wide spectrum of topics and tools during the time in his diverse research group.

My research projects have been highly interdisciplinary and I have benefited from interactions with collaborators and mentors from different departments. Above all, I would like to thank my co-supervisor Christopher Howe (part I) and Silvia Vignolini (part II) for many helpful meetings, trust, support and guidance in many aspect of projects and my wider career development. Only through them the specific research projects became possible!

I would also like to thank Jeremy Baumberg for the numerous inspiring interactions while using his lab space, winter schools, events of the nanotechnology doctoral training centre (NanoDTC), at the coffee machine and in meetings. I am grateful that he took over the official role as my supervisor and financial hub after the move of my core group. Similarly, I would like to express my gratitude to Erika Eiser for helpful discussions and support with department related administrative work in Ulli's absence, including serving as the official host for the visiting student Daniel Härtter.

I would like to acknowledge all researchers who contributed directly to the work presented in this thesis. They are mentioned in detail in the acknowledgements of each chapter, but I would like to extend a special thanks to some of them for their contribution to each part of the thesis.

For thesis part I, I would like to thank Paolo Bombelli (Howe group) for invaluable frequent theoretical and practical guidance on biophotovoltaics and the much needed constant supply of fresh cell cultures. Daniel Härtter was an important contributor during his 6-month research visit in 2014-15 which I arranged and supervised, and that was enabled by Erika and Ulli. Our co-work period was both productive and highly enjoyable on a personal level. I would also like to thank Otti Crooze for letting me and Daniel work in his algae-lab and for interactions with his group.

For thesis part II, I thank Bevery Glover and Edwige Moyroud for a long and fruitful collaboration during which I learned a lot about the biology of plants and bee vision. Pedro Cunha (Steiner group) was an important guide early on in the project and I am grateful to him for equipment training together with Tom Mitchell (Nanoscience Centre). I would also like to thank Bodo Wilts (Steiner group) who was always helpful and ready to share his substantial knowledge on structural colours in nature.

My work and life in Cambridge would not have been the same without my amazing Steiner group colleagues in Cambridge: Karl Gödel, Raphael Dehmel, Jonathan Lim, James Dolan, Harry Beeson and Xiaoyuan Sheng. Especially Karl and Raphael, with whom I shared an office, have enriched my time and contributed to the solution of many smaller research problems. I would also like to sincerely thank the wider Steiner group (Michael, Maik, Sven, Ahu, Alessandro, Stefano, Antonio, Gen, Ilja) the Vignolini group (Rox, Bruno, Giulia, Villads, Lisa, Olimpia), Howe group (Jack, Toby, Ruth, David, Clayton), as well as nanophotonics, optoelectronics and biological and soft systems groups (especially Sam, Jerome, Johannes, Hannah, Robin, Florian, Heather, Maxim, Ture, Zhongyang). My appreciation also goes to the NanoDTC, Winton Scholar (especially Nalin, Jan, Hajime) and Trinity Hall communities for the many fun and enlightening interactions.

A special thanks goes to stellar technical staff and administrators who have been an immense help and have become personal friends. I want to thank especially Gary Large, Jenny Molloy and Angela Campbell. I am also immensely grateful for support from Anthony Barnett, as well as Emily, Alison, Karishma, Gilly, Kim, Alex, Richard and Suresh.

I would also like to thank the many funding bodies who have made my PhD research and related travels possible: the Winton Programme for physics of sustainability, the Mott Fund for physics of the environment, Cambridge Home and European Trust, the Studienstiftung des Deutschen Volkes, the EPSRC nanotechnology doctoral training centre (NanoDTC), the Cambridge Philosophical Society, my college Trinity Hall, the Open Plant Fund as well as the Cambridge synthetic biology strategic research initiative (SynBio SRI).

It turns out that a PhD project (just like everybody always says) is a challenging undertaking with long result-less time periods, countless failed experiments and inconclusive data. It extends into funding restrictions as well as science politics, and long week(ends) spent writing right-of-passage documents (such as this thesis) and the uncertainty of job opportunities. All the more important it becomes to acknowledge that the safety net and personal support of my amazing family is one of the most valuable assets in my life. I thank my incredible parents Karen und Ronald Wenzel, but also my wider family including grandparents and brother who have always believed in me and unconditionally supported me to get where I am today. The most amazing recent addition to my family is Martina Yopo Diaz, without whom it would have been inconceivable to finish this document without loosing sanity. Thank you very much for your great support in so many ways.

List of relevant publications

Part I I started the interdisciplinary and largely independent project on biophotovoltaics as a new collaboration between the Steiner and the Howe group. The presented chapters have a high content of new research results. I developed both many theoretical and experimental methods for the project and intend to publish not yet submitted aspects of this work in the near future.

[1] **T. Wenzel**, D. Haertter, P Bombelli, C. Howe, U. Steiner; *Porous translucent electrodes enhance current generation from photosynthetic biofilms.* **Nature Communications** (in peer-review)

[2] A.J. McCormick, P. Bombelli, R.W. Bradley, R. Thorne, **T. Wenzel** and C.J. Howe (02/2015); *Biophotovoltaics: Oxygenic photosynthetic organisms in the world of bioelectrochemical systems.* Energy & Environmental Science 2015, 8, 1092-1109

[3] L.F.R. Murillo* and **T. Wenzel*** (*shared authors) (03/2017); *Welcome to the Journal of Open Hardware.* Journal of Open Hardware 2017, 1; non peer-reviewed launch editorial

[4] **T. Wenzel** and R. Lamboll (09/2016); *GOSH, that's handy.* Lab times (10th anniversary edition 04-2016, P.48-49); non peer-reviewed invited magazine article on the Global Open Science Hardware movement

[5] **T. Wenzel** (02/2016); *Open Hardware is an opportunity for Synthetic Biology research.* PLoS Synthetic Biology Blog; non peer-reviewed invited article

Part II The photonic structure part of my PhD project is a substantial extension to a pre-existing collaboration between the Steiner, Vignolini and Glover group, and has been focused to one major publication, with several further options for detailed methodological follow-ups.

[6] E. Moyroud*, **T. Wenzel*** (*shared first authors), R. Middleton, H. Banks, P. J. Rudall, A. Reed, G. Mellers, P. Killoran, M. M. Thomas, U. Steiner, S. Vignolini, B. J. Glover (10/2017); *Disorder in convergent floral nanostructures enhances signalling to bees.* Nature

[7] S. Vignolini, M.M. Thomas, M. Kolle, **T. Wenzel**, A. Rowland, P.J. Rudall, J.J. Baumberg, B.J. Glover and U. Steiner (12/2011); *Directional scattering from the glossy flower of Ranunculus: how the buttercup lights up your chin.* Journal of The Royal Society Interface 9(71):1295-301

List of abbreviations

ATP adenosine triphosphate (cellular energy carrier molecule).

AZO aluminium doped zinc oxide.

BES bioelectrochemical system.

BPV biophotovoltatic (device).

CV cyclic voltammetry.

DET direct electron transfer.

DI deionized.

DSSC dye-sensitised solar cell.

ETC electron transport chain.

FC fuels cells.

FDTD finite-difference time-domain (method).

FTO fluorine-doped tin oxide.

IPA isopropanol alcohol.

ITO indium tin oxide.

LED light emitting diode.

LUMO lowest unoccupied orbital.

MET mediated electron transfer.

MFC microbial fuel cell.

NADH nicotinamide adenine dinucleotide (reduced form) (cellular electron carrier molecule from carbon oxidation).

NADPH nicotinamide adenine dinucleotide phosphate (reduced form) (cellular electron carrier molecule from photosynthesis).

PBS phycobilisome.

PDMS polydimethylsiloxane (flexible polymer).

PEDOT:PSS poly(3,4-ethylenedioxythiophene) polystyrene sulfonate (conductive polymer).

PEM proton exchange membrane.

PFPE perfluorpolyether polymer.

PMMA polymethyl methacrylate (acylic resin/polymer).

SEM scanning electron microscopy.

SHE standard hydrogen electrode.

SRG solar radiation reaching ground level.

TCO transparent conductive oxide.

TEM transmission electron microscopy.

UV ultra-violet.

UV-vis ultra-violet-visible.

Part I

Structure-function interplay of biophotovoltaic interfaces

Chapter 1

Introduction to microbial photovoltaic current generation

This chapter briefly motivates and introduces research on biophotovoltaics (BPV), also referred to as microbial solar cells. This overview is partially based on a review publication which I co-authored (Energy and Environmental Science, 2015 [1]) and which provides an additional in-depth discussion of the research on oxygenic photosynthetic organisms in bioelectrochemical systems. BPV research has mainly been conducted by biochemistry focussed laboratories, and only the main insights of the field are summarised here in order to introduce the reader of this more technical thesis (featuring nanotechnology, modelling, and electrochemical measurements).

Acknowledgements

This section is a summary of the field in my own words, but it is strongly informed by the review paper published with Alistair McCormick, Paolo Bombelli, Robert Bradley, Rebecca Thorne and Christopher Howe. As a non-leading author of this study I would like to thank the team, especially Paolo Bombelli, for the gathering of valuable information and figures, which ultimately supported this chapter and my PhD research.

1.1 My motivation for biophotovoltaic research

As resource consumption and environmental awareness increases globally, there is a need to find more sustainable methods for energy and material production. It is likely that some of the main advances will come from a better utilisation of biological organisms in technological processes. Living organisms are promising because they self-replicate and are thus cheap to produce, self-repair, catalyse complex and specific reactions under mild

conditions, and are biocompatible as well as biodegradable. They are also very durable compared to pure enzyme based systems.

To contribute to the fields of biological energy conversion and the understanding of biointerfaces, I investigated photocurrent generation from photosynthetic microorganisms, specifically cyanobacteria. This multidisciplinary project was developed in a collaboration with the Howe group (Department of Biochemistry). The group pioneered BPV technology [2, 3] in which a pure-culture biofilm of photosynthetic microorganisms associated with an anode produces electrical current. This technology is of interest for the study of bio-energetic processes, for sustainable energy production (see artwork in figure 1.1), as well as for environmentally friendly water desalination and electrically supported biosynthesis of organic fuels.

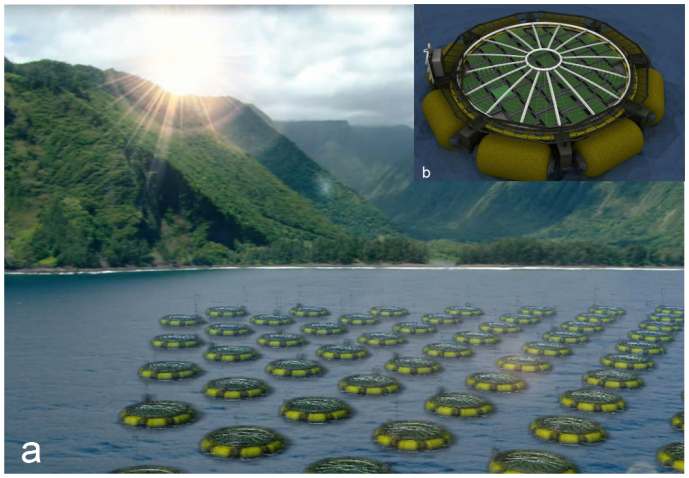

Figure 1.1: An artists vision for future biophotovoltaic units in application. (a) Bay with floating BPV devices. (b) A BPV power station unit. [Figure credit: EPSRC project-media from Christopher Howe, Alison Smith and Adrian Fisher]

There are examples of non-photosynthetic bacteria that are able to metabolise feedstock and transfer 40 % to 100 % of the thereby generated electrons to the external environment [4, 5]. But for biophotovoltaic devices, the fundamental mechanisms in which the current leaves the microbial cells have to be understood before currently low efficiencies can be overcome [6]. In order to systemically explore the role of biointerface electrodes and bioenergy dynamics in biofilms, I initiated this project in the Steiner group (Department of Physics) as a feasible extension of earlier work in terms of electrode design, structuring of active materials and imaging. Additional aspects such as device architecture and genetic variations on the electron transfer where also explored to optimise measurements and design suitable reference experiments.

1.2 Electroactivity in biological organisms

Every living cell transports electrons internally via various biochemical intermediates (redox molecules). Some microbes are also able to exchange electrons with the environment outside of the cell, in a process termed exoelectrogenic activity. A device exploiting this phenomenon to utilise biological energy is called bioelectrochemical system (BES). While electroactive organisms have been known for a long time [7], this topic acquired exponentially increasing scientific attention only in recent years (see figure 1.2). Light harvesting BES are especially promising, because of the prevalent and large amount of solar light available as energy source and because they can be cultured easily without an organic food source.

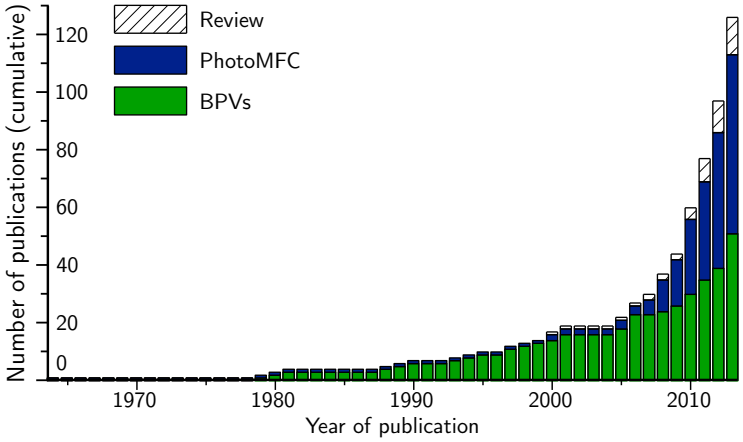

Figure 1.2: Historical overview of BPV and photoMFC studies. Only 38 BPV studies were published from 1964 to 2008. In contrast, during the last five years 71 articles have appeared in scientific journals. The presented data is based on the number of articles mentioning BPVs (or synonyms) in the citation database Web of Science. [Figure from [1] CC BY 3.0]

The best studied bioelectrochemical systems are those that generate electricity by oxidising a food resource (microbial fuel cells, MFCs) [8]. The microorganisms in these devices are purely reliant on organic molecules as external energy source. Bacteria in MFCs are often not oxygen tolerant, which results into difficulties when handling these microorganisms, as they die when exposed to oxygen or air.

Within light harvesting BESs, a number of systems can be distinguished (figure 1.3). There are mixed systems, in which an external feedstock is used together with sunlight, either containing chemoautotrophs or mixed cultures, phototrophic and heterotrophic. Extensive reviews exist for these devices [9, 10]. In plant-MFCs or photo-MFCs, the energy input is purely light, but photosynthetic organisms [11, 12] or components [13]

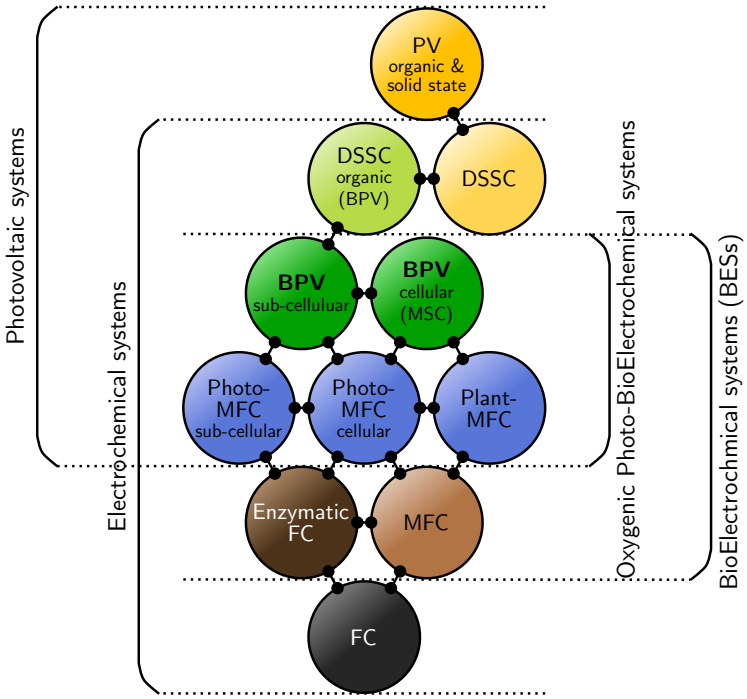

Figure 1.3: The study of biophotovoltaic systems lies at the interface of photo-electrochemical and bioelectrochemical (BES) research. These include a wide range of devices capable of generating electrical outputs, including systems powered by solar light (photovoltaic (PVs) and dye sensitized solar cells (DSSC)) and (in-)organic substrates (fuels cells (FCs)). When at least one of the components catalysing the electrochemical process is biological (e. g. entire cells, enzymes, biologically derived pigments) these systems are defined as BESs. FCs containing biological components (typically heterotrophic bacteria) that are fuelled by organic substrates and are defined as microbial fuel cells (MFCs). Similarly, the integration of photoactive biological components with PVs, where the generation of electrical current is directly or indirectly driven by light, are called BPVs or photoMFCs. [Figure derived from [1] CC BY 3.0]

are only used to produce intermediate energy carriers, which are further processed by non-photosynthetic organisms.

Biophotovoltaic devices do not need any external organic food source, nor heterotrophic organisms to establish exoelectrogenic activity. They are a bioelectrochemical systems containing primarily oxygenic photosynthetic organisms. BPVs can include a wide variety of sub-cellular or cellular photosynthetic components, such as purified oxygenic photosynthetic reaction centres, photosystem II (PSII) [14, 15], thylakoid membranes [16, 17], entire organisms such as cyanobacteria [2, 18] or green algae [3, 19].

While subcellular BPVs are an important platform to study biological processes and intracellular electron transfer, they lack the stability of entire organisms, making applications of these systems less attractive. Cyanobacteria are simpler than eukaryotic algae and possibly more efficient in their photosynthesis. This makes them an ideal system to study the underlying processes of extracellular electron transfer. Specifically, this work

focuses on pure-culture cellular mediator-less photosynthetic electrochemical systems [2, 3].

1.2.1 Extracellular electron transfer

In the paragraphs above, cyanobacteria are described as promising biocatalysts for electricity generation in BPV devices. This remains only a potential goal, as the photoelectrons need to be transferred efficiently from the intracellular space to the anodic surface. These electron transfer processes have been poorly exploited so far and are not yet well understood in photosynthetic organisms [3]. As summarised in figure 1.4, electrons can generally be transferred via a direct electron transport (DET) (e.g. by redox proteins in the outer membrane) or via mediated electron transport (MET). MET is electon transport by soluble small molecules that can carry electrons through the medium between surrounding cells or to an external anode material. It can occur via small molecules produced and excreted by the organisms (e.g. flavins from *S. oneidensis MR1* or phenazines from *Pseudomonas spp.*), artificially added electrolytes (e.g. ferricyanide $[Fe(CN)_6]^{3-}$), and even the oxidation of metabolites that can transport electrons to the electrode once but that cannot be reused cyclically (figure 1.4 c). Based on the organisms used, all mechanisms can exist in parallel in one electrochemical system.

MET with artificial electron mediators has the disadvantage of chemicals having to be added to the system. Both artificially and self-mediated systems have many technological shortfalls of liquid electrolytes such as leakage due to seal imperfections, evaporation,

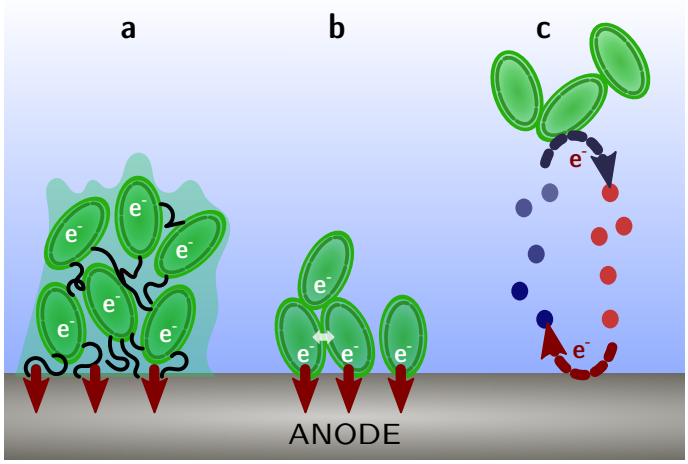

Figure 1.4: Mechanisms of microbial extracellular electron transfer in bioelectrochemical systems. The fundamental mechanisms for extracellular electron transfer to an electrode include (**a**) direct electron transfer by nanowires produced by the organisms that connect the cells and electrode, (**b**) electron transfer across direct contacts of organisms with the electrode and (**c**) electron transfer mediated by redox molecules in solution.

corrosion and degradation. Current research on dye sensitised solar cells (DSSCs) focuses on replacing electrolytes for these reasons [20]. Furthermore, concentrations of electrolytes in combination with living cells have to be substantially lower than those used in DSSCs, creating diffusion limitations in many cases. Diffusion rates are even lower inside biofilms [21].

In contrast, high electron transfer rates have been reported for DET via conductive bacterial filaments in non-photosynthetic organisms, so called 'microbial nanowires' [22–24]. This mechanism has been confirmed in *Geobacter spp.* (using long conductive type IV pili) and *Shewanella oneidensis MR1* (using an outer membrane cytochrome and cell extrusions), see figure 1.5. The coulombic efficiency of the electron transfer via filaments has been claimed to be 'practically 100 %' [4, 5], whereas the resulting voltage depends on the redox potential of the protein complexes involved. Electron export efficiencies for different microorganisms have been reviewed [25].

Thus, the most promising approach is to utilise mediator-less direct extracellular electron transfer present in some microorganisms. This has the advantage of decreasing over-

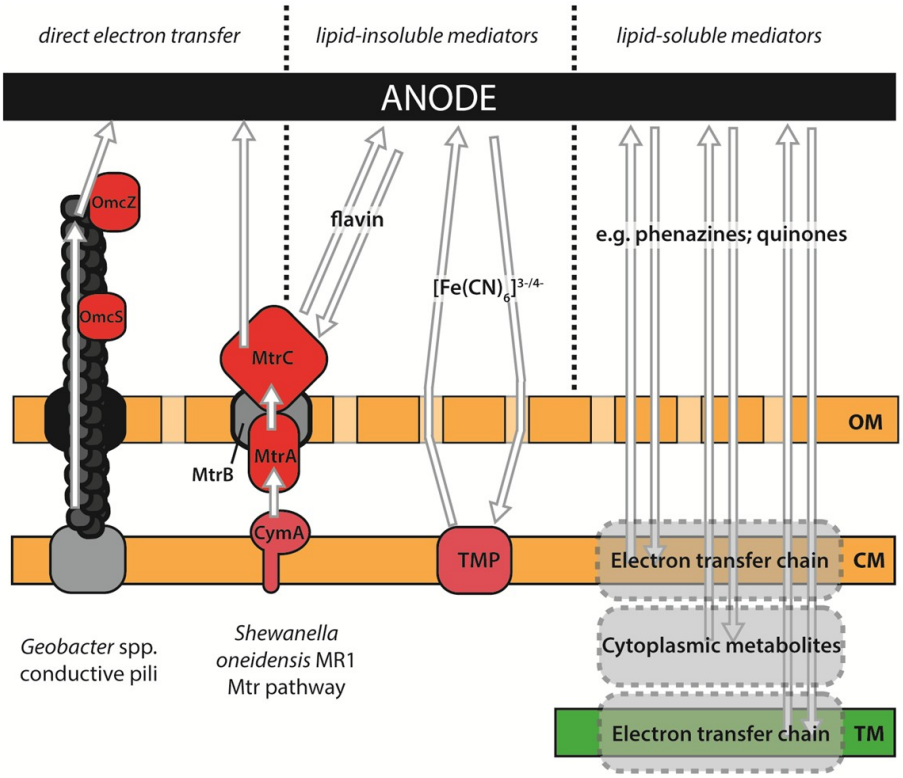

Figure 1.5: Summary of known mechanisms for electron export in exoelectrogenic species. DET has mainly been studied in two organisms. MET can be facilitated either by lipid-insoluble mediators (usually reduced by transmembrane proteins (TMP)) or by lipid-soluble molecules, which can oxidise substrates in lipid bilayers or the cytoplasm. **OM** outer membrane, **CM** cytoplasmic membrane, **TM** thylakoid membrane. [Figure from [1] CC BY 3.0]

potentials and the avoidance of electron shuttle loss as well as diffusion limitations [26–29]. The presence of conductive 'nanowires' in cyanobacteria has been reported, [24, 30, 31] but no evidence so far has been shown, linking the proposed conductive structures to the cellular electron transfer chain in these species. Even the mechanisms of electron transfer between the membranes inside of cyanobacteria remain speculative. Further work is needed to explore the mechanisms of intra- and extracellular electron transport and possible DET in photosynthetic organisms.

1.3 Summary of processes in biophotovoltaics

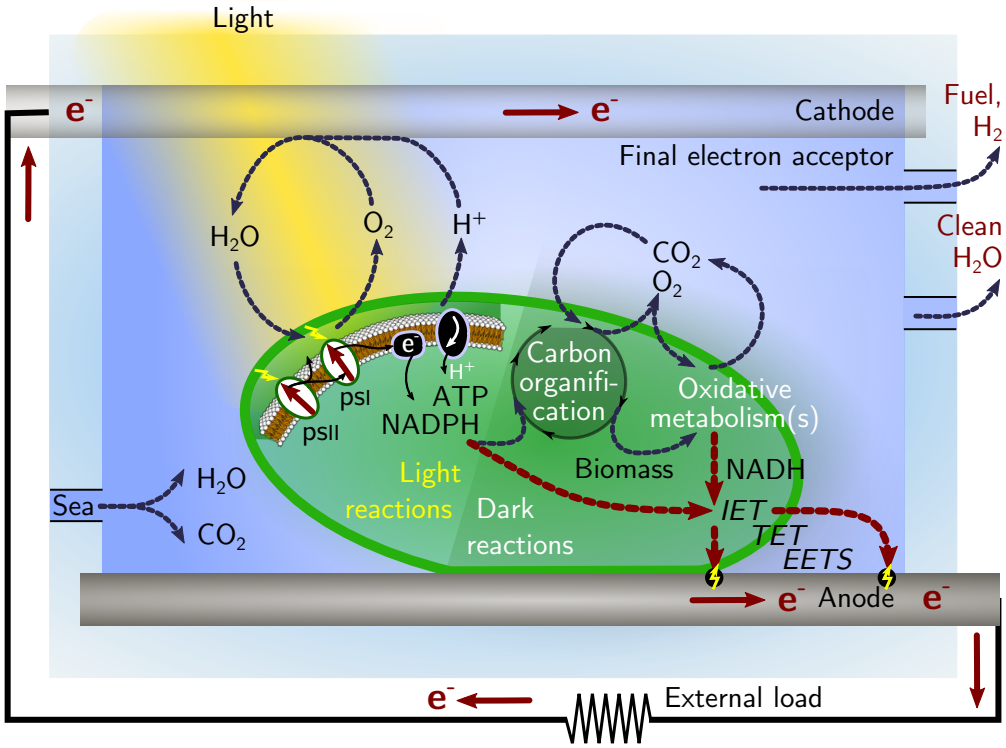

Figure 1.6: Fundamental components of biophotovoltaic (BPV) systems. Intracellular, transmembrane and extracellular electron transport systems (IET, TETS and EETS, respectively) are shown in greater detail in figure 1.4 and figure 1.5.

Figure 1.6 contextualises cellular electron transfer in photosynthetic biofilms with a summary of possible processes in a bioelectrochemical device. Light energy is absorbed by cells internally and used to split water into electrons, oxygen and protons. Electrons are ultimately stored in cellular redox molecules (mainly NADPH) and sugar (which can be re-digested in some organisms). From there, electrons may be exported out of the cell through the organism's membranes, as summarised in previous sections. The protons and electrons reaching the outside of cells drive an external electrical current via anodic

(electron carrier oxidation) and cathodic reactions (water recombination or hydrogen production).

1.4 Bioelectrosynthesis – the reverse process

Higher (eukaryotic) cells use the cellar 'power station' compartments chloroplasts (photosynthesis) and mitochondria (respiration) to generate electrons for the biosynthesis of energetically expensive molecules (figure 1.7). Currents in bioelectrochemical devices are a fraction of those electrons. However, the principle of exoelectrogenic activity in microbes can also be reversed. Some microorganisms can utilize electrical energy via extracellular electron transfer for the conversion of chemical compounds. Bioelectrochemical systems have been used to drive electrosynthesis of biofuels (higher alcohols) from CO_2 [32, 33], for waste water treatment [34–36], and in all combinations for bioremediation, electro-fermentation, electro-respiration [26, 37–39]. Among those technologies, light-dependent cathode-microbe interactions have also been reported [40–42].

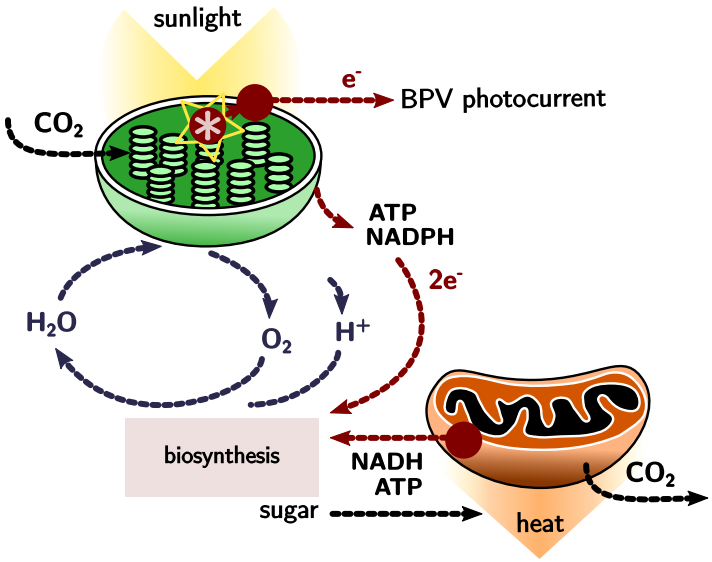

Figure 1.7: Scheme illustrating electron generation and usage for biosynthesis in eukaryotic cells. When supplementing electrons to electroactive organisms, naturally generated energy carriers are complemented and can lead to higher yields of metabolically expensive target molecules.

Even though microorganisms cannot easily be controlled and modified to suit specific applications, they are promising biocatalysts. They are self-regenerating, potentially low-cost, adaptive to energy sources and can be either more specific or more versatile than their inorganic equivalents.

Chapter 2

Translucent structured electrode design and testing

2.1 Significance and contributions

This chapter introduces the key electrode fabrication methodologies and characterisation results used in this work with biophotovoltaic devices (BPVs). Electrode structuration methods were derived from the areas of dye sensitised solar cells (DSSC), photonic materials and enzyme electrochemistry. In contrast to these areas, during this work with living organisms as a biocatalyst, electrodes needed to be structured on the large length scale of biological organisms rather than that of individual molecules. Adapting the methods posed challenges to fabrication and characterisation approaches in terms of the scalability of template sizes as well as material volumes and its properties of transparency and conductivity. For this reason, the chapter is based on custom protocols with original data, while drawing on the best practices in the field. It provides a background on properties, fabrication, structuration, and characterisation of transparent electrodes.

When designing electrode materials, it is often desirable to freely combine known material properties, such as transparency, conductivity, flexibility, differences in energy bands, and morphologies. Furthermore, to allow for reliable repetitions of experiments and sufficient sample dimensions, it is necessary to fabricate these materials and structures in a cheap, scalable, sustainable, and highly replicable manner. Unfortunately, tuning material properties and structuration is a major challenge that has not yet been achieved for many applications, especially in a systematic fashion.

The following sections detail approaches to address the aforementioned design challenges in a suitable way for BPVs. The most important design parameters in a BPV context are transparency (because light has to pass through the material in some cases to supply energy to lower lying cells), structure (here as systematic study parameter),

biocompatibility (enabling the electrode to be used as biointerface), and sufficient conductivity of thick electrode films.

Acknowledgements

The data and development of protocols in this chapter are exclusively my work, except for the optimisation of the colloid assembly and nanoparticles filling. I developed this collaboratively with the visiting student Daniel Haertter, who I supervised for six months from November 2014 to April 2015. A few individual included photos may have been taken by Daniel. I'm also grateful to my supervisors Ullrich Steiner and Christopher Howe, collaborator Paolo Bombelli, and advisor Erika Eiser for pointing me towards resources, advising on the correct design criteria, identifying possible shortfalls of the electrodes to drive appropriate characterisation, and general support for me and Daniel. Interactions with the wider Steiner Lab and Optoelectronics Group have also been invaluable, because they represent a significant concentration of expertise in the field.

2.2 Electrode design and structuration

2.2.1 Transparent electrodes

In general, there is a trade-off between good electric conductivity and high transparency. For instance, metals have a high conductivity because of free moving electrons in the material. At the same time they are opaque (except for very thin films), because the same electrons can be excited by incoming visible light waves, which leads to reflection or absorption and does not let them pass through the material. Semiconductors are an exception. They have an optical bandgap between the valence and conduction band, see figure 2.1 a, which restricts the wavelength of light they can absorb and scatter. An incoming light wave must have a higher energy than the bandgap in order to excite an electron from the valence to the conduction band. When the bandgap is large ($>$3 eV), the material is transparent to visible light and only absorbs irradiation of higher energy (e.g. UV-light).

While transparent semiconductors such as titanium dioxide can be used to conduct electrons in suitable applications, the presence of the bandgap imposes restrictions on the source of electrons, and the conductivity is limited by the low number of free charges in the conduction band. The number of free electrons can be increased, however, by doping the semiconductor with different suitable atoms. At high doping levels (several weight percent [44]), some metal-oxide semiconductors can achieve metal-like conductivity while maintaining transparency to visible light $>$80 %. The band-model scheme in figure 2.1 b

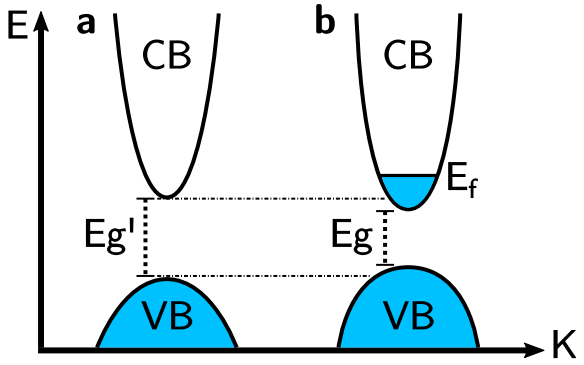

Figure 2.1: Band-model schemes of (a) metal oxide semiconductor and (b) TCO (doped), after [43]. In a semiconductor, the bandgap of energy E_{g}' separates the valence (VB) and conduction band (CB). Heavy n-type doping with metal-ions shifts the Fermi energy E_{f} into the conduction band and the semiconductor becomes degenerate (metal-like conductive). The high concentrations of doping atoms (electron donors) and oxygen defects eventually merge with the bands, decreasing the gap energy to E_{g}.

demonstrates the increased availability of charge carriers in the conduction band (e.g. on the order of $10^{21}\,\mathrm{cm}^{-3}$ for ITO). This popular class of materials is referred to as transparent conductive oxides (TCOs) [45, 46], see figure 2.2 for examples. The three best known high performing TCOs are tin doped indium oxide - normally referred to as indium tin oxide (ITO), flourine doped tin oxide (FTO), and aluminium doped zinc oxide (AZO). However, many further potential TCOs are studied in this ongoing field of research e.g. antimony doped tin oxide (SbTO). There are a few polymer semiconductor materials with similar but generally worse properties, such as PEDOT:PSS. Graphene is also transparent and conductive, but only two-dimensional and thus unsuitable for most 3d structuration methods.

While TCOs are generally transparent as well as conductive, several electrode design parameters influence their transparency. The absorption of a material increases exponentially with thickness, giving the materials a clear colouration up to an opaque appearance for films thicker than a few hundred nanometres. Absorption is also strongly affected by the crystal structure, presence of defects, and quality of doping, which depends on the material processing protocol restricted by the choice of structuration procedures.

2.2.2 Electrode structuration on different length scales

The morphologies that are most relevant to electrode structuration for electrochemistry are size-controlled three-dimensional pore networks on the nanometre or micrometre length scale. These structures are desirable because they change the interaction area with liquid media and catalysts, while avoiding manufacture restrictions associated with strictly periodic structures as often required in the field of photonics. Nevertheless, these

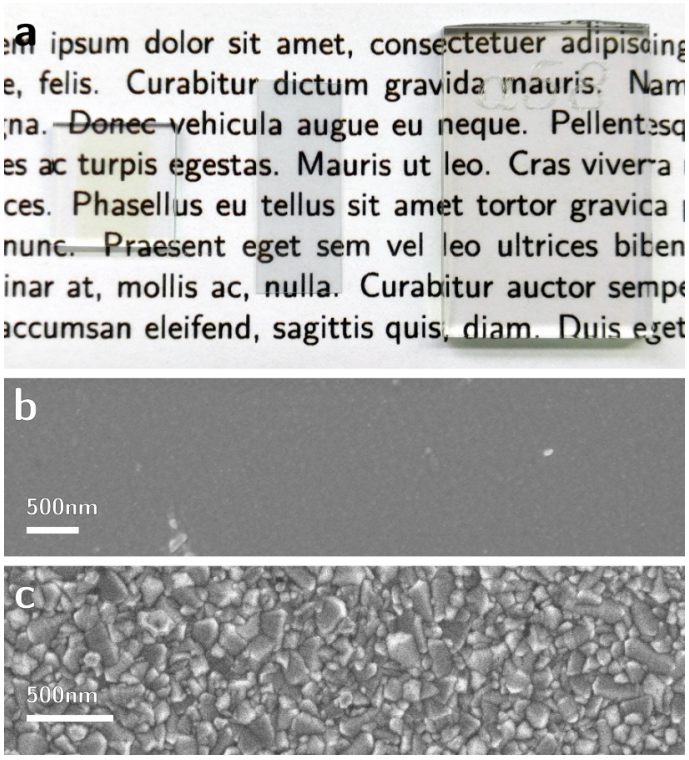

Figure 2.2: Commercial TCO substrates (Sigma Aldrich): (a) from left to right – ITO on glass (15 Ω/sq) and PET (100 Ω/sq), and FTO on glass (8 Ω/sq). ITO and FTO mainly differ in surface roughness, cost (FTO is cheaper) and heat & chemical stability (FTO is more resistant). Surface roughness of (b) ITO and (c) FTO (SEM images).

structures require a huge number of pore replications over the macroscopic electrode area. Simple porosity (several to hundreds of nanometres) can be achieved by using nanoparticles of the desired size and blade- or spin-coat them onto a substrate, see Porous ITO nanoparticle films.

More complex 3d morphologies usually require the self-assembly of polymeric materials, such as blockcopolymers, self organisation of colloids or directed crystal growth [20, 47]. These polymeric structure templates can subsequently be filled with electrode materials such as metals, TCOs, or semiconductors and the template can be removed by etching or thermal treatment. There are a number of pathways to fill polymer templates with electrode materials. The most important ones with regard to TCOs are electrodeposition, sol-gel chemistry, and filling with nanoparticle suspensions.

In electrodeposition, a polymer template on a conductive substrate is transferred into an electrolyte solution which contains the required ions for the semiconductor. The ions are deposited by applying a voltage to the substrate, which leads to an electrochemical deposition reaction on the substrate surface. The semiconductor first covers the exposed conductive surface and then grows into the pores of the polymer template [48]. The challenge to create TCOs with this method is to introduce the proper amount of doping

in the material in order to achieve good conductivity, because doping ions tend to be excluded from the growing crystals for which a perfect lattice is energetically favourable. Less conductive semiconductors can also be created with this method, but the structures grow very slowly, making it unfeasible to fill multiple micrometre thick structured films. Depending on the deposited material, the soft polymeric template can also be destroyed by crystal formation during electrodeposition, which is a common problem e.g. when working with zinc oxide.

Sol-gel chemistry is a chemical procedure used to form gels and solid films from a blend of chemical solutions. It provides more control over the correct amount of doping (because it does not depend on crystal growth from a surface) and it is easier to fill large volumes (because there is no dependence on high sample conductivity which thus cannot limit the processing speed). Sol-gel procedures have been published to create ITO [49, 50] and FTO [8] (without the use of hydrofluoric acid), but the few replication attempts in the context of this work did not yield transparent and conductive films. A challenge when using sol-gel chemistry is the shrinkage of the material during annealing, which often leads to cracks in the structure.

Lastly, the method successfully employed in the context of the study was filling a polymer template with a suspension of TCO (in this case ITO) nanoparticles. Sintering nanoparticles causes less shrinkage and introduces an additional porosity on the length scale of the nanoparticles in the material. It is easy, replicable and scalable, but potentially more expensive. See Templated inverse opal structuration for detail.

Porous ITO nanoparticle films

To create electrode films that are several micrometers thick and have a porosity of 10-100 nm throughout the film, a simple recipe was created as a variation of existing practices [51]. In short, ITO (or other TCO) nanoparticles were suspended in a viscous solvent which allowed blade-coating them manually. The films were sintered to form final electrodes.

Nanoparticle film electrodes were formed on a conductive FTO glass substrate (8 Ohm/sq, Sigma Aldrich) from a commercial ITO nanoparticle dispersion (<100 nm) 30 % wt in isopropanol (IPA) (Sigma Aldrich). First, 2.5 g of nanoparticles (dry weight) were mixed with 10.7 ml terpineol (a-Terpineol 96+%, SAFC supply solutions). The IPA was then evaporated off in a rotary evaporator at 55 °C and vacuum pumping, see figure 2.3 a. FTO glass was prepared by applying two stripes of Kapton tape (Polyimide Tape from RS Components) as distance spacer, and the ITO-particle-terpineol paste was applied between the tape strips. Excess paste was removed by sliding a glass pipette rod over the spacers (blade-coating) to yield an even film, see figure 2.3 b. Next, the

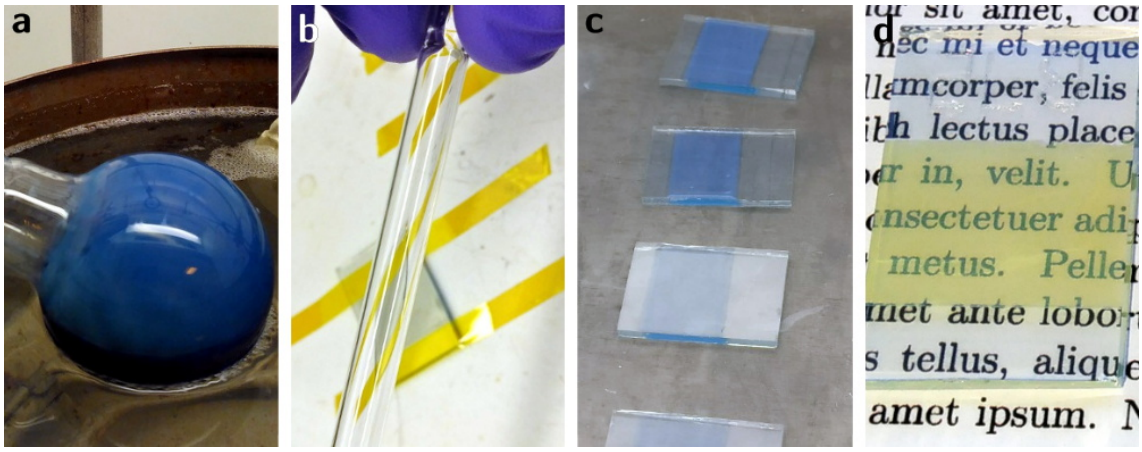

Figure 2.3: Method to create electrodes with nanometre-sized pores. (a) Mixing a viscous paste; (b) Blade-coating the paste onto conductive substrates; (c) Heat-annealing the paste to burn off solvent; (d) Finished electrode.

electrode was left to settle at room temperature for ca. 20 minutes. The Kapton tape was removed manually, see figure 2.3 c. Finally, the electrodes were annealed following a heat ramp procedure: 3 h heat ramp from room temperature to 300 °C holding the temperature for 1 minute; 10 min ramp to 325 °C holding for 5 min; 10 min ramp to 375 °C for 5 min; 10 min to 450 °C for 15 min; 10 min to 500 °C for 15 min; off.

The final films were even, almost entirely crack free, and translucent-yellow, see figure 2.3d, with pores between 10 and 100 nm, see figure 2.12. The method is described in more detail on DocuBricks.

Templated inverse opal structuration

A protocol was developed for this thesis work to create an inverse opal like thick electrode film with pores on the micrometre length scale. First, a structure template was fabricated by depositing close-packed polystyrene (PS) microspheres [52] with a diameter of tens of micrometres, which was consequently filled with commercial TCO nanoparticles and sintered [53, 54], see figure 2.4.

The colloidal template was assembled in a simple custom-made frame which allowed the creation of an $A = 2.4\,\mathrm{cm}^2$-sized homogeneous colloid film, see figure 2.4 b, on a conductive FTO glass substrate (8 Ohm/sq, Sigma Aldrich). The substrate was tightened in the frame, which consisted of two aluminium sheets sandwiching a silicone O-ring, and with a hole in the upper sheet of the same size as the O-ring inner-diameter. More details of this frame are described in the online documentation on DocuBricks.

The microporous electrodes were templated by polystyrene microshperes with an average diameter of 40 µm (Dynoseeds TS 40 from Microbeads). Due to their size, they settled from suspension within minutes. The frame enables convective assembly of

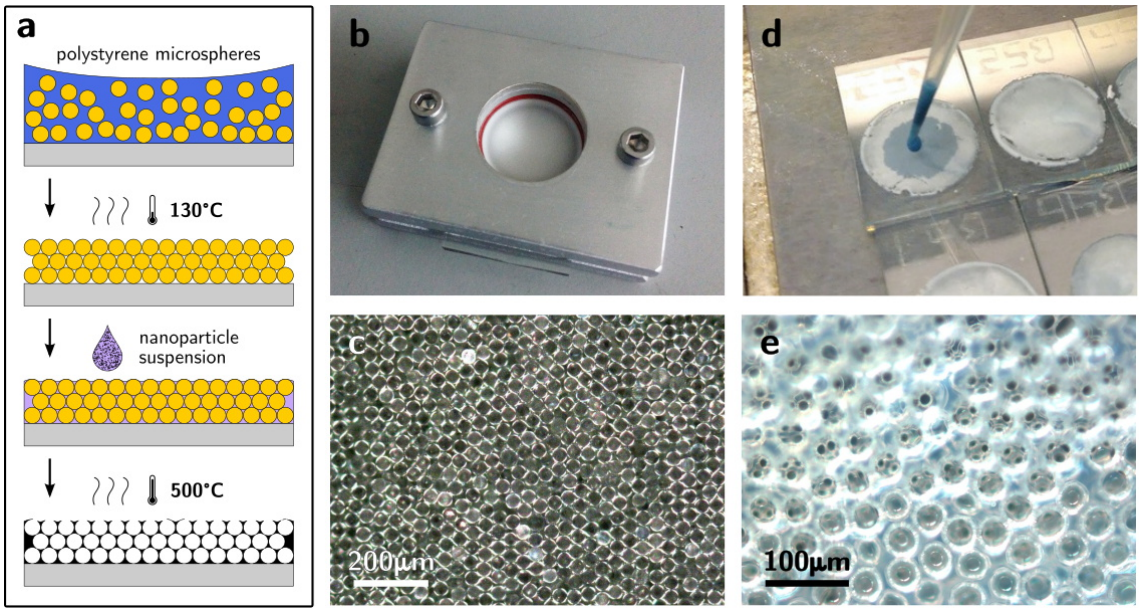

Figure 2.4: Method for fabricating colloid-templated inverse opal like TCO electrodes. (a) Scheme of the main process steps. (b) Assembling the colloid or polymer microsphere template from suspension. (c) Microscope image of a template before the annealing step. (d) Repeated filling of the template with TCO nanoparticle suspension (here ITO). (e) Microscope image of the TCO structure (here ZnO), sintered and with burned-out template.

colloids [52], but the large microspheres here settled on the substrate quickly, decreasing the influence of meniscal forces on the assembly. The used microshperes were also not sufficiently mono-disperse to form colloidal crystals (opal structure), but formed close-packed layers that were sufficient for the purpose of this study.

In order to create a template of suitable size, the colloid concentration can be estimated. The volume packing factor for the final randomly close-packed colloid template can be assumed as ca. $\Phi = 0.6$ [55]. The height h of the template can be estimated

$$h = \frac{V \cdot N}{\Phi \cdot A} \tag{2.1}$$

where $V = 4/3\ \pi \cdot (1/2\ d)^2$ is the volume and N the number of colloid spheres with diameter d (here 40 µm). Further, by using the colloid material density ρ (1.05 g/ml for polystyrene) and the total suspension volume V_s, and the concentration of colloids in water in weight percent c_w

$$c_w = \frac{N \cdot V \cdot \rho}{V_s \cdot 100} \tag{2.2}$$

$$= \frac{\Phi \cdot h \cdot A \cdot \rho}{V_s \cdot 100} \tag{2.3}$$

$V_S = 450\,\mu l$ of suspension proved to be a suitable amount of aqueous solution for to fill the custom assembly frames. Consequently, to obtain a template of $h = 120\,\mu m$ (ca. 3 colloid diameters high), a 4 %wt suspension is estimated. 5 %wt suspension in deionised water was used to compensate for a fraction of colloids sticking to the assembly frame.

A homogeneous area (ca. $2\,cm^2$) of close-packed spheres was obtained when drying the suspension at 30 °C in an oven over night, see figure 2.4 b and c. After assembly in the device, the template was annealed for 10 min at 130 °C on a hotplate to slightly melt the polymer spheres. This improved the adhesion in subsequent filling steps and also determined the sphere contact size, which became the interconnection pore size of the final structure.

To convert the polymer-colloid opal to a TCO inverse opal electrode, the template was filled with a TCO nanoparticle dispersion (30 % wt ITO (<100 nm) in isopropanol (IPA), Sigma Aldrich). The solvent of the suspension was exchanged before use, because IPA tends to wet the tips of the structure, leaving few open pores that can serve as entry points for biocatalysts into the structure, see figure 2.5 a. Drying and re-suspending the nanoparticles (10 % wt) in absolute ethanol (Sigma Aldrich) led to more favourable results, see figure 2.5 b.

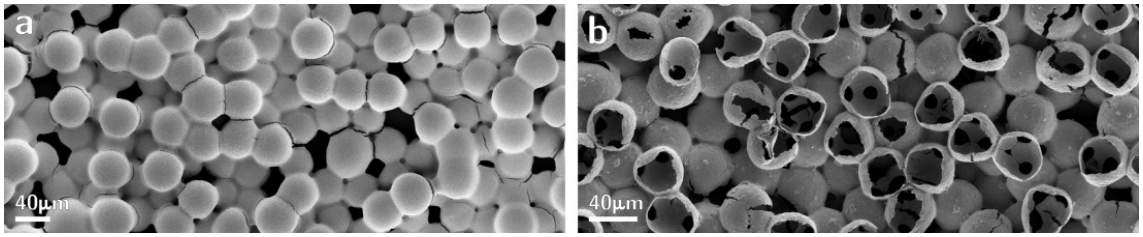

Figure 2.5: SEM images of ITO inverse opal like structured electrodes. The templates were filled with ITO nanoparticles suspended in solvents with different template wetting properties: (a) IPA and (b) ethanol.

The polystyrene opal was placed on a hotplate at 45 °C for quick drying and filled 3 times with 25 µl of ITO suspension, see figure 2.4 d. The template was burned out on a hotplate inside a fume hood by heating the anodes to 500 °C, which simultaneously sintered the nanoparticles, finishing the electrode. For this purpose, the following heat ramp procedure was used: 3h heat ramp from room temperature to 300 °C holding the temperature for 1 minute; 10 min ramp to 325 °C holding for 5 min; 10 min ramp to 375 °C for 5 min; 10 min to 450 °C for 15 min; 10 min to 500 °C for 15 min; off.

Final electrode structures were porous, as predicted, with pore sizes of 40 µm and 10 µm connections, and additionally featured the smaller 10-100 nm pores (see figure 2.11).

2.2.3 Hybrid structures

An alternative approach to creating an electrode structure entirely out of a conductive and transparent material is to use a hybrid structure. Such structures are fabricated from a non-conductive but very transparent material such as glass (silicon dioxide or undoped titanium dioxide) and coated with a thin conductive layer (e.g. TCOs). For thick structured electrode films (between few micrometers and millimetres thickness), this can lead to improved transparency and widen the choice of materials and processing methods. E.g. sol-gel chemistries of silicon dioxide are well-developed and can be exploited in a wider set of conditions [56]. Depending on the pore size of the structure, a thin electrode layer can be deposited through thermal evaporation, which is relatively cheap and scalable. For more control over the layer thickness and in order to access the surface inside of narrow pores, chemical vapour deposition and atomic layer deposition are also employed. This approach has been used successfully in the past to create a large (2.3–3.3 mm pores) transparent electrode scaffold [57] for the use of eukaryotic algal cells in BPVs.

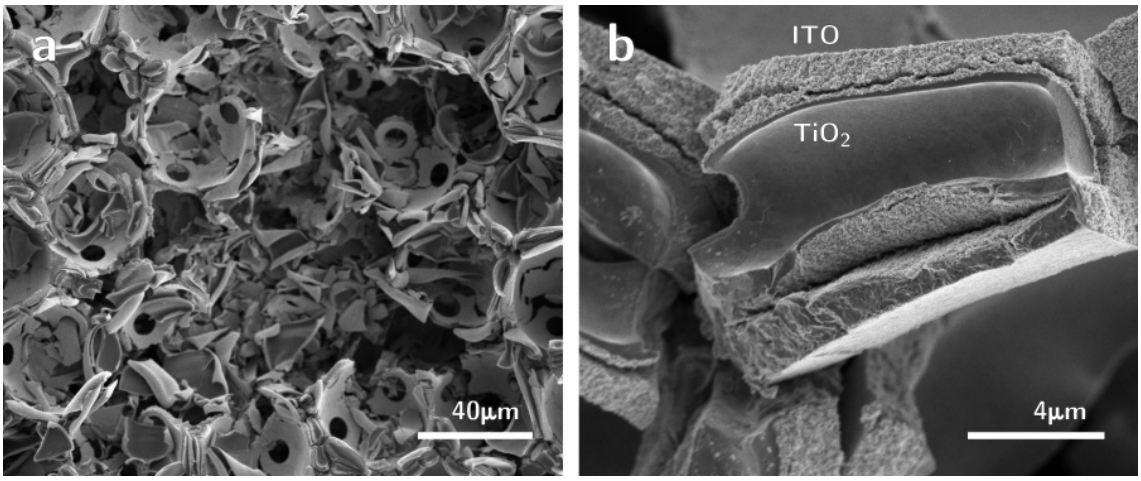

Figure 2.6: Electron microscopy images taken of a hybrid material with an attempted inverse opal structure. For this purpose, the polymer template was first coated with ITO nanoparticles, and then filled with non-porous TiO_2 via sol-gel chemistry. The structures did not survive the annealing process.

During this work, the attempt was made to fabricate a hybrid-material inverse opal structure by combining titanium dioxide (TiO_2) sol-gel chemistry (procedure from [58] without the addition of block-copolymer) with a layer of ITO nanoparticles. Creating an electrode structure with enhanced transparency in this way was not successful, because the different material shrinkage rates during annealing caused the structure to fracture, see figure 2.6.

2.3 Characterisation of electrodes

2.3.1 Biocompatibility of electrodes

For the use of electrodes as a biointerface, they obviously need to be biocompatible. In the case of ITO, there is a published track-record of biocompatibility [18, 59–61]. Non-toxicity has also been documented for some organic semiconductors [62–65] as well as gold and carbon/graphite electrodes [28].

For many other electrode materials, biocompatibility is less studied and not always easy to anticipate. There are a number of possible toxicity issues to consider when using an electrode material in the new context of biointerfaces. Many ion-based materials such as TCOs slowly leak metal ions into solution, which can be poisonous to microorganisms when elements are used with antimicrobial or toxic properties such as silver, copper, cadmium and lead. Porous electrodes can enhance ion leaking because the large surface area increases the area of leakage and corrosion significantly. Corrosion is also a major problem for biological uses of metals and alloys such as steel. Furthermore, when biocompatible materials are nanostructured, they can change their properties and become toxic [66]. Biocompatibility of nano-materials is an ongoing area of research [67, 68].

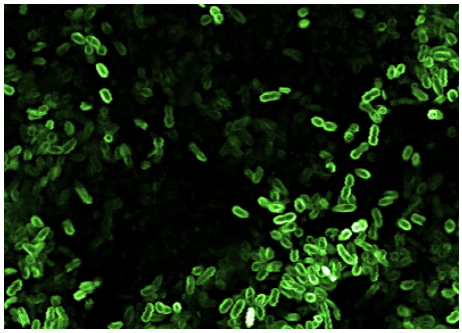

Figure 2.7: False-coloured confocal microscope image showing the autofluorescence of *Synechocystis* sp. PCC 6803 cells in BG11 medium living on a micro- and nano-structured zinc oxide (ZnO). The maintained autofluorescence is an indicator that cells can survive on the material.

In the context of BPV research, the cheap semiconductor zinc oxide (ZnO) and doped variants are of potential interest but might have toxic effects on microorganisms [69, 70]. In an exploratory part of this study, the auto-fluorescence was studied of *Synechocystis* cyanobacteria on a ZnO-nanoparticle electrode with additional inverse opal templated larger pores. Auto-fluorescence is the fluorescence of naturally present light-harvesting proteins in photosynthetic organisms, and it is used as an indication of the viability of such organisms. *Synechocystis* were placed on the porous ZnO sample (without applying a voltage) and their florescence observed under a confocal microscope (see figure 2.7),

with no signs of reduced viability. This positive test result is a first indication that ZnO based TCOs could be suitable for BPVs, but that was not further investigated here.

2.3.2 Resistance characterisation of electrodes

Sample preparation

For impedance spectroscopy testing, microporous electrode samples were prepared on ITO-coated glass substrates (to avoid an additional material interface) with the same protocol as described in Templated inverse opal structuration. They were then placed upside down on a second ITO-glass substrate which was freshly blade coated with ITO nanoparticle paste (see below), then annealed again to sinter the paste and provide a good contact. After the annealing, electrodes were filled with room-temperature curing epoxy (EPO-TEK optical epoxy, 301-1LB kit) to provide handling stability.

ITO nanoparticle films were also prepared on commercial ITO-coated glass substrates with the blade coating protocol outlined in Porous ITO nanoparticle films, and by spin-coating at different speeds. Commercial ITO-coated glass samples without any nanoparticle coating were annealed with the other samples to provide an appropriate conductivity reference (the conductivity of ITO reduces during the high temperature treatment). The mechanical junction of two individually annealed film samples provided a less reliable contact than the sintered microporous films, possibly causing a slight overestimation of their ohmic resistivity.

The overlap area probing the material films was about $0.25\,\mathrm{cm}^2$. The clean end pieces of the ITO-glass substrates were contacted with silver paste and crocodile clips.

Resistance measurements

Resistance of electrodes is generally characterised by the number of free charges and their mobility. Mobility depends strongly on the crystallinity, defects, and geometry of electrodes, such as the grain boundaries of sintered nanoparticles. The resistance of each material and fabrication process must thus be determined experimentally.

The electrical resistance of thin electrode films can be determined by 4-point probe measurements. This is an electrical impedance technique that physically separates the application of current to the substrate from the measurement of voltage, which eliminates the contact resistance of the probing pins and leads to more accurate measurements. Here, the sheet resistivity of the nanoparticle film electrodes on a non-conductive glass substrate was determined by four point probe (S302 Lucas Labs and Keithley 2400) to be $100 \pm 10\,\mathrm{Ohm\,cm}^{-2}$. The thickness of the films was $8.9 \pm 0.6\,\mu\mathrm{m}$, as found by scanning over scratches with a Dektak 6M stylus profiler. Non-porous ITO on PET electrodes

with a surface resistivity of 100 Ohm/sq. were used as purchased from Sigma Aldrich, and their resistance was experimentally confirmed.

Impedance spectroscopy is an alternative, more general method to determine the resistance of samples. By applying an alternating current potential at different frequencies and recording the amplitude and phase response of the system (here the electrode), the system's impedance can be characterised. Impedance is a generalised definition of resistance that can be described by an equivalent circuit diagram of the sample which may e.g. contain a combination of ohmic resistors and capacitors. Impedance spectroscopy was employed as the measurement technique across films. By measuring dry electrode-'sandwich'-samples, their resistivity could be estimated across the ITO-films as a function of film thickness. Obtained values were then compared to that of thicker inverse opal structure electrodes, which contained potentially conductivity limiting narrow connection elements in its 3d structure.

Sandwich samples with an area of approximately 0.25 cm^2 were built either by attaching two nanoparticle film samples on ITO glass substrate together with two paper-clips or by sintering an inverse opal like electrode onto a film (see details above). Electrode impedance spectroscopy measurements were performed across the enclosed films, using the following parameters on a Biologic SP-300 Potentiostat: Scan at 0 V from 1 MHz to 1 Hz, with 40 points per decade, a sinus amplitude of 5 mV, and waiting 0.1 periods before each frequency.

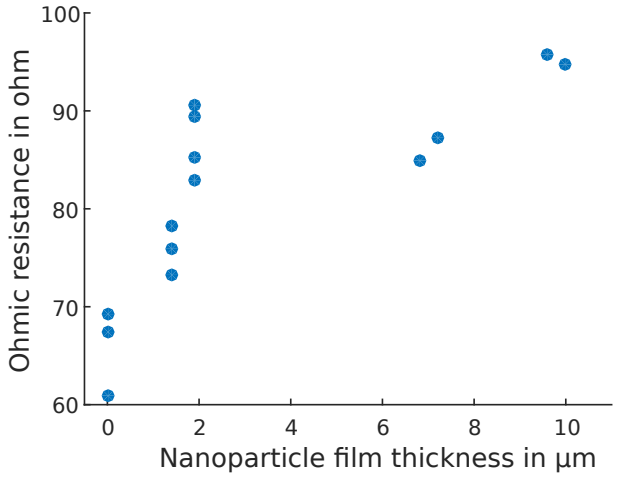

Figure 2.8: Resistance of different ITO nanoparticle film thicknesses. Data points represent the ohmic resistance (averaged real part of impedance measurement results) of dry nanoporous ITO 'sandwich' samples on an ITO glass substrates for different film thicknesses. Zero thickness refers to a pair of ITO substrates without a sandwiched coating. Four samples containing a 130-150 µm thick microporous ITO layers made from the same nanoparticles had comparably low resistance values of $110 - 165\,\Omega$.

Impedance measurements of the electrodes did not yield an imaginary component (e.g. when visualised in a Nyquist plot), which means that the nanoporous or microporous films only exhibit resistance and no capacitance. Furthermore, the real part (resistance) of the measurements was noisy but stable (non-frequency dependent = ohmic). Thus, the ohmic resistance of electrodes in this study was simply determined as the average of the real part of the recorded impedance. Without any nanoparticle coating (thickness 0), the temperature treated ITO glass junctions exhibited a resistance of ca. 65 Ω. 10 µm thick sandwiched nanoparticle films had a slightly higher resistance of ca. 95 Ω (figure. 2.8). The ca. 140 µm thick inverse opal electrodes displayed similarly low (purely ohmic) resistance of ca. 115 Ω. The low value indicates that the structure does not significantly limit the conductance of templated electrodes.

2.3.3 Characterisation of optical electrode properties

When light passes through a structured translucent material, a combination of four processes can take place: transmission, reflection, absorption, and scattering. ITO and FTO generally transmit visible light (figure 2.2), reflect infra-red light (which is why they are used in heat-insulating windows) through excitation of conduction band electrons, and absorb UV-light that has a higher energy than the optical bandgap of the semiconductor. The absorption of high energy UV-light leads to the formation of free

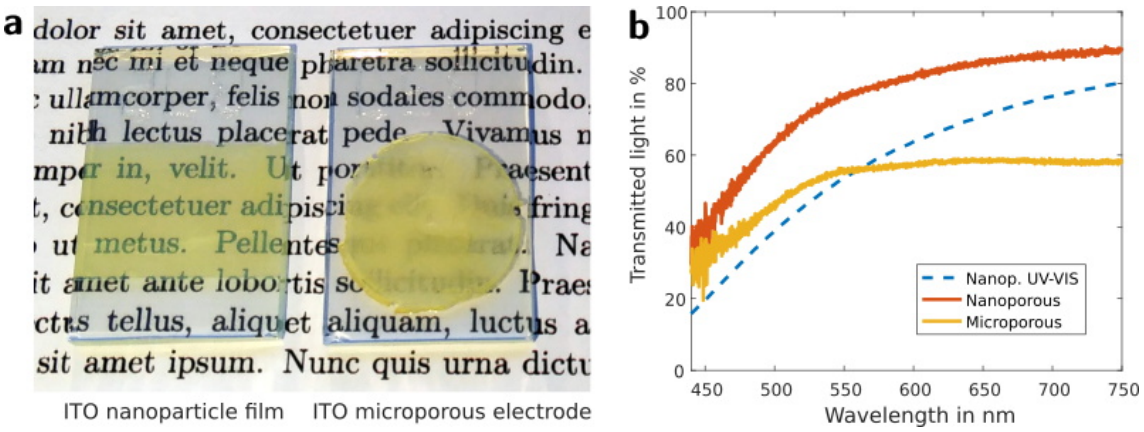

Figure 2.9: Macroscopic appearance of the translucent electrode material. (a,b) Photographs of nano- and microporous ITO nanoparticle films on FTO-glass substrates, respectively. The microporous structure scatters visibly more light compared to the nanoporous morphology. (b) Transmission spectra of the two electrode types in (a) versus a FTO-glass reference. Integrating sphere measurements record the total transmitted light, while the UV-vis spectrometer data (dashed line) only captures the light transmitted along the optical axis omitting the scattered transmitted light. The microporous electrode transmits less light because of increased scattering caused by the internal interfaces which leads to increased backscattering.

radicals on the surface of the material. These radicals are toxic to bacteria, which is why ITO and other high bandgap semiconductors can be used as so-called self-cleaning materials (in sunlight). This means TCO-based BPVs need to be UV protected. ITO has a high refractive index of ca. $n_{\mathrm{ITO}} = 1.8$ for solid films (here probably slightly less due to the Bruggemann effective medium formed by nanoparticles and small pores [71]). This high value results in strong interfacial reflections (ca. 8 % of light reflected at ITO-air, compared to 4 % at glass-air interfaces with $n_{\mathrm{glass}} = 1.5$). In micro-structured electrodes, this leads to multiple scattering of light at internal interfaces and causes the electrodes to be translucent instead of transparent. This effect contributes strongly to the appearance of inverse opal electrode structures, see figure 2.9 a. Additionally, thick layers of the only weakly absorbing material led to a noticeable amount of colouration (yellow or light-blue for ITO, depending on the degree of tin oxidation).

Wavelength dependent optical behaviour of samples was characterised with spectrometers. In the simplest case of a UV-vis spectrometer, light is passed through the surface normal of a sample (or through a cuvette) and the spectral components are analysed in transmission. Scattered light is not considered in this case, underestimating the transmission of scattering samples. This is demonstrated for an ITO nanoparticle-film electrode in figure 2.9 b (dashed line), using uncoated FTO-glass as optical reference (blank).

To also capture the scattered transmitted light (all light that is neither scattered back nor absorbed), an integrating sphere can be used. This hollow sphere with a standard-white coating internally reflects and conserves the transmitted light at all angles, enabling quantitative comparative measurements. Results for the same electrode structures are shown in figure 2.9 b (solid lines). The transmission spectra in figure 2.9 b were recorded with a Varian Cary 300 UV-vis spectrophotometer, and with an Ocean Optics FOIS-1 integrating sphere linked to an Ocean Optics USB4000 spectrometer. Ca. 50 % of the visible spectrum was diffusely transmitted through the dry inverse opal film, and ca. 80 % through the dry nanoparticle film. Note the increased transmission, compared to the dashed line recorded by UV-vis spectrophotometry, which is due to the scattered transmitted light. Scattering and absorption (visual colouration of the electrode) were more strongly pronounced in this electrode than in previously described ITO-based inverse opal structures (e.g. in [72] ca. 80 % of the visible spectrum was transmitted), due to the unusually large thickness of the electrode.

2.3.4 Characterisation of microscopic electrode structuration

Microscopy is the general method of choice to visualise structures and distributions in samples. Optical microscopy is useful and versatile method, but can only be used to

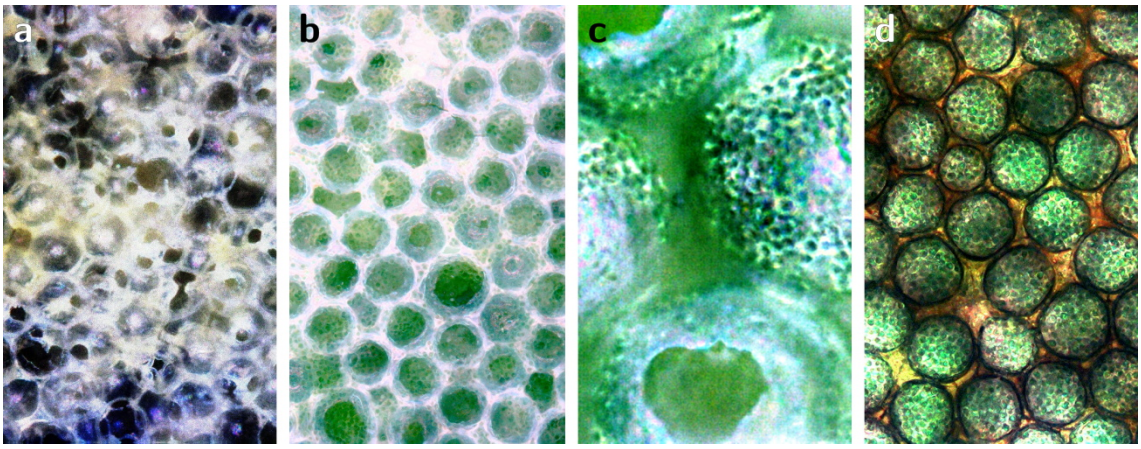

Figure 2.10: Optical microscope images of cyanobacteria in templated electrodes with 40 µm voids in bright-field 20x (a) dark-field 20x & 100x (b,c) and transmission 20x (d).

image objects larger than its resolution limit (about half a micrometer in its standard form). Here, it could be used because the inverse opal templated structure is significantly larger than the resolution limit. In contrast to most other imaging methods, optical microscopy allows to visualise the inside of electrodes, because TCO electrodes are transparent or translucent to visible light. The method can thus be used to study the shape of electrodes and how cyanobacteria (here *Synechocystis* with a cell diameter of about 2 µm) populate the structure.

In bright-field (reflection) optical microscopy, the sample is illuminated through the objective and reflected light from the sample is collected through the same objective. This configuration is not capable of creating a good image of the thin, transparent ITO-walls of the inverse opal structure (figure 2.10 a). Instead, dark-field mode can be used, where the optical pathway of illumination and image acquisition are separated by passing the illuminating light exclusively through an outer cone of the objective. In this configuration, light directly reflected by the surface (specular reflection) is not collected

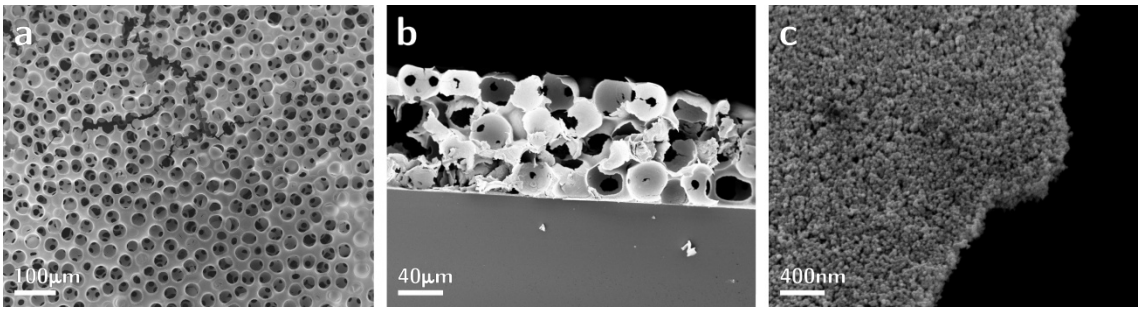

Figure 2.11: SEM-images of an inverse opal structured porous electrode film made from sintered ITO nanoparticles. (a) Top view, (b) cross-section of fractured electrode, (c) high-magnification top-view, showing the nanometer-sized pores between nanoparticles.

(e.g. a glass slide or piece of metal would appear black). Instead, the scattered light, e.g. by the ITO nanoparticles or bacterial pigments, is collected in the centre of the objective with high contrast (see figure 2.10 b,c). Another useful mode is transmission microscopy, where light is passed through the translucent sample. Here, absorption of the electrode material becomes emphasised, because light has to pass through the entire film (figure 2.10 d).

Optical microscopy was conducted with an Olympus BX60 microscope and Olympus UMPlanFl 20x and 100x objectives. For all images of figure 2.10, multiple photos were taken at manually adjusted different focal depths with an AxioCam MRc 5 (Zeiss) camera and Z-stacked with CombineZP software. Slight adjustments were made to the colour balance and contrast of the image to yield optimal results.

More control and higher resolution can be achieved with scanning electron microscopy (SEM), see figure 2.11 and 2.12. Since the TCO electrodes are conductive, they can be imaged directly. Samples for cross-sectional imaging (figures 2.11 b and 2.12 c,d) need to be sputter coated with a thin layer of noble metal to avoid charging of the glass substrate. The surface of structure cross-sections, details of connecting pores (e.g. figure 2.11 c) and pores on the nanometer scale can be examined with this technique.

SEM-images were recorded with a Leo Gemini 1530 VP SEM with a Schottky-emitter consisting of a zirconium oxide coated tungsten cathode and an in-lens secondary electron detector.

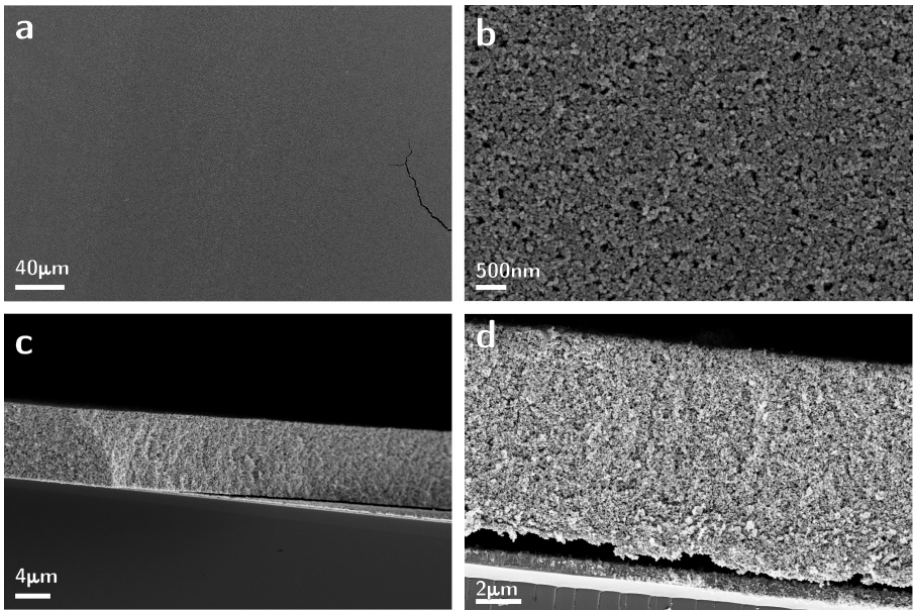

Figure 2.12: SEM-images of a porous electrode film made from sintered ITO nanoparticles. (a,b) Top views at different magnifications (the crack-defect in (a) was pictured to provide image contrast and was not characteristic for the sample), and (c,d) cross-section views of fractured electrodes.

2.4 Discussion

It was shown that biocompatible and translucent electrodes with structures on different length scales could be successfully fabricated. Cyanobacteria were able to populate the inside of templated inverse opal electrodes, and the conductivity of those electrodes did not appear to be limited strongly by their thickness or by their structure.

While the nanoparticle film electrodes were usually crack free up to a thickness of 10 µm, the inverse opal structured electrodes contained a large number of cracks. The fractions have the positive effect of providing additional entry points for microorganisms to the structure. For other applications, cracks could be circumvented by balancing the material addition per steps and the temperature annealing protocols. It might also be worthwhile exploring sol-gel chemistry procedures, in conjunction with templating approaches, in order to avoid additional created pores on the 10 to 100 nm length scale (if unwanted) and to allow the use of a wide array of materials at reduced cost. However, it seems challenging to apply sol-gel protocols to the large length scales demonstrated here.

Furthermore, there seems to be scope to explore the benefits of organic electrode materials, which have proven to be superior in some biological applications due to their softness [73–76]. Organic semiconductors tend to be less transparent, but could be used in hybrid materials, e.g. as a coating produced by electrodeposition. The work with semiconductors for bio-anodes and cathodes in general could also prove useful to reduce unwanted side reactions as well as cost, once bioelectrochemical reaction pathways are better known and the bands of semiconductor electrodes can be aligned accordingly.

Chapter 3

Biophotovoltaic techniques for quantitative bioenergy measurements

3.1 Significance and contributions

This chapter introduces experimental methods for biophotovoltaic measurements, sample preparation, energetics, and control experiments. Because little systematic techniques exist yet in the growing field of biophotovoltaics, a complete set-up was developed and characterised for this thesis. The chapter contains data and information on appropriate light sources, the design of bioelectrochemical devices, controlled parallel biophotovoltaic (BPV) measurements in up to 12 channels and the importance of the control of temperature and background signals in the culture medium.

There was also an indirect outcome of the work presented in this chapter: To make these hardware designs and procedures more accessible to researchers, I led the development of an infrastructure tool-set called DocuBricks which contains software for the documentation of hardware projects, a database and guidelines. It enables the high-quality communication of open source hardware designs and has received attention in the media and the field of Open Innovation. As an extension of this work, I became co-editor-in-chief of the Journal of Open Hardware.

Acknowledgements

All the content of this chapter (custom concepts, hardware design, planning of measurements, data acquisition, analysis, presentation and description) is exclusively my work, except for collaborative contributions by the visiting student Daniel Haertter, who I supervised for six months from November 2014 to April 2015. He contributed to the design, assembly and control of the solar simulator and the 3D printed base of electrochemical devices. The advice of Paolo Bombelli has also been an important factor

contributing to the presented results. He helped with suggestions e.g. for cathode materials and starting measurement parameters, as well as the supply of cyanobacteria cells. His pioneering experience in this emerging field was an asset especially during the development of experimental techniques. I am also grateful to my supervisors Ullrich Steiner and Christopher Howe for advising me and helping to identify possible shortfalls of the measurements in order to further optimise my procedures. Interactions with the wider Steiner Lab, especially technology savvy Karl Goedel and Raphael Dehmel, have also been of great help for the general progress of the work.

3.2 BPV energetics

Understanding the energy levels involved in the generation of electricity in BPVs is essential for the design of effective devices and measurement techniques. Biophotovoltaic devices generate electric energy though photo-electrons generated by living photosynthetic organisms on the anode, and a cathodic reaction taking place at a lower potential (here the recombination of oxygen and protons to water). The energy levels involved in this process are detailed in the schematic diagram in figure 3.1. The starting point of photosynthesis is photocatalytic water splitting, during which the electrons are gained. This is achieved through the absorption of two photons by the two photosystems (PSII

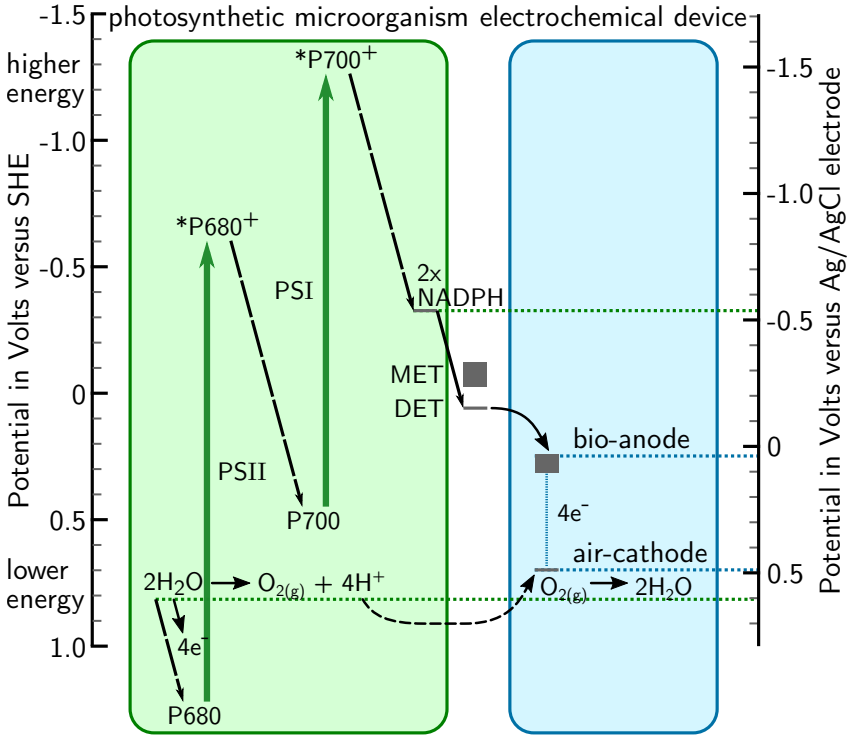

Figure 3.1: **BPV energy scheme.** Energy levels inside photosynthetic organisms and charge transfer to external electrodes of biophotovoltaic devices.

and PSI), which form the characteristic Z-Scheme. The derived electrons may be stored through the production of NADPH molecules and can leave the cells via extracellular electron transfer (MET & DET). The literature suggests similar values for redox-potentials of electron export in known organisms [77]. Taking interfacial energy transfer losses into account, these potentials determine the maximum voltage that can be generated in the device, versus the fixed potential of a platinum air-cathode. In practice, the cathode potential of air-cathodes does not reach the theoretical level of water splitting [77], which is indicated by the higher position of the cathode level in the scheme. In summary, figure 3.1 indicates the electrochemical potential range in which to expect biological electron transfer processes and illustrates the measured electrode potential of bioanode types used in this work.

3.3 BPV experimental techniques

This is a brief introduction of the methodologies and bioelectrochemical characterisation results used in this work with biophotovoltaic devices (BPVs). Section 3.3.1 details procedures to grow and quantify relevant biological organisms, while section 3.3.2 introduces the most important types of bioelectrochemical measurements.

3.3.1 Cell culture and quantification

A number of different photosynthetic organisms have been used for bioelectrochemical current generation. This work focuses on the photosynthesis model organism *Synechocystis* sp. PCC 6803. Its photosynthetic proteins and electron transfer chain is comparably well studied: it closely resembles that of algae and many plants, and genetic tools are available for the organism. For comparison, the cyanobacterium *Nostoc punctiforme* was used, and the non-photosynthetic bacterium *Shewanella oneidensis*.

Photosynthetic bacteria growth and handling

A stock of *Synechocystis* sp. PCC 6803 and *Nostoc punctiforme* cells was created by placing ca. 20-100 µl of cells (each) in Eppendorf tubes together with glycerol (ca. 1:1 ratio). The samples were shock-frozen with liquid nitrogen and stored at -80 °. For the cell-cultures used in experiments, stock-samples were defrosted at room temperature and grown on an agar plate with BG11 medium for a week, before one colony was transferred into liquid BG11 medium. The cells were then routinely cultured in aqueous BG11 supplemented with about 1 mM $NaHCO_3$ and maintained in sterile conditions at 23-30 °C under continuous moderate light of 40-50 µmol photons/m^2/s and shaking of 160 rpm.

Before transferring cells into electrochemical devices, they were concentrated via centrifugation (ca. 2000 g for 10 min). A small volume of cells (120 - 160 µl) containing 134 nmol chlorophyll-a was pipetted into devices pre-filled with BG11 medium, after uninoculated reference measurements. The heavy cell suspension quickly settled onto the anode to form a biofilm before the cell-suspension could mix with the bulk electrolyte.

Chlorophyll quantification

For quantitative biophotovoltaic measurements, it is important to use the same amount of cells or chlorophyll-a in each device. Therefore, the chlorophyll content of the concentrated cell suspension has to be quantified before it can be used. The quantification was achieved following an established method [78] to extract the chlorophyll from cells with solvent (here methanol) and correlate the absorbance of solutions at two wavelengths (A_{665} @ 665 nm and A_{652} @ 652 nm) to chlorophyll a ($\mathrm{Chl_a}$) concentration. The following equation correlated the chlorophyll a concentration with the two absorbance values in methanol

$$\mathrm{Chl_a} = (18.22 \cdot A_{665} - 9.55 \cdot A_{652}) \cdot \beta \tag{3.1}$$

where $\beta = (\mathrm{vol_{methanol}} + \mathrm{vol_{suspension}}) \ / \ \mathrm{vol_{suspension}}$ is the dilution factor for the cell-suspension in methanol [78]. Prior to the measurement of absorbance in a UV-vis spectrometer, the freshly suspended cells in methanol (99.8 %m, Sigma-Aldrich) were slowly shaken in a cool area for 15 minutes to break the cells open and dissolve the pigments, and then spun down at high speed (e.g. 14k RPM) in a centrifuge to separate the heavier cell components such as the cell wall from pigments in solution. The solids collected in the tube bottom after centrifugation was grey in colour, signifying that the green pigments have been removed.

Shewanella bacteria

Shewanella oneidensis bacteria do not contain chlorophyll, and thus the quantification protocol from above could not be applied. However, the same amount of concentrated cell suspension was added to each *Shewanella* containing device (140 µl each, cells were separated by repeated pipetting with a 1 ml tip). *Shewanella oneidensis* also contains pigments, and these red coloured molecules are also involved in the extracellular electron transfer, and thus directly relevant to measurements here. As an alternative reference point for absolute cell numbers and pigment concentration, transmission spectra were recorded at different cell densities, see Fig. 3.2.

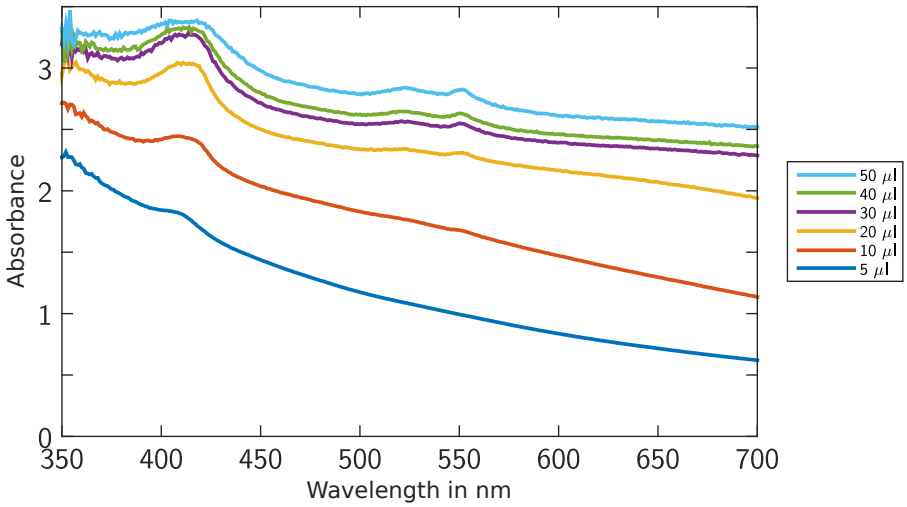

Figure 3.2: UV-VIS absorption spectra of liquid *Shewanella* cell-culture at different dilution ratios. The amount of concentrated cells between 5 µl and 50 µl (see legend) was added to 1 ml of LB medium (reference solution) for each measurement. 140 µl of concentrated cell-culture was used per device for electrochemical measurements. This data serves as a reference for the amount of cellular pigments added to devices.

3.3.2 Conducting bioelectrochemical measurements

While the field of BPV is still relatively small and only recently receiving increased attention [1], a wide range of bioelectrochemical measurement techniques have already been applied in the related field of microbial fuel cell studies such as chronoamperometry, cyclic voltammetry, impedance spectroscopy, square wave voltammetry and corrosion & depletion measurements with electrochemical quantification of gases and nutrients in solution. For bioelectrochemical measurements in this thesis however, I relied on only two relatively basic modes of measurements, namely chronoamperometry and cyclic voltammetry. Living organisms are complex samples with millions of unidentified chemical compounds, some of which can have unknown electrochemical signatures. Because of this complexity, it remains speculative whether techniques (such as impedance spectroscopy [79–82]) that rely heavily on intricate interpretations and theoretical modelling can deliver valuable insights for the majority of bioelectrochemical studies.

Chronoamperometry

Chronoamperometry (derived from the Greek word *chronos*) simply means the observation of electrical current over time. It is an ideal tool with which to study the amplitude and temporal behaviour of an effect such as light induced electron generation at the anode. For example, figure 3.3 shows a data fragment of a chronoamperometry measurement with one of my BPV devices under short light irradiation periods with different

intensities. The peak values (data points during 60 seconds around the peak value indicated in blue) and their magnitude with respect to the preceding dark current baseline (indicated in red) can easily be extracted directly from the measurements.

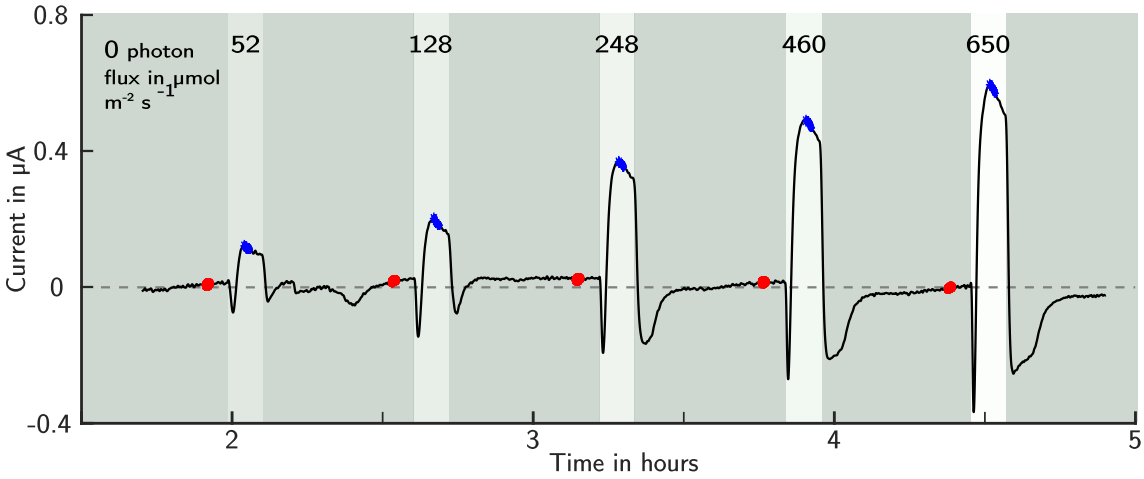

Figure 3.3: Electron generation over time (chronoamperometry) of a single BPV channel with *Synechocystis* bio-anode. The light response data was acquired during several periods of illumination with increasing photon flux, as indicated by the values at the top of the graph and background shading.

Cyclic Voltammetry

Cyclic voltammetry is the equivalent of optical spectroscopy in the field of electrochemistry, as it reveals information about the different electrochemical processes appearing in the device at their respective electrode potentials. This is achieved by slowly changing an applied voltage to the device in both directions (negative and positive) with a potentiostat (an external multichannel power source). This, in turn, changes the potential of the electrodes systematically and their thermodynamic ability to accept or donate electrons to molecules in the solution of the electrochemical device. Reduction and oxidation reactions at the anode and cathode can be separated and analysed in this way [83, 84] .

In order to relate the values obtained in different experiments to each other, a suitable reference electrode should be used as a third electrode in cyclic voltammetry measurements. A reference electrode does not participate in electrochemical reactions, but the potential (or voltage) of the working electrode (the electrode under investigation, here the anode) is measured against the fixed potential of the reference electrode. Here, a reference electrode composed of an encapsulated silver wire with silver chloride solution (Ag/AgCl) was used. It has a known potential of -210 mV with respect to the standard hydrogen electrode (SHE). The potential of the counter electrode (the third electrode, here the cathode of the device) is usually shifted to a value by the potentiostat that guarantees the non-limiting supply of electrons to complete the circuit.

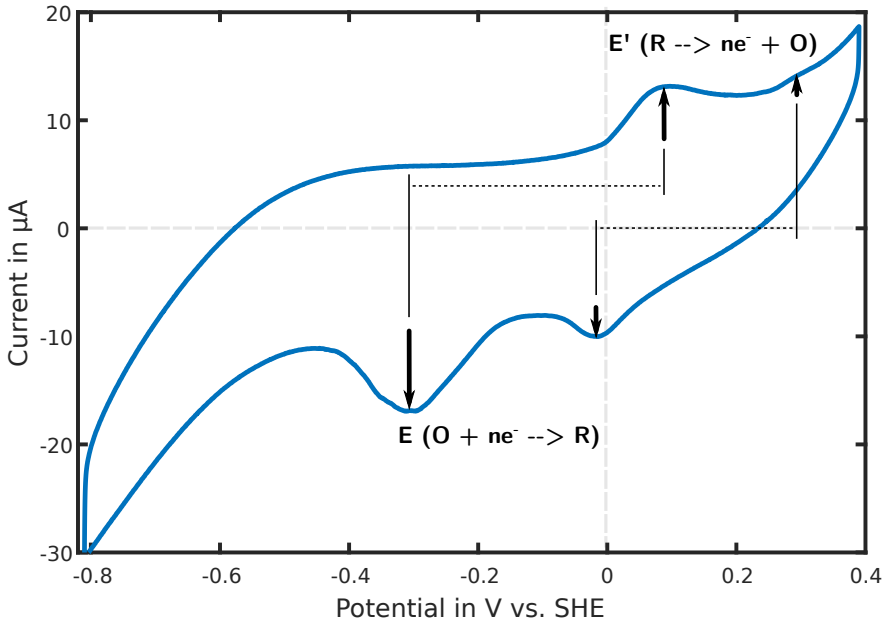

Figure 3.4: Data of cyclic voltammetry measurement at a scan rate of 0.5 mV/s, *Synechocystis* nanoporous bioanode in BG11 media and with Ag/AgCl reference electrode. Arrows indicate the position of oxidation (electron donation to the anode) and reduction (electrode acceptance from the anode to reduce redox molecules in solution) peaks.

Figure 3.4 shows a recorded cyclic voltammetry measurement as an example. The current generated at a particular voltage follows a hysteresis with peaks. This is caused by irreversibility in the system (see also next section on limitations) and reactions with redox active molecules in solution. The two oxidation and reduction peaks in this example indicate the presence of two reversible redox active species. For each redox reaction appearing at the anode, the Nernst equation

$$\Delta\mathrm{E} = \Delta\mathrm{E}^\circ + RT/nF \cdot \ln([\mathrm{O}]/[\mathrm{R}]) \tag{3.2}$$

relates the measured potential difference $\Delta\mathrm{E}$ to the concentration of reduced species $[\mathrm{R}]$ and oxidised species $[\mathrm{O}]$ (having lost n electrons with respect to R), with the ideal gas constant R, Faraday's constant F, temperature T and the difference of standard reduction potentials of the redox species $\Delta\mathrm{E}^\circ$.

Following the Nernst equation, a redox-species causes a peak in current during site voltammetry because of the following mechanism: If we consider the start of the sweep at low electrode potentials, the oxidation of a redox species in solution is prevented by the counteracting voltage. When the increasing voltage during cyclic voltammetry approaches the oxidation potential of a molecule in solution, species close to the surface of the electrode start reacting and cause an increase in current ($\mathrm{R} \rightarrow n \cdot e^- + \mathrm{O}$, see figure 3.4). More reduced species diffuse from the solution to the electrode surface and the current increases further. When the diffusion layer has grown far enough away from

the electrode surface to prevent fresh molecules arriving as fast as they react, a peak is reached and the current starts to drop for higher voltage values. The inverse process appears when the voltage ramp is reversed and oxidised species are reduced again. The height of the peaks as well as their location can shift for (*i*) species with slow electron transfer reactions, (*ii*) low chemical reactivity, or (*iii*) at high voltage scan rates. In such cases, the redox potentials can be extrapolated from a series of scans at varying speeds.

The generation of electrons by bio-catalytic water splitting depends on the input energy of the illuminating light source, but not on the electrode potential of the anode which is in contact with the photosynthetic microorganisms. These independently produced electrons can, however, only be collected in a BPV device if the bio-anode potential is lower than the energy of electron export processes (see Fig. 3.1). Thus, measuring the electron collection as a function of anode potential by cyclic voltammetry (CV) ideally results in an s-shaped curve characterised by a quick rise in current to a stable value at the potential of the electron export processes, and an equivalent current drop during the backwards scan [83].

Losses

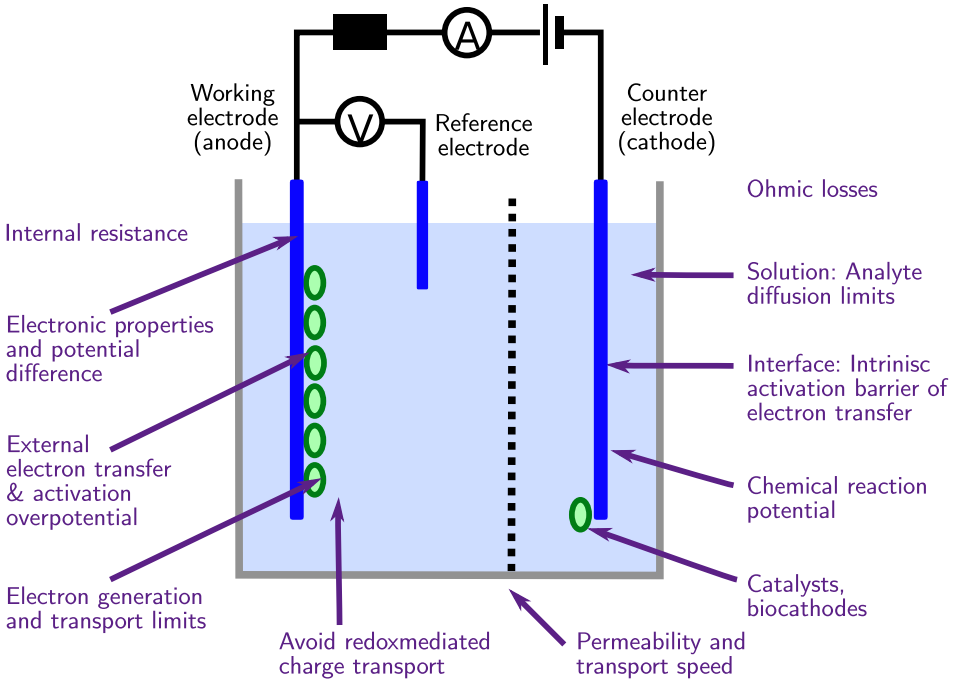

Figure 3.5: Schematic visualisation of a bioelectrochemical unit with working, reference, and counter electrode, positions of measurement points and voltage application by a potentiostat, and indication of various losses, that can appear at different points of the electrochemical unit.

Energy losses can occur at many places in the bioelectrochemical unit [29, 85], as indicated in figure 3.5. For example, the conductivity of electrodes and solution, large distances and chemical reaction overpotentials can limit measurements. Where relevant, the parameters will be discussed in more detail in section 3.5 when describing the design and testing of custom biophotovoltaic devices.

3.4 Custom solar simulator for bioenergy measurements

Solar simulators are standardised light sources used in photovoltaic research that mimic the solar spectrum at a standard intensity of 1000 W/m^2, referred to as 'one sun'. Commercial solar simulators are classified by the criteria of (*i*) match with the solar spectrum, (*ii*) irradiance homogeneity, and (*iii*) temporal stability. They tend to be expensive piece of equipment used to illuminate very small areas of several square centimetres. The requirements for a sun-imitating illumination source in biological research are often very different. A large area on the order of square metres needs to be affordable illuminated with a relatively constant, roughly sun-like-white spectrum of visible light (see figure 3.6). Its intensity should match real-world locations (e.g. 194 W/m^2 average in Madrid) rather than the much higher solar simulator standard (which would damage biological tissues). At the same time, the temperature control of illuminated biological samples is a chal-

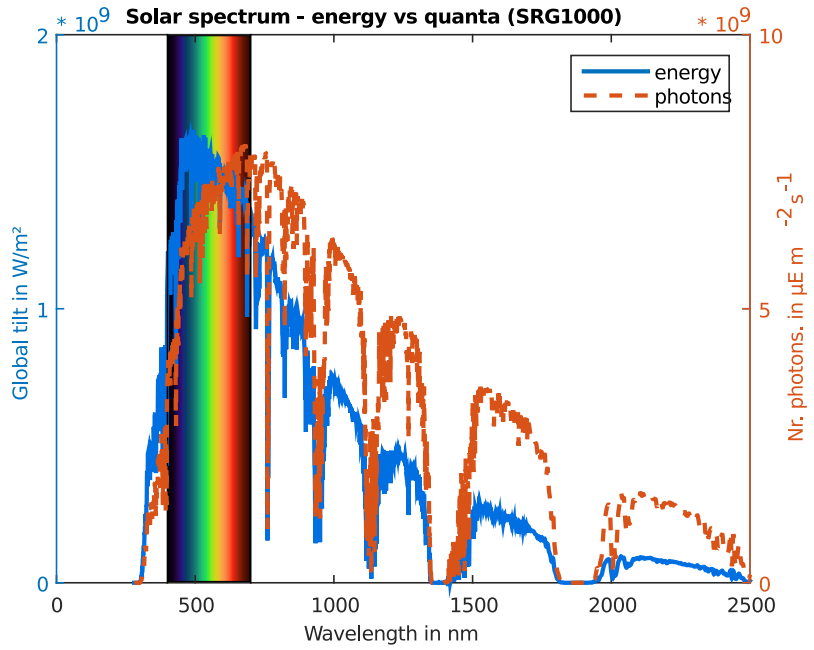

Figure 3.6: The solar spectrum at ground level in terms of energy and photons. The relatively small region of visible light is schematically indicated.

lenge. In this context, most of the infra-red light (heat) of the solar spectrum can be omitted from the light source in favour of better temperature control and experiment reproducibility. UV components also have to be excluded at high-intensities to reduce photo damage.

To meet these criteria, I had to design my own custom bio-solar-simulator, covering only the visible light spectrum while illuminating a large area. I chose an LED-based approach to avoid the challenges of heat management, dimming and large amounts of spectral filtering necessary when using, for instance, a Xenon arc lamp. Because real-world solar irradiances are large, the choice was constrained to very high power and broad-angle LEDs rather than the more common LEDs, which have previously been used to match the solar spectrum [86, 87].

3.4.1 Design and construction of an LED light source

The design of the LED bio-solar-simulator contains only three types of high-power LEDs, which jointly cover the visible light spectrum with a relatively good match to sunlight, see yellow curve in figure 3.7.

The light source mainly consists of two different tones of white LEDs (Lumileds Luxeon M LXR8-RW50 and Cree CXA1304) complemented by a cyan-coloured (peak at 505 nm) LED (Lumileds Luxeon Rebel LXML-PE01-0070). In white LEDs, a fluorescent dye emits a broad light spectrum. The dye, in turn, is excited by blue light emitted from

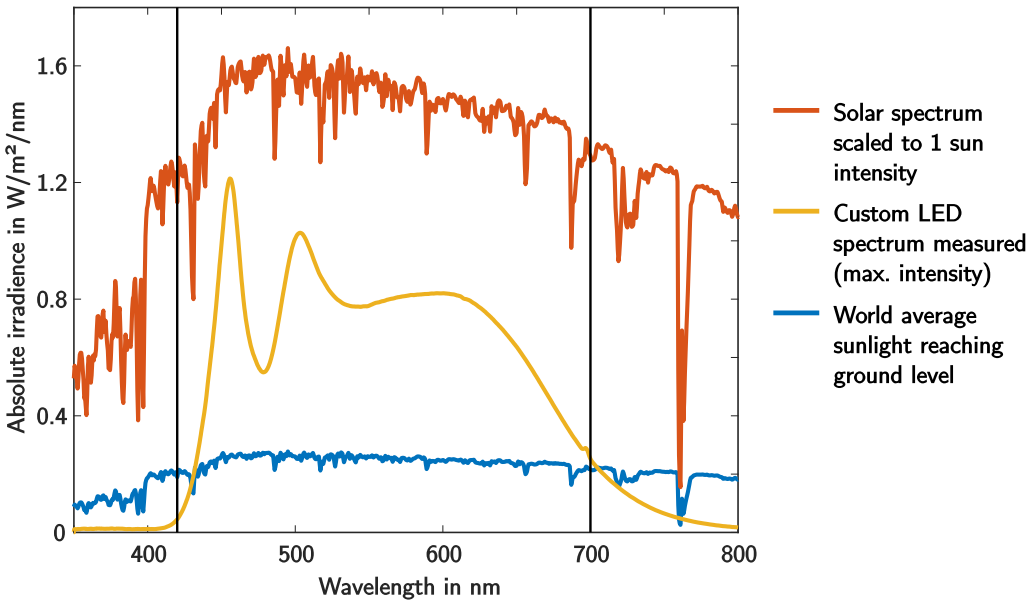

Figure 3.7: Illuminating light source. Spectrum of custom LED light source (yellow) at maximum intensity compared to the solar spectrum (red) (reference AM 1.5 Spectrum by ASTM, global tilt) at intensities of 1000 W/m^2 (solar simulator standard) and the world average sun intensity reaching ground level (blue).

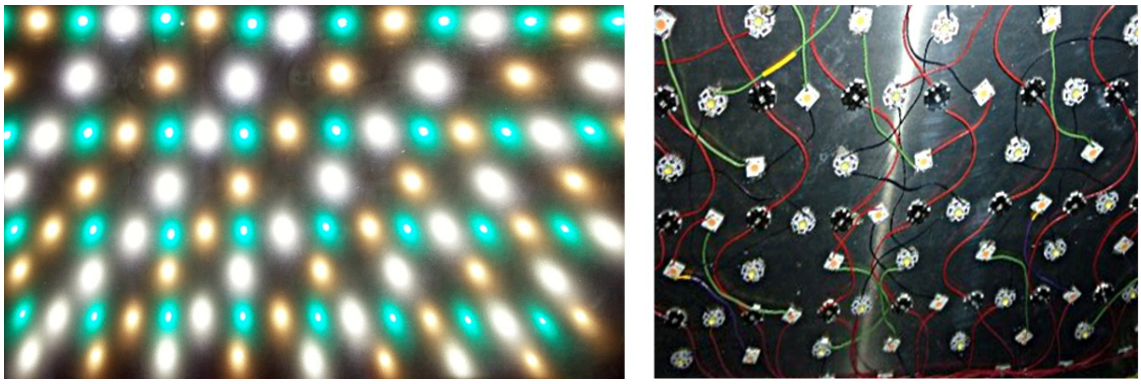

Figure 3.8: Photographs of bio-solar-simulator LEDs. (Left) LEDs in operation at low light level. The array of LEDs was viewed through a polycarbonate sheet and a weak diffuser layer separating the light source from the experimental chamber. (Right) Soldered LEDs on aluminium sheet.

the LED semiconductor junction (corresponding to the leftmost peak in the spectrum shown in figure 3.7). The cyan-coloured LED emits one broader peak at the location of the white LEDs' spectral gap between the blue excitation peak and the fluorescence maximum. When combined, the three LEDs produce a very even spectrum in the visible light range.

An evenly spaced array of the three LED over an area of just under a square metre made up the final light source, see figure 3.8. The number of respective LEDs was chosen in a suitable ratio to compensate for relative intensity differences. All LEDs were glued with (heat-)conductive epoxy onto a large aluminium sheet/heatsink, and where appropriate they were additionally soldered onto contact-pad stars. A suitable enclosure was designed. The LED-on-aluminium sheet formed the lid of the enclosure, complemented by additional heatsinks and cooling fans (see figure 3.9). Cooling of the LEDs is important to ensure conformity of the LED properties (which can change at high temperatures), long lifetimes, and to prevent overheating at full power operation. The enclosure was designed to contain two sections, see figure 3.9 left: (*i*) a closed upper metal and metal-compound lined part (containing LEDs, wires, a temperature sensor and an optical diffuser sheet, Lee Filters 420 Light Opal Frost) and (*ii*) a lower part used for high-humidity bioenergy experiments, which was separated from the top by a mechanically stable and UV absorbing polycarbonate sheet. The lower part was made human-accessible via a hinged front sheet (open in figure 3.9). While the movable front sheet was made from the same mechanically stable metal-polymer compound sheet (5 mm Black Foamalux, Engineering & Design Plastics Ltd. Cambridge) as the top compartment, the other walls were made from a thicker polymer foam with better heat insulation properties (Black Matt/Gloss Skybond, Engineering & Design Plastics Ltd. Cambridge). The non-conductive panels used in the lower part of the enclosure were

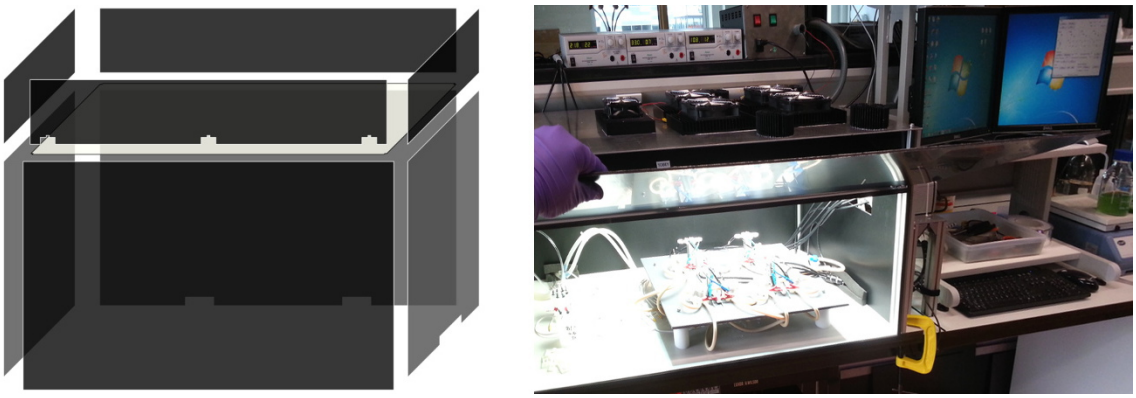

Figure 3.9: Enclosure for bio solar simulator. (Left) Schematic of the contained panels; (Right) Photograph of the set-up in use, with opened front-panel.

additionally shielded electromagnetically from the outside (by metal grids), completing a Faraday cage for low-noise electrochemical measurements.

One of the major design challenges of the light source was the identification of suitable power sources, which could deliver sufficient current to LEDs (several Ampere) while also being current limited (instead of the more common voltage limiting devices). The light output of LEDs is connected to the applied electrical current. Operating LEDs with a power source that is voltage and not current controlled can lead to light flux instabilities and possible failure of the LEDs, because the LED resistance can vary with external parameters, such as temperature. Furthermore, LEDs are most commonly dimmed by pulse-width modulation (variations of fast on-off switching), which appears as a change of light intensity to the human eye, but induces a different energy economy in photosynthetic organisms [88, 89].

To avoid these side effects, one current limiting power source was used for each of the three LED types (2x Manson HCS-3302 up to 32 V_{DC} and 15 A (cyan and Lumileds), Manson HCS-3304, up to 60 V_{DC} and 8 A (Cree) to ensure simple changes in light irradiation. The LEDs were wired in a combination of parallel and series configurations, to comply with the power limits of each source.

3.4.2 Light calibration and testing

To characterise the irradiation source, it is not only important to capture the spectral intensity distribution (which can be done with any spectrometer), but also the absolute irradiation at different dimming levels. This has been achieved by calibrating the spectrometer (Ocean Optics USB4000) with an irradiance reference light source (Ocean Optics LS-1-CAL). During calibration and measurements, light was channelled to the spectrometer by a 600 µm cladded optical fibre (Ocean Optics QP600-2-VIS/BX, 400-2100 nm) with a cosine-corrector (diffuser) fibre cap (Ocean Optics CC-3), removing the

bias which would otherwise be caused by the directionality of incident light. The resulting distributions shown in figure 3.10 indicate a continuous increase of light irradiation with LED driving current (note that more spectra were recorded at low driving currents resulting into an uneven spacing between curves).

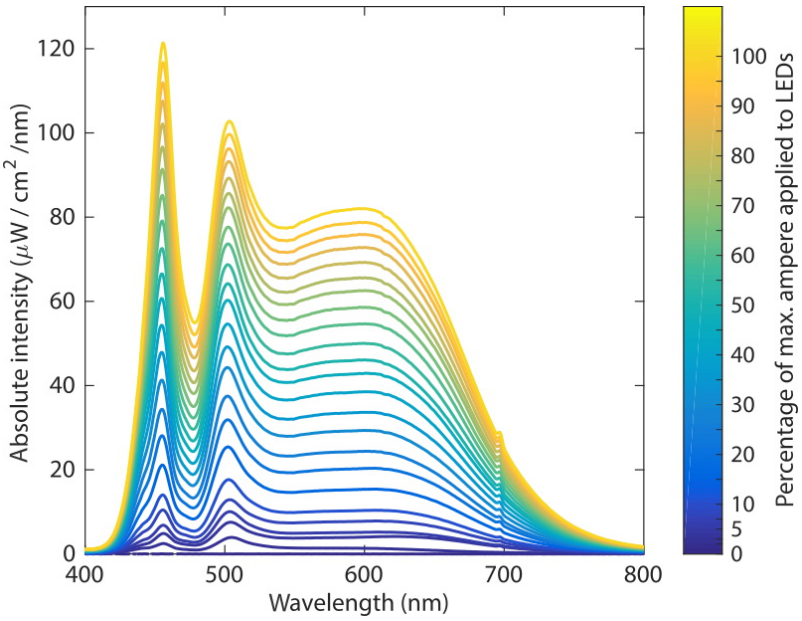

Figure 3.10: Absolute radiation levels of the custom large area LED solar simulator at different LED driving currents.

3.5 Custom biophotovoltaic devices

For this work devices for photo-bioelectrochemical measurements had to fulfil seven criteria: (*i*) accommodate upright air cathodes (they need to be upright in order be positioned close to the anode while not blocking the light and preventing microorganisms from settling and gas bubbles from being trapped); (*ii*) allow the exchange of anodes from the bottom of devices between uses; (*iii*) allow good temperature control of individual devices (devices heat up during illumination which can effect measured currents, see below for temperature-sensitivity analysis); (*iv*) accommodate an optional reference electrode close to the anode; (*v*) allow the use of relatively large volumes of buffer, to avoid nutritional depletion effects; (*vi*) have an open top in order to allow light (the energy source) to enter the device loss free, and in order for possible (oxygen) gas bubbles to escape the devices; and (*vii*) the devices had to be compact and affordable enough to operate 12 devices in parallel within the irradiation area of the bio-solar-simulator. Parallel measurements with the same batch of bacteria culture and under the same high-intensity light source were essential to obtain reliable mean results in experiments.

3.5.1 Design of biophotovoltaic devices

Figure 3.11 depicts the electrochemical devices used as part of this work for photo electricity measurements with up to 12 parallel channels. The devices were 3D printed to enable a compact, shareable design with temperature control via hollow walls using a circulating water bath. Anodes (various materials on FTO-glass) were inserted from the bottom on a printed anode holder, and sealed with an O-ring. Three pieces of platinum nanoparticle based air cathodes with a combined area of ca. 6 cm^2 were arranged upright and close to each anode opening. A removable 3D printed lid allowed the attachment of a reference electrode as well as temperature sensors. The schematic device cross-sections in figure 3.11 b indicate the location of each of these elements.

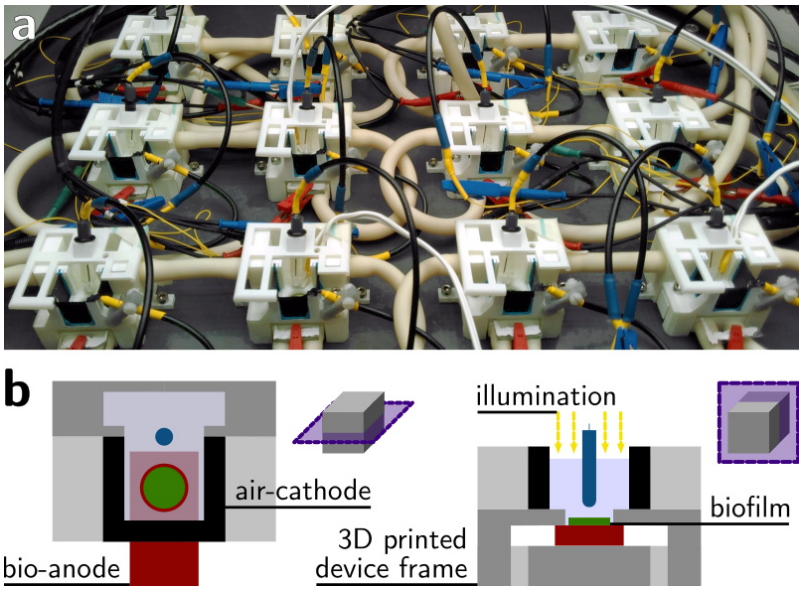

Figure 3.11: Design of biophotovoltaic devices. (**a**) Assembled and connected 3D-printed devices, incl. reference electrodes with blue connectors, positioned in the homogeneous illumination area. (**b**) Two schematic perspectives of cuts through a device indicating the locations of electrodes and biofilm.

The devices were printed on a Projet 3500HD Max 3D printer depositing Visijet M3X acrylic material with an accuracy of 0.025 mm. The support material (VisiJet S300) was washed out with hot sunflower oil and IPA. Upright air-cathode windows (carbon paper with Pt-nanoparticles, Alfa Aesar 45372 Hydrogen Electrode/Reformate) were sealed into the 3D printed device with dental silicone (Zhermack, Elite HD+ Super Light Body). The anodes were tightened in the device with screws and sealed with a nitrile O-ring. A good contact between the anode edges and the connector-clamp was ensured by conductive silver paste.

3.6 Quality control

The presented architecture of BPV devices is the result of several design iterations, improving the hollow-device-wall area for water cooling (e.g. extension to the anode-sample holder), fragility (rounded edges for improved stability of extrusions) and leakage (e.g. optimisation of slots for air cathodes). Chapter 4 also describes that the cathode is non-limiting for the observed photocurrents in this study. Instead of detailing practical device aspects, this section focuses on the quality control of biophotovoltaic measurements, specifically testing the influence of temperature and electrochemical background signals caused by the growth medium of cyanobacteria (BG11).

3.6.1 Testing temperature dependence

Electrochemical measurements are generally temperature dependent; for instance, temperature appears as a factor in the Nernst equation (see section 3.3.2). At the same

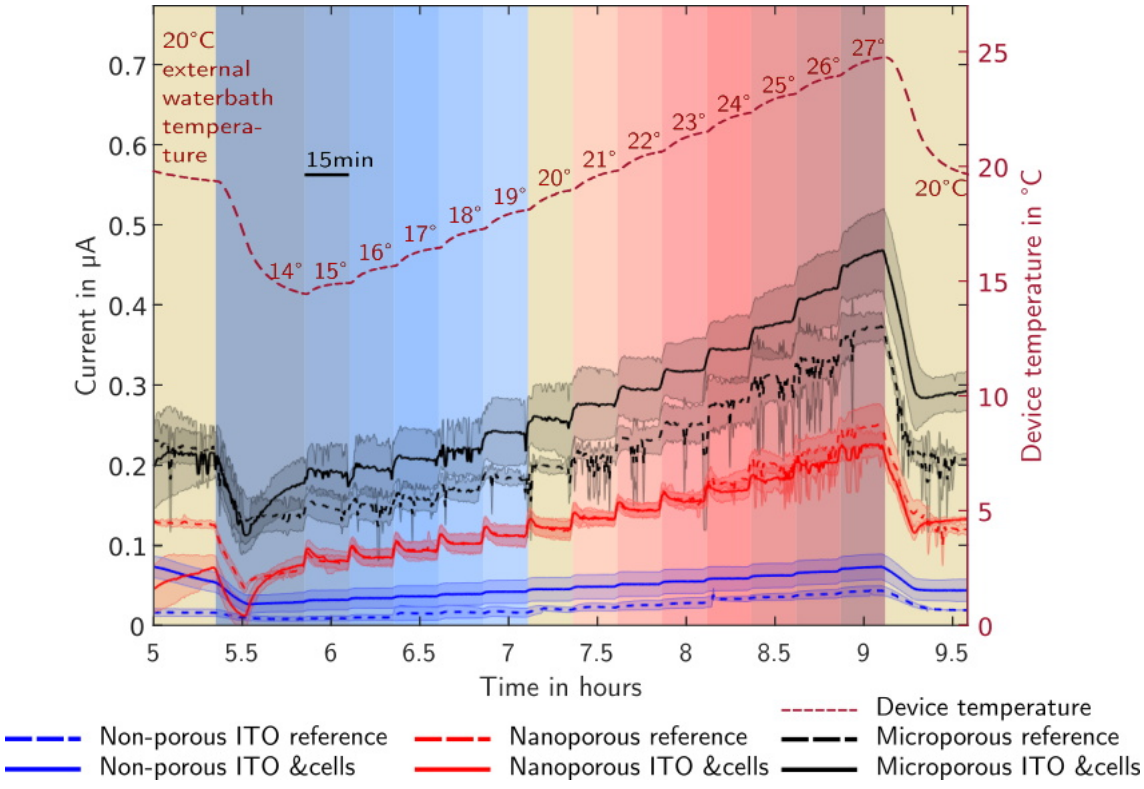

Figure 3.12: Variation of BPV device temperature during operation. The current generated by three anode types with different porosities shows a strong temperature dependence (with and without biological organisms). Shown are the temperatures measured inside the devices (dark red dashed line and background colouration), mean currents across abiotic anodes (dashed lines), anodes with *Synechocystis* cells (closed lines), and their standard deviations (shaded areas). The averages and error margins stem from four measurements per device type.

time, an increasing number of biophotovoltaic studies often report results recorded at different temperatures (e.g. 21 °C [90], 22 ° ± 2 °C [91], 24 ° ± 1 °C [92] and 30 °C [93]) or do not report a temperature value.

To study this parameter systematically, the temperature of the external cooling/heating circuit passing through the hollow walls of the devices was varied in 1 °C steps during BPV operation in the range between 14 °C and 27 °C (see temperature labels in figure 3.12). The temperature inside the devices (measured close to the BPV anode with a PT-1000 sensor) is shown as a dashed line in figure 3.12. The response of the dark-currents to temperature changes were drastic. For each of three anode types with different porosities, the current output changed by more than ± 50 % for a temperature variation of ca. ± 6 °C around 20 °C. The temperature dependence did not change in the presence of microorganisms except for the constant addition of a small dark-current (microbial production of electrons from sugar digestion in the dark).

The demonstrated temperature dependence highlights the need for an accurate temperature control. Note that when comparing results of different biophotovoltaic studies, a 100 % difference can arise from the choice of operating temperatures in the 14 °to 25 °C range.

When measuring the temperature during BPV illumination (with external water bath temperature control), a small ca. 1 °C variation can be observed at high photon flux values (see figure 3.13). Because of the high temperature sensitivity of the system this

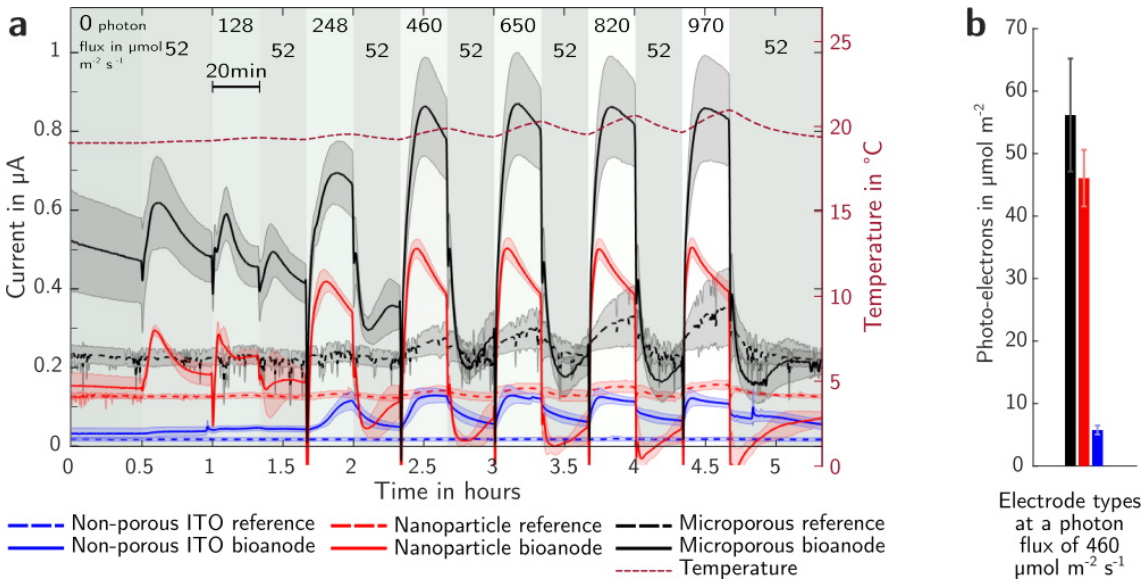

Figure 3.13: Current generated by electrochemical devices (in half cell mode at 0.2 V vs. Ag/AgCl) with and without biofilms (*Synechocystis*) operated at different light intensities. The electrolyte in the devices was BG11 medium without supplementary phosphate buffer. The temperature curve corresponds to the values measured in the electrolyte close to the anode.

can lead to visible photocurrents in the absence of electroactive microorganisms (see dashed black and red lines corresponding to porous, sensitive anodes). The strong shape correlation between measured temperature curve and current changes indicates that warming up and device cooling was indeed the main source of the observed variations during illumination of abiotic devices.

Side note: As further detailed in chapter 4, the protocol for light 'on' and 'off' times had to be balanced for the reproducible measurement of photocurrent peak-values. In contrast to later measurements recorded in this study (see also figure 3.3), the dark-time between illuminations was not long enough in the measurements of figure 3.13 for the dark current to recover its pre-illumination base-level. This caused a steady drop of the current baseline with increasing illumination intensities.

3.6.2 Background measurements of cell culture medium

Another important test seemingly absent from the literature are measurements of the components of the growth medium used for the cultivation of electroactive microorganisms (here BG11). In order to understand background signals and electrolyte dynamics, chronoamperometry and cyclic voltammetry were conducted on devices without cyanobacteria, but with 50-times increased concentrations of the components contained in BG11. Commercial non-porous ITO electrodes on PET were used as anodes.

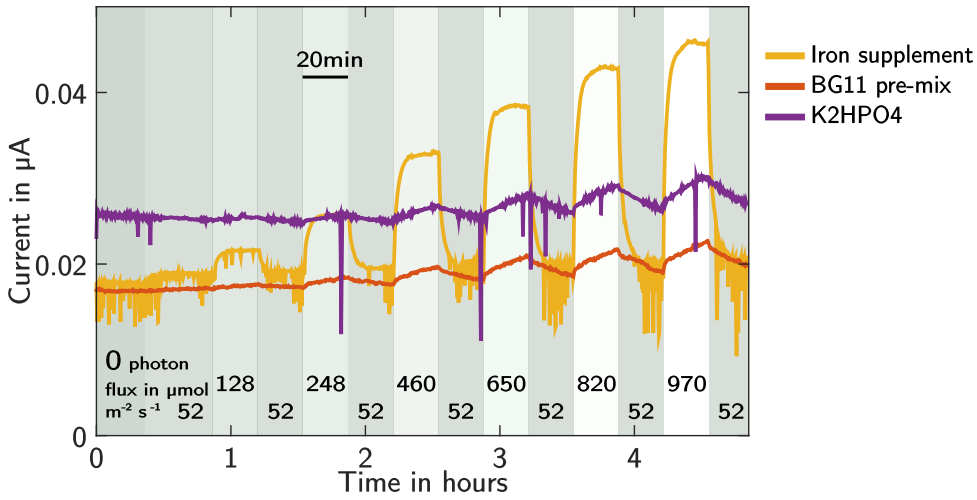

Figure 3.14: Chronoamperometry data from three measurement devices with non-porous ITO electrodes filled with different electrolytes, exposed to a series of illumination intensities. 2 mM ferric ammonium citrate was added to the yellow channel, '100× BG11' pre-mix (diluted to 50×) was the electrolyte in the red channel, and a 8.8 mM K_2HPO_4 solution was measured in the purple channel. Note: The channels differ by a small and constant dark-current offset, which has been subtracted in other measurements presented in this thesis.

BG11 is made from 1 litre DI water, two multi component mixes (10 ml of '100× BG11' and 1 ml 'trace elements'), and four separately sterilised solutions (*i*) 1 ml ferric ammonium citrate (1.11 g in 100 ml) (*ii*) 1 ml K_2HPO_4 (3.05 g in 100 ml H_2O), (*iii*) 1 ml Na_2CO_3 (2.0 g in 100 ml H_2O) and (*iv*) 10 ml $NaHCO_3$ (8.4 g in 100 ml H_2O). The pre-mix of 100 times concentrated BG11 minerals contain for each litre DI water: 149.6 g $NaNO_3$, 7.49 g $MgSO_4$, 3.6 g $CaCl_2$, 0.6 g Citric acid and 1.12 ml of 0.25M solution Na_2EDTA at pH 8. The 100ml trace element pre-mix consists of 0.286 g H_3BO_3, 0.181 g $MnCl_2$, 0.022 g $ZnSO_4$, 0.039 g Na_2MoO_4, 0.008 g $CuSo_4$ and 0.005 g $Co(NO_3)_2$.

Most BG11 ingredients did not have any electrochemical response in the relevant window of electrode potentials. Pure DI water, 50× enriched Na_2CO_3, $NaHCO_3$, K_2HPO_4 and 100× BG11 mix (diluted to 50×) did not result in redox peaks or a photo-response. However, one BG11 component, ferric ammonium citrate, was found to have an effect on measurements at increased concentrations (0.111 g in 200 ml DI water, equals to 2.0 mM or 50× concentrated with respect to BG11). Trace elements were not tested because of their low concentration in the medium. Ferric ammonium citrate induced a clear light-response (see figure 3.14, recorded at 0.2 V vs. Ag/AgCl reference electrode). For its concentration in BG11, this light response was only noticeable over the background noise for the most sensitive measurements in this study.

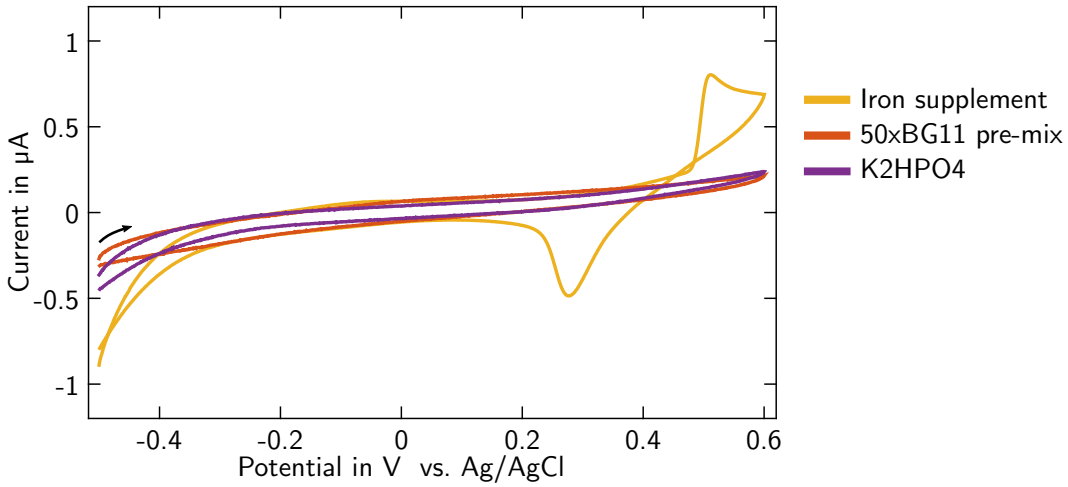

Figure 3.15: Cyclic voltammetry data from three devices with different electrolytes (non-porous ITO electrodes, scan rate 4 mV/s, photon flux 650 µmol/m^2/s^1). 2 mM ferric ammonium citrate in DI water (iron supplement) was filled into devices with data shown in yellow, BG11 pre-mix (diluted to 50×) was electrolyte in the red device, and 8.8 mM K_2HPO_4 solution in the purple channel.

During cyclic voltammetry measurements, only concentrated ferric ammonium citrate in DI water exhibited distinctive redox peaks, as shown in figure 3.15. This peak-pair is also observable at lower concentrations of BG11 and during BPV operation (see figure 3.4 for comparison).

3.7 Discussion

This chapter introduces the energetic boundary conditions of the BPV measurements and the most important experimental techniques. It also contains descriptions of two important custom instruments which I designed for the quantitative study of bioelectrochemical photocurrents.

First, the design of an LED light source suitable for bioenergy measurements was described. In contrast to solar simulators used in non-biological photovoltaic research, this light source is dimmable in the range of average light intensities occurring in real world locations (and is thus less intense than the bio-unfriendly standard used in the community). At the same time, it is larger (square metres rather than square centimetres) and emits light in the visible spectral region only (avoiding problems of heat management in biological samples and UV damage).

Secondly, 3d printed electrochemical devices for BPV measurements were developed. Their design allows the optimal positioning of electrodes and the use of water-based temperature control with an external water bath. The device functionality goes beyond the state of the art of currently published BPV devices. Importantly, the compact design enables parallel measurements with 12 devices within the irradiation area of the LED light source, which proved essential for comparative measurements. Furthermore, as discussed in chapter 4, the design and arrangement of cathodes in the devices did not limit the observed photocurrents. This makes the device a useful point of reference for bioelectrochemical measurements using a three-electrode configuration. Non current limiting electrodes are essential to measure overall device efficiencies (such as external photovoltaic quantum efficiency).

This chapter also contains valuable quality control measurements for BPVs, which are currently missing from the literature. In particular, section 3.6 contains evidence about the strong temperature dependence of BPV-related electrochemical measurements. For experimentalists working in bioelectrochemistry it is important to be aware of the temperature sensitivity of this experiment, in order to ensure an appropriate temperature control. The configuration used should therefore be reported in publications (in contrast to current practice in parts of the literature). Additionally, a series of experiments on the cell culture medium and its components clarified observable electrochemical background signals during BPV reference measurements on devices before adding cells. It was shown that devices heat up slightly during light exposure (which can be observed in current increases during reference measurements; which again highlights the importance of temperature control) and that iron supplement (ferric ammonium citrate) in the BG11 medium can lead to photocurrents (when using either increased concentrations or during sensitive measurements).

In summary, this chapter contributes a variety of useful insights into the design of experimental set-ups for biophotovoltaic measurements, as well as systematically acquired knowledge of electrochemical background signals in a popular cell culture medium. The chapter also contains important considerations of device energetics, cell pigment quantification and appropriate illumination (energy source) targeted at more quantitative and comparative measurements in this young area of research.

Chapter 4

Porous electrodes enhance biophotovoltaic current generation

4.1 Significance and contributions

This chapter is based on a manuscript under review at journal Nature Communications at the time of writing. It contains key results of my PhD research on biophotovoltaic cells (BPVs), in which photosynthetic microorganisms can be used to produce electricity directly.

I tested the enhancement of electrical current generated from photosynthetically active bacteria by using electrodes with porosities on the nano- and micrometer length-scale. For two cyanobacteria on structured indium-tin-oxide electrodes, current generation was increased by two orders of magnitude and the photo-response was substantially faster compared to non-porous anodes. These properties highlight porosity as an important design strategy for electrochemical bio-interfaces. The role of porosity on different length scales was studied systematically which revealed that the main performance enhancement was caused by the increased surface area of the electrodes. More complex microstructured architectures which spanned biofilms as translucent 3D scaffolds provided additional advantages in the presence of microbial direct electron transfer. The absence of a clear direct contribution in both studied cyanobacteria, *Synechocystis* and *Nostoc*, raises questions about the role of conductive cellular components previously found in both organisms.

Acknowledgements

The electrode-porosity work for microbial solar cells was my own work and builds on the published expertise of my supervisor's groups. I had the idea for the project, planned it,

designed and performed all measurements and analysed all data, with advice from my supervisors Ullrich Steiner and Christopher Howe. Paolo Bombelli advised me in my search for good initial measurement parameters. Collaboratively and under my supervision, the research student Daniel Haertter contributed to the design and construction of electrochemical devices, the light source, and methods for the manufacture of microporous electrodes with advice from Paolo Bombelli and my supervisors. I wrote the manuscript, but included improvement suggestions from all four collaborators mentioned. I would also like to thank Antonio Abate for advice on conductivity testing across the films as well as interpreting the impedance spectroscopy results and Erika Eiser for discussion and the provision of colloids.

4.2 Introduction

Several microorganisms are able to generate electrons that can be collected and utilised in external circuits [1]. In such devices, bio-anodes are the electrodes that collect electrons from the living bio-catalyst. Bio-anodes in the best studied bioelectrochemical technology, microbial fuel cells, are commonly carbon or metal based, and a large diversity of morphologies has been used [28]. The electrode porosity usually has a strong effect on device efficiency [28], but the associated change in volume, surface area, and organism contact area can rarely be disentangled from the variation of materials themselves that are used to achieve the different morphologies. These complicated correlations currently limit the understanding of design rules for electrochemical bio-interfaces. Furthermore, because of a lack of transparency of most anodes, there has been little work on the benefits of using porous electrodes in microbe-based devices that rely on light absorption, referred to as 'biophotovoltaics', except for one study using larger, eukaryotic, algal cells [57]. While photosynthetic microorganisms are expected to operate with a quantum efficiency of five to ten percent internally, electrode interfaces and microbial electron export pathways currently limit device efficiencies to much lower values [1].

In this study I tested the effect of electrode porosity at different length scales on the performance of bioelectrochemical devices. To achieve this goal, I compared three different electrode morphologies of the same translucent material, as further described in chapter 2. Two photosynthetic microorganisms *Nostoc punctiforme* and *Synechocystis* sp. PCC 6803 were each placed on (*i*) a non-porous indium tin oxide (ITO) electrode, (*ii*) a thick 'nanoporous' ITO nanoparticle film, and (*iii*) a 'microporous' inverse-opal structure made from the same nanoparticles, and their photocatalytic current generation was investigated.

Doped metal oxides are popular transparent electrode materials for a wide range of electronic applications. ITO is one of the best performing transparent electrode materi-

als. It is commonly used as thin film (tens of nanometres thick) in display applications and it was shown to be biocompatible [18, 59, 60]. ITO can be structured using a templating approach and has previously been used as porous glass in electrochemical studies of enzymes [54, 94]. In order to distinguish between the porosity on different length scales, I define nanoporosity as the presence of pores between sintered nanoparticles (10–100 nm), and microporosity as the pores created by microsphere templates (10–40 µm). The templated inverse-opal pores used in this study are unusually large and the electrodes are unusually thick (80–140 µm) in order to accommodate a sufficient number of microorganisms within the structure to absorb incoming light.

The two porosity length scales were chosen to represent biologically relevant regimes of electron transfer from microorganisms to the anode. The extracellular electron export mechanisms in cyanobacteria are still unclear, even for the model organism *Synechocystis* [1, 95]. Research on microbial electrochemical devices distinguishes between direct electron transfer (DET) from microorganisms to electrodes, and mediated electron transfer (MET) facilitated by electrochemically active molecules in solution. Nanopores are not directly accessible by the relatively large microbes but the increased surface area is available for electrochemical interactions with redox-molecules in the aqueous electrolyte, which is relevant for MET pathways. Pore sizes comparable to the cell size in microporous morphologies allow cells to enter the electrode, thereby providing a considerable increase in direct contact area between bacteria and electrode surface.

I used two different cyanobacteria in this study, *Nostoc punctiforme* and the model species *Synechocystis* sp. PCC 6803. With either of these microorganisms as biocatalyst, both porous bio-anodes exhibited a remarkable ca. 300-fold increase in generated peak photocurrent compared to non-porous ITO films that are routinely used for biophotovoltaic devices. I also studied the effects of the different anodes on the non-photosynthetic microorganisms *Shewanella oneidensis* and found similarly dramatic increases in external current generation, with an additional enhancement on microporous electrodes.

4.3 Experimental

4.3.1 Bacteria growth and quantification

Synechocystis sp. PCC 6803 and *Nostoc punctiforme* cells were routinely cultured in BG11 medium supplemented with about 1 mM $NaHCO_3$ and maintained in sterile conditions at 30 °C under continuous moderate light of 40-50 µmol photons m^{-2} s^{-1} and shaking at 160 rpm. Before applying cells to electrochemical devices, they were concentrated via centrifugation (ca. 2000 g for 10 min). A small volume of cells (120 -

160 µl) containing 134 nmol chlorophyll were pipetted into the devices pre-filled with BG11 medium and after un-inoculated reference measurements. The chlorophyll concentration was measured by extracting it from the cell suspension in 99.8 % methanol (Sigma-Aldrich) and then calculating the chlorophyll a concentration from two optical density values, as described previously [78].

4.3.2 BPV operation and measurements

The BPV devices were loaded with the different anode types and filled with a 10 ml volume of BG11 medium (containing small amounts of phosphate) and phosphate buffer (DPBS 10x, D1408 Sigma-Aldrich, pH 7.2) in a mixing ratio of 9:1.07 to obtain an overall phosphate buffer concentration of 10 mM. Experiments referred to as 'no added phosphate buffer' used devices filled only with BG11 medium. The electrochemical measurements were performed with a potentiostat (MultiEmStat by PalmSens) with 12 independent channels. The potentiostat applies a voltage and measures the resulting current with a high resolution of down to 1 nA. Reference measurements were conducted with the connected devices after at least 6 hour waiting time (when chronoamperometry measurements seemed to have reached equilibrium), before adding cyanobacteria. Then, 134 nmol chlorophyll equivalent of cyanobacteria were added to each device (see Bacteria growth and quantification). Measurements were conducted again after a settling time of at least 8 h and usually for a duration of one to three days. The illumination periods with high light intensities were limited to five or seven minutes, while more moderate photon flux densities of ca. 500 $\mu mol/m^2/s$ were used for longer exposures. In the case of the custom LED white light source, the moderate illumination compares to the world average sun intensity reaching ground level within the visible light spectrum. The temperature of the devices was held stable at 25 °C by circulating water from with an external water bath through the hollow device walls.

The number of measurement channels per anode type used to obtain the presented averages and standard deviations vary slightly because the cells that shorted due to water condensation or leakage were not considered. During BPV device measurements with *Synechocystis*, all four devices each with micro- and nanoporous electrodes and three devices with non-porous electrodes delivered uninterrupted data. In half-cell mode, averages were formed of three microporous electrode bearing devices, four with NP-films and three with non-porous electrodes. For *Nostoc* measurements, the numbers were two, four, and two respectively. No increase in *Nostoc* electro-activity was observed after several days in the device, in contrast to the literature [31].

Measurements on *Shewanella oneidensis* bacteria were conducted in half-cell mode at an anode potential of 0.2 V vs. an Ag/AgCl reference electrode in fresh LB medium

without additional phosphate buffer. Data was generated from four devices with micro- and nanoporous electrodes each, and two non-porous ITO electrodes. The devices were covered with Parafilm before measuring, which reduced the oxygen supply. The Parafilm did not create fully anaerobic conditions, since during cyclic voltammetry measurements, the presence of residual oxygen influx could still be detected.

4.4 Results

4.4.1 Electrode design and characterisation

A porous electrode that can incorporate photo-active biofilms must combine the three qualities (*i*) conductivity, (*ii*) translucency and (*iii*) micro-porosity on a length scale that allows cells to enter interconnected pores while also forming biofilms with a thickness up to millimetres. To this end, an inverse opal structure was designed with pores and pore-connections of several micrometers, similar to that of cyanobacterial cells. The inverse opal structure was generated through a templating approach (see section 2.2.2). Polymer micro-spheres of 40 µm in diameter were deposited to form an opal structure, which was annealed to promote sphere adhesion and to control the diameter of the sphere-sphere interconnects, followed by infiltration by a ITO nanoparticle suspension

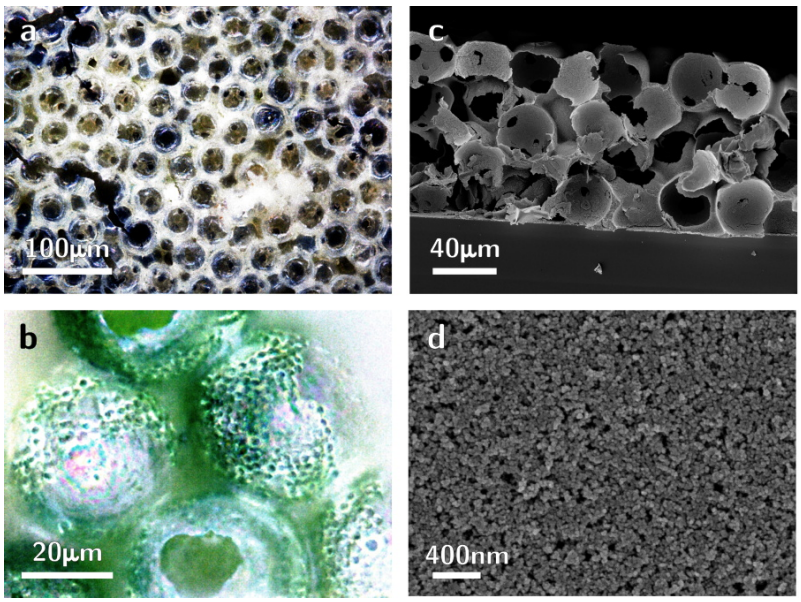

Figure 4.1: **Electrode porosity**. (**a**) Optical bright field microscopy image of an empty microporous electrode. (**b**) Optical dark field microscopy image showing an electrode filled with cyanobacteria (after rinsing with water). Scanning electron microscopy (SEM) images showing (**c**) the cross-section of the electrode and (**d**) the nano-porous structure of sintered nanoparticles.

via capillary forces. Filling the template with nanoparticles (< 100 nm) proved to be the fastest and most reliable method to obtain thick porous films. A final heating step sintered the nanoparticles while burning out the polymer template to leave the inverse structure behind.

The resulting material was diffuse white-yellow, as seen by eye or optical microscopy (figure 4.1 a). After the addition of cyanobacterial cells, the electrode was examined by light microscopy (figure 4.1 b) to confirm the ability of the cells to populate the structure across the entire thickness (here, ca. 0.12 mm). Cells (ca. 2 µm cell-diameter) had to pass through ca. 10 µm wide connections in order to reach all hollow spheres of the inverse opal morphology (see figure 4.1 c and cross-section in d) or reach these spaces via cracks. The nano sized pores of the electrode material (figure 4.1 d) could not be accessed by the bacteria.

To compare the effects of micro-, nano- and no porosity in this study, three different ITO structures were used. A commercial non-porous ITO layer on a PET substrate served as reference (section 2.3.4), and thick nanoparticle films (figure 4.1 c) without and with additional micropores (figure 4.1 c, and section 2.2.1) were employed to assess the interplay of nano- and microporosity on the charge generation by the microorganisms. The relatively large opal unit cell size of 40 µm was chosen to minimise the number of metal oxide water interfaces and thus the back-scattering of light, and to allow the use of larger microorganisms. See chapter 2 for more detail on electrode structures and characterisation.

4.4.2 Photocurrent ratios

During the exposure of devices to light, the photo-current did not stay constant, but reached a peak value followed by a decreasing slope slowly reaching a steady value. The peak photocurrent was defined as the average short-circuit current (0 V external potential between anode and cathode and no reference electrode) measured during one minute around its peak value, minus the dark-current level before each illumination, see figure 4.2. Averaging peak-minute values provided a reliable value that was less dependent on noise and peak shape. Illumination periods where chosen short enough (5-7 min.) and separated enough (20-30 min.) to let the baseline dark-current recover before the next illumination. To account for baseline fluctuations, the magnitude of each photocurrent peak was measured from the preceding dark-current, indicated by red circles. The base level was also taken as average of data during one minute.

To study the effect of electrode porosity on the biophotovoltaic device performance, parallel measurements with equal numbers of cells (based on amount of chlorophyll) were conducted on the three different electrode structures. The peak photocurrent levels

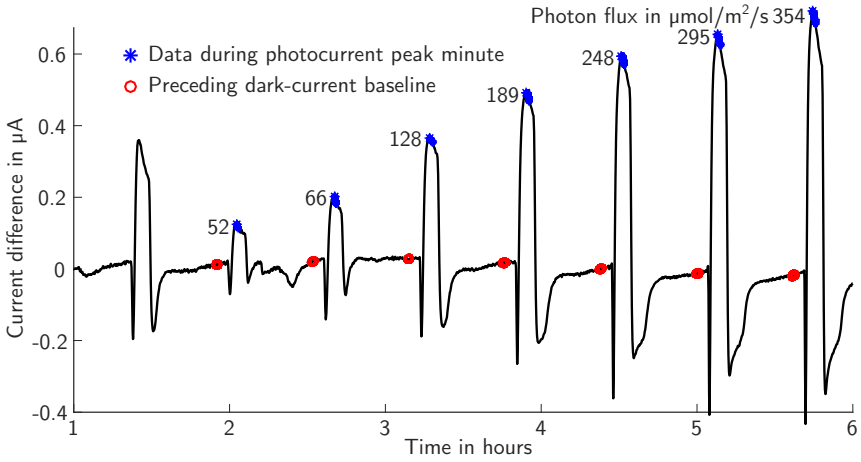

Figure 4.2: **Visual explanation of peak currents.** The first seven photocurrent peaks are shown of an illumination sweep with increasing light intensity. The photocurrent peaks are indicated with stars and irradiance values, along with data points during the peak minute. The data stems from a chronoamperometry measurement fragment of a *Synechocystis* BPV with nanoporous electrode operated at short-circuit.

observed with *Synechocystis* are shown in figure 4.3 a. Both micro- and nanoporous bio-anode based devices substantially outperformed the non-porous ITO electrode with 11.5 and 8.4 $\mathrm{mA/m^2}$ to 0.04 $\mathrm{mA/m^2}$ respectively, while the microporous structure displayed a small but consistent advantage over the film with nanopores only. During the illumination period of seven minutes, the microporous devices reached a peak photocurrent value ∼300 times higher than those equipped with non-porous electrodes.

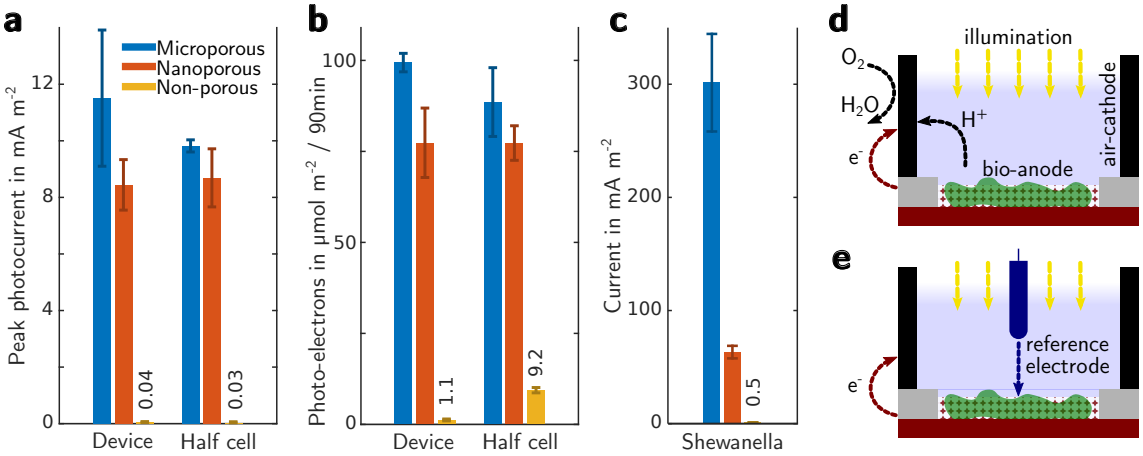

Figure 4.3: **Photocurrent levels by anode type and device configuration.** (**a**) *Synechocystis* peak photocurrents in device mode and half-cell operation, during a photon flux of 460 $\mathrm{\mu m/m^2/s}$. (**b**) As (a), number of collected charges during 90 minutes of illumination at photon flux of 512 $\mathrm{\mu m/m^2/s}$. **(c)** Current generated by *Shewanella* cells for each anode type. (**d,e**) Schematic illustrating the device and half-cell operation, respectively.

In half-cell operation, the total charges collected during a longer period of 90 minutes were larger by more than a factor of 10 with microporous vs. non-porous anodes, see figure 4.3b. Equilibrium values of the photocurrent are difficult to obtain because BPV generated currents tend to fluctuate over time. Photocurrent measurements are also limited by photo bleaching of photosynthetic pigments during illumination and the long time periods necessary for bio-anodes to stabilise after a change of conditions. To quantify the photovoltaic output of the devices, the number of electrons generated during 90 minutes of illumination (figure 4.3 b) was therefore considered as a robust current measure in addition to the recorded peak values (figure 4.3 a).

Similar results were obtained for *Nostoc* bio-anodes, where the current enhancement of devices with a microporous electrode was also higher by a factor of ∼300 compared to non-porous electrodes, with a peak-current of 11.2 $\mathrm{mA/m^2}$, and 30 times more charge collected during 90 minutes (167 $\mu\mathrm{mol/m^2}$).

Figure 4.3 d illustrates the BPV device chamber at 'short-circuit' in which the cathodic water recombination reaction drives the device current and voltage, without an additional force of an externally applied potential. Electrochemical studies commonly use a half-cell configuration instead (figure 4.3 e). There, the anode potential is set with respect to a reference electrode of a stable and known potential, here 0.2 V vs. an Ag/AgCl reference electrode, and the cathode is dynamically shifted to a potential where the cathodic reaction is non-limiting for the measurement. To test whether the cathode limits the peak photocurrents reached in my devices, a set of peak and continuum measurements were performed in half-cell mode, shown alongside the device measurements in figure 4.3 a,b. The highest current levels observed, here in the case of porous anodes, were consistent between device and half-cell operation within each others standard deviations, indicating the absence of cathode limitation.

For comparison with an organism of well-studied ability to perform direct electron transfer [24], an additional test was performed with non-photosynthetic *Shewanella oneidensis* bacteria in the three electrode set-up. The average generated currents were 0.5 $\mathrm{mA/m^2}$, 62 $\mathrm{mA/m^2}$, and 299 $\mathrm{mA/m^2}$ for non-porous, nanoporous, and microporous bio-anodes, respectively (figure 4.3 c), recorded in half-cell mode at an anode potential of 0.2 V vs. a Ag/AgCl reference electrode in fresh LB medium. This corresponded to a more than 100-fold current increase from non-porous to nanoporous electrodes, and a further ca. 5 times increase for the microporous structure.

4.4.3 Light response characteristics

Exposing photosynthetic electro-active biofilms to light gave rise to an initial current peak which typically dropped to steady-state values. For each of the organisms studied

here, the photocurrent rose much faster to its peak value on devices employing one of the porous compared to non-porous electrodes, with little difference between the two pore types (figure 4.4 a and 4.5). The current peaks were reached for porous electrodes after 1–6 minutes, whereas devices with non-porous electrodes required up to over one hour of light exposure to reach a maximum (figure 4.4 a and figure 4.5 expanded regions). The steady-state current reached by non-porous bio-anodes was lower compared to the porous electrodes.

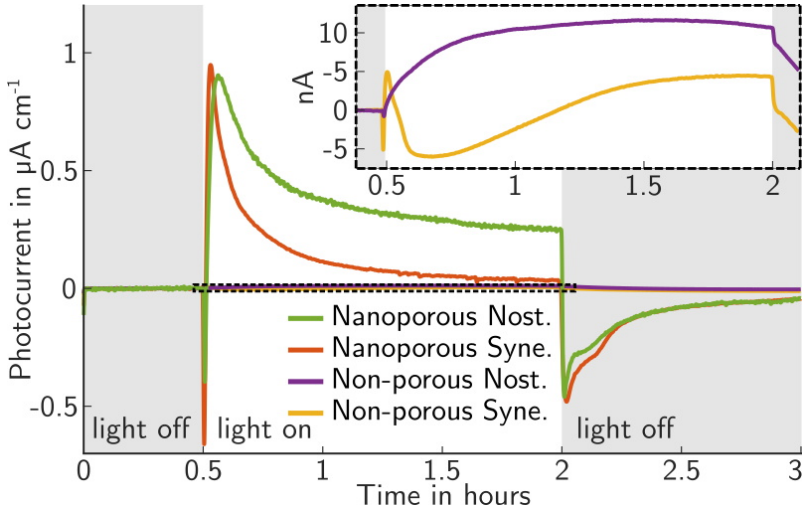

Figure 4.4: **Light response dynamics.** Development of the average BPV-device photocurrent over time at a photon flux density of 512 µmol/m^2/s, for non-porous and nanoporous film electrodes and both *Nostoc* and *Synechocystis*.

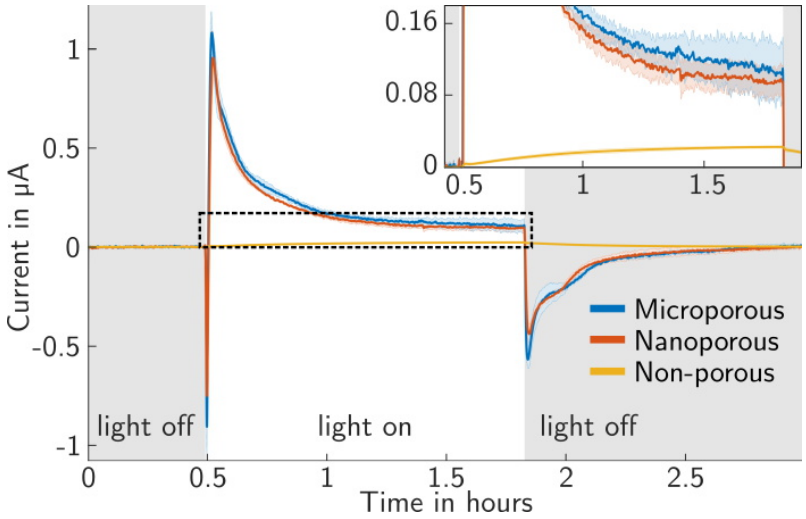

Figure 4.5: **Light response dynamics with reference electrode.** Characteristics of the three different *Synechocystis* bio-anode types over time, operated in half-cell mode at 0.2 V vs. an Ag/AgCl reference electrode. The photon flux during illumination was 512 µm/m^2/s. Averages and standard deviations (shaded) are shown.

The fast photo response of the porous bio-anodes enabled serial experiments studying the peak BPV photocurrent for different light irradiances, see figure 4.6 a,b. The resulting curves show an approximately exponential saturation of photoelectron generation, with higher efficiencies reached at low light levels. The performance advantage of porous electrodes persisted for all irradiation levels. In addition to the use of porous bio-anodes, the need for fast and accurate measurements was addressed (*i)* by adding phosphate buffer to the BG11 medium which increased the electrolyte conductivity, (*ii)* by disregarding preceding dark-current levels, and (*iii)* by choosing dark-times between (short) illuminations that were long enough for the dark current level to recover. For the low light level *Nostoc* measurements (photon flux 0–400 µmol/m^2/s, figure 4.6 b), the irradiation intervals were not long enough to reach the full peak values, which may explain the lower exponential slope for low photon fluxes compared to the *Synechocystis* data.

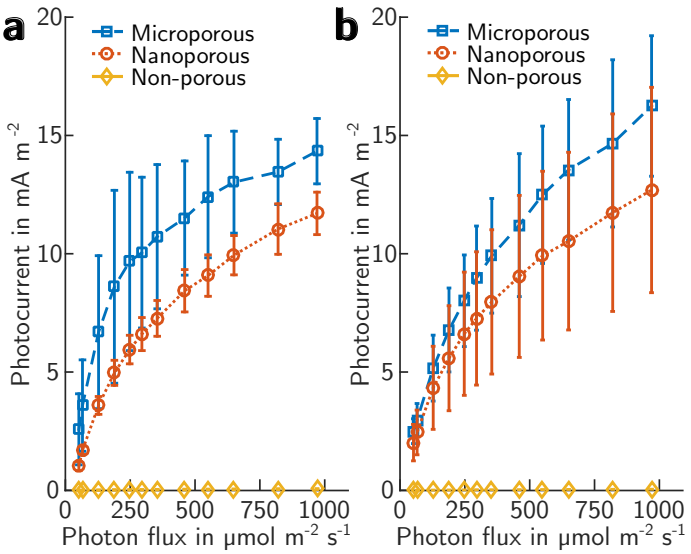

Figure 4.6: **Saturation behaviour.** (**a**) Peak current generated by *Synechocystis* cells on the three anode types at different light levels. The values are averages of the peak minute after subtracting the dark current. (**b**) *Nostoc* biofilm peak photocurrents as in (a).

Surprisingly, in contrast to porous electrodes, non-porous ITO electrodes performed better and responded faster in the absence of phosphate buffer, see figure 3.13, but its performance remained much below that of the microporous electrodes, which collected ten times more electrons during a 20 minute illumination period.

4.4.4 Redox reactions at the bio-anode

The activity of electron-generation by bio-catalytic water splitting depends only on the input energy of the illuminating light source (figure 3.1). By measuring the electron

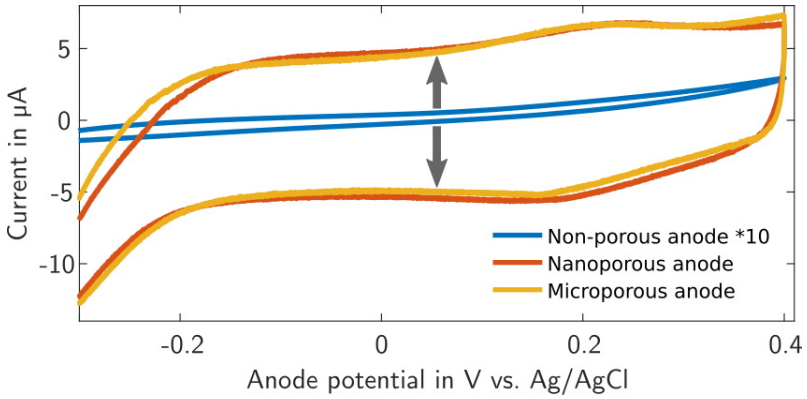

Figure 4.7: **Charging current of porous electrodes broadens cyclic voltammetry (CV) scans.** Example CV data at scan rate of 0.5 mV/s on *Synechocystis* bioanodes differing in porosity. As indicated by arrows, data from scans performed on porous anodes are broadened in comparison to non-porous electrodes (ten times enlarged for clarity) due to enhanced charging currents. They are also more sensitive to detect electrochemically relevant molecules near the electrode, as described in the results section.

collection as a function of anode potential by cyclic voltammetry (CV), the redox activity of downstream electron donating molecules can be characterised. The bio-catalytic activity is slow for most organisms, however, and could not be detected by CV even at scan rates as low as 0.5 mV/s. The porous anodes showed a strong enhancement in electrochemical sensitivity, but also stronger surface charging, leading to high charging currents (non-Faradaic) that broaden the CV hysteresis curve and thus mask bio-catalytic peaks, see figure 4.7.

The increased electrochemical sensitivity of microporous electrodes did however enable the detection of a light dependent reversible peak of a reduction reaction on the anode surface (figure 4.8 a). This peak was not observed on the less sensitive non-porous ITO anodes. The slight shift in peak position with irradiance was probably caused by a pH shift of the BG11-medium electrolyte (no additional phosphate buffer was used in this measurement). Lowering the oxygen content of the electrolyte by purging it with nitrogen gas led to a decrease in peak height (figure 4.9), suggesting its link to photosynthetic oxygen production. This was further confirmed by a measurement without microorganisms, during which the oxygen content was varied by purging with nitrogen or air, and for which the same reduction peak was reduced (nitrogen) and enhanced (air), see figure 4.8 b. The reaction appeared at anode potentials lower than -300 mV, and was well separated from the operating range of presented bio-anodes, which had a measured electrode potential of 50 to 150 mV vs. Ag/AgCl (figure 3.1). This separation is important for device performance, as the electron-consuming reduction of oxygen can compete with the collection of photosynthesis-derived electrons (oxidation reaction) if it takes place at the material- and pH-dependent operating potential of the bio-anode.

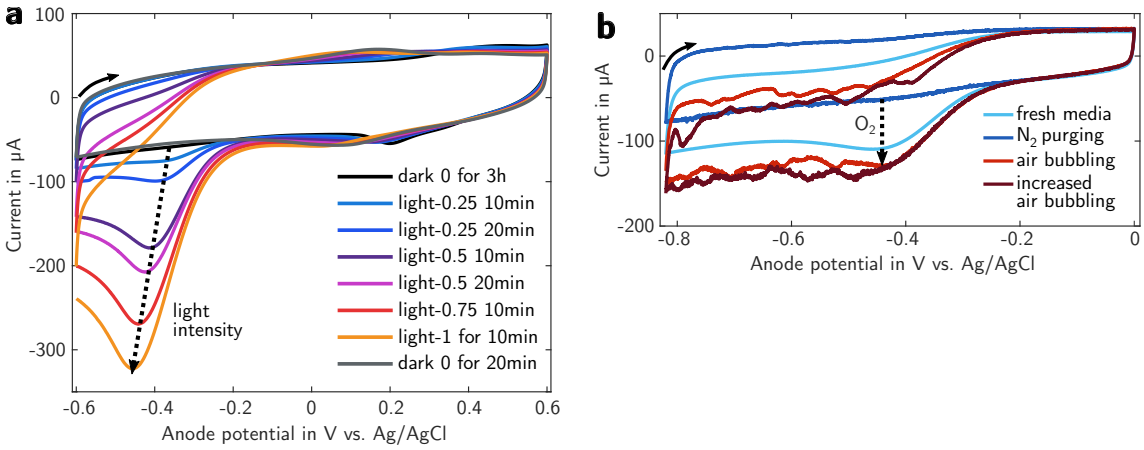

Figure 4.8: **Cyclic voltammetry analysis** of microporous ITO anodes at a scan rate of 4 mV/s with BG11 medium as electrolyte. (**a**) Response of the bio-anode (*Synechocystis*) under exposure to different constant light levels. Light intensity 1 corresponds to a photon flux of 820 µm/m^2/s, and the time indicates for how long the light level was applied by the end of the measurement. (**b**) Scans of abiotic anodes in the dark. The oxygen content of the electrolyte was varied by purging the electrolyte with nitrogen gas or compressed air.

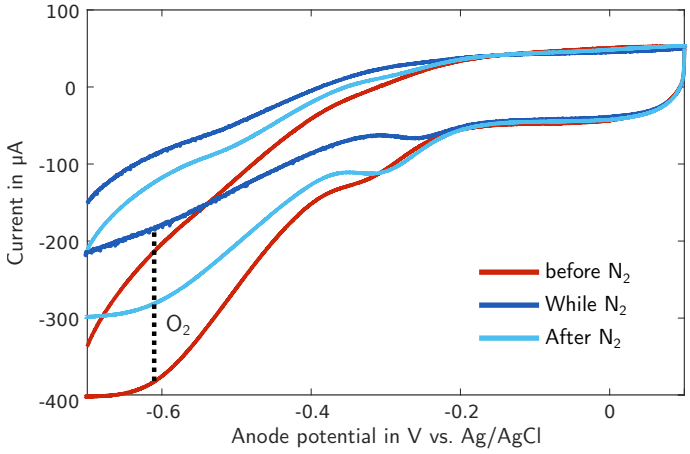

Figure 4.9: **Cyclic voltammetry analysis** of a microporous bio-anode with *Synechocystis* cells at a scan rate of 4 mV/s. Scans from -0.71 to 0.1 V vs. Ag/AgCl at a photon flux density of 295 µm/m^2/s. The tracks were recorded before, while and after purging the electrolyte with nitrogen gas to remove the oxygen released by the photosynthesising organisms.

4.5 Discussion

Translucent conductive electrodes with porosity on two relevant length scales – nanoporous films with pores accessible only by electrolyte, and microporous electrodes with additional pores on the organism's length scale – were successfully created. Two cyanobacteria, *Synechocystis* sp. PCC 6803 and *Nostoc punctiforme*, were applied to these electrodes where they continued to be electroactive for the duration of measurements (at least several days), with no indication of bleaching. During measurements, oxygen reduction at the anode is unlikely to compete with the collection of microorganism-derived electrons, as it takes place at lower anode potentials (–400 mV) than those reached during BPV operation (ca. 100 mV).

In the architecture presented here, the cathode did not limit device performance (observed peak photocurrents), and half-cell measurements were equivalent to overall device performance. Measuring the bio-anode versus a reference electrode (half-cell mode) simplifies the interpretation of results of the anode performance and the presence of a reference potential allows the application of methods such as cyclic voltammetry. However, half-cell measurements can only be related to external quantum efficiencies as defined in the field of solar energy generation, when it is known that an appropriate non-limiting cathode such as the here-presented can be designed to complement it in a full device.

Photocurrents collected from both types of porous electrodes were typically one to two orders of magnitude larger than those from bio-anodes based on non-porous ITO electrodes. The performance advantage varied depending on the metric used (higher for peak currents; lower for charges collected over several hours) and electrolyte conductivity (higher salt levels improved the performance of porous anodes). Photocurrent peak values were also reached faster (up to 90 times) on porous electrodes. Both high performance and fast response demonstrate the importance of a large electrode surface area for the design of electrochemical bio-interfaces.

The fast response of porous bio-anodes enabled the performance of timely serial experiments measuring the dependence of photocurrents on light irradiation. The resulting curves show an approximately exponential saturation behaviour. The correlation of this measurement to the saturated process of photosynthetic electron transfer itself may point to a direct link between the levels of photo-electrons available inside the cell, e.g. as the ratio of NADPH/$NADP^+$ molecules, and the peak number of photo-electrons measured in a BPV device. The magnitude and temporal variation of photocurrent generation is not yet well understood, and would depend on a complex interplay of biochemical processes, including competition with the terminal oxidases, which act as electron sinks [96]. Further research into the role of pigment concentration, saturation of light absorption

and the regulation of terminal electron sinks within the cell will provide valuable insights into biophotovoltaics, as well as into the bioenergetics of photosynthesis in general. The quantitative datasets from the fast-response bio-anodes described here could provide an important contribution towards this goal.

The high electrochemical sensitivity of the porous anodes, particularly the microporous electrode enabling biofilm penetration, also enabled a sensitive real-time detection of the oxygen levels present inside photosynthetically active biofilms by cyclic voltammetry (figure 4.8). Such analyses might provide quantitative insights into oxygenation studies e.g. in mixed biofilms or tissues [97].

Surprisingly, the performance of nano- and micro-porous electrodes was similar for both cyanobacteria. This similarity simplifies design rules of electrodes, requiring simply the sintering of a nanoparticle paste for the manufacture of nanoporous layers instead of more elaborate structuration. It also implies that the dominating extracellular electron transfer mechanism may be self-mediated (no additional electron shuttling molecules were added). If the cyanobacteria were able to inject electrons efficiently into the electrode surface via direct electron transfer (DET), a larger performance increase would be expected for the microporous electrode, because it provides a many-fold increase in organism-electrode contact area compared to the two films. The potential DET-related performance increase was confirmed by using non-photosynthetic bacterium *Shewanella oneidensis*, which is well known to exhibit DET [24] and for which microporous bio-anodes showed a clear (ca. 5-fold) additional advantage over nanoporous films. DET tends to be fast and low-loss [77] and can provide an important contribution to currents collected from electroactive biofilms. The most efficient microbial DET mechanism known is through so-called 'nanowires' in some non-photosynthetic organisms. Nanowires are conductive extracellular pili-like structures that have been shown to transport redox-electrons from within the cell through the insulating extracellular matrix to electrodes [24, 98]. Conductive extracellular pili-like structures (PLS), ca. 10 µm in length, have recently been identified in the cyanobacteria utilised in this study, *Synechocystis* sp. PCC 6803 and *Nostoc punctiforme*, as well as in the cyanobacterium *Microcystis aeruginosa*, and it was speculated that they contribute to extracellular electron transfer in these organisms [24, 30, 31]. According to this hypothesis, the filaments should lead to a strong enhancement in photocurrents when brought in contact with the electrode surface across the entire photosynthetic biofilm, by using the microporous structure. The performance similarity of biofilms on micro- and nanoporous electrodes however suggests that the potential presence of conductive bacterial filaments did not contribute significantly to the photo-electron export in my devices, because the filaments did not connect to the organism's photosynthetic electron transfer chain or to the electrode, or the filaments were not produced.

The measurements presented here suggest a slight advantage of the microporous electrode morphology over the nanoporous film. This advantage might be due to a larger, more accessible electrode surface, a smaller average distance self-mediated small molecules have to travel to reach the electrode, or the fact that biofilms reach further into the microporous electrodes,which therefore probe the photoresponse of bacteria that are exposed to high irradiation levels and thus contain a larger number of available photo-electrons. On the other hand, the performance of microporous electrodes may be negatively affected by increased scattering of the inverse opal structure, which leads to increased reflection and decreased transmission, as well as an increase in electrode resistance with increasing thickness of the electrode.

It is clear that use of porous translucent electrodes offers a dramatic increase in the current density obtainable from photosynthetic microorganisms in biophotovoltaic devices. Their rapid photo-response times may additionally allow these devices to be exploited as a wider tool for the study of photosynthetic electron transfer.

Chapter 5

Structural parameters of photosynthetic energy flux saturation

5.1 Significance and contributions

This chapter contains a model of photosynthetic energy flux. It is complemented by experimental results on cyanobacteria with light harvesting antenna mutations, correlating to model predictions. The model quantifies converted energy, numbers of electrons and sugar that plants and cyanobacteria convert via photosynthesis. Figure 5.1 (copied from the discussion section) presents a schematic summary of quantum efficiencies derived from the model.

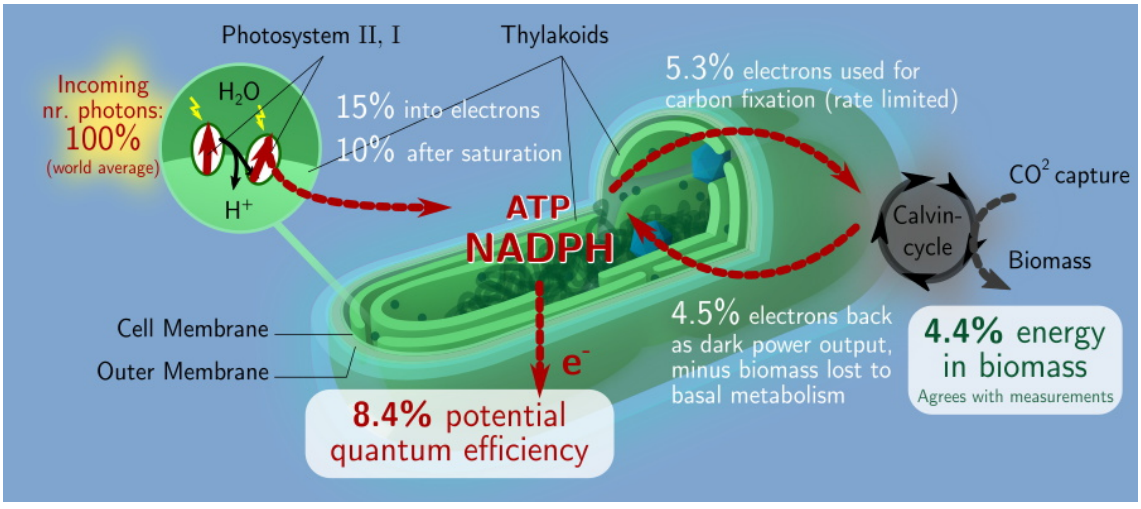

Figure 5.1: Summary of photosynthetic energy conversion and of electron availability in *Synechocystis* cyanobacteria, a model organism for photosynthesis in general.

This theoretical framework enables the comparative evaluation of experimental data from microbial solar cells, advancing BPV to a more general research tool to study the

energetic activity of cyanobacteria and algae. The model takes account of both changing sunlight and shading by stacked biological cells inside biofilms. Both parameters are essential to realistically assess the overall energy availability but have been neglected in relevant existing models. As a proof of principle for the potential implications of predictions derived from the model, one hypothesis was experimentally validated. Namely, high photosynthetically active pigment concentration leads to self-shading in biofilms that is limiting to electron-generation. This was confirmed by experimental data of biophotovoltaic current collected from light harvesting antenna mutant cells. Overall, the framework provides a useful tool to the wider research communities of bioenergy, photosynthesis, and algal cultivation.

Acknowledgements

While I wrote, discussed, programmed, extended and optimised the presented model overall, Paolo Bombelli and the wider Howe group (Dept. of Biochemistry) helped significantly by providing me with an early version of the model as starting point, and with advice on biology-related questions. Paolo's contribution included identifying many of the relevant biological processes, finding references during frequent discussions, and defining the energy input parameters. Paolo also supported my biophotovoltaic pigment mutant measurements with the provision of cell-cultures. All other work, including experiment design, execution, analysis and model comparison, is my own.

5.2 Modelling photosynthetic energy flux saturation

Many theoretical and practical studies have been undertaken to evaluate the solar energy conversion efficiencies of photosynthetic biomass generation. However, few connections have been established between sub-cellular electron harvesting & transfer processes and realistic overall efficiencies. These connections are necessary to evaluate the potential for energy conversion in biophotovoltaic (BPV) technology. Furthermore, most biomass efficiency studies fall short of considering real-world conditions for sunlight energy input, which is well known to strongly affect biomass generation [99] due to rate-limitations in some steps within photosynthesis.

This study estimates the potential electron availability and biomass production in biofilms of the model organism *Synechocystis*. It aims to establish a realistic benchmark by addressing cell internal processes and relevant sun light parameters, such as light intensities at different locations and times of day. This contrasts with previous studies that have discussed the maximum theoretical power output of BPVs [41, 100, 101]. The present study is based largely on the available knowledge of photosynthesis.

Where literature values are disputed, the model parameters were determined by in-house measurements (mostly already included in recent publications by the Howe lab).

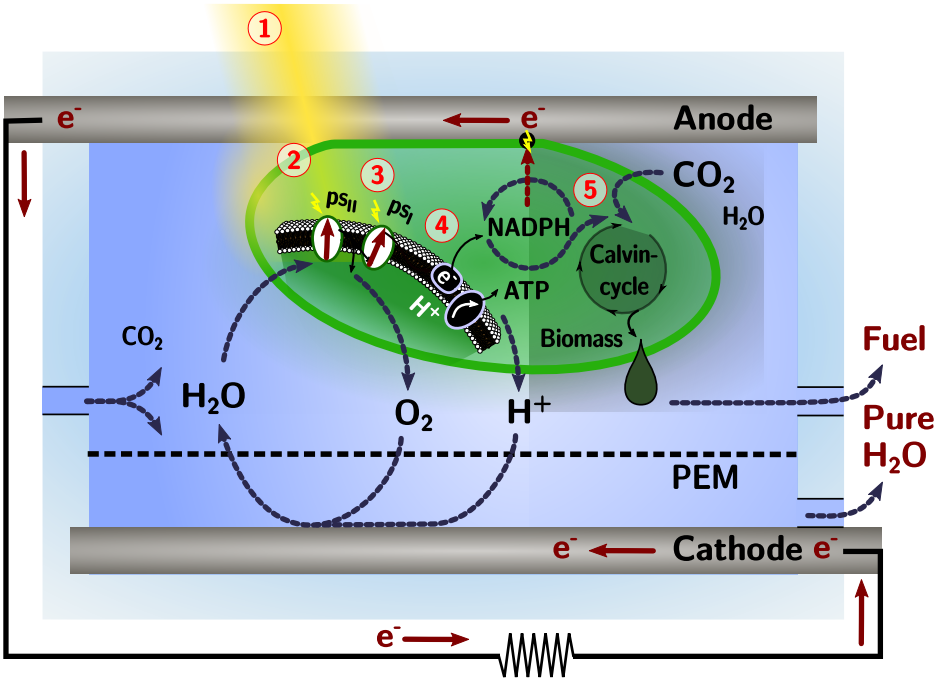

Figure 5.2: Scheme of energy flow through a *Synechocystis* cell depicted in a biophotovoltaic energy harvesting device with PEM. Model steps are indicated by the numbers 1 to 5.

The theoretical analysis includes five stages (figure 5.2, numbers correspond to subsections in this chapter) many of which can be represented by simple factors, while others depend on several physical parameters simultaneously. Results are presented in terms of converted energy and number of energy carriers, referred to in the following as quanta.

The technical limitations of biophotovoltaic devices and life cycle analysis parameters (such as device durability, running costs and energy required for production) are outside of the scope of this study. Instead, this theoretical model focuses on cellular processes. For practical reasons, some real-world parameters such as pH, temperature and concentration of carbon dioxide in the medium [102] were also neglected.

5.2.1 Defining variable solar energy input

Natural photosynthesis and outdoor biophotovoltaic devices are driven by sunlight. This energy input is generalised as solar radiation reaching ground level (SRG) [103]. SRG can be described in terms of light energy (SRG_{energy} in W/m^2) or number of photons (SRG_{quanta} in $E/m^2/s$) irradiating an area of a square meter per second. The latter can be calculated from the spectral energy distribution $E(\lambda)$ of the SRG using the relationship

of wavelength (λ) and photon energy, integrating over the spectrum. E stands for the unit Einstein and represents one mole of photons.

$$\text{Quanta}_{a-b} = \int_{\lambda_a}^{\lambda_b} E(\lambda)\frac{\lambda}{hc}\,\mathrm{d}\lambda, \tag{5.1}$$

where h is the Planck constant and c is the speed of light. The International Electrotechnical Commission (IEC) defined a large SRG-spectrum intensity of 1000 $\mathrm{W/m^2}$ (one sun) as a standard for solar cell testing. This guarantees high output currents while no significant saturation effects are expected in most solar cells. One sun is defined as a constant photon flux, where in reality SRG varies drastically with geographical location, diurnal cycle and season. The intensity of one sun is correlated with observed peak values rather than with average yearly SRGs found on earth.

More realistic SRG values are given in table 5.1 for three locations at different latitudes: London ($51°6'N$), Madrid ($40°4'N$), Riyadh ($24°6'N$) and the world average.

Table 5.1: Average solar radiation reaching ground level for different locations.

Unit of SRG	SRG_{IEC}	London	Madrid	Riyadh	World Average
$\mathrm{W/m^2}$	1000	125	193	251	167
$\mu\mathrm{E/m^2/s}$	6938	871	1346	1794	1166

Due to saturation limitations of photosynthesis, the average energy conversion efficiency of biological systems depends strongly on the variation of sunlight throughout the day. Therefore, it is important to consider the diurnal cycle when estimating photosynthetic performance (instead of using a constant SRG value of one sun). Faster light fluctuations in a real location scenario (e.g. due to water convection or clouds) can also impact photosynthetic efficiency [88, 89, 104], but cannot easily be incorporated into this model. Here, a sinusoidal model of the diurnal cycle $R(t)$ (12 hours light, 12 hours dark) was used, based on a published daylight approximation [105].

$$R(t) = \sin\left(\pi\frac{t - t_{\text{SR}}}{t_{\text{SS}} - t_{\text{SR}}}\right) \cdot \text{Energy}_{\text{day}}/I_R \tag{5.2}$$

$$I_R = \int_{t=0}^{t=24} \sin\left(\pi\frac{t - t_{\text{SR}}}{t_{\text{SS}} - t_{\text{SR}}}\right)\,\mathrm{d}t, \tag{5.3}$$

where t_{SR} and t_{SS} are the times of sunrise and sunset, respectively, and I_R the function's own normalisation factor. The sinusoidal curve re-distributes the average daily light energy ($\text{Energy}_{\text{day}}$) over a 24 h period (figure 5.3). The diurnal model represents an ideal

distribution for clear sky conditions and does not consider seasonal intensity changes. It provides a more realistic scenario for the organisms, with phases of potential excessive radiation (e.g. at noon) and sub-optimal illumination (e.g. dawn or dusk).

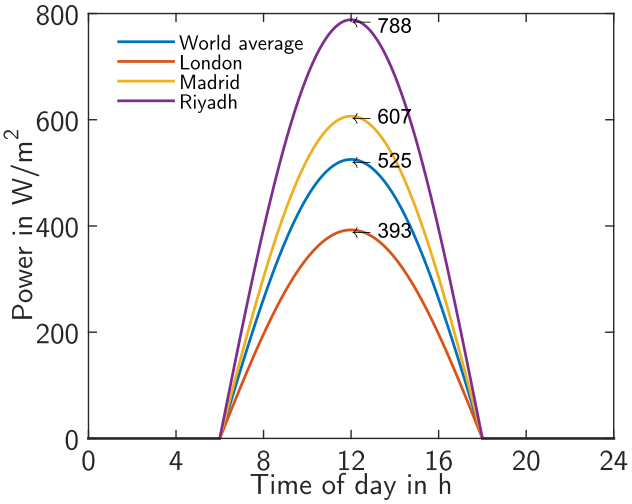

Figure 5.3: Model of the diurnal cycle at different locations.

5.2.2 Photosynthetic absorption limitations

The absorption spectrum of the cell suspension of *Synechocystis* sp. PCC 6803 covers visible wavelengths from 370 nm to 750 nm (see figure 5.4 for a comparison with the SRG spectrum). It results from the absorption of all pigments involved in photosynthesis (chlorophylls, carotenoids, phycobilins) [106] for cells living in a non iron-limiting growth medium (e.g. BG11). Note that in the exceptional case of iron-starvation, cyanobacteria

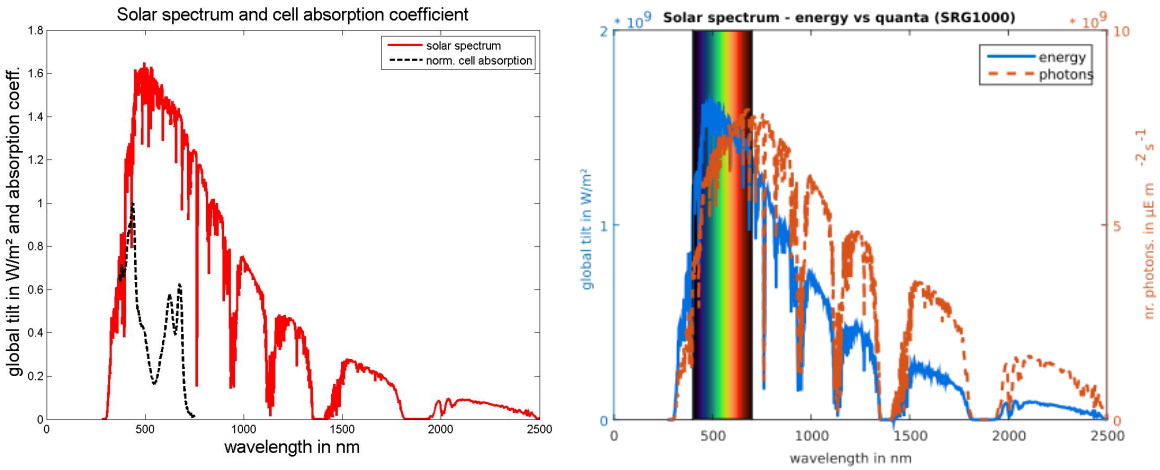

Figure 5.4: Solar spectrum. *Left:* solar spectrum compared to *Synechocystis* cells absorption. *Right:* range of visible light for the solar spectrum in terms of energy (blue) and number or photons (orange).

can replace the phycobilisome with a chlorophyll-based antenna which changes their absorption spectrum.

The SRG that is not absorbed by cellular pigments consists of ultraviolet and infrared radiation which add up to an energy flux of -48.6 % which the organism cannot make use of. Visible light contains more than 50% of the total energy flux of SRG but only one third of its photons because the solar spectrum extends far into the infrared where photons carry less energy. Thus, the photon flux that is absorbed by the organism is even further reduced, by -65.2 %.

Light penetration through cell layers (self-shading)

The light absorbing biofilm was approximated by simple layers of cyanobacterial cells (densely packed without additional water, see figure 5.5) with evenly distributed photosynthetic pigments.

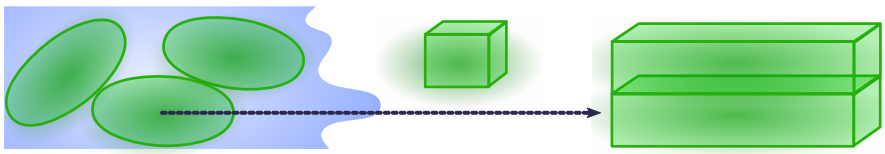

Figure 5.5: Schematic illustration of simplified biofilm layers.

In this scenario, the layer-by-layer absorption is described by an exponential decay curve, see equation 5.4.

$$A(\lambda) = 1 - e^{-\alpha_\lambda l\,[\mathrm{Chl}]} \tag{5.4}$$

with $a(\lambda)$ the measured absorption coefficient [107] (see also figure 5.4), and l the layer thickness (discrete in steps of 2 µm for each cell layer). The chlorophyll concentration of the theoretical layer $[\mathrm{Chl}]$ equals that of an average cell 9.7 mmol Chl /l [107]. The conversion between the very dense packing in this model and the cell density measured in a real biofilm can be made with a single density factor and is equivalent to considering thinner slices to symbolise a layer in this model.

Cells absorb well and are densely packed in pure biofilms. Thus, the top cell layers absorb most of the incoming light (figure 5.6, left). For example, only 1.2 % of energy (or 2.4 % photons) is lost by transmission of visible light through 200 cell layers ($= 0.4$ mm thick theoretical biofilm). Additionally accounting for the cell absorption spectrum, 50.8% of the incoming solar light energy is absorbed by 200 cell layers.

When only the absorption is considered, thicker biofilms yield a higher efficiency. In reality, the optimum biofilm thickness is a trade-off between a large number of photosynthetic pigments (high light absorption between 370 nm and 750 nm) and low metabolic

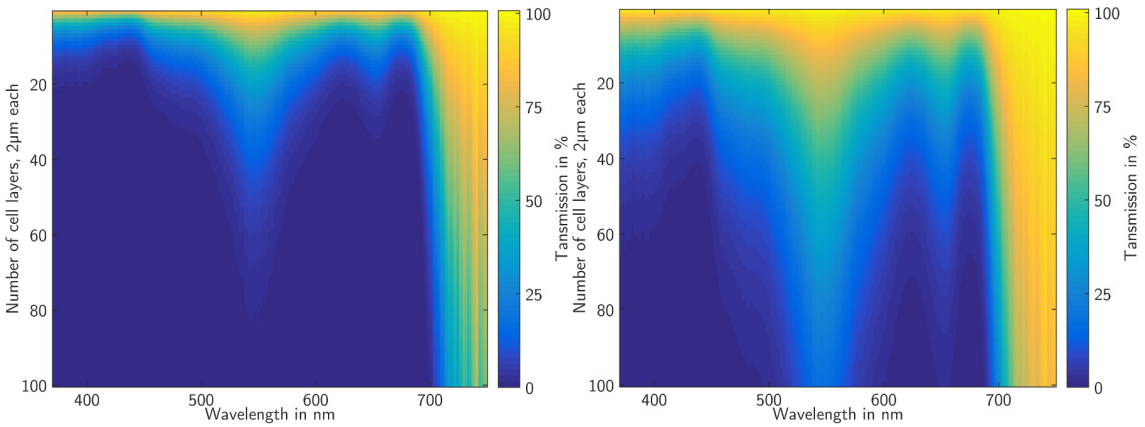

Figure 5.6: Spectral absorption of light by bacterial cell layers. *Left:* no scattering. *Right:* including scattering from cells or added particles.

consumption by the cells for growth and self-repair. In section 5.2.5, the basal metabolic consumption will additionally be taken into account to balance the infinitesimal absorption increase afforded by the addition of further cell layers to already thick biofilms.

Scattering in biofilms

Compared to stirred photobioreactors, a biofilm-system has the disadvantage that some cells are exposed to potentially damaging light intensities, while others stay under very low light conditions in the shadow of layers above. This introduces large saturation losses that need to be addressed by adding a correction for the scattering contribution of cells, especially in the case of the model's assumption of a very dense biofilm. Cyanobacteria

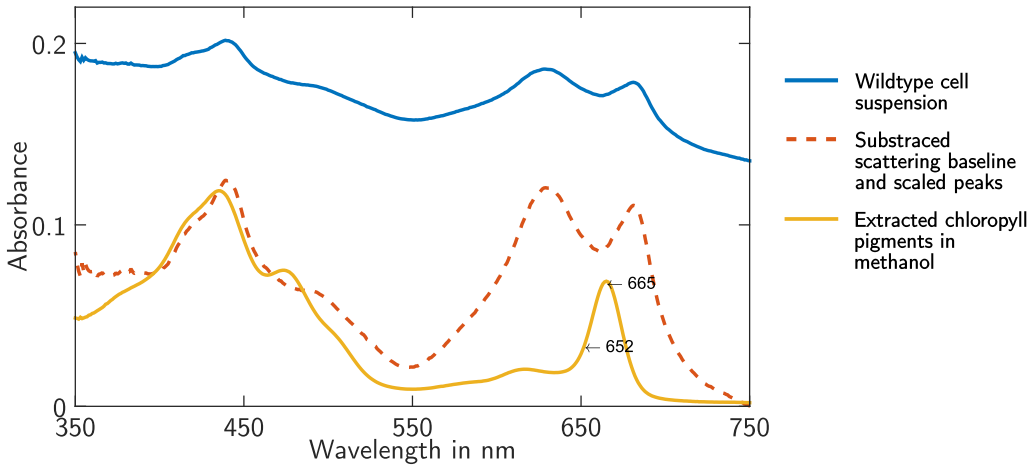

Figure 5.7: Scattering of cell suspension. In simple transmission, absorption spectra of cells are overlaid with their scattering. The extracted chlorophyll in methanol shows a much cleaner absorption curve. The difference between the dashed and the blue line indicate the role of scattering. The curves were divided by their chlorophyll-a content (determinedafter [78]); they now reflect a Chl-a concentration of one nmol/ml.

scatter light to some degree, due to their suitable size, round shape, and slight density difference with respect to the growth medium. This can be observed when measuring the light-loss caused by absorption and scattering by a cell suspension in transmission (figure 5.7, blue line, obtained with a UV-vis spectrometer). The loss becomes apparent when comparing the suspension spectrum to a computationally scattering-corrected absorption spectrum (dashed line in figure 5.7), measurement corrected spectra (integrating sphere measurements in figure 5.4 and 5.14) and methanol extracted chlorophyll pigment only (yellow line in figure 5.7).

As a simplified estimate of this scattering, it is assumed here that light penetrates the biofilm three times better (figure 5.6 right), without considering the wavelength dependence of scattering (short wavelengths (blue) are scattered more than long waves (red)). Scattering can also be tuned artificially by the inclusion of non-absorbing scattering particles into the biofilm.

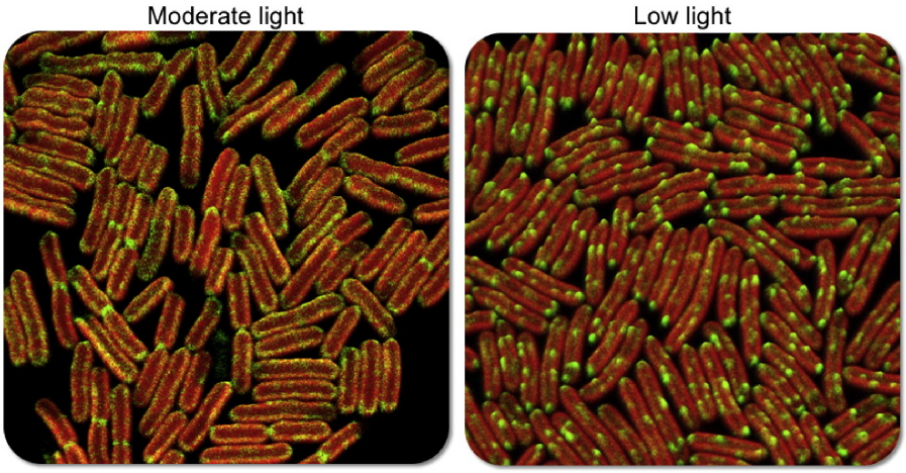

Figure 5.8: Example of light-regulated localization of proteins involved in electron generation. The confocal microscopy images show *Synechococcus* 7942 grown in moderate ($60\,\mu E/m^2/s$) and low light ($6\,\mu E/m^2/s$). The localisation of functional respiratory NDH-1 complexes (green fluorescence) can be observed. Chlorophyll fluorescence (red) indicates the location of thylakoid membranes. The reorganization of NDH-1 complexes in thylakoid membranes correlates highly with the direction of electron flow to respiratory pathway or photosynthetic pathway. [Figure from [108], CC-BY]

Another factor promoting a better light distribution in biofilms is the location of chlorophylls in the thylakoid membrane, leaving the centre of cells more transparent (see also autofluorescence measurements of photosynthetic complexes in figure 2.7). Moreover, the number and location of light harvesting antenna complexes (phycobilisomes), respiratory complexes and the ratio between Photosystem I and II varies dynamically with light irradiation levels on the time scale of few seconds to an hour [108–112] (figure 5.8 exemplifies the light dependent organisation of respiratory complexes). This behaviour

generally improves the distribution of energy between the photosystems and, at high light levels, reduces the photo-damage to light absorbing proteins by reducing their absorption cross-section and channelling energy to alternative cellular components. The adaptation leads to increased transmission of light saturated upper biofilm layers, but the quantitative extent of this absorption adaptation is unknown.

5.2.3 Photosynthetic energy conversion losses

Charge separation

In oxygenic photosynthetic organisms, the photochemical reactions that convert photon-absorption excitations into separated charges take place in two photosystems, named PSII and PSI (figures 5.2, 5.13, 5.9). The unit of quantum changes at this step from photon numbers ($\mu E\,/m^2/s$) to µmol of charge $/m^2/s$.

Both photosystems are very efficient at photon conversion into charges. Values up to 90 % quantum efficiency have been reported for PSI and 84 % for PSII [106]. The ratio of PSII to PSI can vary dynamically as well as its ratio of additionally associated photosynthetically active pigments [112]. To simplify the discussion, an equal division of photons between the systems is assumed, which leads to a loss of about -13 % of absorbed photons. This loss is dissipated as heat and fluorescence without generating charges.

Any dye in photosynthetic organisms (figure 5.4) or band-gap in semiconductor solar cells has a spectral range in which it can absorb photons. There is a direct trade-off between its spectral width (number of photons that can be collected) and the energy that can be utilised as charges, because each excited electron relaxes to the (same) lowest unoccupied orbital (LUMO) of the photosystem. The maximum converted energy that can be determined for single semiconductor band-gap (at 1.34 V) is called the Shockley-Queisser Limit [113]. The Shockley-Queisser trade-off in energy loss can be summarised as follows. The absorption of red light (low energy) generates an excited state of photosynthetic pigments by promoting their electrons into higher molecular orbitals. This excited state is about 1.8 eV higher than the ground level (effective band-gap voltages are 1.48 V for PSI and 2 V for PSII [106]). This value is reached by any absorbed photon from the visible region. Photons with higher frequencies (blue) promote electrons into an excited state at a greater energy (e.g. 3.2 eV) but these decay via ultra-fast internal conversion processes (within femtoseconds) to the LUMO by releasing heat. This lower energy state is the same for all visible light wavelengths.

Some of the energy of the photons with short, 'blue' wavelengths is inevitably lost as heat because of this energetic mismatch between the LUMO of the photosystem and the photon energy. This causes a -32.2 % loss in terms of energy, also taking into account

the reduced number of energy carriers (from 34.0 % absorbed photons to 29.5 % in the form of charges). At this step, 34.4 % of the total incoming solar energy is estimated to have successfully been converted to charges.

Electron generation

The generated charges in PSII are used by photosynthetic organisms to split water (water photolysis) [106, 114]. This process generates electrons (converted under participation of PSI), protons and oxygen. The chain of reactions through which electrons subsequently pass is referred to as the electron transport chain (ETC) (figure 5.9) and accomplishes the primary photosynthetic light reactions:

$$2\,\mathrm{NADP^+} + 3\,\mathrm{ADP} + 3\,p_i + 2\,\mathrm{H_2O} \xrightarrow{8\ \text{photons}} 2\,\mathrm{NADPH} + 3\,\mathrm{ATP} + 2\,\mathrm{H^+} + \mathrm{O_2} \quad (5.5)$$

where p_i is a phosphate group. Two photons per electron ($1/2$ NADPH) are required to complete the reaction, because the reaction involves activations by both photosystems. In other words, the maximum number of electrons generated by this system is only half as large per absorbed photon as a one-step photochemical reaction would be (note that such one-step system would rely on a smaller number of higher energy photons). The quantum efficiency for this step is accordingly 50 %.

The cumulative energy of the consumed charges is not preserved completely through the long ETC. The energetics of reaction intermediates are described by the Z-scheme [114] (figure 5.9, named after its zigzag shape). It starts with water oxidation at a redox potential of $\Delta\mathrm{E}^\circ = 820\,\mathrm{mV}$ vs. SHE and ends with the electron storage molecule NADPH with a redox potential of $\Delta\mathrm{E}^\circ = -320\,\mathrm{mV}$ vs. SHE [106] (2 electrons per NADPH). The primary light reactions can thus be assigned a potential gain of $\Delta\mathrm{E}^\circ = 1140\,\mathrm{mV}$ (equivalent to the energy value of $\Delta\mathrm{G}^\circ = 220\,\mathrm{kJ}$). This follows from equations 5.6 and 5.7, where n represents the number of electrons and F the Faraday constant of 96500 J/V.

$$\begin{aligned}\Delta\mathrm{E}^\circ &= \Delta\mathrm{E}^\circ(\text{beginning}) - \Delta\mathrm{E}^\circ(\text{end}) \\ &= 820\,\mathrm{mV} - (-320\,\mathrm{mV}) = 1140\,\mathrm{mV}\end{aligned} \quad (5.6)$$

$$\begin{aligned}\Delta\mathrm{G}^\circ &= -n \cdot F \cdot \Delta\mathrm{E}^\circ \\ &= -2 \cdot 96500\,\mathrm{J\,V^{-1}} \cdot 1.14\,\mathrm{V} = -220\,\mathrm{kJ/mol}\end{aligned} \quad (5.7)$$

Besides generating and storing electrons, the ETC gives rise to a potential difference across the membrane in which the reactions take place. A large part of this energy is additionally stored in ATP molecules. For the redox potential of ATP dephosphorylation ($\mathrm{ATP} + \mathrm{H_2O} \rightarrow \mathrm{ADP} + p_i$), a Gibbs free energy of $\Delta\mathrm{G}^\circ = -30.50\,\mathrm{kJ\,mol^{-1}}$ is

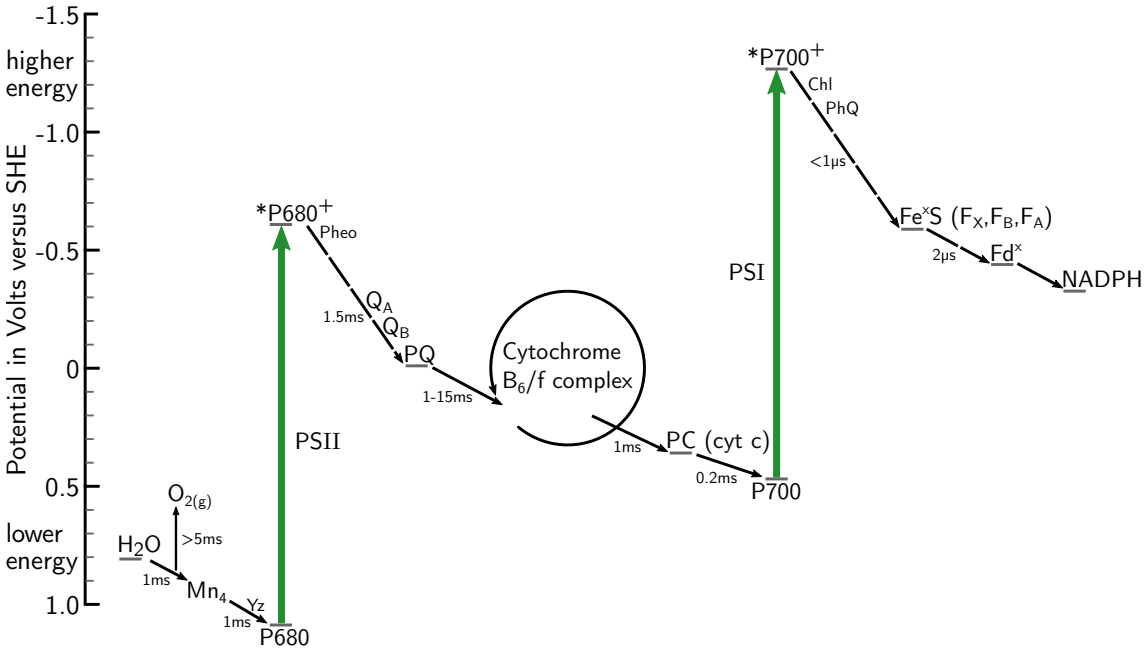

Figure 5.9: Z-Scheme describing the electron transport chain (ETC) in photosynthesis. The diagram illustrates the upper redox energy for accepting an electron from the end of the ETC, namely from NADPH, and the slowest electron transfer steps (rounded values).

assumed [115] (under standard conditions, in cells the energy difference depends on the dynamic ratio of ATP and ADP).

In summary, the primary light reactions consume a minimum of 8 photons and store the energy in the redox potentials of 2 NADPH (4 electrons) and ca. 3 ATP molecules, averaging to an energy of 132.89 kJ/mol per electron. Due to electron transfer losses and the energy level alignment of natural redox molecules, this energy is lower than the value for the created charges and constitutes an energy loss of -60.4 %. This leaves the photosynthetic organisms with a power conversion efficiency of 13.6 % of the initial energy input from the SRG. The unit of quantum changes at this step from generated charges (in µmol of charge $/m^2/s$) to electrons (in µmol of electrons $/m^2/s$). The electrons are present in the form of NADPH (two electrons per molecule).

5.2.4 Photosynthetic electron transport dynamics

Kinetic limitations of electron generation (saturation)

As described in the previous sections, the electron transport chain (ETC) (described by the Z-scheme [112, 116, 117] in figure 5.9) is theoretically expected to generate 4 electrons for each 8 photons absorbed and used in the reaction centres of PSII and PSI where two water molecules are split to release one O_2. The electrons are subsequently used to reduce two $NADP^+$ to NADPH (equation 5.5). While most participating reactions are

fast (picoseconds), some enzymatic dark-reactions take milliseconds to complete and can limit the generation of electrons kinetically. In particular, the release of oxygen might limit the electron supply [118]. The ETC takes about 6 ms [112, 116] (figure 5.9) and requires ca. 2500 molecules of chlorophyll for every mole of oxygen evolved [106, 119].

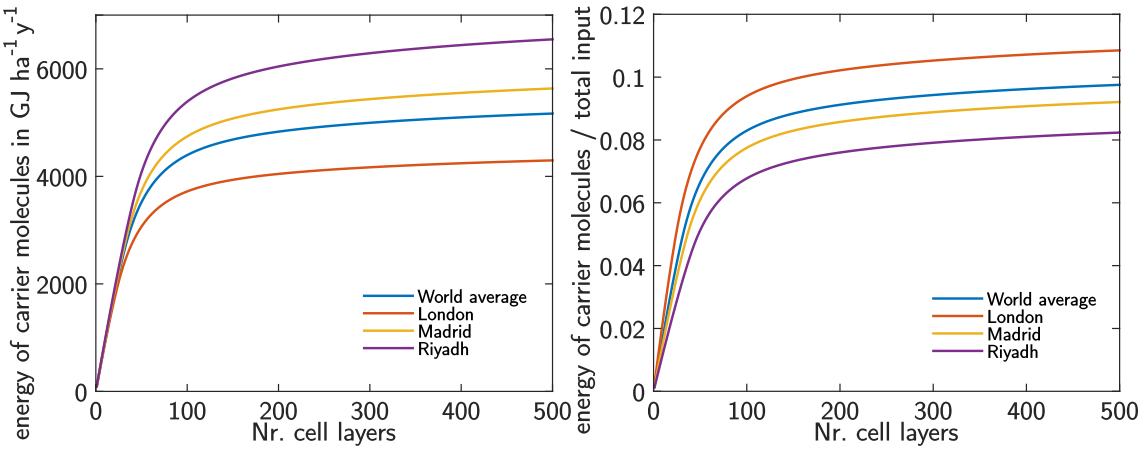

Figure 5.10: Result of ETC saturation on energy conversion in cell layers at different light irradiation levels. *Left:* absolute energy of generated redox molecules. *Right:* energy relative to the SRG.

This kinetic limitation of the ETC causes a saturation limit. Following above considerations and the chlorophyll concentration per layer, the maximum number of photons that can be utilised per cell layer and per second is $12.4\,\mu\,E/m^2/s/layer$.

It is essential to consider the varying light intensity of the diurnal cycle and location dependent SRG values in order to gain realistic estimates of how many cell layers are saturated for how many seconds each average day. The saturated cell-layer dependent electron generation is shown in figure 5.10. In sunny locations, more cyanobacteria operate at their maximum electron production rate and produce a higher output. At the same time, their efficiency is lower because they are saturated for a longer time period. In the following part of this chapter, London is chosen as a sample location for light irradiation values. There, -33.1 % of energy and quanta would be lost due to saturation, storing 9.1 % of sun energy in metabolites.

It should be noted that operating under saturating conditions is undesirable for photosynthetic organisms. While there are some mechanisms for cells to adapt to changing light levels [108, 110, 111], the ongoing absorption without the availability of a reaction partner eventually causes damage to the reaction centres of photosystems (photoinhibition). This results in a high metabolic consumption and long repair times at decreased energy conversion efficiencies. Photoinhibition is not accounted for in this model.

Fast light adaptation and quenching

As briefly discussed in the context of light scattering (section 5.2.2), the photosynthetic apparatus dynamically adapts on the time-scale of minutes to avoid photoinibition. At high irradiation levels, the damage can be caused by free radicals arising from excitations in the reaction centres that cannot be processed by the saturated electron transfer chain.

One adaptation is the rearrangement of light-harvesting proteins in cyanobacteria. The most important mechanism in this regard is the physical coupling and decoupling of phycobilisome antenna molecules. The redox level of plastoquinone in the electron transfer chain leads to a phosphorylation of light harvesting complexes and antenna molecules within 5-10 minutes of a the start of a high irradiation level [112]. This causes their dissociation and a decrease of the absorption cross-section of the complex. The antenna molecules can then couple to less irradiated complexes in inner shaded membranes or to the other type of photosystem (e.g. in response to a change in illumination spectrum), leading to a balance between the photosystems and the cells' metabolic requirements.

The second important adaptation is referred to as non-photochemical quenching. It is a protection mechanism for reaction centres that leads to increased fluorescence as an alternative dissipation pathway for excitation energy in light-harvesting complexes. It is caused by a pigment reaction within few minutes of high irradiation, regulated by the presence of molecular oxygen and a very high pH gradient across the thylakoid membrane [112, 120]. The pigment reaction creates a singlet state just below an excitation state in chlorophyll-a, which moves the excitation away from the reaction centre (in contrast to its normal delivery direction). In the pigment, the excitation dissipates as heat and fluorescence. The absorption cross-section of PSII can be changed as much as 50 % by this mechanism.

No additional loss factor was included in this model for fast light adaptation. This is mainly due to the fact that the decreased conversion efficiency in light saturated cells is partially compensated by the reduced absorption cross-section photosynthetic pigments. This increases the amount of light transmitted by cells, benefiting lower layers in the biofilm (in the model, this is equivalent to enhanced cell scattering). It should also be noted that the emitted fluorescence from cyanobacteria (whether caused by non-photochemical quenching or not) overlaps with their own absorption spectrum, leading to reduced overall energy conversion losses. At the same time, it is difficult to include fast adaptation mechanisms in a non-dynamic model such as this, and specific values for pigment rearrangement and non-photochemical quenching can vary strongly between strains and experimental geometries.

5.2.5 Carbon fixation and respiration

Electron usage for carbon fixation

The reactions for carbon fixation and energy storage in sugars are even more kinetically limited than those in the ETC. In order to complete one Calvin cycle and fix one carbon atom (C), 4 electrons (two NADPH) and 3 ATP are required. The average rate of carbon fixation has been estimated to 0.626 fmol C/µm³/h [121] (average of 34 observations).

Therefore, if the same 200-layer biofilm was used to generate organic carbon (the elementary component of any biofuel), a maximum photon flux of only 1.39 µmol electrons /m²/s/layer would be required to saturate the electron usage of carbon fixation. Under this condition, every electron stored in NADPH would later be contained in sugar, with a very high quantum efficiency of 100 % for the synthesis of sugar from NADPH.

In its most direct form, organic carbon is stored as glucose (6 C), which has a free energy of ΔG =ca. 2870 kJ/mol[1] [122]. 12 NADPH and 18 ATP are used in its production, resulting in an energy efficiency of 90.3 %.

The saturation (under the realistic light conditions chosen in this model) lowers the energy conversion efficiency of light into biomass (organic carbon) down to 4.4 % overall. This value compares well to those reported in the published literature (4.6 - 7 % for micro-algae under ideal light conditions vs. biofilm here) [123–128].

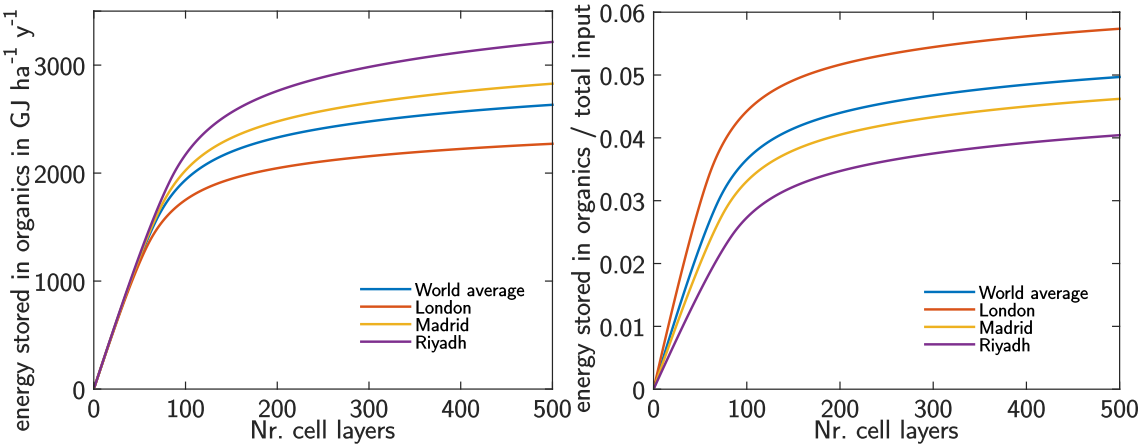

Figure 5.11: Effect of carbon fixation saturation on cell layer absorption and efficiency. *Left:* absolute energy stored in biomass. *Right:* stored energy relative to energy of sunlight.

An analysis of the diurnal cycle for London considering Calvin cycle saturation reveals that almost one-half of the created NADPH molecules cannot be used for carbon fixation (see figure 5.11 right, vs. figure 5.10 right). All of this energy could hypothetically be used for direct electron export to generate electricity in BPV devices or to synthesise alternative energy storage molecules that do not require carbon fixation.

Respiration and basal metabolism

Organic compounds can act as a temporary store for electrons. They can be oxidised again, making their electrons once more available to the metabolism of the cell. Glucose and other organic molecules can thus indirectly contribute to the overall electrogenic activity. Levels of carbon oxidation are species dependent and change with environmental parameters (such as temperature) and their life cycle stage. When oxygen is available to cells (e.g. in BPV devices), respiration is favoured by *Synechocystis* as the carbon oxidation pathway (over fermentation). The maximum respiration rate for *Synechocystis* has been reported to be 0.869 amol O_2/cell/s [129] and four electrons are produced per O_2. In the respiration process, 10 molecules of NADH (which has the same redox potential as NADPH) and 30 molecules of ATP can be recovered from one molecule of glucose (6 C, 12 electrons). This results in a quantum efficiency for this process of 5/6 and an energy efficiency of 97.68 %.

However, not all electrons stored in carbon compounds can be regained. In order to stay alive, repair itself and maintain the compounds necessary for photosynthesis, the organism consumes organic material at a basic metabolic rate. This parameter is inherently difficult to separate from other ongoing processes, as it involves large fractions of organic molecules and because they are utilised at different rates. It has been estimated, however, that the cells' rate of internal organic carbon consumption is ca. 40 times smaller than their maximum rate of organic molecule production [130] (based on

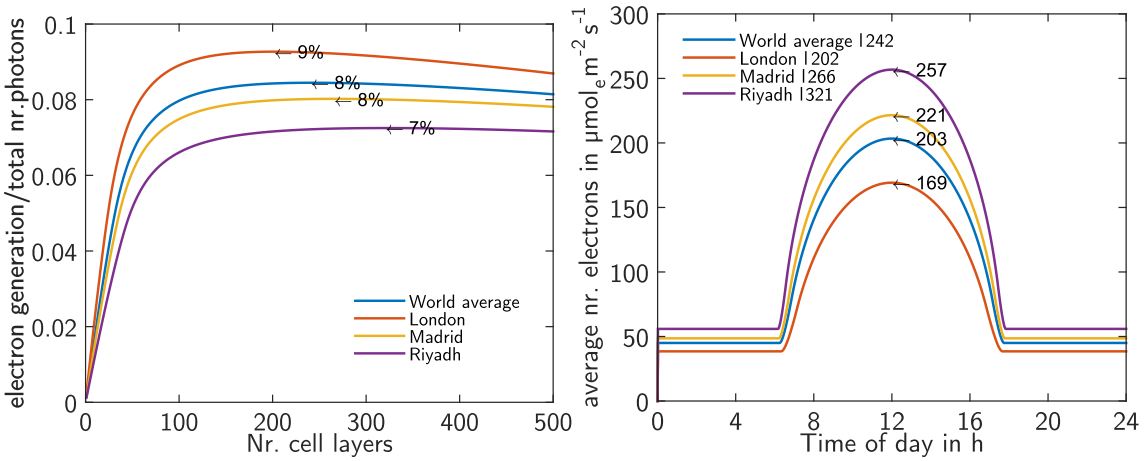

Figure 5.12: Potential pool of metabolically available electrons. *Left:* electrons (including those regained from organic molecules) relative to incoming SRG photons. The theoretical maximum efficiencies are indicated by arrows indicating the optimal number of cell layers for each location. *Right:* generated electrons as a function of diurnal photon flux. The optimal number of cell layers was chosen for each location, as indicated in the figure legend (e.g. 242 layers for the trace corresponding to world average photon flux).

the rate of oxygen uptake). For a 200 cell thick *Synechocystis* biofilm, this would amount to a consumption of 0.0267 µmol electrons /layer/m^2/s (considering the energy value of electrons in glucose).

Energy from the organic electron storage is regained with a delay. It can contribute both to the light and dark current output observed in biophotovoltaic devices [2]. Thus, in contrast to photocurrents, which occur rapidly and only during illumination, respiration-based electron generation is assumed to occur approximately continuously in light and dark.

Following the above considerations for the location of London, 98.1 % of the energy and 83.7 % of electrons stored in carbon could be regained for indirect electrogenic activity after subtracting the basal metabolic rate. The basal energy cost of cell layers balances the gain of additional light absorption and reveals an optimum biofilm thickness of ca. 100 to 400 cell layers, see figure 5.12.

At this stage, it should be noted that the amount of accessible energy in *Synechocystis* in the form of electrons (NADPH), ca. 8 % of SRG energy, is approx. double compared to the energy that could be harvested as biomass, ca. 4 %.

5.3 The role of pigment distribution

5.3.1 Motivation for pigment reduction

As already discussed in detail in this chapter, saturation of electron generation is a bottleneck for photosynthetic efficiencies at uninterrupted relatively high irradiance levels. At the same time, photosynthetically produced organic matter is still globally the largest source of food and energy. Therefore, many lines of research are dedicated to

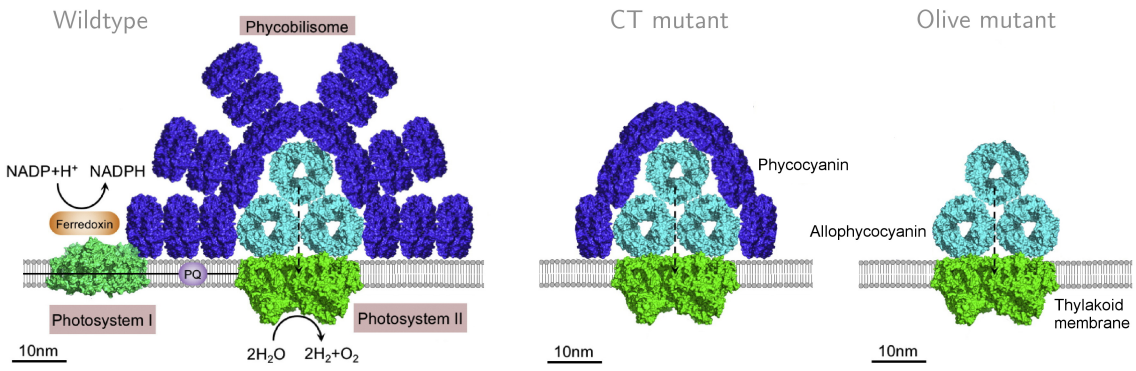

Figure 5.13: Schematic model of *Synechocystis* sp. 6803 thylakoid membrane, showing the phycobilisome–photosystem supercomplex and its mutant forms. The protein structures originate from the PDB database. [Figure modified from [108], CC-BY].

improving photosynthetic processes, related biological material and energy conversion pathways. One approach is to reduce the amount of pigments present in light harvesting complexes. This increases the transparency of cells so that more cell layers can operate at better photosynthetic rates, with less saturation losses. The approach of improving photosynthesis by reducing energy flux saturation has not been investigated systematically as convincing models to link experiment and theory are lacking for many scenarios. This study is a contribution towards this goal, providing a quantitative model that incorporates saturation processes, and exploratory biophotovoltaic measurements with genetically engineered cyanobacteria.

5.3.2 Cyanobacterial antenna mutant BPVs

It has been demonstrated previously that parts of the light-harvesting complex in the cyanobacterium *Synechocystis* sp. PCC 6803 could be removed genetically, which caused

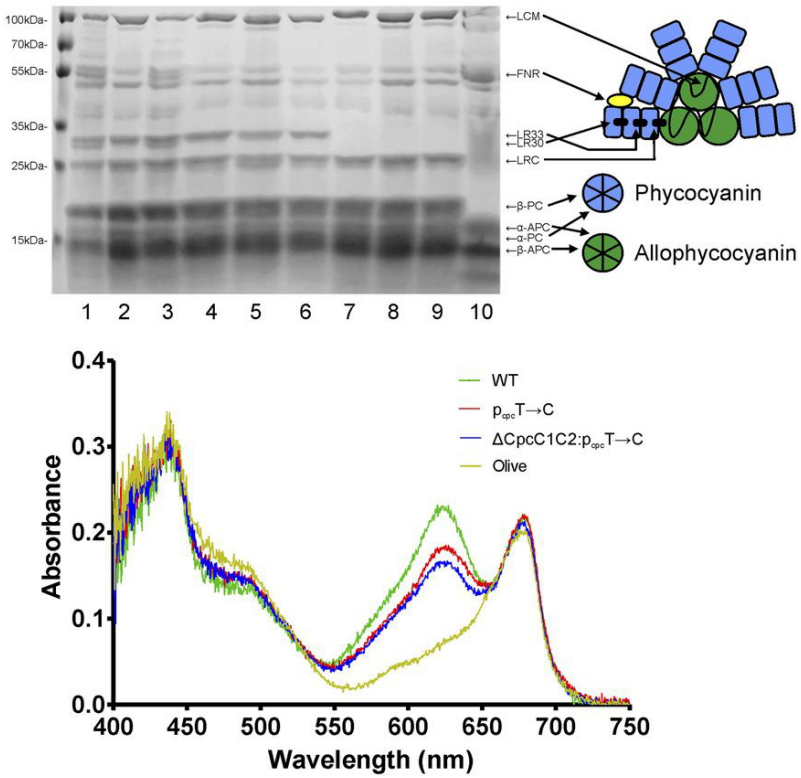

Figure 5.14: Analysis of cyanobacteria phycobilisome (PBS) mutants. *Top:* separation of PBS polypeptides by gel electrophoresis from the wild type (lane 1) to a range of genetic variants (lane 2-10). The identity of specific polypeptides is indicated in the schematic representation of the PBS of *Synechocystis* sp. PCC 6803 (Glazer, 1988). *Bottom:* Spectrum showing the absorbance of the four strains. Values are averages from four biological replicates and are standardized to 750 nm. WT, wildtype. Reprinted with permission from [107].

increased light penetration through cell cultures [107] and, under some illumination configurations, enhanced growth [107, 131]. Specifically, a large antenna complex present in cyanobacteria, the phycobilisome (PBS), was modified (figure 5.13). This complex can associate with PSII and PSI. It harvests photons at a spectral range that differs from 'naked' photosystems (see absorption difference of mutant strains in figure 5.14 bottom) and can transfer this additional gained energy to the reaction centres of the associated photosystem. PBS has a modular build of linked protein units, namely allophycocyanin (cyan in figure 5.13) and (in *Synechocystis* sp. PCC 6803) stacks of phycocyanin discs (indicated in blue). Phycocyanin is used industrially as blue food colour and contributed to the old name of cyanobacteria 'blue-green algae'.

In the following experiments, biofilms of three strains were tested on their ability to generate photocurrents in biophotovoltaic devices (BPVs): the wildtype strain (with ca. three phycocyanin rods per stack), a CT strain with one phycocyanin rod, and a phycocyanin deficient strain referred to as olive mutant. The strains correspond to the green, red, and olive coloured absorption spectra in figure 5.14 bottom, respectively. BPVs are particularly well suited to study the saturation of electron generation because this new method detects photosynthetically generated electrons rapidly. It is, however, not a direct measurement since the export of electrons from *Synechocystis* cyanobacteria is subject to a chain of biochemical pathways which are not fully understood. These pathways

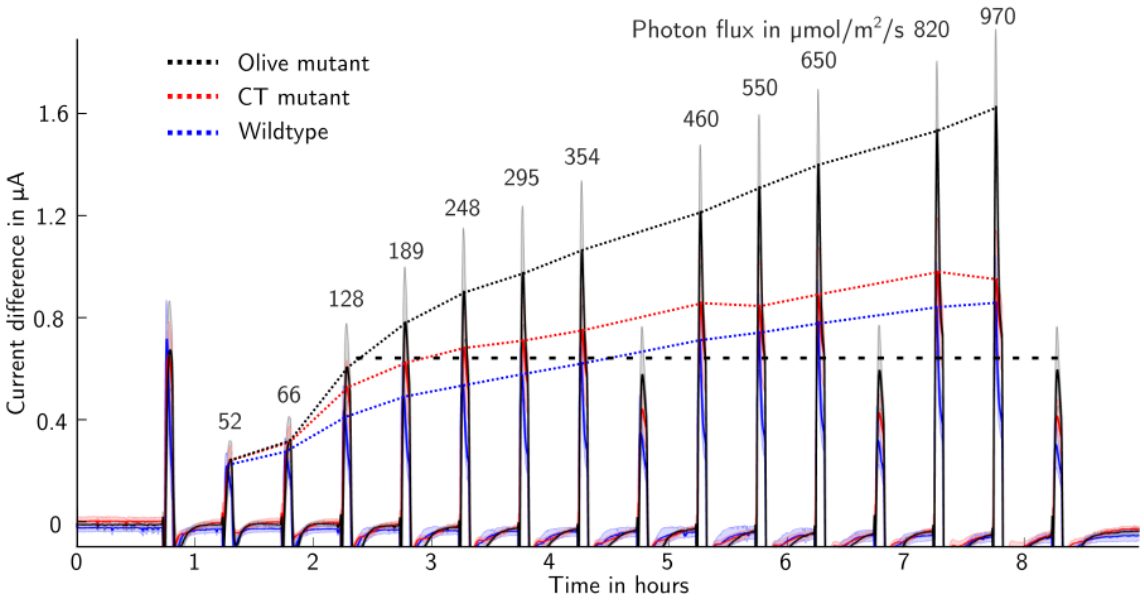

Figure 5.15: Experimental data of the photo-electric response of antenna mutant cyanobacteria strains in biophotovoltaic devices. The mean value and standard deviation (shading) is given for the four BPV channels per strain on nanoporous ITO anodes with 1 cm^2 area. Photocurrents peak quickly when the biofilms are irradiated with light and reach consistent maxima for corresponding white light irradiation levels (spectrum given in figure 3.10).

might involve limiting conversions and cellular regulation processes [1]. The following experimental data explores the electron export from *Synechocystis* sp. PCC 6803 mutants, but does not provide a proof of direct correlation between electron generation and electron export saturation.

5.3.3 Experimental results

The dependence of biophotovoltaic photocurrent saturation (as a function of light irradiance) was tested with respect to the pigment distribution in bacterial biofilms by using the aforementioned antenna mutant strains, and a custom-built LED white-light source (figure 3.10).

To date, it has rarely been achieved to quantitatively compare BPV photocurrents of different strains reliably in biophotovoltaic devices. The challenge of strain comparison lies in the biological variability. While a single culture batch tends to exhibit relatively consistent parameters, e.g. when measured under different conditions or with different electrodes (see chapter 4 for comparison), different batches show differing absolute amounts of photo-electroactivity which can occasionally deviate strongly from the norm. Genetic variants inherently form different bacterial batches and are thus difficult to compare in absolute terms without large numbers of biological replicates. Here, comparability was attempted by measuring device 4-5 sample replicates per bacterial batch, considering only the fast-occurring peak current values (figure 5.15) and by considering the saturation trends rather than comparing absolute photocurrent values of different strains. The experimental methods were the same as described in the pre-

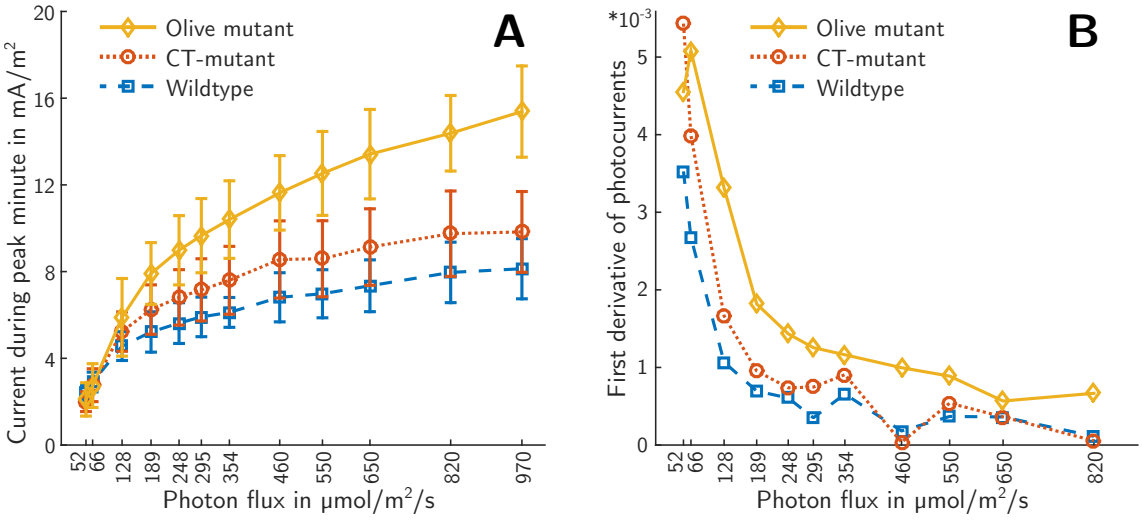

Figure 5.16: Analysed data from the biophotovoltaic response of two antenna mutant strains and wildtype *Synechocystis* cyanobacteria. The data is given for four BPV devices per strain. **A** Peak photocurrents. **B** First derivative of saturation curves in A.

ceding chapter 4. Ca. 134 nmol chlorophyll-a worth of cyanobacteria suspension of the different stains were added to each device with a 1 cm^2-area anode and measured at 22 °C. Because the mutants also differ in cell size and chlorophyll content [107], this corresponds to ca. $3.2 \cdot 10^9$ cells and 69 theoretical biofilm layers for wild-type cells, and ca. $5.1 \cdot 10^9$ cells and 80 theoretical biofilm layers for olive mutants.

The chronoamperometry data in figure 5.15 was replotted in figure 5.16 A to show light-irradiance – photocurrent trends more clearly. For all cell-types, a clear saturation trend can be observed, as the ratio of light irradiation vs. photocurrent decreases at high irradiation values. When considering the slope of the saturation curve (figure 5.16 B), olive mutants (the phycocyanin antenna deficient strain) showed less saturation at higher light levels. Photocurrents and saturation trends obtained for the CT-mutant strains were similar to that of the wildtype, which is why this strain was not further considered.

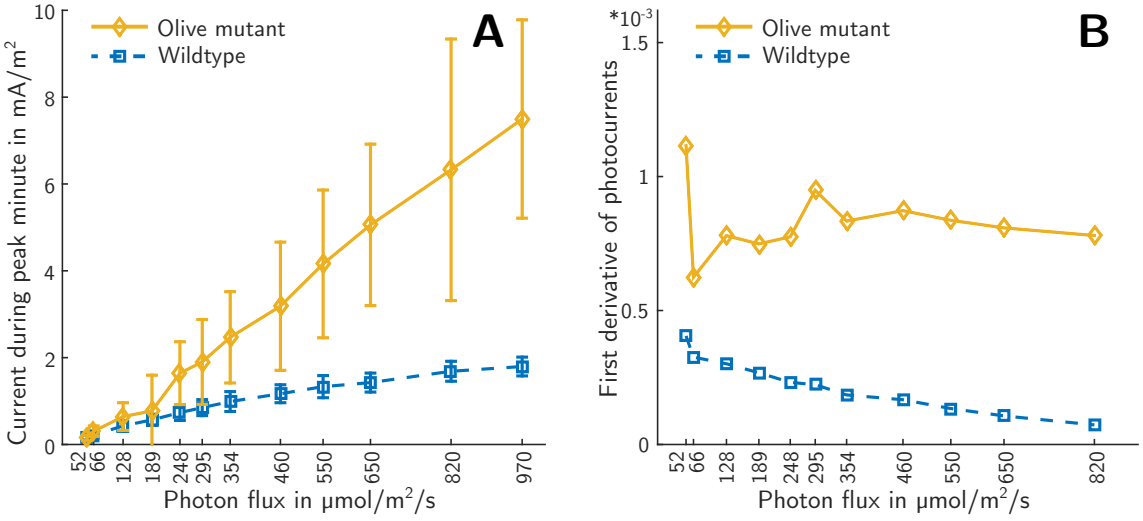

Figure 5.17: Biophotovoltaic response of olive mutants and wildtype *Synechocystis* cyanobacteria. The data are an average of five BPV devices per strain. **A** Peak photocurrents. **B** First derivative of saturation curves in A (smoothed)‘.

In a repeat experiment without CT-mutant cells (figure 5.17) photocurrent peaks were unusually low, especially for wildtype cells (figure 5.17 A), which could have been due to a damaged cell culture. However, similar saturation trends became apparent, with higher saturation losses for wildtype cells when irradiation levels were increased (figure 5.17 B).

5.3.4 Energy flux saturation in theory and practice

A photosynthetic energy flow model (as detailed earlier in this chapter) was compiled for the parameters used during experiments. (*i*) The same white light source spectrum from experiments (figure 3.10) was used (instead of sunlight) and the same light levels.

(*ii*) The strains have different cellular chlorophyll concentrations (9.7 and 8.3 amol/µm^3 for wildtype and olive mutant cells respectively [107]). But in experiments, the same amount of chlorophyll-a (134 nmol) was applied to each device (1 cm^2 biofilm area). In the model, the different concentrations were compensated by the number of (theoretical) cell layers (ca. 69 wildtype and 80 olive cell layers). Lastly, (*iii*) the absorption coefficient as used for each cell line, as given in figure 5.14 bottom (after being standardised to 1 mole chlorophyll/litre), with no light scattering factor. Model-data for the saturated photo-electron generation are given in figure 5.18. They show electrons generated before entering the Calvin cycle, as dark-currents were disregarded in the data analysis of experiments.

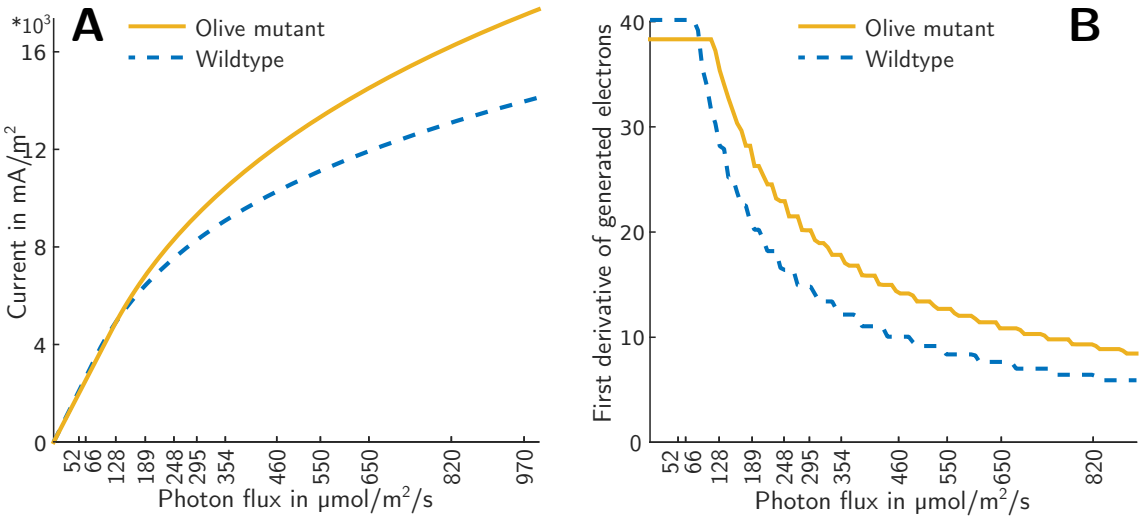

Figure 5.18: Result of the model for the intracellular photocurrent generation of 60 cell layer thick biofilms consisting of olive mutants and wildtype *Synechocystis* cyanobacteria. **A** Photocurrents based on the strains' differing absorption coefficients. **B** First derivative of saturation curves in A.

The model reflects a difference in saturation behaviour for the two strains and an advantage for olive mutants at high photon flux. Any change in the slope of data in figure 5.18 A is due to saturation caused by the rate limited electron transfer chain. Interestingly, wildtype cells exhibit even stronger saturation in experiments than predicted by the model. Furthermore, the saturation onset lies at lower photon flux values in experiments ($< 128\,\mu mol/m^2/s$, see figure 5.16 B) than in the model (ca. $300\,\mu mol/m^2/s$ with a scattering factor of 3), and only becomes comparable when disregarding the scattering factor (figure 5.18). However, the inclusion of scattering is likely to make the model more realistic and other reasons for the increased saturation such as oxygen release [118] or electron export mechanisms might cause the observed difference. Note that the discrete steps in the saturation slope of the model (figure 5.18 B) are caused by the assumption of dense cell layers. Each step represents the saturation of one cell

layer. In reality, saturation would occur in thylakoid membrane areas within individual cyanobacteria, which would not, on average, not lead to a discrete behaviour in biofilms. Nevertheless, the presented saturation model can (for the first time) partially explain the experimentally found saturation behaviour of biofilms.

5.4 Discussion

The model attempts to capture the saturation behaviour of photosynthetic electron generation in biofilms by complementing theoretical parameters (realistic energy input, biofilm layers and electron transfer mechanisms) with recently published bio-energetic values of the model organism *Synechocystis* sp. PCC 6803. Figure 5.19 provides a schematic summary of model-derived quantum efficiencies. The model is used to associate the current output of a biophotovoltaic device (BPV) with the corresponding amount of electrons in the organisms available for export per second. The predicted electron availability in biofilms varies according to the photon flux in different locations from lunchtime Riyadh ($257\,\mu mol\,e/m^2/s = 16.4\,A/m^2$) to the dark current (caused by respiration) expected in London at night time ($39\,\mu mol\,e/m^2/s = 2.1\,A/m^2$, figure 5.12).

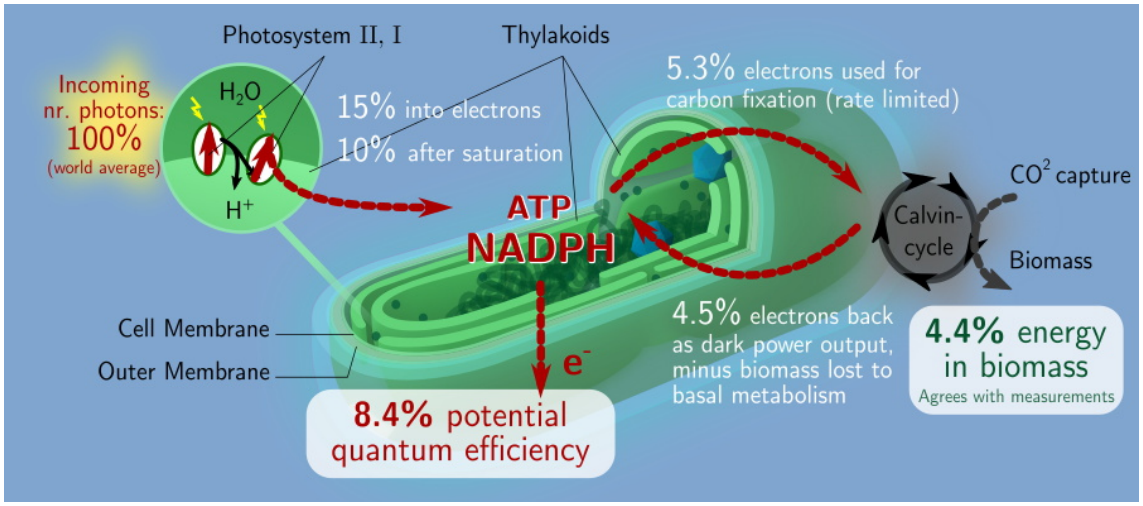

Figure 5.19: Summary of photosynthetic energy conversion efficiencies and electron availability in *Synechocystis* cyanobacteria, a model organism for photosynthesis in general.

The model was designed to only account for the energetic parameters believed to have the strongest effect on electron generation and for which reasonable assumptions could be made based on measurement data (own or derived from the literature). Based on these assumptions, the optimal cyanobacteria biofilm thickness range and resulting electron availability was estimated for real world locations. Further competing mechanisms in cyanobacteria that use up electrons, in addition to biomass generation, may be a valuable

extensions of the model. This requires further experimental and theoretical studies to estimate their effect on presented model parameters. Additional mechanisms which could influence the model predictions include: (*i*) a quantitative consideration of non-photochemical quenching at high light intensities backed by fluorescence measurements; (*ii*) the effect of photoinhibition, damage caused to photosystems at high irradiation levels associated with an efficiency drop and slow, active cellular repair or replacement; (*iii*) cyclic electron flow around photosystem I, believed to account for losses up to 20 % under light limiting conditions [112]. This pathway allows PSI-energised electrons from ferredoxin (Fd in figure 5.9) to flow back to the cytochrome B_6/f complex, leading to ATP generation without light activation of PSII; (*iv*) the regulation of terminal oxidases and flavor-diiron proteins that specifically act as intracellular electron sinks [1, 96]; (*v*) the changing availability of carbon dioxide in the cell medium; (*vi*) energetic differences between growth and stationary phase of bacterial metabolism; and (*vii*) the extrapolation of the energy available to the cell from the number of NADPH/NADH and ATP/ADP molecules. Assigning an energetic value to these molecules is a more dynamic process than so far presented. For example, the redox value of ATP is dependent ($\pm$ 100%) on the concentration ratio of ATP and ADP which changes in different cell-compartments and varies during the diurnal cycle.

The addition of scattering to the assumptions of a theoretical biofilm (discussed in section 5.2.2) had a noticeable effect on the overall efficiency of model predictions. It seems therefore worth exploring potential technological solutions to optimise scattering in these systems. This could e.g. be achieved by introducing scattering particles into the biofilm. Counteracting light distribution limitations technically (by using evanescent wave-guides) has been applied previously [132–134], increasing the light intake more than 10 fold. This principle has already been demonstrated in a biophotovoltaic device [135]. Scattering particles for DSSCs have also been proposed in the literature [136].

The comparison of model predictions for wildtype and photosynthetic antenna mutant cyanobacteria (differing in absorption spectra) show qualitative agreement with trends in experimental (saturation slope) data, confirming the predictive power of the model. Even though photosynthesis is known to dynamically adapt to changing light conditions to some degree, the comparison of this non-kinetic model to experiments can be justified by the experimental procedure of only considering the initial photocurrent peak after a dark time (which is then followed by a decline within several minutes, stabilising at a lower photocurrent level). In accordance with any published BPV efficiency [1], experimentally observed photocurrents (collected on the outside of cells) were very small compared to intracellular predictions for electron generation. Nevertheless, it is interesting to compare saturation slopes of experiment and model as an hypothesis generator for future investigations. For example, photocurrents showed a saturation onset at lower light levels

and more overall saturation than predicted (especially wildtype cells). This increased saturation could be due to delays in oxygen release from photosystems [118] or cyclic electron flow [112]. It is unlikely to be an effect of photoinhibition, because the reference light peaks between increasing irradiation steps do not show a decrease for the duration of measurements (dashed line in figure 5.15). It is also unlikely to be an overall limitation of the electron export rate from cyanobacteria, because preliminary data show that the overall collected current can be drastically increased by adding glucose feedstock to *Synechocystis* sp. PCC 6803 BPVs. The sugar leads to a strong increase of respiration in the bacteria, which generates electrons independent of light irradiation and demonstrates their higher capability to export electrons. This study could be further extended to include the parameters of third party experimental data such as referenced in [107]. This parameter comparison might reveal additional possibilities to refine model assumptions.

In summary, both antenna mutant BPV experiments and the model advance the current state of knowledge on photosynthetic energy flux saturation, a process that is not well understood but that is nevertheless highly relevant in many research areas. The model resulted in practical predictions for experimental parameters such as biofilm thickness which are currently missing from the scientific literature. The comparison of the model with experiments was in qualitative agreement but also raised interesting questions concerning the large electron export rates in biophotovoltaic devices at low light irradiation, during which electrons were expected to be utilised for carbon fixation, and the low export rate at intermediate irradiation levels, which were not yet expected to be subject to energy flux saturation. These questions should be addressed in future studies refining the presented tools and incorporating further experimental methods such as florescence measurements on BPV devices.

Chapter 6

Conclusions

Biophotovoltaics (BPV) is a newly described biophysical effect and one of the first examples of bio-integrated technology which successfully interfaces electronic with biological systems. It may be a stepping stone towards technologies that can utilise biological capabilities for engineering and the construction of electrical cellular biosensors. Starting this new project required building interdisciplinary research collaborations, creating a conceptual and methodical framework as well as bridging barriers between disciplines.

I designed and built an experimental set-up (chapter 3 and figure 6.1 right) to comparably measure the photo-electric activity of cyanobacteria and of genetically modified species, which generated valuable insight into how photosynthetic organisms handle the energy gained from light. For this purpose, I investigated important reference parameters such as the electrochemical activity of growth media and temperature dependence. This information is currently missing from the scientific debate and especially temperature was found to be a very sensitive parameter that needs to be controlled.

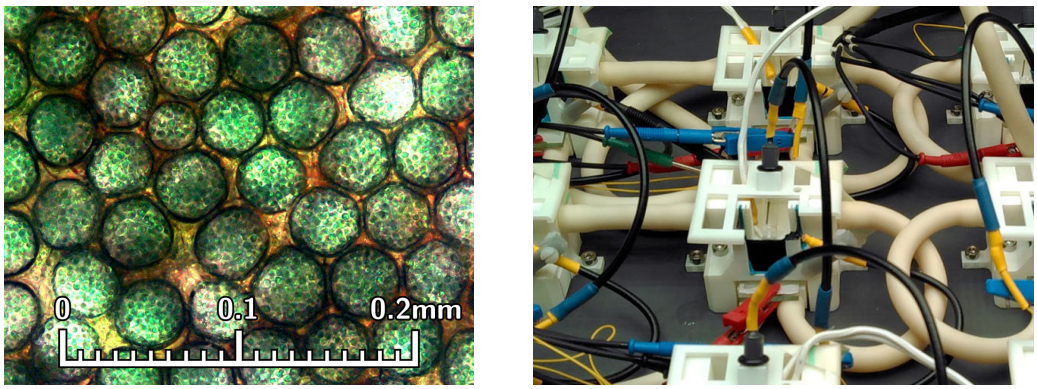

Figure 6.1: *Left:* Optical microscope image of green cyanobacteria inside microstructured translucent electrodes. The large contact area between bacteria and electrode enables fast bio-electric measurements and increases the efficiency of the microbial solar cells by up to a factor of 300. *Right:* 3d printed devices for quantitative, temperature controlled electrochemical measurements of photo-electrons from microorganisms.

Using this set-up, a systematic study of anode morphologies (chapter 2) revealed that large electrode surface areas enhance photocurrents by two orders of magnitude (chapter 4), identifying structuration as key design criterion for bioelectrochemical interfaces. Electrodes with additional micrometer-sized pores allow enhanced direct contact with bacteria, but with the tested cyanobacteria (figure 6.1 left) this did not result in a photocurrent increase, disproving recent speculations in the literature.

I also created a mathematical model (chapter 5) to estimate the light-energy utilisation in biofilms quantitatively, with useful implications for the wider field of plant science and bioenergy. Bringing both theory, genetic modification, and photo-current measurements together, it details how pigment concentration and distribution affect the light-level dependent saturation of electron harvesting biofilms. With nanoporous BPV anodes (developed in chapter 4) and the biological example of differences in light-absorbing pigments, the photon-irradiance dependent saturation of photosynthesis was demonstrated experimentally and correlated qualitatively with model predictions.

According to the model predictions of average photosynthetic electron fluxes (chapter 5), its comparison to experiments and the discussion in the literature [1], the extracellular export of electrons from cyanobacteria is thought to be the main bottleneck to more efficient and sensitive biophotovoltaic devices. Much is still to be learned about the working principles of this electron transfer. The experimental methods developed for this thesis enable the much faster and more sensitive detection of bacterial photocurrents, but no particular electrochemical signal was observed that could be used to identify a candidate redox molecule capable of shuttling photo-electrons from cyanobacteria to electrodes. Based on literature predictions that the utilised cyanobacteria may be capable of direct electron transfer (DET) by means of bacterial-nanowires [24, 31], an important goal of this thesis was the detection and exploitation of this transfer mode. DET tends to be fast and low-loss compared to mediated electron transfer [77]. Instead of exploiting it, however, evidence was found supporting that no direct transfer takes place at relevant electron flux levels (chapter 4). For future studies aiming to elucidate electron export pathways, a focus on mediated transport might lead to more information about molecules and intermediate membrane proteins involved.

References

[1]A. J. McCormick, P. Bombelli, R. W. Bradley, R. Thorne, T. Wenzel, and C. J. Howe, "Biophotovoltaics: oxygenic photosynthetic organisms in the world of bioelectrochemical systems", Energy Environ. Sci. **8**, 1092–1109 (2015).

[2]P. Bombelli, R. W. Bradley, A. M. Scott, A. J. Philips, A. J. McCormick, S. M. Cruz, A. Anderson, K. Yunus, D. S. Bendall, P. J. Cameron, J. M. Davies, A. G. Smith, C. J. Howe, and A. C. Fisher, "Quantitative analysis of the factors limiting solar power transduction by Synechocystis sp. PCC 6803 in biological photovoltaic devices", Energy Environ. Sci. **4**, 4690 (2011).

[3]A. J. McCormick, P. Bombelli, A. M. Scott, A. J. Philips, A. G. Smith, A. C. Fisher, and C. J. Howe, "Photosynthetic biofilms in pure culture harness solar energy in a mediatorless bio-photovoltaic cell (BPV) system", Energy Environ. Sci. **4**, 4699 (2011).

[4]K. P. Nevin, H. Richter, S. F. Covalla, J. P. Johnson, T. L. Woodard, A. L. Orloff, H. Jia, M. Zhang, and D. R. Lovley, "Power output and columbic efficiencies from biofilms of Geobacter sulfurreducens comparable to mixed community microbial fuel cells", Environ. Microbiol. **10**, 2505–14 (2008).

[5]D. Xing, Y. Zuo, S. Cheng, J. M. Regan, and B. E. Logan, "Electricity generation by Rhodopseudomonas palustris DX-1", Environ. Sci. Technol. **42**, 4146–51 (2008).

[6]C. I. Torres, "On the importance of identifying, characterizing, and predicting fundamental phenomena towards microbial electrochemistry applications", Curr. Opin. Biotechnol. **27C**, 107–114 (2014).

[7]M. C. Potter, "Electrical Effects accompanying the Decomposition of Organic Compounds", Proc. Royal Soc. B **84**, 260–276 (1911).

[8]Y. Yang, G. Sun, and M. Xu, "Microbial fuel cells come of age", J. Chem. Technol. Biotechnol. **86**, 625–632 (2011).

[9]M. Rosenbaum, Z. He, and L. T. Angenent, "Light energy to bioelectricity: photosynthetic microbial fuel cells", Curr. Opin. Biotechnol. **21**, 259–64 (2010).

[10]D. P. B. T. B. Strik, R. a. Timmers, M. Helder, K. J. J. Steinbusch, H. V. M. Hamelers, and C. J. N. Buisman, "Microbial solar cells: applying photosynthetic and electrochemically active organisms", Trends Biotechnol. **29**, 41–9 (2011).

[11]R. S. Berk and J. H. Canfield, "Bioelectrochemical Energy Conversion", Appl. Microbiol. **12**, 10–2 (1964).

[12]A. E. Inglesby, D. a. Beatty, and A. C. Fisher, "Rhodopseudomonas palustris purple bacteria fed Arthrospira maxima cyanobacteria: demonstration of application in microbial fuel cells", RSC Adv. **2**, 4829 (2012).

[13]A. Badura, D. Guschin, T. Kothe, M. J. Kopczak, W. Schuhmann, and M. Rögner, "Photocurrent generation by photosystem 1 integrated in crosslinked redox hydrogels", Energy Environ. Sci. **4**, 2435 (2011).

[14]D. Gerster, J. Reichert, H. Bi, J. V. Barth, S. M. Kaniber, A. W. Holleitner, I. Visoly-Fisher, S. Sergani, and I. Carmeli, "Photocurrent of a single photosynthetic protein", Nat. Nanotechnol. **7**, 673–6 (2012).

[15]O. Yehezkeli, R. Tel-Vered, J. Wasserman, A. Trifonov, D. Michaeli, R. Nechushtai, and I. Willner, "Integrated photosystem II-based photo-bioelectrochemical cells", Nat. Commun. **3**, 742 (2012).

[16]M. Rasmussen, A. Shrier, and S. D. Minteer, "High performance thylakoid bio-solar cell using laccase enzymatic biocathodes", Phys. Chem. Chem. Phys. **15**, 9062–5 (2013).

[17]M. Rasmussen and S. D. Minteer, "Investigating the mechanism of thylakoid direct electron transfer for photocurrent generation", Electrochim. Acta **126**, 68–73 (2014).

[18]P. Bombelli, M. Zarrouati, R. J. Thorne, K. Schneider, S. J. Rowden, A. Ali, K. Yunus, P. J. Cameron, A. C. Fisher, I. D. Wilson, C. J. Howe, and M. A. J, "Surface morphology and surface energy of anode materials influence power outputs in a multi-channel mediatorless bio-photovoltaic (BPV) system.", Phys. Chem. Chem. Phys. **14**, 12221–9 (2012).

[19]M. Rosenbaum, U. Schröder, and F. Scholz, "Utilizing the green alga Chlamydomonas reinhardtii for microbial electricity generation: a living solar cell", Appl. Microbiol. Biotechnol. **68**, 753–6 (2005).

[20]T. Prakash, "Review on nanostructured semiconductors for dye sensitized solar cells", Electron. Mater. Lett. **8**, 231–243 (2012).

[21]P. S. Stewart, "Diffusion in Biofilms", J. Bacteriol. **185**, 1485–1491 (2003).

[22]G. Reguera, K. D. Mccarthy, T. Mehta, J. S. Nicoll, M. T. Tuominen, and D. R. Lovley, "Extracellular electron transfer via microbial nanowires", Nature **435**, 1098–1101 (2005).

[23]D. R. Lovley, "Live wires: direct extracellular electron exchange for bioenergy and the bioremediation of energy-related contamination", Energy Environ. Sci. **4**, 4896 (2011).

[24]Y. A. Gorby, S. Yanina, J. S. McLean, K. M. Rosso, D. Moyles, A. Dohnalkova, T. J. Beveridge, I. S. Chang, B. H. Kim, K. S. Kim, D. E. Culley, S. B. Reed, M. F. Romine, D. A. Saffarini, E. A. Hill, L. Shi, D. A. Elias, D. W. Kennedy, G. Pinchuk, K. Watanabe, S. Ishii, B. Logan, K. H. Nealson, and J. K. Fredrickson, "Electrically conductive bacterial nanowires produced by Shewanella oneidensis strain MR-1 and other microorganisms", Proc. Natl. Acad. Sci. **103**, 11358–63 (2006).

[25]U. Schröder, "Anodic electron transfer mechanisms in microbial fuel cells and their energy efficiency", Phys. Chem. Chem. Phys. **9**, 2619–29 (2007).

[26]K. Rabaey and R. a. Rozendal, "Microbial electrosynthesis - revisiting the electrical route for microbial production", Nat. Rev. Microbiol. **8**, 706–16 (2010).

[27]B. E. Logan, "Scaling up microbial fuel cells and other bioelectrochemical systems", Appl. Microbiol. Biotechnol. **85**, 1665–1671 (2009).

[28]J. Wei, P. Liang, and X. Huang, "Recent progress in electrodes for microbial fuel cells", Bioresour. Technol. **102**, 9335–44 (2011).

[29]J. Babauta, R. Renslow, Z. Lewandowski, H. Beyenal, and P. Taylor, "Electrochemically active biofilms: facts and fiction. A review", Biofouling, 37–41 (2012).

[30]S. Sure, A. Torriero, A. Gaur, L. Li, Y. Chen, C. Tripathi, A. Adholeya, M. Ackland, and M. Kochar, "Inquisition of microcystis aeruginosa and synechocystis nanowires: characterization and modelling", Antonie Van Leeuwenhoek **108**, 1213–1225 (2015).

[31]S. Sure, A. Torriero, A. Gaur, L. Li, Y. Chen, C. Tripathi, A. Adholeya, M. Ackland, and M. Kochar, "Identification and topographical characterisation of microbial nanowires in nostoc punctiforme", Antonie Van Leeuwenhoek **109**, 475–480 (2015).

[32]C. Li, L. Ding, H. Cui, L. Zhang, K. Xu, and H. Ren, "Application of conductive polymers in biocathode of microbial fuel cells and microbial community", Bioresour. Technol. **116**, 459–65 (2012).

[33]K. J. J. Steinbusch, H. V. M. Hamelers, J. D. Schaap, C. Kampman, and C. J. N. Buisman, "Bioelectrochemical ethanol production through mediated acetate reduction by mixed cultures", Environ. Sci. Technol. **44**, 513–7 (2010).

[34]H. Liu, R. Ramnarayanan, and B. E. Logan, "Production of electricity during wastewater treatment using a single chamber microbial fuel cell", Environ. Sci. Technol. **38**, 2281–5 (2004).

[35]L. T. Angenent, K. Karim, M. H. Al-Dahhan, B. A. Wrenn, and R. Domíguez-Espinosa, "Production of bioenergy and biochemicals from industrial and agricultural wastewater", Trends Biotechnol. **22**, 477–85 (2004).

[36]R. a. Rozendal, H. V. M. Hamelers, K. Rabaey, J. Keller, and C. J. N. Buisman, "Towards practical implementation of bioelectrochemical wastewater treatment", Trends Biotechnol. **26**, 450–9 (2008).

[37]K. P. Nevin, T. L. Woodard, A. E. Franks, Z. M. Summers, and D. R. Lovley, "Microbial electrosynthesis: feeding microbes electricity to convert carbon dioxide and water to multicarbon extracellular organic compounds", MBio **1** (2010) 10.1128/mBio.00103-10.

[38]M. Rosenbaum, F. Aulenta, M. Villano, and L. T. Angenent, "Cathodes as electron donors for microbial metabolism: which extracellular electron transfer mechanisms are involved?", Bioresour. Technol. **102**, 324–33 (2011).

[39]R. a. Rozendal, A. W. Jeremiasse, H. V. M. Hamelers, and C. J. N. Buisman, "Hydrogen Production with a Microbial Biocathode", Environ. Sci. Technol. **42**, 629–634 (2008).

[40]X. Cao, X. Huang, P. Liang, N. Boon, M. Fan, L. Zhang, and X. Zhang, "A completely anoxic microbial fuel cell using a photo-biocathode for cathodic carbon dioxide reduction", Energy Environ. Sci. **2**, 498 (2009).

[41]S. Malik, E. Drott, P. Grisdela, J. Lee, C. Lee, D. a. Lowy, S. Gray, and L. M. Tender, "A self-assembling self-repairing microbial photoelectrochemical solar cell", Energy Environ. Sci. **2**, 292 (2009).

[42]Y. Wu, K. Guan, Z. Wang, B. Xu, and F. Zhao, "Isolation, identification and characterization of an electrogenic microalgae strain", PLoS One **8**, e73442 (2013).

[43]L. Gupta, A. Mansingh, and P. Srivastava, "Band gap narrowing and the band structure of tin-doped indium oxide films", Thin Solid Films **176**, 33–44 (1989).

[44]H. Kim, C. Gilmore, A. Piqué, J. Horwitz, H. Mattoussi, H. Murata, Z. Kafafi, and D. Chrisey, "Electrical, optical, and structural properties of indium–tin–oxide thin films for organic light-emitting devices", J Appl Phys **86**, 6451–6461 (1999).

[45]T. Minami, "Transparent conducting oxide semiconductors for transparent electrodes", Semicond Sci Tech **20**, S35 (2005).

[46]A. Klein, C. Körber, A. Wachau, F. Säuberlich, Y. Gassenbauer, S. Harvey, D. Proffit, and T. Mason, "Transparent conducting oxides for photovoltaics: manipulation of fermi level, work function and energy band alignment", Mater **3**, 4892–4914 (2010).

[47]P. Docampo, S. Guldin, M. Stefik, P. Tiwana, M. C. Orilall, S. Hüttner, H. Sai, U. Wiesner, U. Steiner, and H. J. Snaith, "Control of Solid-State Dye-Sensitized Solar Cell Performance by Block-Copolymer-Directed TiO2 Synthesis", Adv. Funct. Mater. **20**, 1787–1796 (2010).

[48]L. Li, U. Steiner, and S. Mahajan, "Improved electrochromic performance in inverse opal vanadium oxide films", J. Mater. Chem. **20**, 7131 (2010).

[49]T. Sunde, M. Einarsrud, and T. Grande, "Optimisation of chemical solution deposition of indium tin oxide thin films", Thin Solid Films **573**, 48–55 (2014).

[50]M. Mirzaee and A. Dolati, "Effects of tin valence on microstructure, optical, and electrical properties of ITO thin films prepared by sol–gel method", J Sol-gel Sci Techn **75**, 582–592 (2015).

[51]S. Ito, T. Murakami, P. Comte, P. Liska, C. Grätzel, M. Nazeeruddin, and M. Grätzel, "Fabrication of thin film dye sensitized solar cells with solar to electric power conversion efficiency over 10%", Thin Solid Films **516**, 4613–4619 (2008).

[52]N. D. Denkov, O. D. Velev, P. A. Kralchevsky, I. B. Ivanov, H. Yoshimura, and K. Nagayama, "Two-dimensional crystallization", Nature **361**, 26–26 (1993).

[53]Z. Gu, S. Kubo, A. Fujishima, and O. Sato, "Infiltration of colloidal crystal with nanoparticles using capillary forces: a simple technique for the fabrication of films with an ordered porous structure", Appl Phys **74**, 127–129 (2002).

[54]K. P. Sokol, D. Mersch, V. Hartmann, J. Z. Zhang, M. M. Nowaczyk, M. Rögner, A. Ruff, W. Schuhmann, N. Plumeré, and E. Reisner, "Rational wiring of photosystem II to hierarchical indium tin oxide electrodes using redox polymers", Energy Environ. Sci. **9**, 3698–3709 (2016).

[55]S. Torquato, T. M. Truskett, and P. G. Debenedetti, "Is random close packing of spheres well defined?", Phys. Rev. Lett. **84**, 2064–2067 (2000).

[56]C. J. Brinker and G. W. Scherer, *Sol-gel science: the physics and chemistry of sol-gel processing* (Academic press, 2013).

[57]R. Thorne, H. Hu, K. Schneider, P. Bombelli, A. Fisher, L. M. Peter, A. Dent, and P. J. Cameron, "Porous ceramic anode materials for photo-microbial fuel cells", J. Mater. Chem. **21**, 18055 (2011).

[58]S. Guldin, P. Docampo, M. Stefik, G. Kamita, U. Wiesner, H. Snaith, and U. Steiner, "Layer-by-Layer formation of Block-Copolymer-Derived TiO2 for Solid-State Dye Sensitized solar cells", Small **8**, 432–440 (2012).

[59]J. Selvakumaran, J. L. Keddie, D. J. Ewins, and M. Hughes, "Protein adsorption on materials for recording sites on implantable microelectrodes", J Mater Sci Mater Medicine **19**, 143–151 (2008).

[60]H. Dewi, F. Meng, B. Sana, C. Guo, B. Norling, X. Chen, and S. Lim, "Investigation of electron transfer from isolated spinach thylakoids to indium tin oxide", Rsc Adv **4**, 48815–48820 (2014).

[61]K. Knoche, E. Aoyama, K. Hasan, and S. Minteer, "Role of nitrogenase and ferredoxin in the mechanism of bioelectrocatalytic nitrogen fixation by the cyanobacteria anabaena variabilis SA-1 mutant immobilized on indium tin oxide (ITO) electrodes", Electrochim Acta **232**, 396–403 (2017).

[62]L. J. del Valle, F. Estrany, E. Armelin, R. Oliver, and C. Alemán, "Cellular adhesion, proliferation and viability on conducting polymer substrates", Macromol. Biosci. **8**, 1144–51 (2008).

[63]G. G. Malliaras, "Organic bioelectronics: a new era for organic electronics", Biochim. Biophys. Acta **1830**, 4286–7 (2013).

[64]N. K. Guimard, N. Gomez, and C. E. Schmidt, "Conducting polymers in biomedical engineering", Prog. Polym. Sci. **32**, 876–921 (2007).

[65]X. Cui and D. C. Martin, "Electrochemical deposition and characterization of poly(3,4-ethylenedioxythiophene) on neural microelectrode arrays", Sensors Actuators B Chem. **89**, 92–102 (2003).

[66]A. Nel, T. Xia, L. Mädler, and N. Li, "Toxic potential of materials at the nanolevel", Science **311**, 622–627 (2006).

[67]A. Suresh, D. Pelletier, and M. Doktycz, "Relating nanomaterial properties and microbial toxicity", Nanoscale **5**, 463–474 (2012).

[68]S. Sabella, R. Carney, V. Brunetti, M. Malvindi, A. Noura, G. Vecchio, S. Janes, O. Bakr, R. Cingolani, F. Stellacci, and P. Pompa, "A general mechanism for intracellular toxicity of Metal-Containing nanoparticles", Nanoscale **6** (2014) 10.1039/C4NR01234H.

[69]A. B. Djurisic, Y. Leung, A. M. Ng, X. Xu, P. K. Lee, N. Degger, and R. Wu, "Toxicity of metal oxide nanoparticles: mechanisms, characterization, and avoiding experimental artefacts", Small **11**, 26–44 (2015).

[70]S. Manzo, M. Miglietta, G. Rametta, S. Buono, and G. Francia, "Toxic effects of ZnO nanoparticles towards marine algae dunaliella tertiolecta", Sci Total Environ **445**, 371–376 (2013).

[71]A. Solieman and M. Aegerter, "Modeling of optical and electrical properties of in2o3:sn coatings made by various techniques", Thin Solid Films **502**, 205–211 (2006).

[72]Y. Liu, K. Peters, B. Mandlmeier, A. Müller, K. Fominykh, J. Rathousky, C. Scheu, and D. Fattakhova-Rohlfing, "Macroporous indium tin oxide electrode layers as conducting substrates for immobilization of bulky electroactive guests", Electrochim. Acta **140**, 108–115 (2014).

[73]R. a. Green, N. H. Lovell, G. G. Wallace, and L. a. Poole-Warren, "Conducting polymers for neural interfaces: challenges in developing an effective long-term implant", Biomaterials **29**, 3393–9 (2008).

[74]R. a. Green, N. H. Lovell, and L. a. Poole-Warren, "Cell attachment functionality of bioactive conducting polymers for neural interfaces", Biomaterials **30**, 3637–44 (2009).

[75]P. Roach, T. Parker, N. Gadegaard, and M. Alexander, "Surface strategies for control of neuronal cell adhesion: A review", Surf. Sci. Rep. **65**, 145–173 (2010).

[76]C.-H. Lu, Y.-S. Hsiao, C.-W. Kuo, and P. Chen, "Electrically tunable organic bioelectronics for spatial and temporal manipulation of neuron-like pheochromocytoma (PC-12) cells", Biochim. Biophys. Acta **1830**, 4321–8 (2013).

[77]U. Schröder, "Anodic electron transfer mechanisms in microbial fuel cells and their energy efficiency.", Phys. Chem. Chem. Phys. **9**, 2619–29 (2007).

[78]R. Porra, W. Thompson, and P. Kriedemann, "Determination of accurate extinction coefficients and simultaneous equations for assaying chlorophylls a and b extracted with four different solvents: verification of the concentration of chlorophyll standards by atomic absorption spectroscopy", Biochim. Biophys. Acta - Bioenerg. **975**, 384–394 (1989).

[79]A. K. Manohar, O. Bretschger, K. H. Nealson, and F. Mansfeld, "The polarization behavior of the anode in a microbial fuel cell", Electrochim. Acta **53**, 3508–3513 (2008).

[80]Z. He and F. Mansfeld, "Exploring the use of electrochemical impedance spectroscopy (EIS) in microbial fuel cell studies", Energy Environ. Sci. **2**, 215 (2009).

[81]X. Dominguez-Benetton, S. Sevda, K. Vanbroekhoven, and D. Pant, "The accurate use of impedance analysis for the study of microbial electrochemical systems", Chem. Soc. Rev. **41**, 7228–46 (2012).

[82]N. S. Ramaraja P Ramasamy, "Electrochemical Impedance Spectroscopy for Microbial Fuel Cell Characterization", J. Microb. Biochem. Technol. (2013) 10.4172/1948-5948.S6-004.

[83]F. Harnisch and S. Freguia, "A basic tutorial on cyclic voltammetry for the investigation of electroactive microbial biofilms", Chem Asian J **7**, 466–475 (2012).

[84]E. Marsili, J. B. Rollefson, D. B. Baron, R. M. Hozalski, and D. R. Bond, "Microbial biofilm voltammetry: direct electrochemical characterization of catalytic electrode-attached biofilms", Appl. Environ. Microbiol. **74**, 7329–37 (2008).

[85]F. Zhao, R. C. T. Slade, and J. R. Varcoe, "Techniques for the study and development of microbial fuel cells: an electrochemical perspective", Chem. Soc. Rev. **38**, 1926–39 (2009).

[86]I. Fryc, S. Brown, and Y. Ohno, "Spectral matching with an LED-based spectrally tunable light source", in Spie, optics and photonics, Vol. 59411, Proc. 5th Int. Conf. Solid State Lighting (2005).

[87]C. Lee, T. Yang, S. Liao, and K. Chang, "LED-spectrum shaping by optical filter achieves tunable daylight simulator", in Spie, optical design and engineering (2009).

[88]J. U. Grobbelaar, L. Nedbal, and V. Tichý, "Influence of high frequency light/dark fluctuations on photosynthetic characteristics of microalgae photoacclimated to different light intensities and implications for mass algal cultivation", J. Appl. Phycol. **8**, 335–343 (1996).

[89]H. C. P. Matthijs, H. Balke, U. M. van Hes, B. M. A. Kroon, L. R. Mur, and R. A. Binot, "Application of light-emitting diodes in bioreactors: flashing light effects and energy economy in algal culture (chlorella pyrenoidosa)", Biotechnol. Bioeng. **50**, 98–107 (1996).

[90]A. Laohavisit, A. Anderson, P. Bombelli, M. Jacobs, C. J. Howe, J. M. Davies, and A. G. Smith, "Enhancing plasma membrane nadph oxidase activity increases current output by diatoms in biophotovoltaic devices", Algal Research **12**, 91–98 (2015).

[91]P. Bombelli, T. Müller, T. W. Herling, C. J. Howe, and T. P. J. Knowles, "A high power-density, mediator-free, microfluidic biophotovoltaic device for cyanobacterial cells", Adv. Energy Mater. **5**, 1401299–n/a (2015).

[92]L. Darus, T. Sadakane, P. Ledezma, S. Tsujimura, I. Osadebe, D. Leech, L. Gorton, and S. Freguia, "Redox-polymers enable uninterrupted day/night photo-driven electricity generation in biophotovoltaic devices", J. Electrochem. Soc. **164**, H3037–H3040 (2017).

[93]X. Wei, M. Mohammadifar, W. Yang, and S. Choi, "A microscale biophotovoltaic device", in 2016 IEEE sensors (Oct. 2016), pp. 1–3.

[94]T. Noji, K. Kawakami, J. Shen, T. Dewa, M. Nango, N. Kamiya, S. Itoh, and T. Jin, "Oxygen-Evolving porous glass plates containing the photosynthetic photosystem II Pigment-Protein complex.", Langmuir **32**, 7796–805 (2016).

[95]D. J. Lea-Smith, P. Bombelli, R. Vasudevan, and C. J. Howe, "Photosynthetic, respiratory and extracellular electron transport pathways in cyanobacteria", Biochim. Biophys. Acta **1857**, 247–255 (2016).

[96]R. W. Bradley, P. Bombelli, L. D. J, and C. J. Howe, "Terminal oxidase mutants of the cyanobacterium synechocystis sp. PCC 6803 show increased electrogenic activity in biological photo-voltaic systems.", Phys. Chem. Chem. Phys. **15**, 13611–8 (2013).

[97]T. Schenck, U. Hopfner, M. Chávez, H. Machens, I. Somlai-Schweiger, R. Giunta, A. Bohne, J. Nickelsen, M. Allende, and J. Egaña, "Photosynthetic biomaterials: a pathway towards autotrophic tissue engineering", Acta Biomater **15**, 39–47 (2015).

[98]N. S. Malvankar, M. Vargas, K. P. Nevin, A. E. Franks, C. Leang, B. Kim, K. Inoue, T. Mester, S. F. Covalla, J. P. Johnson, V. M. Rotello, M. T. Tuominen, and D. R. Lovley, "Tunable metallic-like conductivity in microbial nanowire networks", Nat. Nanotechnol. **6**, 573–579 (2011).

[99]R. J. Ritchie and a. W. D. Larkum, "Modelling photosynthesis in shallow algal production ponds", Photosynthetica **50**, 481–500 (2012).

[100]A. a. Shastri and J. a. Morgan, "Flux balance analysis of photoautotrophic metabolism", Biotechnol. Prog. **21**, 1617–26 (2005).

[101]L. Mao and W. S. Verwoerd, "Genome-scale stoichiometry analysis to elucidate the innate capability of the cyanobacterium Synechocystis for electricity generation", J. Ind. Microbiol. Biotechnol. **40**, 1161–80 (2013).

[102]J. M. Heinrich, I. Niizawa, F. A. Botta, A. R. Trombert, and H. A. Irazoqui, "Analysis and design of photobioreactors for microalgae production I: method and parameters for radiation field simulation", Photochem. Photobiol. **88**, 938–51 (2012).

[103]National Renewable Energy Laboratory, *Solar radiation for different locations*, 2014.

[104]C. Vejrazka, M. Streefland, R. Wijffels, and M. Janssen, "The role of an electron pool in algal photosynthesis during sub-second light–dark cycling", Algal Research **12**, 43–51 (2015).

[105]G. Bisht, V. Venturini, S. Islam, and L. Jiang, "Estimation of the net radiation using MODIS (Moderate Resolution Imaging Spectroradiometer) data for clear sky days", Remote Sens. Environ. **97**, 52–67 (2005).

[106]D. O. Hall and K. Rao, *Photosynthesis*, Institute of Biology's studies in biology (Cambridge University Press, 1999).

[107]D. J. Lea-Smith, P. Bombelli, J. S. Dennis, S. a. Scott, A. G. Smith, and C. J. Howe, "Phycobilisome deficient strains of Synechocystis sp. PCC6803 have reduced size and require carbon limiting conditions to exhibit enhanced productivity", Plant Physiol. (2014) 10.1104/pp.114.237206.

[108]L.-N. Liu, "Distribution and dynamics of electron transport complexes in cyanobacterial thylakoid membranes", Biochim. Biophys. Acta **1857**, 256–265 (2016).

[109]L.-N. Liu, S. J. Bryan, F. Huang, J. Yu, P. J. Nixon, P. R. Rich, and C. W. Mullineaux, "Control of electron transport routes through redox-regulated redistribution of respiratory complexes", Proc. Natl. Acad. Sci. **109**, 11431–11436 (2012).

[110]H. Dau and O. Canaani, "Short-term adaptation of higher plants to changing light intensities and evidence for the involvement of phosphorylation of the light harvesting chlorophyll a,b protein complex of photosystem ii", J. Photochem. Photobiol. **55**, 873–885 (1992).

[111]M. Ritz, J.-C. Thomas, A. Spilar, and A.-L. Etienne, "Kinetics of photoacclimation in response to a shift to high light of the red alga rhodella violacea adapted to low irradiance", Plant Physiol. **123**, 1415–1426 (2000).

[112]P. G. Falkowski and J. A. Raven, *Aquatic Photosynthesis*, 2nd ed. (Princeton University Press, Princeton, 2007), p. 512.

[113]W. Shockley and H. J. Queisser, "Detailed Balance Limit of Efficiency of p-n Junction Solar Cells", J. Appl. Phys. **32**, 510 (1961).

[114]R. Hill and F. Bendall, "Function of the two cytochrome components in chloroplasts: a working hypothesis", Nature **186**, 136–137 (1960).

[115]J. M. Berg, L. Stryer, and J. L. Tymoczko, *Biochemistry*, 6th ed. (W H Freeman & Co, Gordonsville, Virginia, U.S.A., 2006), p. 120.

[116]R. E. Blankenship, *Molecular mechanisms of photosynthesis* (Blackwell Science, 2002).

[117]C. Bowsher, M. Steer, and A. Tobin, "The light reactions of photosynthesis", in *Plant biochemistry*, Vol. 15, 1st (Garland Science, Aug. 2008) Chap. 4, pp. 65–92.

[118]J. J. Plijter, S. E. Aalbers, J.-P. F. Barends, M. H. Vos, and H. J. van Gorkom, "Oxygen release may limit the rate of photosynthetic electron transport; the use of a weakly polarized oxygen cathode", Biochim. Biophys. Acta **935**, 299–311 (1988).

[119]R. Emerson and W. Arnold, "THE PHOTOCHEMICAL REACTION IN PHOTOSYNTHESIS", J. Gen. Physiol. **16**, 191–205 (1932).

[120]D. R. Ort, "When there is too much light", Plant Physiol. **125**, 29–32 (2001).

[121]A. Krupke, N. Musat, J. Laroche, W. Mohr, B. M. Fuchs, R. I. Amann, M. M. M. Kuypers, and R. a. Foster, "In situ identification and Ni and C fixation rates of uncultivated cyanobacteria populations", Syst. Appl. Microbiol. **36**, 259–71 (2013).

[122]N. A. Campbell, M. R. Taylor, and J. B. Reece, *Biology*, 8th ed. (Pearson/Benjamin Cummings, 2007), p. 523.

[123]R. E. Blankenship, D. M. Tiede, J. Barber, G. W. Brudvig, G. Fleming, M. Ghirardi, M. R. Gunner, W. Junge, D. M. Kramer, A. Melis, T. a. Moore, C. C. Moser, D. G. Nocera, A. J. Nozik, D. R. Ort, W. W. Parson, R. C. Prince, and R. T. Sayre, "Comparing photosynthetic and photovoltaic efficiencies and recognizing the potential for improvement", Science **332**, 805–9 (2011).

[124]M. Janssen, J. Tramper, L. R. Mur, and R. H. Wijffels, "Enclosed outdoor photobioreactors: light regime, photosynthetic efficiency, scale-up, and future prospects", Biotechnol. Bioeng. **81**, 193–210 (2003).

[125]X.-G. Zhu, S. P. Long, and D. R. Ort, "Improving photosynthetic efficiency for greater yield", Annu. Rev. Plant Biol. **61**, 235–61 (2010).

[126]X.-G. Zhu, S. P. Long, and D. R. Ort, "What is the maximum efficiency with which photosynthesis can convert solar energy into biomass?", Curr. Opin. Biotechnol. **19**, 153–9 (2008).

[127]G. C. Dismukes, D. Carrieri, N. Bennette, G. M. Ananyev, and M. C. Posewitz, "Aquatic phototrophs: efficient alternatives to land-based crops for biofuels", Curr. Opin. Biotechnol. **19**, 235–40 (2008).

[128]D. A. Walker, "Biofuels, facts, fantasy, and feasibility", J. Appl. Phycol. **21**, 509–517 (2009).

[129]A. J. McCormick, P. Bombelli, D. J. Lea-Smith, R. W. Bradley, A. M. Scott, A. C. Fisher, A. G. Smith, and C. J. Howe, "Hydrogen production through oxygenic photosynthesis using the cyanobacterium Synechocystis sp. PCC 6803 in a bio-photoelectrolysis cell (BPE) system", Energy Environ. Sci. **6**, 2682 (2013).

[130]H. Knoop, M. Gründel, Y. Zilliges, R. Lehmann, S. Hoffmann, W. Lockau, and R. Steuer, "Flux balance analysis of cyanobacterial metabolism: the metabolic network of Synechocystis sp. PCC 6803", PLoS Comput. Biol. **9**, e1003081 (2013).

[131]J.-H. Kwon, G. Bernát, H. Wagner, M. Rögner, and S. Rexroth, "Reduced light-harvesting antenna: consequences on cyanobacterial metabolism and photosynthetic productivity", Algal Research **2**, 188–195 (2013).

[132]E. E. Jung, M. Kalontarov, D. F. R. Doud, M. D. Ooms, L. T. Angenent, D. Sinton, and D. Erickson, "Slab waveguide photobioreactors for microalgae based biofuel production", Lab Chip **12**, 3740–5 (2012).

[133]M. D. Ooms, L. Bajin, and D. Sinton, "Culturing photosynthetic bacteria through surface plasmon resonance", Appl. Phys. Lett. **101**, 253701 (2012).

[134]S. C. Pierobon, M. D. Ooms, and D. Sinton, "Evanescent cultivation of photosynthetic bacteria on thin waveguides", J. Micromec. Microeng. **24**, 045017 (2014).

[135]N. Samsonoff, M. D. Ooms, and D. Sinton, "A photosynthetic-plasmonic-voltaic cell: Excitation of photosynthetic bacteria and current collection through a plasmonic substrate", Appl. Phys. Lett. **104**, 043704 (2014).

[136]J. Ferber and J. Luther, "Computer simulations of light scattering and absorption in dye-sensitized solar cells", Sol. Energy Mater. Sol. Cells **54**, 265–275 (1998).

Part II

Function of variation in optical structures of biological systems

Chapter 7

Photonic surface structures in flowers

7.1 Introduction

The research presented in this second part of the thesis approaches the interaction of light and biointerface structuration from a different angle. It investigates the surface structures created by natural organisms (plants) and how light interactions with these structured biointerfaces lead to functionality (a colouration effect). This work is a significant extension of my MPhil research project on structural colours in plants.

Structural colours, in contrast to pigment-based colours, are caused by interactions of light with structured materials. In other words, these colours are created by scattering and constructive interference of light instead of absorption. Structures on the length scale of light waves have the strongest colour dependent scattering effect, which is why many structural colours have a small unit size of ca. 100 nm to few micrometers [1]. The more photonic structural elements are present in a small space (and interact with light in the same way), the stronger the optical effect and the more compact and lightweight the structure [2]. Therefore, many well-known structural colours are based on multilayers or highly periodic nanostructures, usually combined with an underlying contrast-generating layer containing a dark absorbing pigments (usually melanin). If the material choice is limited (for example to organic materials in biological systems), structural colouration is a way to extend the available range of colours [3, 4]. Some optical appearances, such as (metal free) metallic colours or iridescence (change of colour with the angle of observation), can only be produced by structural colours [5, 6]. This type of colouration is common in animals [7–11].

In plants, structural colours have received much less attention, even though several occurrences have been demonstrated in this kingdom. Among them are three-dimensional photonic structures in flowers [12], glossy flowers [13, 14], multilayers in fruits and leaves [15, 16], size-controlled scattering particles [17], and surface stria-

tions [18–21]. Different biological functions of such colours have been discussed, including the mimicry of insects for the purpose of pollination [17, 19], enhanced colouration and contrast effects [22] and protection of plant leaves from UV induced damage [12, 16].

A particularly interesting example of photonic surface structures in nature (and subject of this thesis part) are striations, i.e. parallel surface wrinkles in the cuticle of flowers. They are thought to originate from buckling caused by anisotropic growth of the underlying plant organ [23]. In the first study describing the structure, they have been compared to optical diffraction gratings with an iridescent appearance [18]. In addition to a possible colouration effect, they are likely to have several other functions. Those could include tactile cues [24, 25] for pollinating insects and self-cleaning properties caused by enhanced hydrophobicity [25, 26]. Surface striations have also been observed in animals, where they are likely to perform different functions, making a photonic investigations of striations even more worthwhile. Specifically, they have been described in beetles [27], spiders [28, 29] and several snakes [30, 31]. The eastern indigo snake *Drymarchon couperi* was even named after the blue hue due to its iridescence.

7.2 Disorder is intrinsic in natural photonic structures

Man-made photonic surface structures are usually designed and manufactured perfectly periodically, in order to achieve a maximum constructive light interference effect. In nature, however, surface structures often exhibit some degree of local order, but are inherently disordered [32–34]. In some species including the *Morpho* butterfly, this disorder in orientation of individual photonic structural elements has been shown to contribute to the multi-directionality of the optical effect [35, 36]. Beyond widening the angular range of view, disorder in (semi-) periodic structures is often seen as an unfortunate negative and inevitable effect in nature rather than a possible design feature. Surface striations are no exception to such natural disorder, but it will be shown in chapter 8 and 9 that the balanced disorder present in flower striations leads to a functional optical effect.

7.3 Surface striations are widely distributed in flowers

The main families of flowering plants (angiosperms) [38] have been surveyed for surface striations in a long-term study between the Glover, Steiner and Vignolini groups in Cambridge (unpublished). Figure 7.1 summarises the finding that quasi-ordered striations are present in 11 of these 12 taxa (indicated in red in figure 7.1 panel (M)). A

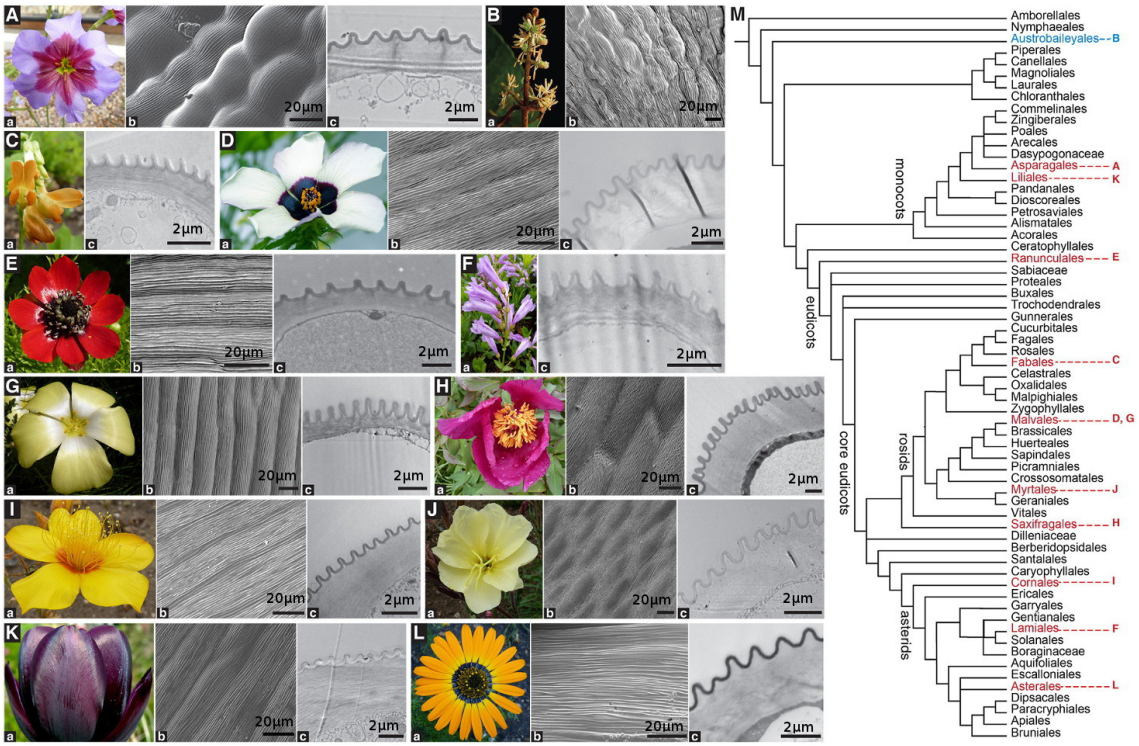

Figure 7.1: **Floral grating-like structures in angiosperms.** The presence of ordered or quasi-ordered parallel cuticular striations on flat tabular cells was identified in *Trimenia moorei* (**A**), *Leucocoryne purpurea* (**B**), *Lathyrus aureus* (**C**), *Hibiscus trionum* (**D**), *Adonis aestivalis* (**E**), *Penstemon barrettiae* (**F**), *Grielum humifusum* (**G**), *Paeonia mascula* (**H**), *Mentzelia lindleyii* (**I**), *Oenothera stricta* (**J**), *Tulipa* 'Queen of the Night' (**K**), and *Ursinia speciosa* (**L**). These 12 species belong to distantly related genera of the major clades of the angiosperm phylogenetic tree (M). a: photograph of flower. b: SEM of epidermal surface of the attractive organ (petal, tepal or bract). c: TEM of transverse section of abaxial (C, F, K) or adaxial (A, B, D, E, G, H, I, J, L) epidermis. [figure by E. Moyroud from [37]]

similar directional scattering effect (creating a blue-UV enhanced colouration) could be demonstrated to arise from the striations of all these flowers (see chapter 9). *Trimenia moorei* (blue in (M)) is the only species from the first-branching angiosperm lineages in which striations were fond, but optical measurements were not performed, as no fresh material was available. The identified striation-displaying flowers are only very distantly related. Their phylogenetic distance is comparable to a wide spread over the animal class of arthropods, which contain spiders, crabs and insects. It is therefore assumed that the striations are a result of convergent evolution and have arisen during the coinciding period of the development of flower pollinating insects [39–41].

The following chapters discuss many of the currently unknown mechanisms and functionalities of floral striations, including differences in structural parameters, similarities of their optical effect, mechanisms of colour generation and biological significance.

Chapter 8

Analysis and fabrication of disordered photonic striations

8.1 Significance and contributions

The research of this thesis part was based on the assumption that the disorder in previously studied striations on the surface of flowers (reference [18]) may be significant. It is however a challenge to measure, simulate and manufacture (well-defined) disordered structures, compared to their ordered periodic counterparts. In this chapter I present the research tools that I developed to assess the role of disorder in floral striations. I programmed custom Matlab libraries to analyse the disorder present in flowers from large sets of transmission-electron-microscopy images prepared by collaborating plant-scientists from London, created a simplified model of the structure in discussion with my physics colleagues, and wrote simulations that provided an understanding of the various disorder parameters and geometrical constraints of the structure. I also advanced nano-structure manufacturing and replication methods in order to reliably reproduce the very fine structural differences that were created when introducing controlled disorder to nano- and microstructures. The methods and data of this chapter form a substantial part of a recently accepted manuscript at the journal Nature of which I am a shared first author (see List of relevant publications [37]).

Acknowledgement

This is a continuation of my MPhil project. The methods described in this chapter are therefore also an extension of those developed during my MPhil research. The extracted striation parameters, performed and analysed finite-difference time-domain simulations, and manufactured artificial grating masters are my own work. I also manufactured grating casts and conducted cross-sectional SEM on these samples. The optical goniometer

measurements included in this chapter were performed by Rox Middleton in the Vignolini group and analysed by me. Silvia Vignolini and Ullrich Steiner both contributed with valuable advice, materials, guidance and feedback. I would also like to thank the Steiner group members Bodo Wilts, for advice, and Pedro Cunha, for support during the early stages of the project and advice on high-precision e-beam lithography.

8.2 Physics of grating interference

This section provides a brief overview of photonic effects in gratings and thin films, as relevant to surface striations in flowers or simplified grating models thereof. The optical effect of diffraction gratings is based on the interference of light from its periodic elements, leading to the wavelength dependent enhancement of light at some angles, and the cancellation of electromagnetic radiation at others (figure 8.1).

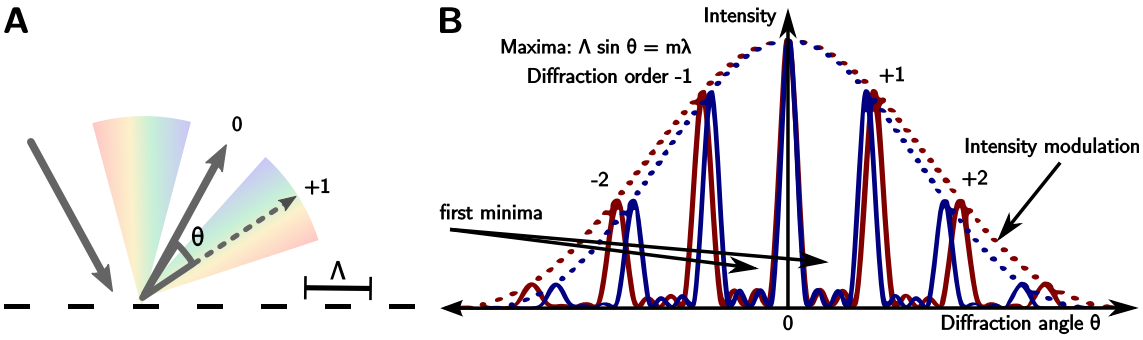

Figure 8.1: **Schematic explanation of grating diffraction.** (**A**) Light scattered by periodic gratings (with period Λ) interferes constructively. The effect is wavelength (λ) dependent, leading to iridescence in the far-field when illuminated with white light. (**B**) The angular position of diffraction maxima (m) is mathematically defined by $\Lambda \sin\theta = m\lambda$ at normal light incidence. The intensity between maxima decreases with an increasing number of grating elements and the peaks become sharper. The hull (dotted line) describes the height of intensity maxima and corresponds to the distribution obtained for an individual slit of the same width.

Two-dimensional slits or reflecting metal stripes on surfaces cannot easily be extrapolated to three dimensional gratings, as their cross-section parameters affects their diffraction orders [42]. Furthermore, the rectangular shape of gratings with constant height (made from transparent dielectric materials) can lead to thin film interference (like colours on soap bubbles). This is caused by the small size of scattering elements (here ca. 100 nm - 2 µm) and intermediate air spaces, which effectively act as a layer of intermediate refractive index ($n_{1/2}$) (figure 8.2).

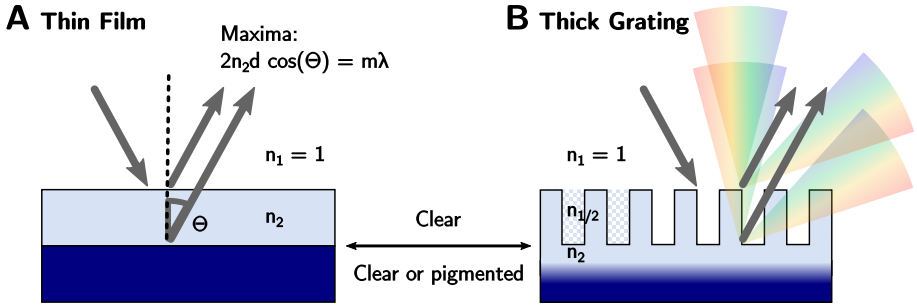

Figure 8.2: **Schematic explanation of thin film interference.** (**A**) Light of wavelength (λ) reflected from transparent thin films (with refractive index n_2) interferes constructively at certain angles (Θ): $2n_2 d\cos(\Theta) = m\lambda$. This causes an illumination dependent colouration of the transparent film. (**B**) This effect can also appear in rectangular gratings that form a layer of effective intermediate refractive index ($n_{1/2}$), introducing colouration fringes into grating diffraction orders.

8.3 Floral surface striations and their analysis

Floral striations are one-dimensional grating-like photonic structures on the surface of insect attracting plant organs (petals in most cases). They are quasi-ordered lines propagating along the long-side of the petal, i.e. radiating outwards from the centre. For example in the light-yellow pigmented *Grielum humifusum* flower (figure 8.3 A), surface striation can be observed by optical and electron microscopy (figure 8.3 B-D).

The photonic effect of these petals is an interplay of a number of key structural parameters describing the striation and its variation (disorder). For floral striations,the size (height and width) and spacing of their cross-sections was considered (figure 8.4). These parameters also enabled a comparison to grating-like structures. To obtain these parameters for 11 species identified in distant branches of flowering plants (angiosperms) (described in chapter 7 and figure 7.1), a large number of transmission electron microscopy (TEM) images of petal cross-sections (such as in figure 8.3 D) was prepared

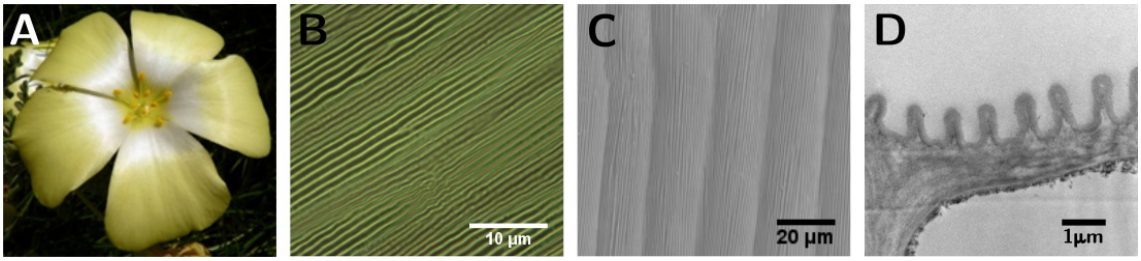

Figure 8.3: **Floral surface striations.** Surface striations on a *Grielum humifusum* flower petals. (**A**) Photograph; (**B**) optical microscopy image; (**C**) top-view SEM image of a petal cast in epoxy; (**D**) cross-sectional TEM image.

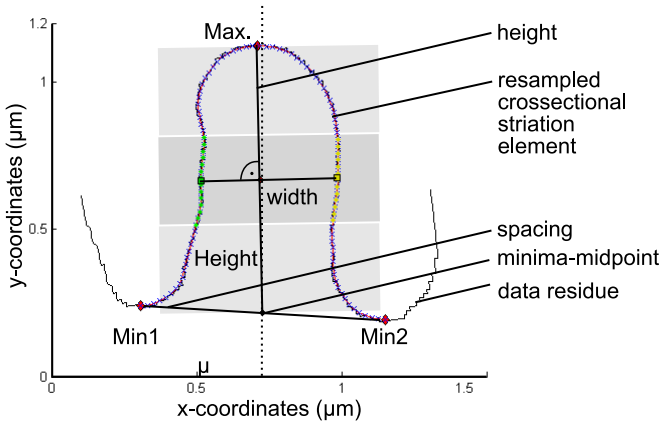

Figure 8.4: **Striation size parameters.** Schematic of one striation extracted from a TEM image, illustrating how height, width and spacing were determined.

by Paula Rudall and Hannah Banks from Kew Gardens London with the methodology described in reference [43].

The average and standard deviation of the striation parameters height, width, and spacing were extracted for each flower species from multiple cross-sectional TEM images. This was achieved by detecting the outer striation edges in Matlab from the variable image material. Then, non-striation edges were removed manually. Next, the undulation caused by the shape of underlying cells was removed using a low-order polynomial fit. Pixels of consecutive striation edges were sorted, scaled (according to the scale bar of the TEM image) and noise filtered, before local extrema were detected with the Matlab peakdet function. Before determining the striation height (distance between maximum

Species	Height μm	σ_H μm	Width μm	σ_W μm	Spacing μm	σ_D μm	Number of striations analysed
Adonis aestivalis	0.59	0.15	0.52	0.09	1.4	0.39	72
Grielum humifusum	1	0.20	0.53	0.09	0.97	0.16	111
Hibiscus trionum	0.73	0.27	0.73	0.16	1.3	0.29	74
Leucocoryne purpurea	0.74	0.29	0.96	0.31	2.1	0.86	141
Lathyrus aureus	0.67	0.20	0.44	0.09	0.98	0.25	118
Mentzelia lindleyii	0.53	0.17	0.45	0.11	0.92	0.24	323
Oenothera stricta	0.72	0.23	0.62	0.16	1.1	0.3	195
Paeonia mascula	1.1	0.34	0.64	0.12	1.2	0.34	270
Penstemon barretitiae	0.48	0.20	0.66	0.15	1.4	0.42	343
Tulipa 'Queen of the Night'	0.55	0.18	0.61	0.12	1.2	0.3	150
Ursinia speciosa	0.75	0.22	0.88	0.19	1.6	0.4	319

Figure 8.5: **Disorder in cuticular striations for different flowers.** The table lists the average value and standard deviation in μm of the dimensions (height and width) and the distances between striation minima (spacing), for the striations of different species as obtained from the TEM images. The last column lists the number of unique striation cross-sections analysed for each species.

and minima), spacing (distance between minima) and width (by averaging the position of the striation mid-points), each striation element was resampled with the algorithm interparc (by John D'Errico 2012, MathWorks File Exchange). The obtained parameter averages and standard deviations for each flower species are summarised in figure 8.5.

8.4 Simulating disordered photonic striations

Optical measurements on fresh flower petals are key to describe the photonic effect of striations in the context of other optical characteristics of flowers such as petal shape and pigmentation. Such measurements are presented in the next chapter. This chapter links the observed optical signatures to the disordered morphology of the stripes. Currently there is no known photonic effect that could explain the behaviour of disordered striations. Simulations of a simplified striation system were used to identify the source of the colouration and its characteristics.

Simulating disordered photonic structures is a difficult undertaking with few standard tools available. Most notably, photonic simulations are usually based on periodic boundary conditions, which simplify the system significantly and allow the computation of the problem. These boundaries cannot be applied to disordered systems. A suitable simulation scenario was developed in the numerical finite-difference time-domain (FDTD) simulation software Lumerical, as described in this section. The FDTD method uses the leapfrog approach to integrate time dependent differential equations (here the Maxwell equations) [44].

8.4.1 Approach

For the purpose of the simulations, the cross-sectional plane of floral striations (the only plane in which the scattering effect appears) was approximated by a rectangular disordered grating. Within the Lumerical software, a dielectric grating with a refractive index of 1.5 was created as a material estimation of epoxy, which was later utilised to manufacture artificial samples (note: transparent dielectrics can be approximated by a constant refractive index in the visible range, but most biological materials display dispersion [45] which further depends on embedded pigmentation [46]). Since periodic boundary conditions could not be used, the usual procedure to simulate only one grating element was extended to 100 elements with non-periodic boundary conditions and a light source with the Gaussian intensity profile tending towards zero intensity at the edges of the simulated area. The size of the area for grating elements was chosen to roughly match the optical resolution obtained from good goniometer measurements as well as an estimation of the relatively short coherence length of sunlight, for which only the local

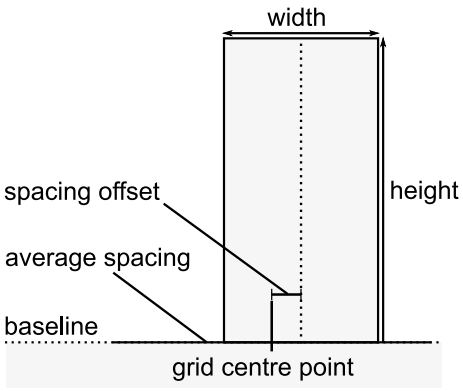

Figure 8.6: **Geometric representation of striation size parameters.** Schematic of the translation of extracted striation parameters from figure 8.4 into the rectangular model system used for experimental and theoretical purposes.

order in the structure leads to constructive interference. A virtual monitor captured the reflected near-field and calculated the far-field response of the structure. Disorder was introduced to grating elements systematically by computing randomised offset values following a Gaussian distribution based on the standard deviation from pre-determined floral values, and truncated at twice the standard deviation. The spacing disorder was modelled by offsets around a fixed lattice (figure 8.6). In order to ensure comparability, the disorder parameters were seeded, so that they vary between different simulation iterations, but not between simulation-sets with different statistical parameters.

100 grating elements (some of which at the edge are poorly illuminated) of around 1 µm each correspond to an illuminated area of only ca. 0.1 mm. This represents a sensible physical range (as discussed above) and the small area enabled a relatively fast computation together with the simplicity of the structure. However, only little disorder can be represented by such few elements. Each individual simulation result leads to a pixelated appearance determined mainly by chance, as demonstrated by the panels in figure 8.7. An average of 60 implementations (as used for simulations in this study) leads to an illuminated length equivalent to about 6 mm, yielding more realistic values and a more representative scattering distribution. The alternative strategy of simulating a larger area with e.g. 6000 grating elements in one simulation would lead to a poor comparison with experiments, because the light source in the simulations is perfectly coherent and would lead to interference between similar striation elements that are far apart, which is not present under less coherent sunlight illumination.

The examples in figure 8.7 demonstrate that the reduction in intensity of the first order interference (characteristic for perfectly ordered gratings) can already be observed also for a small number of simulation cells, but becomes representative only when averaged over larger sample numbers. Similarly, the appearance of a coloured directional scattering effect (characteristic for quasi-ordered surface striations) becomes representa-

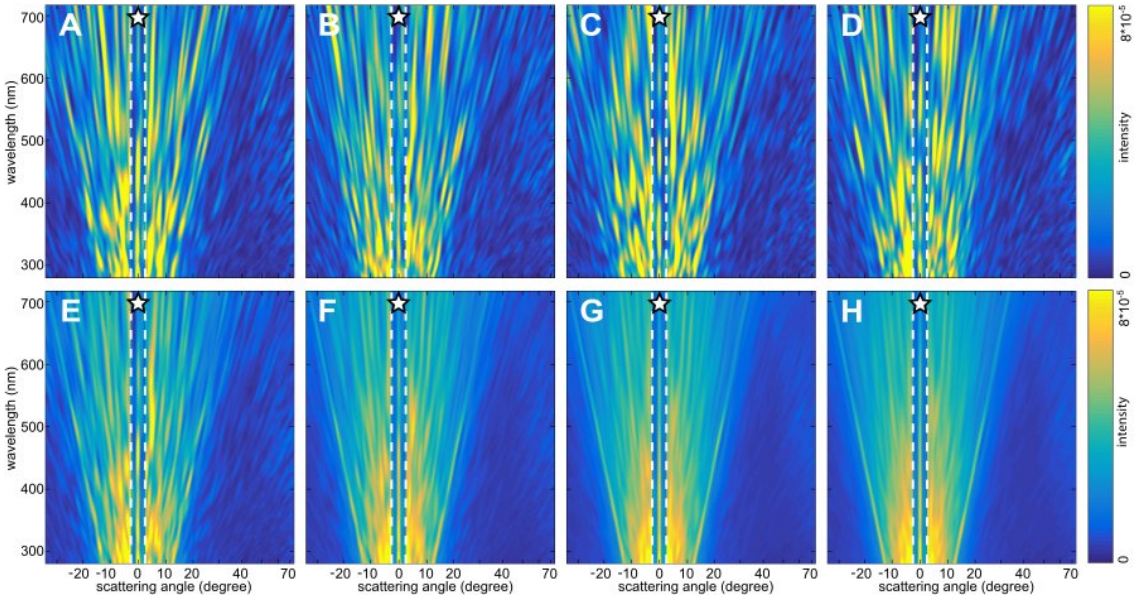

Figure 8.7: **FDTD spectral averaging for disorder analysis.** FDTD simulation results of rectangular gratings with dimensions equivalent to experimentally determined *Hibiscus trionum* parameters: 730 nm height, 730 nm width, 1300 nm spacing; standard derivations: 0.27 in height, 0.16 in width and 0.29 in spacing. (**A** to **D**) are scattering plots of individual FDTD simulation results and (**E**) is an average of (A to D). (**F**), (**G**) and (**H**) are averages over larger sample numbers: 20x, 40x and 60x respectively.

tive only at sufficient simulations numbers. This dependence on averages also confirms that in order to capture the colour dependent scattering in a real flower petal covered by disordered striations it is necessary to average a number of measurements taken in the same scattering geometry or to illuminate a large area (several square millimetres). In fact, depending on the size of the illuminated area, the measurement of a semi-disordered surface may have a similar appearance to the averages shown here, or appear randomly pixelated as reported in reference [47]. A suitable minimum illumination area is larger on strictly parallel artificial grating samples compared to flower petals, because floral stri-

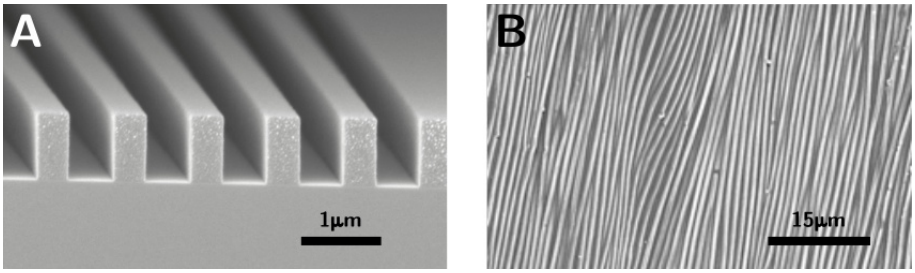

Figure 8.8: **Variation of size parameters along striations.** SEM images of surface gratings: (**A**) cross-section of artificial PMMA grating on silicon wafer without variation along lines. (**B**) Top view on floral striations of *Mentzelia lindleyii* with varying striation cross-sections in the direction of their propagation.

ations vary slightly in their direction of propagation (figure 8.8 A vs. B) which provides more parameter variation for the same 2D area.

8.4.2 Modelling the angle-dependent scattering of floral striations

As described in the previous section, surface striations were abstracted to disordered rectangular gratings to study the parameter space of the photonic structure. This model system was studied with FDTD simulations as shown in figure 8.9 for the parameters determined from *Hibiscus trionum* flowers. It clearly shows the change from grating diffraction orders in (A) to a distinct scattering pattern enhanced for shorter wavelengths in (B) which remains similarly strong even at much higher disorder values than present in the flowers, even when the diffraction orders have completely disappeared (C). This new scattering effect can be described as a scattering confined to the angular range of about $\pm 25^\circ$ that increases in intensity for shorter wavelengths (blue-UV colour) – from here on it will be referred to as '**blue halo**'.

Very similar scattering distributions were obtained for the parameters derived from disordered striations of all 11 analysed flowers, see figure 8.10. All of them display enhanced scattering of wavelengths corresponding to blue and UV light within the halo scattering cone and almost disappeared diffraction orders. The main difference between the results for the different flower parameters is determined by the average spacing of neighbouring striations, which broadens the angular range between diffraction orders

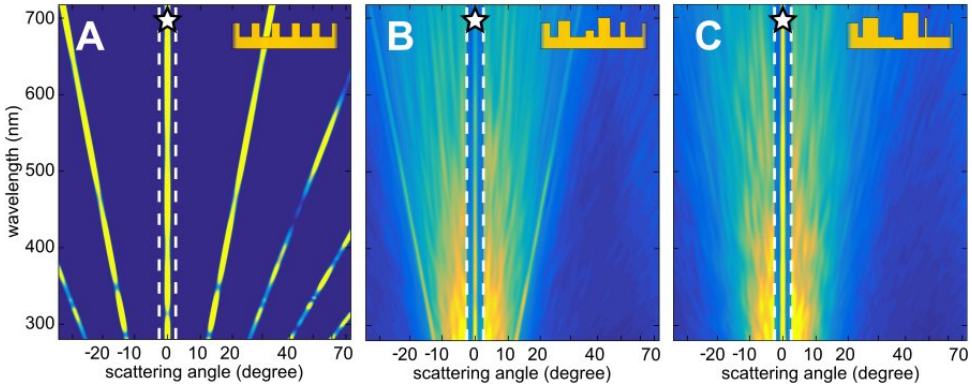

Figure 8.9: **Disorder in simulated striations.** FDTD simulation results for rectangular gratings: (**A**) ordered grating with the average parameters found in *Hibiscus trionum* flowers (730 nm height, 730 nm width, 1300 nm period length); (**B**) as (A), but including disorder in the parameters according to *Hibiscus trionum* TEM analysis (standard derivations: 0.27 in height, 0.16 in width, 0.29 in periodicity); (**C**) as (B) with twice the disorder found in *Hibiscus trionum*. The bands denoted by stars in (A to C) containing the 0-order reflections were reduced in intensity by a factor of three.

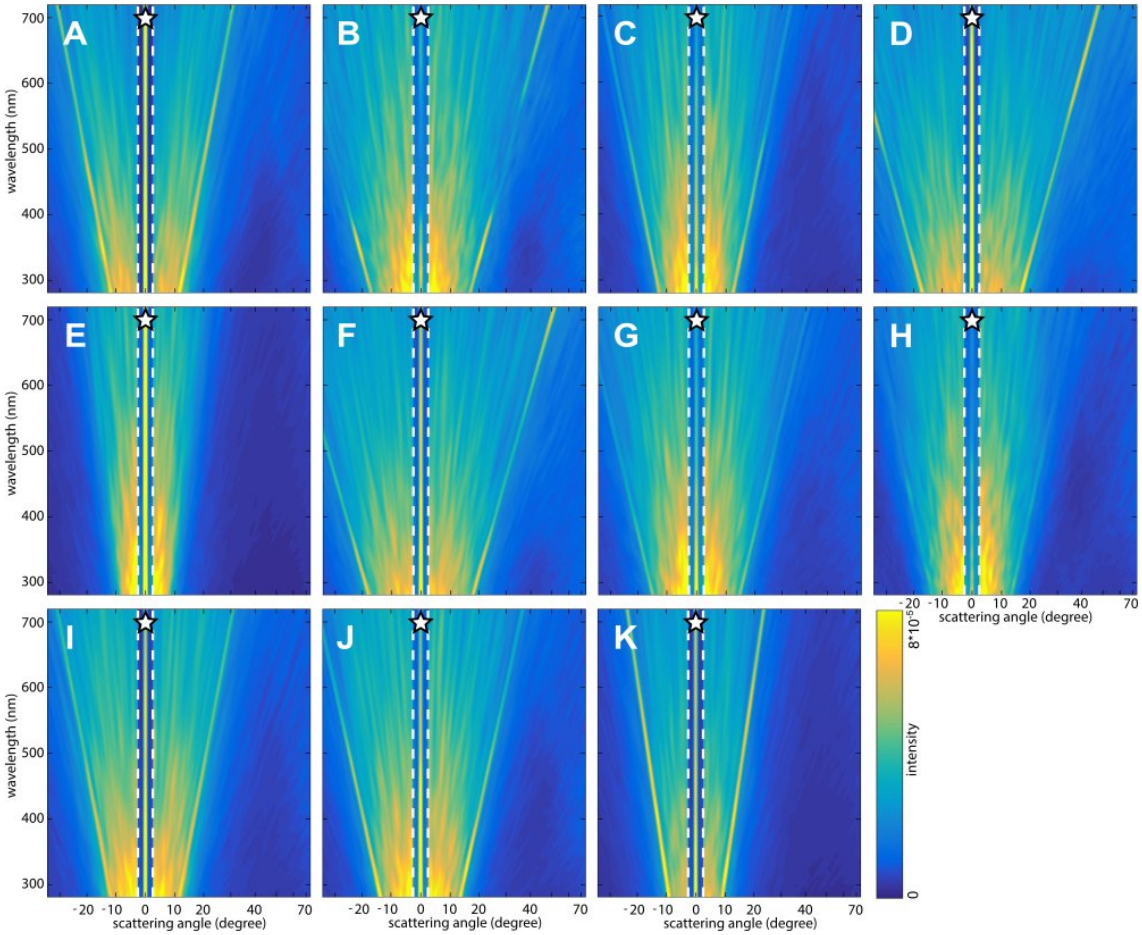

Figure 8.10: **Simulated effect of disorder in striations for different flowers.** FDTD simulation of the scattering response of rectangular gratings with parameters and disorder according to the measured flower parameters of (**A**) *Adonis aestivalis* (**B** *Grielum humifusum*, (**C**) *Hibiscus trionum*, (**D**) *Lathyrus aureus*, (**E**) *Leucocoryne purpurea*, (**F**) *Mentzelia lindleyii*, (**G**) *Oenothera stricta*, (**H**) *Paeonia mascula*, (**I**) *Penstemon barrettiae*, (**J**) Tulipa 'Queen of the Night', (**K**) *Ursinia speciosa*. The bands denoted by stars containing the 0-order reflections were reduced in intensity by a factor of three.

and also the spread of the halo. In this model system, some flowers retain more residual iridescence than others. Overall, this agrees well with our observations when handling the flowers in terms of the occasional presence of weak diffraction orders and UV-blue scattering enhancement that is confined to small reflection angles. This simulation overview provides an impression of how the relatively parameter independent halo effect of quasi-ordered surface striations leads to a similar flower appearance even though the parameters of different species vary.

When studying the simulation results of the disordered rectangular grating model system with the parameters determined from natural flower samples (or the TEM images thereof), certain common characteristic scattering trends can be observed (the blue halo). In the optical data obtained from fresh flower petals, these trends are also visible

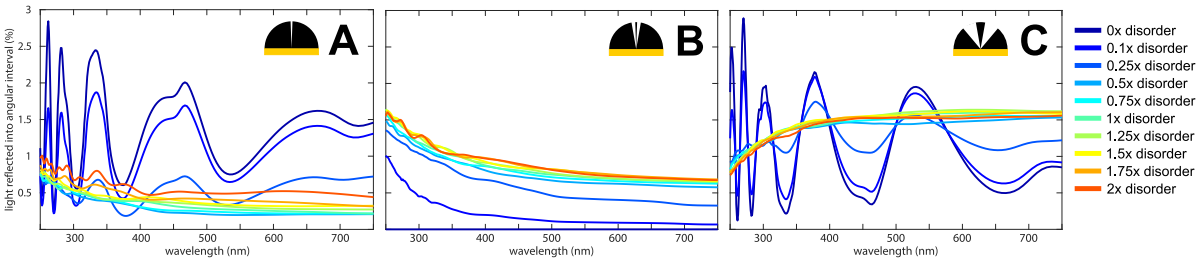

Figure 8.11: **Simulated angular spectra of disordered striations.** Spectra from FDTD simulations of rectangular gratings with disorder parameters derived from *Hibiscus trionum*. (**A**) Specular reflection integrated over the $-2\,^\circ$ to $+2\,^\circ$ angular range with respect to the (normal) angle of incidence. (**B**) Spectral scattering of the grating obtained by integrating over the $-10\,^\circ$ to $+10\,^\circ$ angular range, excluding the region of specular reflection. (**C**) Scattering into the $-40\,^\circ$ to $+40\,^\circ$ angular range excluding the angular regions of (A) and (B). The colour code in A-C indicates how the spectra change with increasing disorder ranging from 0 (no disorder) over 1x disorder (corresponding to *Hibiscus trionum* parameters) to 2 (twice the standard deviation of natural disorder).

(chapter 9 section 9.4.1) but less well defined because of its overlap with other floral properties such as pigmentation and petal curvature. The simplified model allows the study of the photonic effect independently of other optical properties of flower petals while demonstrating good qualitative agreement with the natural system (compare simulations to figure 9.11 D & F)

Figure 8.11 shows the spectral behaviour of three different angular intervals when increasing disorder from zero (perfectly periodic grating) to 1x disorder (corresponding to *Hibiscus trionum* parameters: 730 nm height, 730 nm width, 1300 nm spacing and standard derivations: 0.27 in height, 0.16 in width, 0.29 in spacing) to twice the disorder observed in *Hibiscus trionum* striations. 1x disorder corresponds to the data shown in figure 8.7 H. The reduction in specular reflection can be observed in (A), along with the reduction in thin film interference caused by the grating quasi layer of intermediate refractive index (figure 8.2). (B) shows the fast rise of the blue halo with increasing disorder and the stability of the effect for a wide range of disorder values. This region (B) was chosen to be smaller than the experimentally determined full extent of the halo (ca. -25 °to $+25\,^\circ$), in order not to overlap with the first diffraction orders at low disorder. (C) Contains the short wavelength parts of the first diffraction orders and the angles next to the high-intensity region of the blue halo. In (C), the quick decay of the first order diffraction components can be observed, along with the increased long wavelength scattering response in this angular region. Note that the light reflected into this region is spread out over an angular range more than four times as large as the interval in (B), reducing the scattered light intensity per viewing angle.

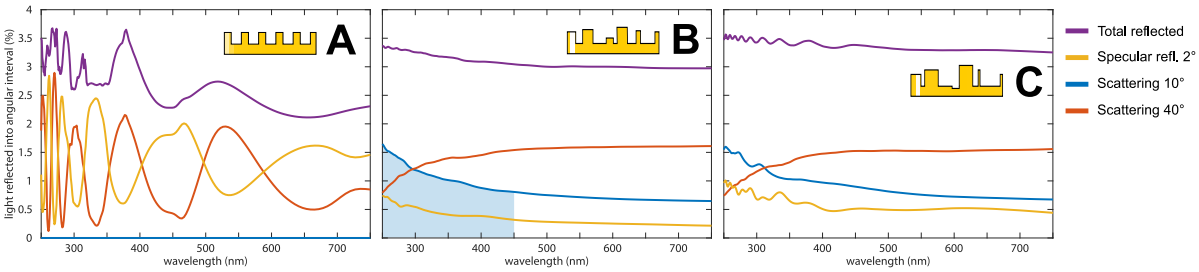

Figure 8.12: **Effect of simulated disorder levels on striation appearance.** Spectra from FDTD simulations of rectangular gratings corresponding to the *Hibiscus trionum* size and disorder parameters. The spectral response is shown for the same three angular intervals as in figure 8.11 along with the total amount of reflected light. The sub-plots correspond to one implementation of disorder each: (**A**), no disorder, (**B**), *Hibiscus trionum* disorder, (**C**,) twice the floral disorder.

Figure 8.12 shows the relative amount of light reflected into each of the angular intervals from figure 8.11 for 3 specific disorder implementations (0x, 1x and 2x). As in the previous figure, note that the interval corresponding to the orange curve is more than four times larger then that corresponding to the blue line. Without disorder no light is reflected into the 10° interval (A), but once the blue halo (shaded blue area) is established (B), it is robust with respect to the amount of disorder present in the striations (C). Figure 8.12 also shows the spectra of the total reflected light, integrated over all angles (purple). This total reflected light exhibits a small colouration effect towards short wavelengths at the disorder amount corresponding to natural parameters (B). However, this small predicted overall colouration is not as strong as the concentration of short-wavelength light at small reflection angles (and its relative absence at large angles). I conclude therefore that the blue halo effect is mainly based on concentration of the reflected light in an angular cone for these wavelengths, rather than an overall scattering efficiency enhancement.

8.5 Manufacture of disordered grating structures

In the previous sections of this chapter, the optical effect of floral surface striations was attributed to the disorder in these photonic structures by FDTD simulations of a simplified model system. Simulations are, however, only predictions of real systems. To verify these predictions, artificial micro-structured samples of the disordered rectangular grating model were designed, manufactured, and optically analysed. The simulations were used to guide the design [48] of an artificial disordered structure displaying the blue halo effect without overlapping diffraction orders. Different test squares were manufactured with e-beam lithography in thin films, moulded in flexible polymer and then cast in optically

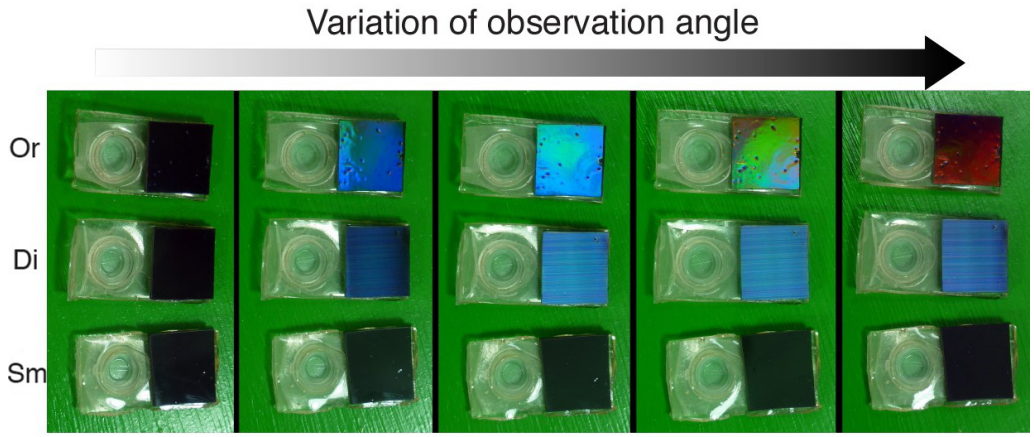

Figure 8.13: **Appearance of artificial flowers.** Angle-dependent appearance of black-pigmented artificial flowers with a smooth surface (Sm), disordered (Di) or regularly ordered (Or) rectangular striations. These samples were key to perform visual bee experiments. [Figure credit: Edwige Moyroud]

and UV transparent epoxy with the addition of pigment. Representative examples of the resulting 2 x 2 cm test-squares are shown in figure 8.13. As expected, the ordered grating (Or) displayed a clear change within a wide range of colours with changing observation angle. The disordered grating (Di) showed the halo. It appears blue to the human eye that cannot perceive UV light, with little colour variation for small observation angles. Test-squares without surface structuration (Sm) did not change their colour from the black of the background pigment at any angle. Optical measurements revealed a very good match with simulation predictions (figure 8.15).

As with the optical analysis and simulations, the disordered nature of samples poses a challenge in micro- and nano-manufacturing. As ordered grating, the floral striations parameters (e.g. 700 nm width and 1300 nm spacing) are still processable by photolithography techniques. Once disorder is introduced and sub-100 nm features emerge, e-beam lithography is needed. It requires long runtimes to create 2 x 2 cm test-squares wit ca. 30 nm resolution, which was necessary for behavioural bee experiments.

8.5.1 Approach

Standard lithographic processes can be used to design and manufacture custom rectangular surface structures. Nano- and micro-manufacturing processes for thick structures (such as striation-like disordered rectangular gratings in contrast to only one layer of molecules [49]) are based on the chemical processing of atomic bonds in thin polymer films on a solid substrate (here silicon wafers) [50, 51]. Here, PMMA-polymer films were structured with the highest available resolution tool, an e-beam lithography system [51]. E-beam lithography is a high energy scanning electron microscope (SEM)

where the electron beam is used to break the chemical bonds of the polymer (positive resist) instead of imaging the sample. Alternatively, negative resists (such as SU8) can be used in lithography methods, where chemical bonds are formed (not broken) as a consequence of exposure to radiation. After processing in a chemical bath to wash away polymer areas with broken PMMA bonds, this master structure was moulded in a flexible rubber-like polymer, from which several hard epoxy samples could be made. This process is summarised in scheme A of figure 8.14.

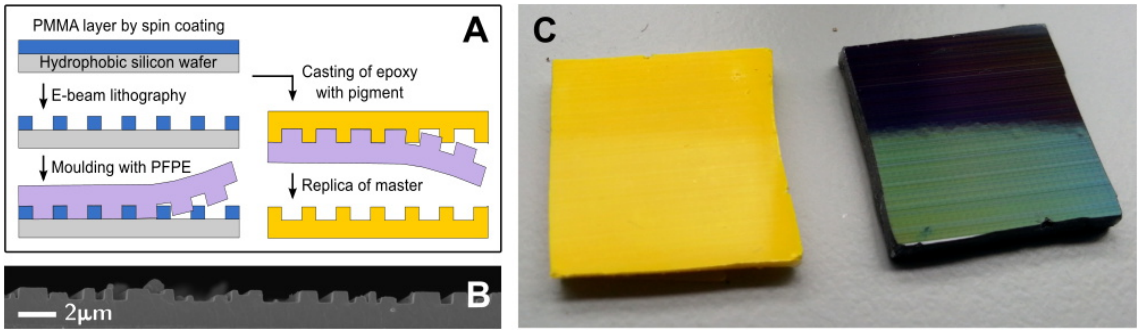

Figure 8.14: **Manufacturing artificial striations with disorder.** (**A**) schematic of grating manufacturing method; (**B**) SEM image showing the cross-section of an artificial disordered epoxy grating with two height levels; (**C**) Photograph of final epoxy cast samples with blended-in yellow and black background pigmentation (below a thin top-coat of clear epoxy).

The polymer film was first be deposited on a clean silicon wafer. To avoid fine features of PMMA to detach from the wafer, it was pre-coated with a UNISOL adhesion layer. The PMMA film was then spin coated from solution. This process was optimised to yield a film thickness of the maximum required lithographic structure, as no material can be added later on in the process. Structures as thick as *Hibiscus* striations (ca. 730 nm) are a challenge for this technique, which is commonly used for much thinner structures. Multilayer coatings are an option, but each additional step can introduce undesirable imperfections and impurities, especially in a manual small-batch research facility. Here, a successful protocol was developed spin-coating high molecular weight PMMA 950 A9 solution with 15 % (volume) of additional anisole solvent content to decrease its viscosity. The solution was spin-coated in a multi-step automatic protocol with an acceleration of 2000 RPM/s (RPM = rounds per minute): (1) 500 RPM for 5 s to spread the solution everywhere on the 8 cm^2 wafer piece; (2) 2000 RPM for 4 s to achieve an even distribution of the solution and (3) 3000 RPM for 45 s to establish the final film thickness. The spun PMMA films were annealed on a hotplate at 100 °C for 15 minutes.

The patterns were created with an e-beam lithography system at 50 kV at beam currents between 2 - 5 nA with a resolution of 30 nm. Higher resolutions can be achieved with this system, but there is a trade-off between write-speed, accuracy and the high

currents needed to write the large structures required by biological experiments. The spacing and width of grating elements were varied around a periodic lattice, similar to the FDTD simulations, with twice the standard deviation found in *Hibiscus trionum*. A precision development protocol [52] was used to dissolve the exposed polymer parts (a mixture of 7-parts isopropyl alcohol and 3-parts of deionised water).

The PMMA on silicon master structure was moulded into a perflouropolymer (PFPE) [53, 54] in a nitrogen flow-through chamber with UV curing at 365 nm. The resulting very high resolution mould was required to achieve sufficient accuracy for disordered striations (better than commonly used PDMS moulds [55, 56]). Epoxy casts were created from the moulds using EPO-TEK optical epoxy (301-1LB kit) with the addition of pigments (black (carbon black) or a yellow (naples yellow light (PY41) pigments, 62.5mg per ml of epoxy). Perfectly ordered gratings were produced in the same way as the controlled disordered striations. Similarly, omitting the e-beam pattering step yielded flat reference samples.

The final epoxy-gratings (figure 8.14 B,C) were analysed by the optical goniometer measurements described in section 9.2, see figure 8.15. The ordered grating (A) shows clear and sharp diffraction orders (iridescence), while the measurement on a disordered sample in figure 8.15 B reveals a blue halo very similar to that predicted in simulations (compare to figure 8.7 H).

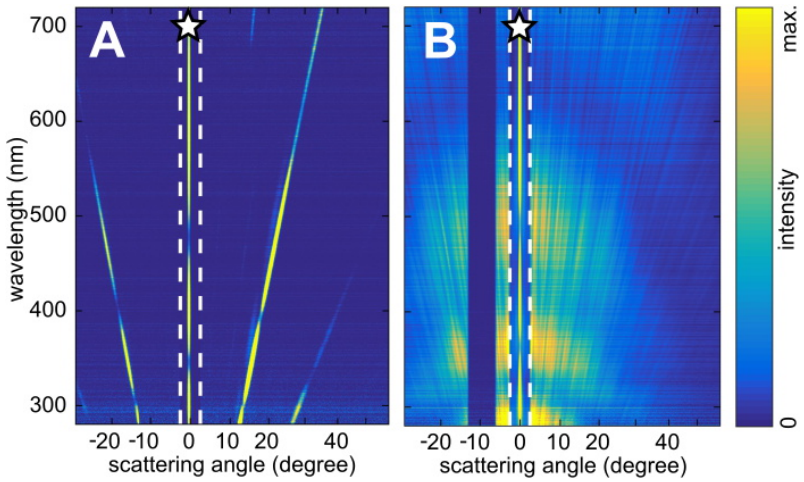

Figure 8.15: **Optics of artificial striations with disorder.** Results of optical goniometer measurements of artificial gratings based on *Hibiscus trionum* parameters. (**A**) Ordered grating and (**B**) with twice the natural *Hibiscus* disorder in width and periodicity and two height levels produced with method from figure 8.14 and addition of black pigment to the epoxy. The bands denoted by stars in (A, B) containing the 0-order reflections were reduced in intensity by a factor of three compared to the other regions in the graph.

8.5.2 Height limitations of thin-film processing

It is challenging to introduce height variations into lithographically produced structures. A variation in height of grating elements was however found in all analysed flower-petal striations and contributes to a homogeneous halo effect in these samples.

In the case of artificial rectangular gratings, thin film interference can alter the visual appearance of samples, as described in section 8.2. This becomes apparent in the simulation result in figure 8.16 A, where only spacing and width of striations were varied at a constant film-height. The quasi layer containing both air and grating teeth has an effective intermediate refractive index and results in thin film interference fringes, enhancing some and cancelling out other wavelength intervals. This effect cannot be observed on flowers because there is no well defined planar interface of strongly differing refractive indices and striations are always height disordered.

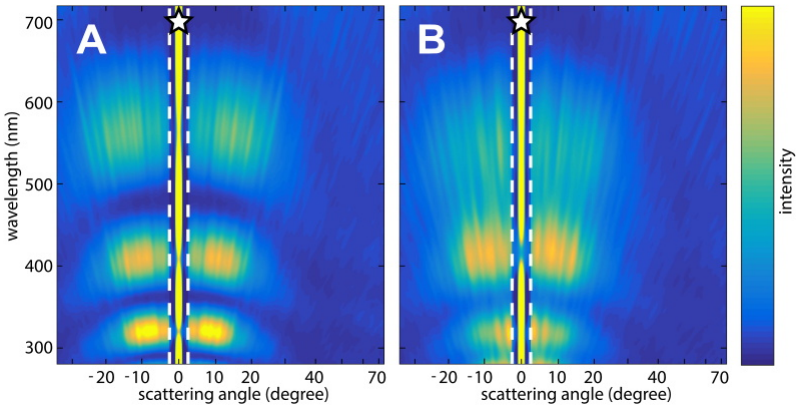

Figure 8.16: **Role of height variability in disordered gratings.** FDTD simulation results of rectangular gratings corresponding to the *Hibiscus trionum* parameters. (**A**) Without variation in height. (**B**) One intermediate height level introduced at random in 40 % of positions of the grating.

E-beam lithography on does not allow the continuous variation of height levels. But, by fine-tuning the e-beam experimental parameters, the height constraint was at least partially relaxed, allowing the introduction of one intermediate level (figure 8.14 B). The height variation was enabled by dosage variation of the e-beam lithography process. As expected from simulations (figure 8.16 B), this laterally averages thin film interference, thereby reducing the radial fringes in the spectra (figure 8.15 B).

The single intermediate height level introduced by e-beam dosage variation leads in practice to a range of similar intermediate levels because of proximity effects during exposure and development. In other words, the thickness of each strip is affected by the shape of the neighbouring stripes. This gives rise to a small lateral variation of the stripe heights, as colourfully visible on the grating master under an optical microscope (figure 8.17). The colours of different stripes arise from individual thin film interferences

because a thickness variation in this range causes a sensitive thin-film colour change of the transparent master PMMA film on a highly reflective silicon wafer. These stripes can not be observed in the final (solid) epoxy casts, but the small variations of the intermediate height levels cause a thickness fluctuation of the (different) effective grating/air thin-film. This, in turn, contributes to spectral averaging in the optical far-field, reducing the radial fringes in artificial gratings (figure 8.15 B).

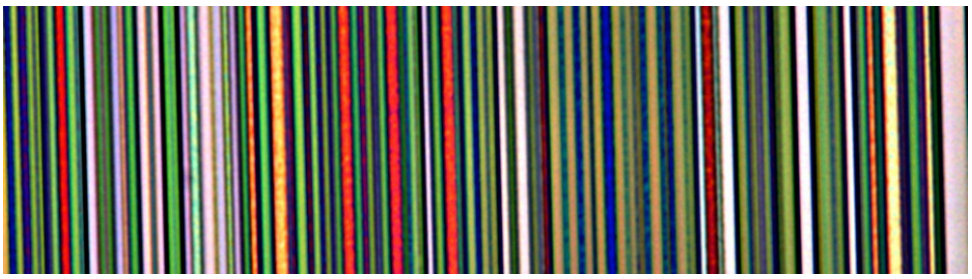

Figure 8.17: **Height disorder in thin-film structuration.** Optical microscopy image of a disordered grating master (PMMA on silicon wafer). Thin film interference gives rise to a highly thickness dependent colour to stripes. Green corresponds to the full height of the PMMA film and white to the uncovered wafer, while the other colours correspond to the level written with medium-dosage e-beam lithography, effected by proximity effects (see slight variation in cross-sectional SEM image in figure 8.14 B for comparison).

8.5.3 Material stability at the nano-scale

An unexpected problem had to be solved, when the usage of the samples in bee experiments revealed that ethanol affected the nano-structured surfaces. Epoxy is known to be a solvent stable resin, and it is not expected to react to a rinsing procedure with a mild organic solvent such as ethanol. Ethanol is routinely used in bee-experiments in order to remove the scent left behind on samples by bees as a signal to future pollinators [18]. It was found however that the optical effect of ordered and disordered gratings significantly diminished over time and an atomic force microscopy investigation revealed that grating elements swelled and deformed even after brief contact with ethanol, see figure 8.18. Neighbouring high-aspect ratio elements collapsed onto each other and swelling caused these double-lines to undulate, significantly distorting the intended local topology of the structure.

This is a classic example of the way in which properties of nano materials can change compared to bulk properties [57]. As a consequence of this finding, the design of artificial flowers for the experiments was changed in a way that bees do not land on the attracting surface itself so that it does not need to be cleaned with solvent (e.g. figure 8.13 and designs in chapter 9).

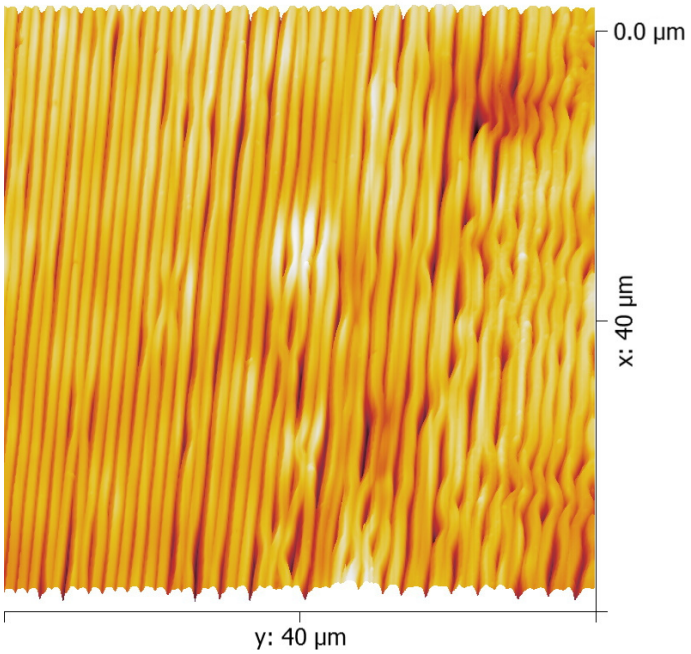

Figure 8.18: **Solvent swelling of epoxy nanostructures.** Atomic force microscopy image of an ordered grating cast in epoxy after washing with ethanol.

8.5.4 Role of polarisation

Note that surface structuration of dielectric materials such as epoxy induces polarisation effects changes [58, 59]. On ordered gratings as well as disordered gratings, the continuous surface is interrupted by stripes on the length scale of visible light only in one direction, leading to a slightly increased scattering when the polarisation is in plane

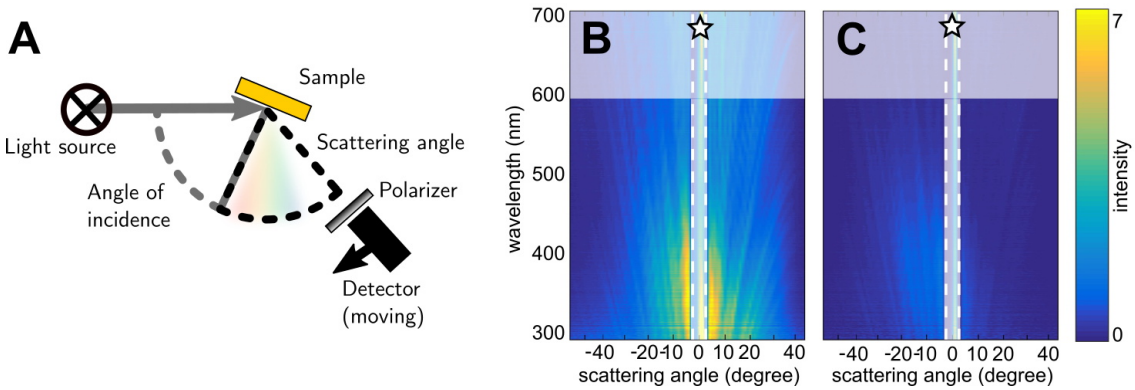

Figure 8.19: **Polarisation effect of artificial striations.** (**A**) Scheme of the experimental setup used to measure polarisation; unpolarised light from the source is used to illuminate the samples. The scattered signal in the plane perpendicular to the direction of the striation is collected in the two polarisation channels. (**B**,**C**) Scattering measurements form the black artificial flower cast with disordered striations and polariser-axis (B) parallel and (C) perpendicular to the direction of the striation.

with striations (see optical measurements in figure 8.19). Bees and other pollinators are able to see linear polarisation [60, 61], but it is still unclear whether the polarisation effect persists for non-rectangular striations on real petals, and whether it enhances the visibility of the blue halo arising from the surface patterns in real flowers. This should be investigated in a future study.

8.6 Discussion

For the purposes of simulations and manufacturing, floral surface striations were modelled by rectangular gratings with disorder in height, width and spacing. This specific model system has not been analysed in the literature, but disorder in sub-wavelength 3-dimensional triangular gratings has been theoretically explored as a strategy for anti-reflection coatings on LEDs [62, 63], in practice, however, these seem very challenging to manufacture due to their small feature size. The most closely related work to this chapter is a theoretical study analysing the effect of height disorder in rectangular gratings [64]. A blue halo-like effect around the zero-order diffraction peak was reported with similarities to the results obtained here (e.g. figure 8.10). The same study observes that the halo-like effect does not resemble a simple superposition of diffraction orders from a range of ordered structures. More recently, Johansen et al. [48] have reported an experimental approach to create gratings with height-offset-areas through a combination of lithography and dry-etching. Johansen et al. confirm that coloured scattering effects can be obtained with disordered gratings.

The simulations and manufacturing process did not take the possible undulation of the flower substrate into account, which is typically caused by underlying cells of the flower petals. The simplified simulations are however in line with the feasible manufacturing feasible lithographic protocols described above. Qualitatively, smooth undulations simply focus and defocus (blur on average) the scattering effect, compared to planar ordered gratings [65]. Recently, it has been shown that disordered striations can be designed using shape memory polymer layers [66, 67]. While this method provides less control over the specific shape and disorder, it provides access to a larger parameter space, particularly for height disorder and long-scale undulations, which cannot be created with conventional thin-film lithography techniques (as described in section 8.5.2). Their initial findings confirm the hypothesis that undulations do not strongly effect the overall appearance of disordered surface striations.

The structure replication process with PFPE moulds [53, 54] preserved detailed features best and caused least damage to the master sample (e-beam patterned PMMA film on silicon). While high-resolutions can also be achieved with polydimethylsiloxane (PDMS) composites [56], they tended to damage grating-lines upon detachment from

the master sample, which is mainly attributed to PDMS swelling [50]. The PFPE protocol can also be executed faster, because it involves a fast UV-light curing step instead of slow temperature enabled cross-linking and the manufacture of several layers. It should be noted that both methods are unsuitable to mould fresh flower samples, because of the used solvents and curing steps. Instead, flower structures were moulded (e.g. for imaging purposes in figure 8.3 C) with dental-supply silicone as previously reported [22, 68].

Combined, the theoretical and experimental techniques presented in this chapter can be applied to study biomimetic disordered structural colours on surface striations in the animal kingdom[27–31] or similar structural colours. Other biological organisms will have evolved their structural colour for different purposes. Therefore, applying the described techniques to these systems is likely to yield different insights into the striation parameter space and its biological significance.

Chapter 9

Disorder in floral photonic structures is functionally significant

9.1 Significance and contributions

This chapter discusses the biological functionality of floral surface striations in pollinator interactions. In the collaborative project, we found proof that the disorder in photonic structures (namely surface striations) enables distantly related flowers to produce an enhanced visual signal. We identified the optical effect and showed that it (and thus the presence of disorder in biological photonic structures) can be functionally beneficial. Structures created by nature are not perfectly ordered but rather contain at least small amounts of disorder. This is usually seen as a limitation of natural systems. We found, however, that this slight disorder in the widespread structure on the surface of flowers leads to a an advantage by changing the visual properties of its surface from transparent/ iridescent to a robust blue-UV (figure 9.1), particularly visible to insects. This effect and its functionality have never been reported before.

Acknowledgement

The research presented in this chapter is the result not only of my own work, but of a highly collaborative project. In particular, all bee vision experiments have been conducted by collaborators from the Department of Plant Science (especially Beverley Glover and Edwige Moyroud). Their descriptions of corresponding experimental techniques (bumblebee experiments, differential conditioning experiments, and foraging speed experiments) are provided in this chapter for completion. I investigated the theoretical and physics-experimental basis for this project, with guidance from Silvia Vignolini and Ullrich Steiner. In discussion with the Cambridge plant-scientists, I designed and created artificial flower samples according to my simplified model of the structure found

in nature. I also analysed all non-bee experimentation related data including optical measurements. The optical data was recorded by Rox Middleton and based on previous optical measurements conducted by myself and Silvia Vignolini.

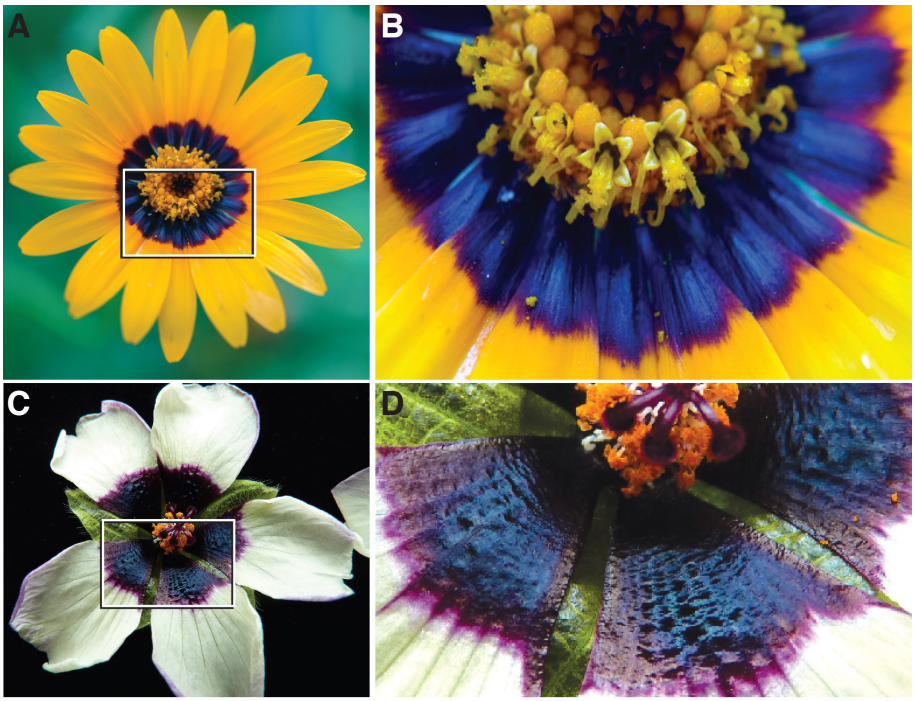

Figure 9.1: **Examples of flowers with a blue halo effect visible to the human eye.** The blue halo effect is best seen by the human eye on a dark pigmented background. The flowers of *Ursinia calendulifolia* (**A**-**B**) and *Hibiscus trionum* (**C**-**D**) present a striated epidermis at the base of the petal that overlaps the darkly pigmented zone. The presence of anthocyanin pigment produces the dark purple colour [21] while the presence of disordered striations produces the blue halo effect visible in a close-up view of the base of the ray florets (B) or of the proximal region of the petals (D). [Figure credit: Edwige Moyroud]

9.2 Measuring photonic surface scattering effects

The optical effect of photonic structures has to be studied on the biological sample itself in order to ensure it's visibility alongside any other optical sample characteristics. Simplified model systems can only be a clarifying extension to the study of the original system (see chapter 8 for the characterisation of the model system). Besides systematic disorder in the photonic structure, biological samples tend to be complex and usually not perfectly flat. Therefore it is important to assess the visibility of an optical effect of real samples, before advancing the detailed understanding of structure parameters with simplified artificial samples. An effect that involves the scattering of light into different directions, such as the expected response from surface striations, requires measurements

of (at minimum) the spectral behaviour (the effect change as function of the wavelength of light) at different scattering angles. The later can be measured with a goniometer, as illustrated in figure 9.2.

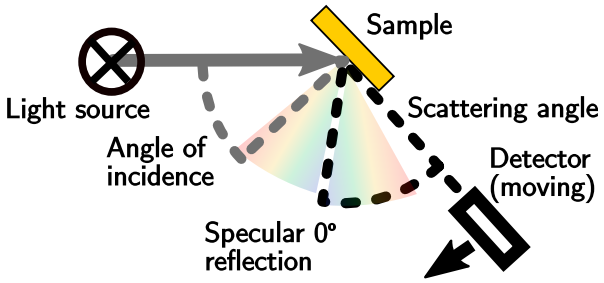

Figure 9.2: **Schematic representation of optical goniometer measurements.** Collimated light from a broad-spectrum UV-vis lamp irradiated the sample at variable angles of incidence (defined relative to the surface normal of the sample). The light scattered by the sample is collected with a fibre (connected to a spectrometer) at an angular range relative to the position of specular reflection (here defined as zero degree).

Using a goniometer set-up, reflected light scattered by the sample can be detected in a wide range of angles by moving the detector step-wise around the sample. The detector was coupled to a spectrometer by an optical fibre in order to also capture the spectral response at each angle. The instrumentation used to implement the set-up shown in figure 9.2 includes an Ocean Optics HPX 2000 xenon light source (wavelength-range of 185 - 2000 nm) coupled into an optical fibre (Avantes 50 µm diameter) leading into a collimator (Thorlabs RC08SMA-F01). The illuminating light spot size on the sample was ca. 2 mm in diameter. Scattered light was collected by a collimator on the outlet optical fibre (Avantes 600 µm diameter) at a ca. 20 cm distance to the sample, and passed to a spectrometer (Avantes Avaspec 2048). All measurements were recorded with respect to the reflection from a white scattering reference (Spectralon Diffuse Reflectance Standard SRS-99).

In the case of one-directional surface structuration such as flower striations which cause an anisotropic scattering response, it is important to identify the direction of striations first (e.g. with an optical microscope). The scattering response of samples was then recorded in two directions: (*i*) with striations perpendicular and (*ii*) parallel to the plane of detector rotation. The scattering effect of a one-dimensional structure only influences the measurement perpendicular to the pattern and the data recorded parallel to the striations serves as control measurement.

Reflectance curves are the simplest way to present data recorded with a goniometer set-up. They show spectra at selected angles. In the case of one-dimensional photonic structures, the corresponding spectra taken in the two different orientations can be plotted side-by-side for comparison. Figure 9.3 A - C shows such reflectance curves obtained

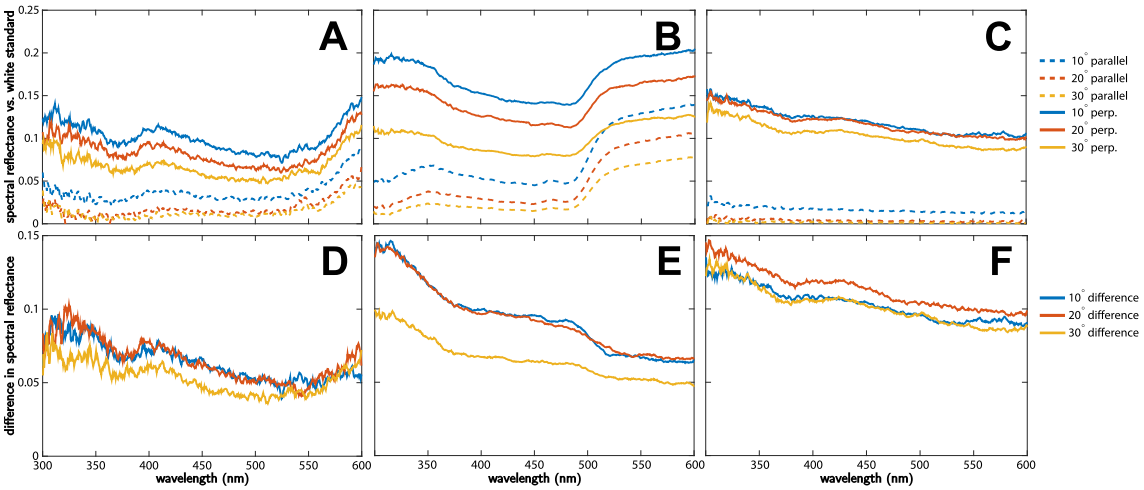

Figure 9.3: **Spectral reflectance curves.** (**A**-**C**) Individual reflectance spectra of three flowers are shown at scattering angles of 10 °, 20 °and 30 °. They were recorded in the plane parallel and perpendicular to the direction of surface striations. (**D**-**F**) Reflectance difference after subtracting parallel from perpendicular orientation measurements. (**A**,**D**) *Adonis aestivalis*; (**B**,**E**) *Oenothera stricta* reflectance reduced by a factor of 10 to fit plot limits; (**C**,**F**) *Hibiscus trionum*.

from samples of three different flower species (relative to the reflection of a white standard). The lower panels (D - F) show the difference between the orientations (spectra taken in perpendicular minus spectra in parallel mode). This representation reveals that striations cause enhanced scattering of short wavelengths (corresponding to blue and UV light) over a range on reflection angles. The specular reflection (where the angle of incidence matches the angle of reflection, set to 0 °) is not shown in figure 9.3.

9.2.1 Bee vision in context

When investigating photonic effects in flowers, it is important to consider their appearance to bees (the main group of pollinators for the flowers investigated here). Bees have a different visual system compared to humans. They are light sensitive in different spectral regions. Most notably, bees can see UV light (which is invisible to humans) but do not see red. They are also more sensitive to changes in hue than humans. In the context of this work, a goniometer data representation was chosen to highlights the visibility of optical effects to bees more directly.

Using the *Hibiscus trionum* flower as an example, figure 9.4 shows the method that was used for data representation in terms of bee photoreceptor sensitivity. The goniometer dataset recorded in the planes perpendicular and parallel to striations is shown as a heat map at the top left of the figure. It contains the reflectance curves (figure 9.3) for every recorded angle with their intensity displayed in a blue to yellow colour scale.

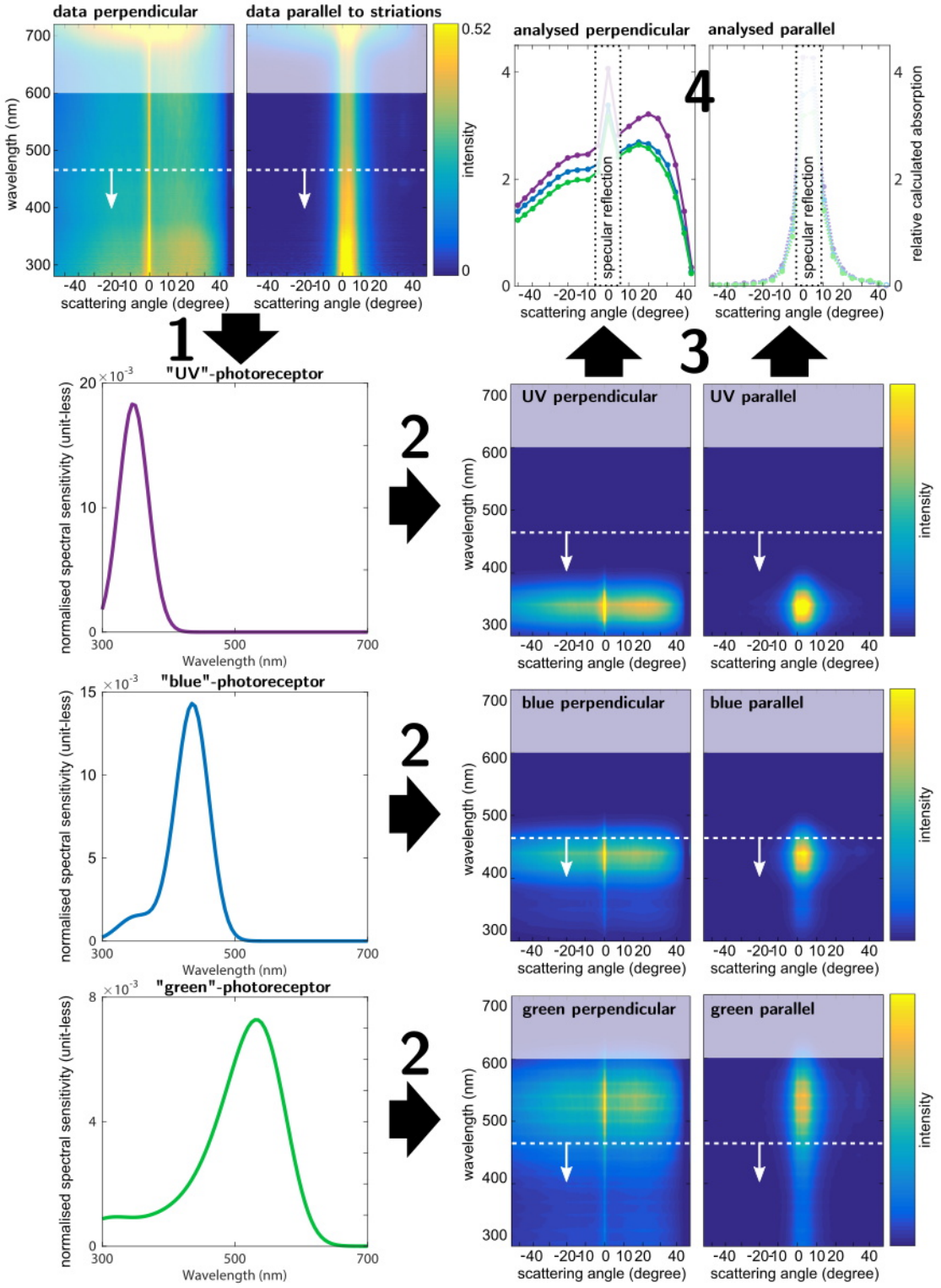

Figure 9.4: **Schematic explanation of data processing for spectral sensitivity plots.** (1) Optical measurements of the *Hibiscus trionum* flower; (**2**) spectral sensitivity curves of bee-eye receptors [69], normalised to their integral; (**3**) multiplication of (1) and (2); (**4**) relative calculated absorption of light per bee receptor and angle, after spectral integration of (3).

(**1**) The recorded spectrum at each angle was then multiplied by the normalised photoreceptor sensitivity for all the three bee-eye receptors (figure 9.4 left). The sensitivity curves were normalized to their integral to avoid a bias during integration in step (4).
(**2**) The resulting weighted data is shown in figure 9.4 right. They correspond to the signal range each bee receptor type would receive at the measurement angles. It should be noted that the bee receptor sensitivity curves overlap in parts [69]. Especially the receptor with the sensitivity peaking for green colours has a substantial sensitivity for blue and UV wavelengths. Using this representation leads to an underestimation of the physical separation of colour intervals. At the same time, bees are very sensitive to changes in hue, which means that even small colouration changes in this representation can have a significant effect on a target visibility. The spectral range >600 nm invisible to bees was shaded out and the area of highest halo intensity (coinciding with the sensitivity range of the two higher-wavelength photoreceptors) was indicated with a dashed-line.
(**3**) An integration in wavelength was performed in order to obtain one data point per receptor for each angle. Additionally, the spectra were averaged at intervals of 5 degrees to simplify the graphs and their interpretation. The data processing for this representation does not consider the spectrum of sunlight as light-source (instead it gives a better physical characterisation of the effect at each wavelength) and it does not consider the absolute photon flux reaching the eye (which is dependent of the light-level and irradiance spectrum).
(**4**) In the final data representation (figure 9.4 top-right), spectra recorded in the plane perpendicular/parallel to the striation direction are shown as darker/lighter colours respectively. The comparison demonstrates the presence of scattered light at angles outside the specular reflection as well as the enhancement of scattering for shorter wavelengths.

9.2.2 Visual differences for bees

Another method to investigate colour perception in bees is the colour hexagon [70, 71]. In this model, each reflectance curve is related to one location in the hexagon that signifies the potential corresponding physiological excitation in the bee eye. This location quantifies the relation in terms of three pure stimuli of the receptors E(U), E(B) and E(G), peaking in the UV, blue and green, respectively. The centre of the hexagon represents both no-signal (dark) and the colour of background adaptation. The so-called van Kries adaptation is the method used to describe how bees perceive colours in relationship to a reference (background) colour, e.g. green leaves [71, 72].

The adaptation of bee vision to background colour is a key processing step in the hexagon method and has an important influence on how visual cues (equal to optical spectra in terms of data) are likely to be perceived by bees. Since bees only have one

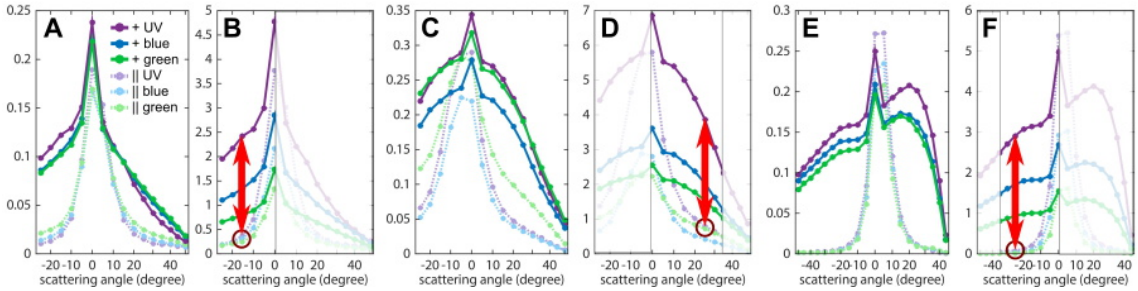

Figure 9.5: **Schematic explanation of the effect of background adaptation. A**, **C** and **E** show the unchanged bee-sensitivity graphs for *Adonis aestivalis*, *Oenothera stricta* and *Hibiscus trionum* respectively, as described in figure 9.4. **B**, **D** and **F** show the corresponding graphs that result from the normalisation used in bee hexagons (with van Kries adaptation and the sun illumination spectrum). The angles not plotted in figure 9.6 were shaded out.

receptor that is sensitive in the green and yellow range of wavelengths, many human-visible colours lead to a very similar stimulus, which in turn competes for attention with the more rare blue and UV signals of flowers. However, a background limitation to green leaves can magnify small colour changes in this range. In the case of surface striations, for example, short wavelengths are slightly enhanced for scattering angles larger than ca. 5 ° (figure 9.3). For the same flowers, the corresponding bee sensitivity graphs are shown in figure 9.5 A, C & E. Indeed, the line for to the UV-peaking photoreceptor tends to be slightly higher than the others (in the measurements taken perpendicular to the surface striations, e.g. at 25 °). However, the underlying pigmentation of the petal mainly contributes to the green line, counteracting the effect of striations. When applying the sun illumination spectrum and background adaptation to green leaves (figure 9.5 B, D & F) blue and UV scattering becomes much more relevant to the hue of the sample. The red arrows indicate the difference between the visual appearance of the two directions on striated samples, especially for the UV related stimulus.

Finally, the spectra in figure 9.5 B, D & F were plotted (between the specular reflection angle 0 ° and scattering angles up to 35 °) in the colour hexagon (figure 9.6). Values for 25 ° are shown in figure 9.6 A-C for the gionometer measurements taken parallel (blue) and perpendicular (red) to the direction of surface striations. It shows the clear separations of the colour loci of the two scan directions at a 25 ° scattering angle. The loci corresponding to light reflected parallel to the striations tend towards the centre of the hexagon with increasing scattering angle due to the larger relative content of green light and low light intensity. The loci of light reflected perpendicular to the striations remain distinguishable when the detection angle is varied. The model assumes that bees can reliably perceive the difference of colours separated by at least 0.1 units in the

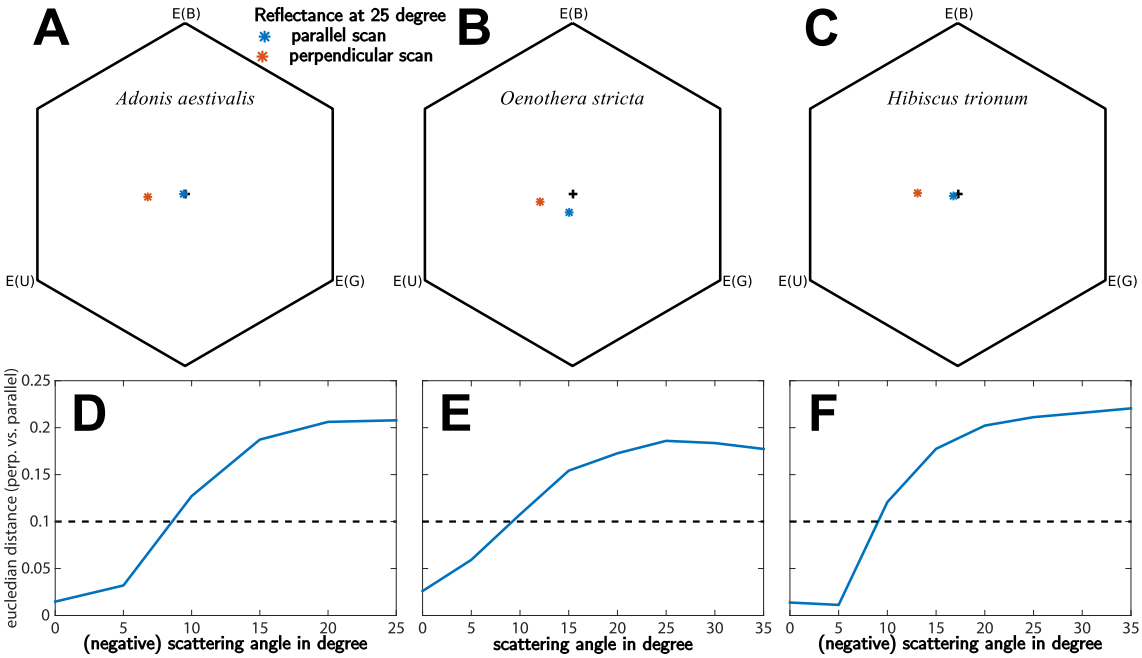

Figure 9.6: **Bee vision colour hexagon.** The hexagons in (**A**-**C**) show the colour-loci of recorded optical spectra in parallel and perpendicular direction to floral surface striations of three species at a scattering angle of 25 °. Panels (**D**-**F**) show the corresponding euclidian distances in the hexagon for each pair (perpendicular - parallel) of spectral reflectance spectra at the same scattering angle.

hexagon. This value is exceeded by all flowers in this example, as indicated by the dashed threshold line in the relative-distance plots in figure 9.6 D-F.

9.3 Techniques of bee experiments

9.3.1 Artificial flower design

The key part of the designed artificial flowers were 'test-squares' acting a stimulus for bees. The epoxy 20 mm x 20 mm test-squares contained a black (carbon black) or a yellow (naples yellow light (PY41)) pigment (62.5mg per ml of epoxy). The surface of the epoxy square was either smooth and glossy, or overlaid with manufactured disordered or ordered gratings. The micro-fabrication techniques used to create the surface structuration are detailed in chapter 8 section 8.5.

Artificial flowers used in differential conditioning experiments were constructed from black microcentrifuge tubes (10 mm diameter, 1.5ml volume) around which 20 mm x 40 mm strips of 3 mm-thick transparent Devcon high-strength 2-ton epoxy resin were mounted. The test-squares were added to the top of the transparent strips. These artificial flowers were mounted on 12 cm long wooden skewers and orientated so that

their surface was 35 ° from vertical, facing upward, and the lid of the microcentrifuge tube was left attached and open to act as a feeding reservoir for foraging bees.

Artificial flowers used in foraging speed experiments had a modified design: the detached lid of a transparent microcentrifuge tube (10 mm in diameter), acting as a feeding device for foragers, was inserted in a 20 mm x 40 mm strip of 3-mm-thick transparent epoxy resin and a test-square was added to the top of the transparent strip to act as a stimulus. Here, the artificial flowers were directly laid flat on the floor of the arena.

9.3.2 Bumblebee experiments

Flower-naive colonies of buff-tailed bumblebees *Bombus terrestris* (audax), were connected to test arenas (100 x 70 x 30 cm) by a gated transparent Perspex tube (15 mm diameter, 30 cm long) as described in [18]. For each experiment, foragers from 3 different colonies were used. The room temperature was kept constant at 21 °C. 14 h/day illumination was provided by Sylvania 36W Professional Activa 172 tubes on the ceiling of the room. The frequency of these lights was kept over 200 Hz, above the bee-flicker fusion frequency, by special Philips HF-B 236 TLD ballasts [73]. Adjustable lamps with a frequency above 200 Hz fitted with daylight bulbs were placed above the colony entrance to control flower illumination. The colony was fed daily with fresh 30 % sucrose solution and pollen grains supplied three times a week. Foragers were hand-marked with water-based Thorne^{TM} queen marking paint in various colour combinations to distinguish them individually during experimentation.

9.3.3 Differential conditioning experiments

During the training phase, each individual was allowed to familiarise with the feeding set-up: three training flowers (as described above but without any 'test-square') containing $30\,\mu l$ of a $30\,\%$ sucrose solution were randomly positioned in the arena and an individual bee was introduced into the arena and allowed to feed until it returned to the hive. A bee was considered trained once it had completed three successful bouts of foraging. During the test phase, six differential conditioning artificial flowers (as describe above) were randomly positioned in the arena. Three flowers presented a pigmented smooth test-square with 15 µl of a 0.12 % quinine solution and three flowers displayed a similarly pigmented test-square overlaid by a manufactured grating with 15 µl of 30 % sucrose solution in the feeding well. An individual trained bee was released into the arena and the flowers it successively visited were recorded. A flower was considered 'visited' whenever a bee made contact with it. After each visit, the flower was refilled with sucrose or quinine solution and moved to a new position in the arena, randomising also the position of the other non-visited flowers, so that the position of the 6 flowers constantly changed

throughout the experiment. Flowers (landing areas but not test-squares) were cleaned with 20 % ethanol solution between each foraging bout and between individuals. For each pair-wise comparison (black smooth vs. black blue halo; black smooth vs. black iridescent, yellow smooth vs. yellow blue halo), 10 independent bees were tested (30 in total) and each bee was tested to a minimum of 120 choices (on black pigmented flowers) or 80 choices (yellow pigmented flowers).

9.3.4 Foraging speed experiments

New individual bees were used for foraging tests, different from those having completed the differential conditioning experiment, but trained as above. During the test phase, three foraging speed flowers, all displaying identical black smooth test-squares and offering 15 µl of a 30 % sucrose solution, were set 30 cm apart from each other in the arena (position 1). An individual bee was introduced to the arena and its foraging bout (from the time it landed on flower 1, then visited flower 2 and landed on flower 3) was recorded with a Panasonic Lumix DMC-FZ38 camera. A large reward in the form of 100 µl of 30 % sucrose solution was offered to the bee at the end of the foraging bout to allow it to fill up and encourage return to the hive. Parts of the flowers contacted by bees were then cleaned with 20 % ethanol and set 30 cm apart from each other in a new location (position 2). The experiment was repeated with the same bee but with flowers in position 2. For foraging bouts 3 and 4, the same bee was then asked to forage on three flowers set at position 1, then position 2 successively, but this time the flowers were associated with black test strips overlaid with a manufactured disordered grating. For foraging bout 5 and 6, the same bee was successively recorded foraging on the three flowers at position 1 and 2 again, but this time the flowers displayed black test strips overlaid with a manufactured perfect grating. This series of 6 foraging bouts alternating between position and type of test-strips was repeated with two new positions for the flowers (position 3 and 4), and the entire procedure was repeated as a whole another 4 times minimum to ensure that at least 6 complete foraging bouts on each flower type were recoded for each individual. This routine enabled us to control for the variability in foraging speed between foragers (as each bee performed the experiment on each type of flower) and any potential effect of the position of the flowers in the arena. Ten individuals were independently tested in total. The training phase and test phase were repeated twice, each time with 10 new bumblebees, once alternating between smooth and manufactured disordered gratings associated with a yellow pigment, and once with smooth and manufactured disordered gratings associated with a blue pigment.

9.4 Results

9.4.1 Floral surface striation parameters and optical signatures

This study focuses on the photonic effect of floral surface striations, but the overall optical response of a flower [14, 74] is be affected by many other factors such as the shape of the insect attracting organ and their pigment content [75, 76]. For this reason, the anatomical parameters of petal cross-sections and the optical scattering properties of fresh flower samples were studied in detail for each of the exemplary 11 species: *Leucocoryne purpurea*, *Lathyrus aureus*, *Hibiscus trionum*, *Adonis aestivalis*, *Penstemon barrettiae*, *Grielum humifusum*, *Paeonia mascula*, *Mentzelia lindleyii*, *Oenothera stricta*, *Tulipa* 'Queen of the Night' and *Ursinia speciosa* (see also figure 7.1).

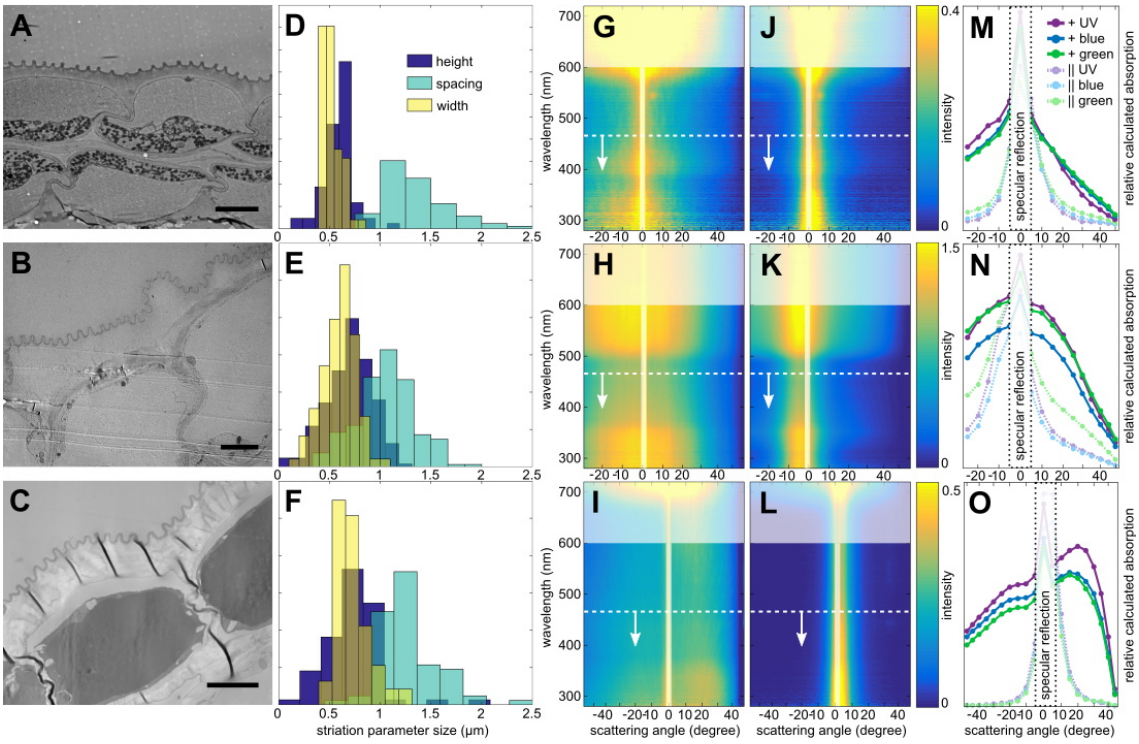

Figure 9.7: **Optical and anatomical properties of cuticular striations.** The anatomical and optical properties of three representative species are shown: *Adonis aestivalis* (top row), *Oenothera stricta* (middle row) and *Hibiscus trionum* (bottom). (**A**-**C**) TEM of petal epidermis with 5 µm scale bars and (**D**-**F**) distributions of striation height, spacing and width. Two-dimensional plots show spectra of the scattered light as a function of collection angle, for a 60 °(**G,H,J,K**) or 45 °(**I,L**) angle of incident light. Angular distribution of the scattered light in the plane perpendicular (**G**-**I**) or parallel (**J**-**L**) to the striation direction. (**M**-**O**) Angle-dependent spectral response mediated on the three photoreceptors in bee eyes: ultraviolet, blue and green. Spectra in the plane perpendicular (darker shades) and parallel (lighter shades) to the striation direction are represented.

The results for three representative flowers (already partially discussed in chapter 8) are shown in figure 9.7. Both a visual inspection of cross-sectional TEM images and a detailed parameter analysis (panels A-D) reveal that all three flowers *Adonis aestivalis* (top row), *Oenothera stricta* (middle row) and *Hibiscus trionum* (bottom) have very clearly formed surface striations from the waxy cuticle layer on the petals. These striations exhibit a strong and slightly different degree of disorder.

Figure 9.7 G-L shows goniometer scattering measurements on the selected flowers. The images are two-dimensional plots showing the spectra of the scattered light in function of collection angle. The intensity of the light is represented in a blue-to-yellow color scale. The color scale is kept constant for measurements on the same flower, but varies from flower to flower. To emphasise the data of greatest importance, the spectral region between 600 and 700 nm which is not perceived by the bees and the 0-order reflection are partially masked, and horizontal dotted lines with downward arrows indicate the enhanced spectral region of the halo. By comparing the optical measurements taken in the plane perpendicular to striations (figure 9.7 G-I) with those taken in parallel, where striations cannot contribute to the optical effect (J-L), it can be concluded that the presence of striations on the petal epidermis had an angular and wavelength dependent optical response.

To demonstrate the photonic effect of striations in a less complex fashion than the goniometer data matrices, a representation of the spectra considering bee-eye sensitivity curves was plotted (figure 9.7 M-O). This custom representation is explained in detail in section 9.2.1 and figure 9.4 of chapter 8. In summary, each of the points in the graph corresponds to an integral over a measured spectrum (at the corresponding collection angle) after it has been weighted with the sensitivity curves of the three types of photoreceptors in bee eyes: ultraviolet (in violet) blue (in blue) and green (in green). The spectra in the plane parallel and perpendicular to the striation direction are reported as lighter and darker colours respectively. On average we observe that the scattering response in the direction perpendicular to the striations is enhanced outside of the specular reflection (especially between $\pm 25\,^{\circ}$) and in the UV-blue wavelength region. From here on, we refer to this directional effect as 'blue halo'.

Figure 9.8 shows the wavelength and the angle dependent scattering behaviour of the petals of *Lecocoryne, Penstemon, Tulipa, Lathyrus*, respectively (equivalent to figure 9.7). The angle of light incidence was 45 degrees for all the measurements. A very similar scattering behaviour results from the presented flowers compared to the three previous examples, despite partially large differences in the disorder properties present in the floral striations of the different species. For very disordered samples (e.g. from *Lathyrus*) the scattering response is still angular dependent but more 'white' or similar for the three photoreceptors.

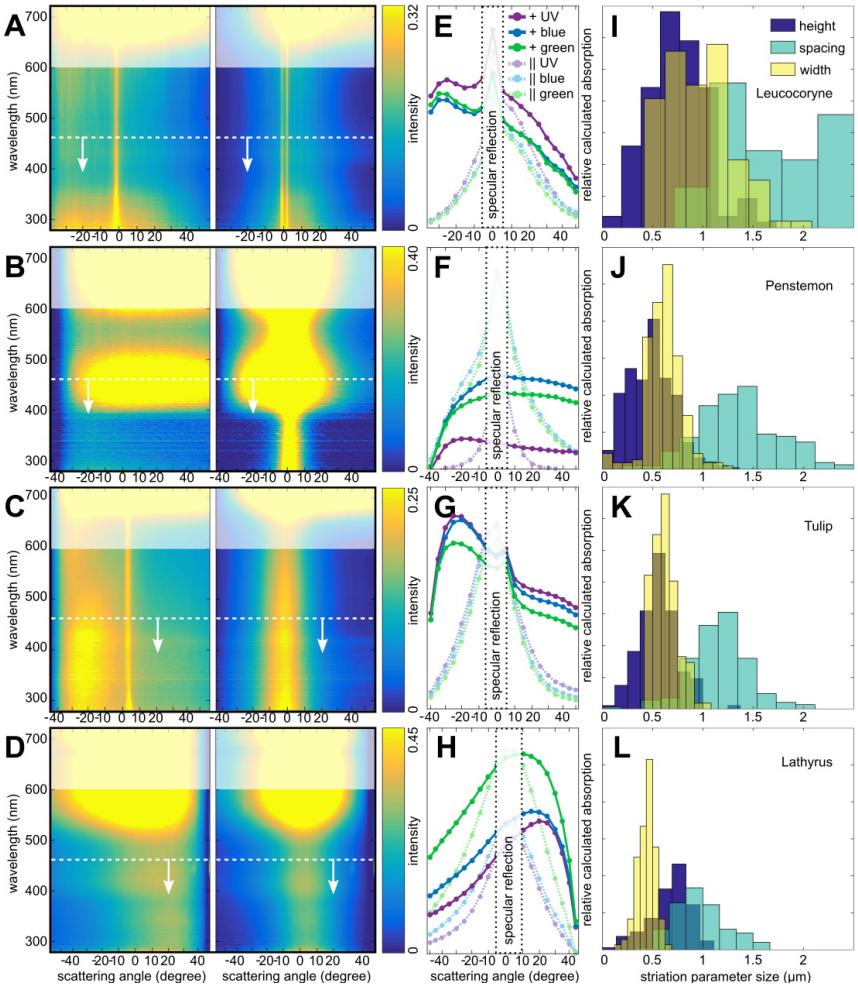

Figure 9.8: **Optical response and anatomical parameters of cuticular striations.** (**A**, **D**) Scattering measurements from flowers with different degrees of disorder, namely *Lecocoryne, Penstemon, Tulipa* 'queen of the night', and *Lathyrus*, respectively. The images are two-dimensional plots showing the spectra of the scattered light in function of the collection angle. The left column shows the angular distribution of the scattered light in the plane perpendicular to the striation direction, while in the right column the direction of striations is parallel to the plane of collection. (**E** to **H**) Angular-dependent spectral response mediated on the three bee photoreceptors.

The data for two further flowers (*Grielum humifusum* and *Oenothera stricta*) are shown in figure 9.9 with comparable optical results at different amounts of disorder observed. This time, the recorded optical spectra are shown for three different angles of incident light onto the sample, in order to demonstrate that the blue halo effect is not specific to the 45 ° inclination angle.

The optical signatures of the final four flowers (*Adonis aestivalis*, *Mentzelia lindleyii*, *Paeonia mascula* and *Ursinia speciosa*) are presented in figure 9.10. The data (panel A-L on left hand side of the figure) was recorded in the same year and with the same set-up parameters as the other data presented in this chapter. It highlights an important

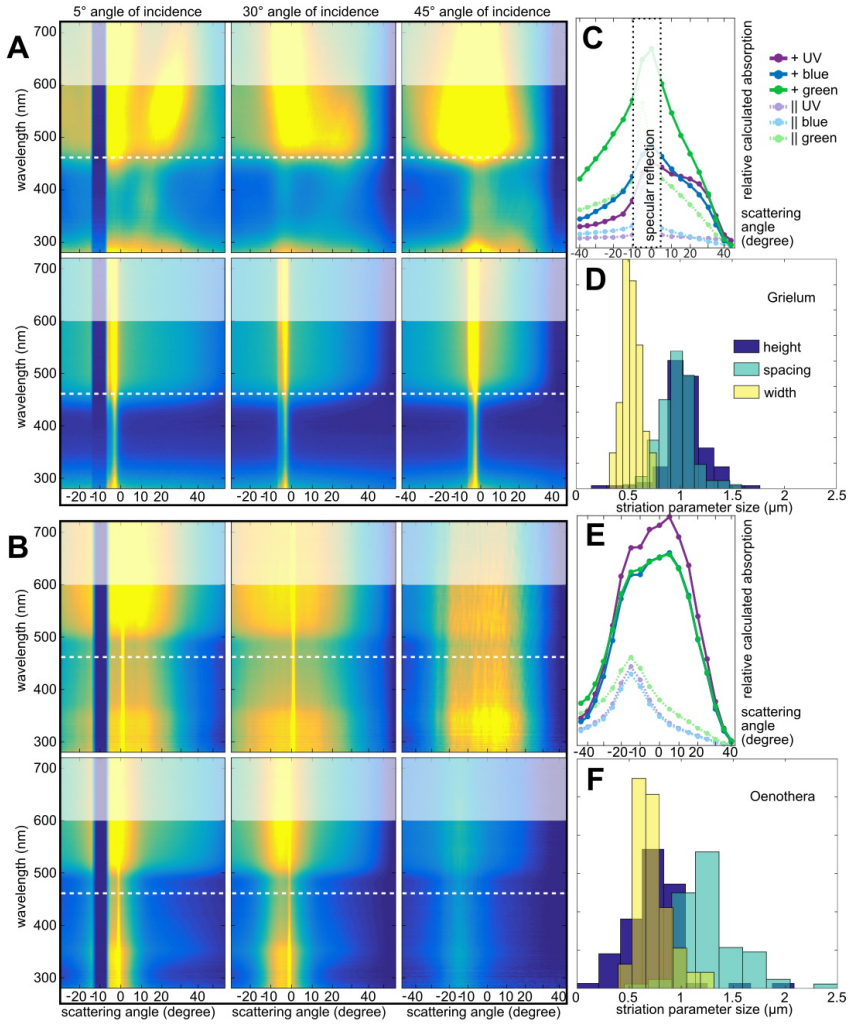

Figure 9.9: **Optical response at different angles of incident light and anatomical parameters of cuticular striations** (**A**,**B**) Scattering measurements at three angles if incident light (5, 30 and 45 degrees) for *Grielum humifusum* (A), *Oenothera stricta* (B). The upper row for each species shows the the scattered light in the plane perpendicular to the striation direction, and the lower measurements in the parallel plane. The intensity of the light is represented in a blue-to-yellow colour scale. The colour scale in the scattering plots is kept constant for each pair of sample orientations, but it varies from flower to flower and between angles of incidence. (**C**,**E**) Angular-dependent spectral response mediated on the three bee photoreceptors. (**D**,**F**) Histograms of the measured striation parameters in terms of spacing and size.

aspect of biological phenotype reproducibility: the development and quality of flower samples depends strongly on growth conditions and weather during the flowering period. Those initial measurements still demonstrated the scattering effect, but display only little colouration. Older data, recorded in previous years with a slightly lower resolution set-up, are presented in the columns on the right side of figure 9.10 (M-T) to demonstrate that the blue halo effect of those species can be more clearly observed in a different batch.

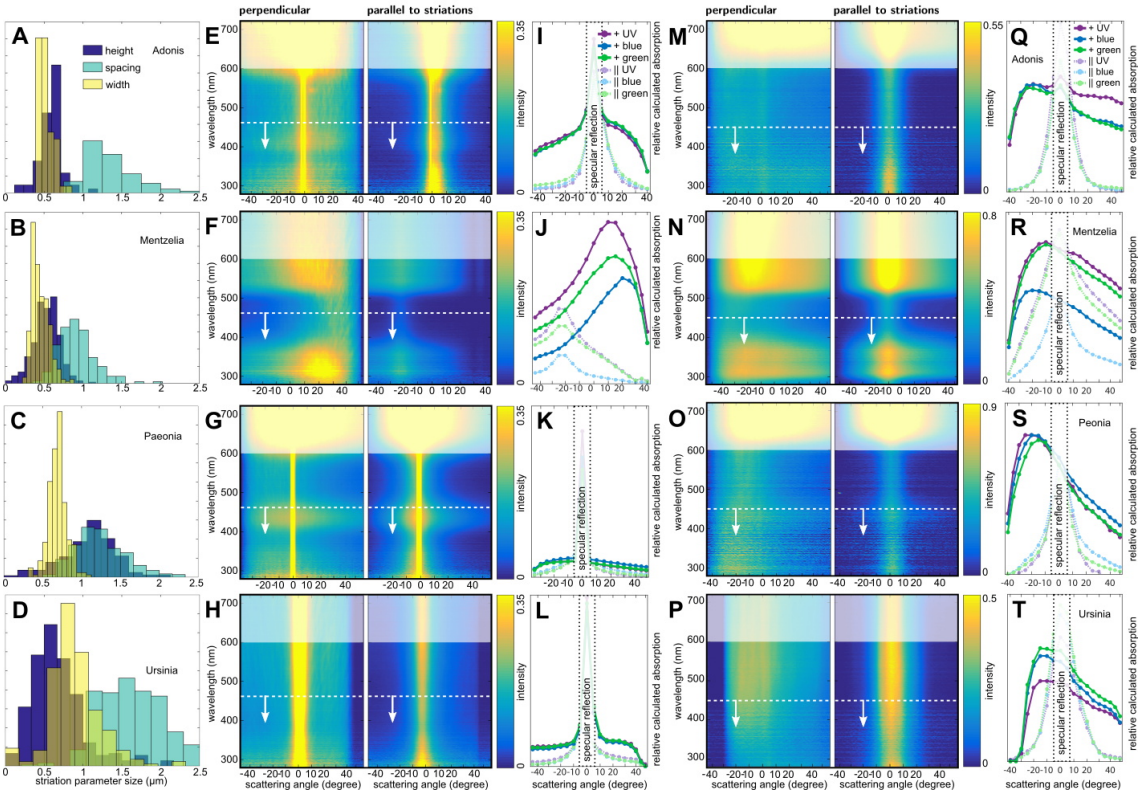

Figure 9.10: **Variation in optics of flower samples.** Sub-figures are shown analogous to those in figure 9.8 for the flowers *Adonis aestivalis* (top-row), *Mentzelia lindleyii* (upper-middle), *Paeonia mascula* (lower-middle) and *Ursinia speciosa* (bottom row). Panels (**M**-**T**) show repeat measurements in a similar configuration taken with flower samples from a different year which show the halo effect clearer, possibly due to more favourable environmental conditions during their respective flowering season.

9.4.2 Separation of surface structure and background pigmentation

As mentioned in the previous section, the overall optical response of a flower depends not only on a the photonic surface structure, but also on other strong optical features, such as pigmentation. The 11 analysed species have a broad variation of colours (figure 7.1). In the spectral regions where they overlap with the effect of the surface striations, it can be difficult to attribute the flower appearance to either of those features. In particular, pigment scattering in the yellow can contribute to a high signal for the green photoreceptor in the presented plots, showing the angular-dependent spectral response mediated on the three bee photoreceptors. This obscures the discovery process for a systematic optical effect of this photonic structure. To investigate the relative contributions of pigments and photonic structures, optical measurements were performed on the epidermal layer of a *Mentzelia* flowers as part of an intact petal and on its own (removing the pigment contribution), see figure 9.11. For the entire petal (A,B), UV and yellow

pigment colouration is visible at all angles and both scanning directions (perpendicular as well as parallel to the direction of the striations). This results in high relative values for the UV and green receptors, respectively (C). Because light is scattered perpendicular to striations for colours corresponding to all three photoreceptors, the optical signal of pigmentation makes it hard to recognise the colour trend of the scattered light (the blue halo) in the sensitivity plot (C). However, when measuring optical response of the striations on the peeled-off epidermis only, most pigments are removed and very little scattering is observed outside of the specular reflection when scanning parallel to the striation direction (E). In this case, the scattering collected perpendicularly to the striations (D) is caused by the structure itself and its subtle halo-colouration becomes more apparent (F). The scattered light is enhanced in the low-wavelength (blue-UV) region, especially between -25 ° and +25 °, where scattering is most intense.

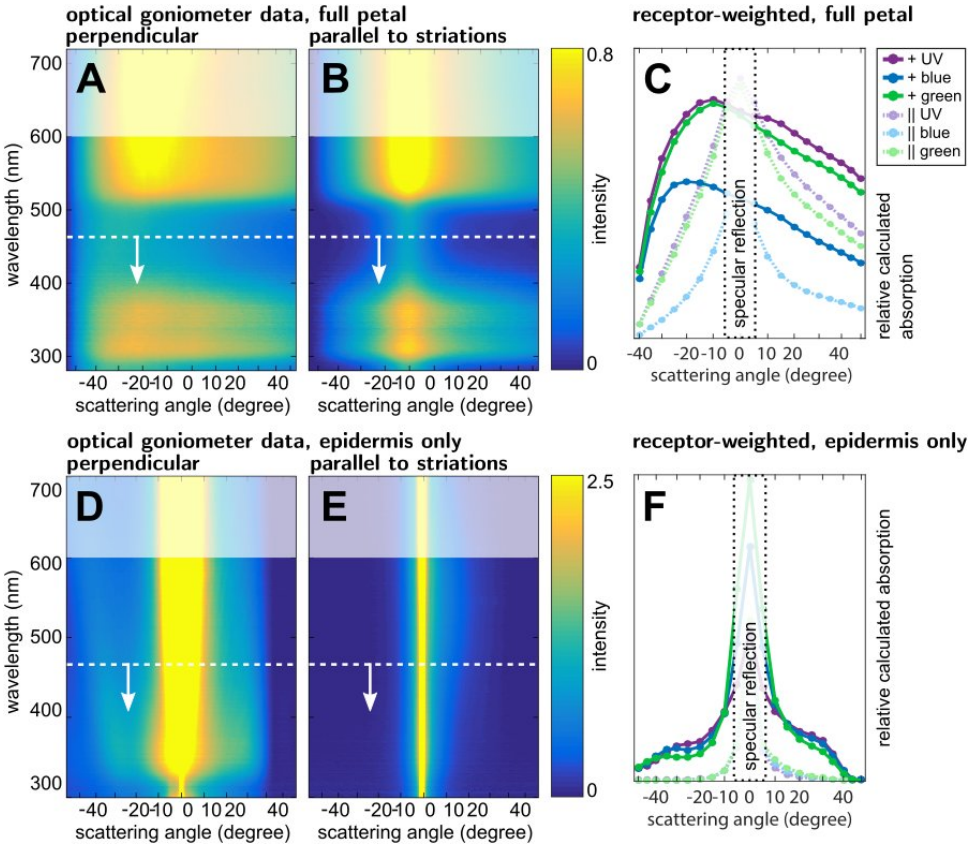

Figure 9.11: **The role of flower pigmentation on its optical response.** Optical measurements at 45 °angle of incident light are presented for a *Mentzelia* flower petal (**A**, **B**, **C**) and its peeled-off epidermal layer (**D**, **E**, **F**).

9.4.3 Bee recognition and foraging tests

It is interesting that the photonic effect of disordered striations can be observed optically, in simulations of a model system (chapter 8 section 8.4) and on physical implementations of the model system (chapter 8 section 8.5). But as an indication of its biological relevance, the visibility of the blue halo on the artificial flower samples had to be tested with bees. It is necessary to perform these experiments with artificial samples, as the many other visual stimuli such as pigmentation, shape, and scent characteristics of real flowers cannot be controlled independently from each other. It is known from previous experiments that bees can distinguish between samples with a perfectly ordered (iridescent) grating and smooth surfaces [18]. If the bees can also distinguish the halo presenting surface from a smooth sample, they are expected to learn to exclusively visit the artificial flowers with the right visual cue in order to obtain the reward (sweet liquid) over the punishment (a bitter substance that bees cannot smell). The two different experimental geometries used in bee experiments are shown in figure 9.12. The signalling surface was presented in a tilted upright position (A) during simple learning experiments (called differential conditioning) and lying down flat (B) for experiments designed to quantify the foraging speed of the pollinator.

The recognition experiments were then repeated on to squares with the same surface features, but different background pigmentation. On the black samples photonic effects

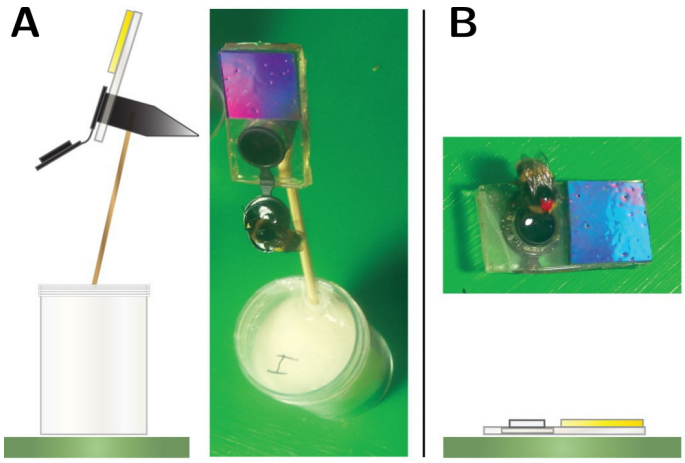

Figure 9.12: **Artificial flowers used in the behavioural experiments.** (**A**) Schematic representation of artificial flowers used in differential conditioning experiments (as yellow square) and picture of a bee feeding on such a flower (with a periodic grating on a black background). Rewards (15 µl 30 % sucrose) or punishment (15 µl 0.12 % quinine solution) are displayed in the lid of the black Eppendorf tube, where bees land to feed. (**B**) Artificial flowers used in the foraging speed experiments and picture of a marked forager feeding on such a flower (same sample type as in (A)). [Figure credit: Edwige Moyroud]

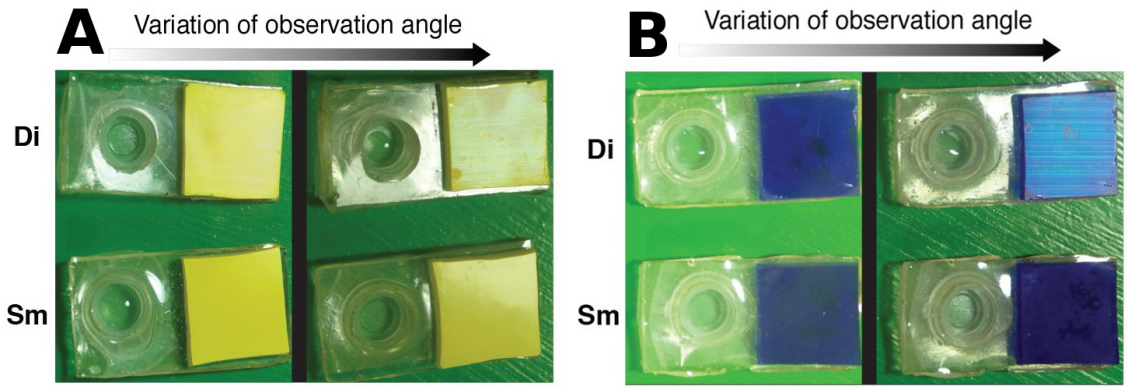

Figure 9.13: **Appearance of yellow and blue pigmented test-squares.** (**A**) Yellow test-squares with a smooth surface (Sm) or overlaid with a manufactured disordered structure (Di) are hardly discernible from each other even when the observation angle varies. (**B**) Blue test-squares with a smooth surface (Sm) or overlaid with a manufactured disordered architecture as in (C) appear identical at certain angles but display different shades and intensity of blue at other angles. [Figure based on material from Edwige Moyroud]

have a very good contrast in the absence of other scattered light from the sample. However, most natural flowers are not black, and the visibility of the blue-UV halo effect needed to be tested against other pigments (here yellow and blue as shown in figure 9.13). The blue halo effect is hardly discernible from the background scattering to the human eye. The appearance to bees is, however, expected to be different because of their distinct visual system (see section 9.2.1 for more detail).

Figure 9.14 contains the statistical results of the bee experiments. Reference tests such as those demonstrating that bees are unable to tell the difference between rewarding and unrewarding solution without clear visual cues were performed but are not shown.

Figure 9.14 A shows the learning behaviour of bumblebees for disordered gratings versus unstructured reference samples with the same (black) pigmentation. The initial 50 % probability of visits to the halo-presenting test-squares changed quickly to almost exclusive visits of these artificial flowers. This clearly demonstrates that bees can see the blue halo on a dark background and learn to recognise it. For iridescent perfect diffraction gratings (figure 9.14 B), the earlier findings on casts from CD gratings [18] could be reproduced. Bees were able to see and learn the difference of iridescence versus a dark background. However, they were slower in learning the visual cue and identifying it as the correct target with confidence. This might reflect the changing colour identity of the iridescent samples which may be more confusing to them than the of the more colour-consistent blue halo.

The learning speed for the halo effect on the yellow and blue pigmented background (figure 9.14 C,D) was even faster than on the black background (the only sample that is

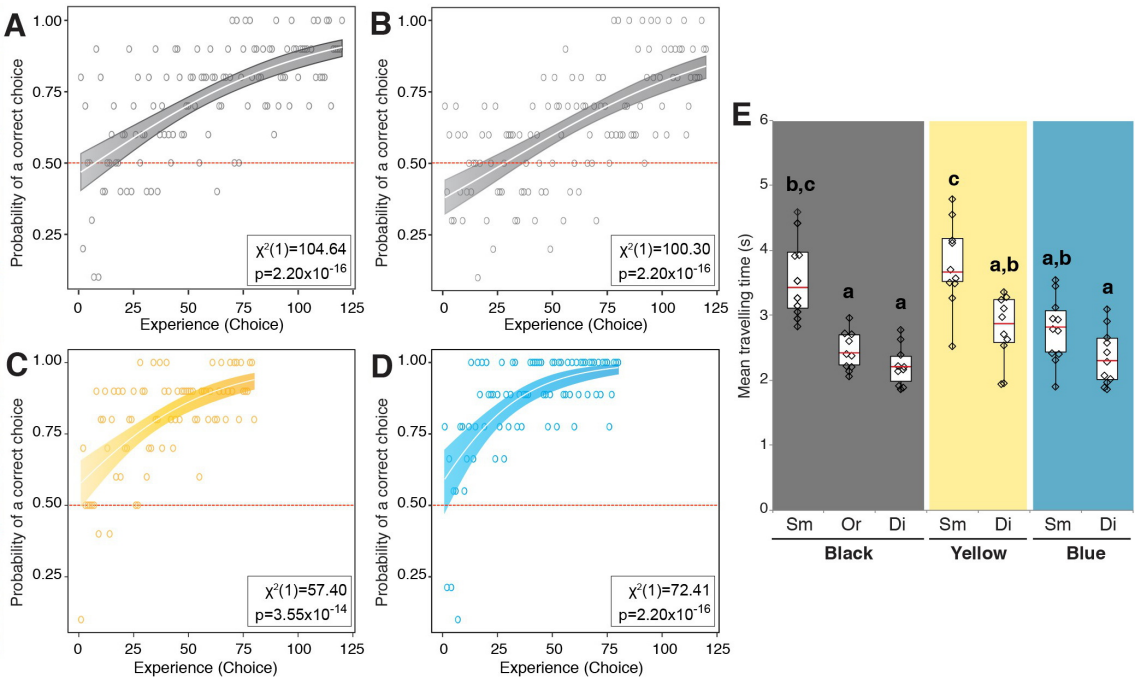

Figure 9.14: **Bumblebee response to the blue halo.** (**A**) Learning curve of ten bees choosing between black smooth and disordered samples. Empty circles represent the mean proportion of bees choosing correctly for each 120 successive choices. (**B**) As in (A) but bumblebees chose between black smooth and ordered. (**C**) As in (A) but bumblebees chose between yellow smooth and disordered. (**D**) As in (A) but 11 bumblebees chose between blue smooth and disordered. (**E**) Distribution of the individual mean travel time between artificial flowers for seven pigment/surface combinations. (A-D) The white curve depicts the fitted binomial logistic model, with the shading showing 95 % confidence intervals on the fitted response. The χ^2 statistic and p-value for the likelihood ratio tests assessing whether or not foragers can learn are given. (E) Median flight time (red line), quartile values (boxes) and total range of flight times are plotted. Diamonds represent mean foraging time of individuals. Letters represent the result of a post-hoc Tukey's HSD test. Group means that share the same letter are not significantly different from one another ($p > 0.001$). [Figure credit: Edwige Moyroud]

easily distinguishable by human eye). It is an interesting result that bees can see the blue halo also on a blue background. This is most likely due to the fact that the halo has an additional strong UV component, which could provide contrast above the overlapping background spectrum of the pigmentation.

Th dynamics of possible pollinator visual-cue interactions was investigated in more detail by the foraging speed experiments, which measured the flight time of bees until they settled on an artificial flower. Figure 9.14 E summarises the results obtained for the same types of artificial flowers used in differential learning experiments. The foraging speed varies for the analysed samples. In general, however, a clear trend was found that the blue halo shortens the travelling time of the bees by up to ca. $1/3$. The

iridescent signal of ordered gratings on a dark background also increased the foraging speed. Interestingly, in this experiment, the travelling time differences for the blue flowers with and without halo were only small. This means that bees are able to see the halo on blue flowers, but they cannot see it as well or identify it as quickly compared to sufficiently different background pigmentation.

9.5 Discussion

Optical measurements on fresh flower petals and artificial photonic samples showed that surface striations produce an optical effect, here termed blue halo. It is defined by a directional scattering of light that is enhanced for short wavelengths at small scattering angles. Bees can see the colouration difference caused by striations as they learn to identify rewarding samples. They are also able to identify these target more quickly, as indicated by up to one-third reduced flight times. The averages of flight times to artificial flowers exhibiting the blue halo was even shorter than those exhibiting iridescence from ordered gratings. This could be caused by an improved target identity [77] of the blue halo, as the colour change is smaller, i.e. it varies less as a function of angle compared to diffraction orders of periodic gratings.

The colours which are enhanced by the hue-change of petals caused by the halo, blue and UV, are colours which are known to be difficult for flowers to produce by conventional pigments [78–84]. Some flowers even employ physiologically difficult methods such as changing the pH to access different organic chemistries that lead to blue pigmentation [52, 80–85]. Several wild species of bees have been shown to prefer blue colours [86–88] which has been associated with the possibility that blue flowers might produce relatively large amounts of nectar [78, 79]. These are all important factors for flowers across the angiosperm phylogenetic tree [38] to evolve simpler methods of generating an insect salient colour such as the blue halo.

The behavioural bee experiments have shown that the blue halo is visible to pollinating bees. This might seem surprising given the small change in colouration caused by striations on real flower petals (figures 9.7 to 9.11) and the limited visibility of the halo to the human eye on scattering backgrounds (figure 7.1 and figure 9.13). This difference in visibility is probably caused by differences between the human and bee visual systems, including different spectral sensitivities and different perception of hues and intensities [70, 72], but also by the bees adaptation to background colours [71], which favours blue and UV colouration with respect to green leaves (figure 9.5). Whether the directionality of a colouration or possible polarisation effects of surface striations (figure 8.19) influences the visibility of the photonic structure to bees, is something that remains to be investigated in future studies.

Whether surface striations truly impact the pollination behaviour of flowers in the wild is a very challenging research question to answer systematically, as flower species differing in the presence of striations also differ in other relevant aspects such as scent, pigmentation and shape [75, 76]. A genetically modified strain differing only in petal surface striations would need to be generated and placed in an environment with comparable conditions (lighting, proximity to hive, etc.). Instead of such a general claim, the presented data specifically shows that bees can identify the photonic effect of surface striations under controlled conditions. The direct visibility of floral striations and striation-casts has been shown previously [18, 77]. The illumination conditions in the bee arena were not optimised for any optical effect and bees could approach the samples from different directions, resulting in variable optical signatures of the artificial flowers. Nevertheless, natural conditions can vary in a wider range, including diffuse light, shadows, flower-movement and also direct sunlight. Other flower properties might, under certain conditions, outweigh the colouration effect of striations.

Chapter 10

Conclusions

The second part of this thesis shows that disordered surface striations on flowers have a photonic effect that generates a biologically significant colouration. The effect, termed blue halo, can be described as directional scattering that is enhanced in the UV-blue wavelength region of the spectrum. This effect is difficult to see for the human eye, particularly in combination with bright pigment colouration, but the bees (with their different visual system) are able to detect the blue halo even on pigmented artificial flowers with overlapping spectral signatures. Furthermore, the flight time of bees to a flower target exhibiting the blue halo was found to be reduced, which is an important parameter in natural pollinator flower interactions because it indicates that bees can quickly recognise striated flowers.

The optical response of disordered striations was measured directly on petal surfaces of 11 plant species. The measurements were presented in 'raw' heat-maps, and in a representation which considers the spectral sensitivity of receptors in bee-eyes. Both sets show increased scattering in the plane perpendicular to floral striation and a trend of hue change towards shorter wavelengths, as characteristic for the blue halo. Proof of visibility of the blue halo to bees was established by behavioural experiments, and for comparison with the expectations derived from optical data, predicted colour loci of measurements perpendicular and parallel to the striations (showing the halo and reference) were plotted in the bee colour-hexagon. The colour-hexagon [70] is the best developed tool for the prediction of colour perception in bees, drawing from predictions on neural processing of stimuli in the visual systems of pollinators. In this theoretical tool, the minimum visible difference of hue is well exceeded by the addition of the blue halo effect to pigmented background colours.

The photonic structure was identified in 11 flowering plant (angiosperm) species that are very distantly related and have evolved independently [38]. These species differ in

disorder parameters, but they converge on similar optical signatures (the blue halo). We therefore assume a convergent evolution [89] of disordered photonic structures in plants.

The cross-sectional parameters (width, height, spacing and relative disorder) of floral striations were determined from a large number of cross-sectional transmission electron microscopy images. This revealed that a significant relative amount of disorder is present in all three parameters for every analysed species. Using the determined sizes and variations, floral striations were modelled by disordered rectangular gratings in silico. Numerical simulations of this simplified model system helped to understand and characterise the photonic effect of the complex biological samples. FDTD simulation tools were adapted to enable the computational investigation of disordered structures, which are both a new application and a challenge for simulations. Detailed characteristics of this new, (controlled) disorder-based photonic effect (the blue halo) were presented.

The optical analyses and bee experiments relied on the nano-manufacture of gratings with three levels of disorder, which is much harder to achieve than comparable ordered gratings, particularly on the large surface areas required for the bee experiments. Guided by simulations, artificial samples were fabricated (those used during behavioural bee experiments) displaying a blue halo but no diffraction peaks. Their optical signature confirmed the design principles predicted by the simulations.

The developed research tool-sets (optical, computational, fabrication) could enable similar investigations in the field of disordered photonic and biomimetic structures. This first proof that optical functionality can be derived from quasi-disordered photonic structures may inspire further discoveries of biological phenomena and possibly technological applications.

References

[1] J. D. Joannopoulos, S. G. Johnson, J. N. Winn, and R. D. Meade, *Photonic crystals: molding the flow of light* (Princeton university press, 2011).

[2] B. D. Wilts, X. Sheng, M. Holler, A. Diaz, M. Guizar-Sicairos, J. Raabe, R. Hoppe, S.-H. Liu, R. Langford, O. D. Onelli, D. Chen, S. Torquato, U. Steiner, C. G. Schroer, S. Vignolini, and A. Sepe, "Evolutionary-optimized photonic network structure in white beetle wing scales", Adv. Mater. 10.1002/adma.201702057.

[3] Y. Zhao, Z. Xie, H. Gu, C. Zhu, and Z. Gu, "Bio-inspired variable structural color materials", Chem. Soc. Rev. **41**, 3297–317 (2012).

[4] M. Crne, V. Sharma, J. Blair, J. O. Park, C. J. Summers, and M. Srinivasarao, "Biomimicry of optical microstructures of *Papilio palinurus*", Europhys. Lett. **93**, 14001 (2011).

[5] S. M. Doucet and M. G. Meadows, "Iridescence: a functional perspective", J. R. Soc. Interf. **6 Suppl 2**, S115–32 (2009).

[6] M. G. Meadows, M. W. Butler, N. I. Morehouse, L. a. Taylor, M. B. Toomey, K. J. McGraw, and R. L. Rutowski, "Iridescence: views from many angles", J. R. Soc. Interf. **6 Suppl 2**, S107–13 (2009).

[7] J. Sun, B. Bhushan, and J. Tong, "Structural coloration in nature", RSC Advances **3**, 14862 (2013).

[8] A. E. Seago, P. Brady, J.-P. Vigneron, and T. D. Schultz, "Gold bugs and beyond: a review of iridescence and structural colour mechanisms in beetles (*Coleoptera*)", J. R. Soc. Interf. **6 Suppl 2**, S165–84 (2009).

[9] T. F. Anderson, "An Electron Microscope Study of Some Structural Colors of Insects", J. Appl. Phys. **13**, 748 (1942).

[10] G. E. Hill and K. J. McGraw, *Bird coloration: mechanisms and measurements*, Vol. 1 (Harvard University Press, 2006).

[11]R. O. Prum and R. H. Torres, "Structural colouration of mammalian skin: convergent evolution of coherently scattering dermal collagen arrays", J. Exp. Biol. **207**, 2157–2172 (2004).

[12]J. Vigneron, M. Rassart, Z. Vértesy, K. Kertész, M. Sarrazin, L. Biró, D. Ertz, and V. Lousse, "Optical structure and function of the white filamentary hair covering the edelweiss bracts", Phys. Rev. E **71**, 011906 (2005).

[13]S. Vignolini, M. M. Thomas, M. Kolle, T. Wenzel, A. Rowland, P. J. Rudall, J. J. Baumberg, B. J. Glover, and U. Steiner, "Directional scattering from the glossy flower of *Ranunculus*: how the buttercup lights up your chin.", J. R. Soc. Interf. **9**, 1295–301 (2012).

[14]S. Vignolini, M. P. Davey, R. M. Bateman, P. J. Rudall, E. Moyroud, J. Tratt, S. Malmgren, U. Steiner, and B. J. Glover, "The mirror crack'd: both pigment and structure contribute to the glossy blue appearance of the mirror orchid, *Ophrys speculum*.", New Phytol. **196**, 1038–47 (2012).

[15]S. Vignolini, P. J. Rudall, A. V. Rowland, A. Reed, E. Moyroud, R. B. Faden, J. J. Baumberg, B. J. Glover, and U. Steiner, "Pointillist structural color in *Pollia* fruit", Proc. Natl. Acad. Sci. **109**, 15712–15715 (2012).

[16]K. R. Thomas, M. Kolle, H. M. Whitney, B. J. Glover, and U. Steiner, "Function of blue iridescence in tropical understorey plants", J. R. Soc. Interf. **7**, 1699–707 (2010).

[17]S. Vignolini, B. Glover, and U. Steiner, "Photonic Structures in Plants", in *Biomimetics in photonics*, edited by O. Karthaus (Taylor and Francis, 2012) Chap. 1, pp. 1–18.

[18]H. M. Whitney, M. Kolle, P. Andrew, L. Chittka, U. Steiner, and B. J. Glover, "Floral iridescence, produced by diffractive optics, acts as a cue for animal pollinators", Science **323**, 130–3 (2009).

[19]B. J. Glover and H. M. Whitney, "Structural colour and iridescence in plants: the poorly studied relations of pigment colour", Annals of Botany **105**, 505–11 (2010).

[20]S. Vignolini, E. Moyroud, B. J. Glover, and U. Steiner, "Analysing photonic structures in plants", J. R. Soc. Interf. **10** (2013).

[21]S. Vignolini, E. Moyroud, T. Hingant, H. Banks, P. J. Rudall, U. Steiner, and B. J. Glover, "The flower of hibiscus trionum is both visibly and measurably iridescent", New Phytol. **205**, 97–101 (2015).

[22]H. M. Whitney, M. Kolle, R. Alvarez-fernandez, U. Steiner, and B. J. Glover, "Contributions of iridescence to floral patterning", Commun. Integr. Biol. **2**, 230–232 (2009).

[23]R. L. A. Kourounioti, L. R. Band, J. A. Fozard, A. Hampstead, A. Lovrics, E. Moyroud, S. Vignolini, J. R. King, O. E. Jensen, and B. J. Glover, "Buckling as an origin of ordered cuticular patterns in flower petals", J. R. Soc. Interf. **10**, 9 (2012).

[24]P. G. Kevan and M. A. Lane, "Flower petal microtexture is a tactile cue for bees", Proc. Natl. Acad. Sci. **82**, 4750–2 (1985).

[25]C. S. Davis, D. Martina, C. Creton, A. Lindner, and A. J. Crosby, "Enhanced adhesion of elastic materials to small-scale wrinkles", Langmuir **28**, 14899–908 (2012).

[26]J. Y. Chung, J. P. Youngblood, and C. M. Stafford, "Anisotropic wetting on tunable micro-wrinkled surfaces", Soft Matter **3**, 1163 (2007).

[27]H. Hinton and D. Gibbs, "Diffraction gratings in phalacrid beetles", Nature **221**, 953–954 (1969).

[28]A. Parker and Z. Hegedus, "Diffractive optics in spiders", J. Opt. A **111** (2003).

[29]D. G. Stavenga, J. C. Otto, and B. D. Wilts, "Splendid coloration of the peacock spider maratus splendens", J. R. Soc. Interf. **13** (2016) 10.1098/rsif.2016.0437.

[30]M.-C. G. Klein and S. N. Gorb, "Epidermis architecture and material properties of the skin of four snake species", J. R. Soc. Interf. **9**, 3140–55 (2012).

[31]E. A. Monroe and S. E. Monroe, "Origin of Iridescent Colors on the Indigo Snake", Science **159**, 97–98 (1968).

[32]R. O. Prum, R. H. Torres, S. Williamson, and J. Dyck, "Coherent light scattering by blue feather barbs", English, Nature **396**, 28–29 (1998).

[33]R. O. Prum and R. H. Torres, "A fourier tool for the analysis of coherent light scattering by bio-optical nanostructures1", Integr. Comp. Biol. **43**, 591–602 (2003).

[34]B. D. Wilts, T. M. Trzeciak, P. Vukusic, and D. G. Stavenga, "Papiliochrome ii pigment reduces the angle dependency of structural wing colouration in nireus group papilionids", J. Exp. Biol. **215**, 796–805 (2012).

[35]S. Kinoshita and S. Yoshioka, "Structural colors in nature: the role of regularity and irregularity in the structure", Phys. Chem. Chem. Phys. **6**, 1442–59 (2005).

[36]A. Saito, "Material design and structural color inspired by biomimetic approach", Sci. Techn. Adv. Mater. **12**, 064709 (2012).

[37]E. Moyroud, T. Wenzel, R. Middleton, P. J. Rudall, H. Banks, A. Reed, G. Mellers, P. Killoran, M. M. Westwood, U. Steiner, S. Vignolini, and B. J. Glover, "Disorder in convergent floral nanostructures enhances signalling to bees", Nature (2017) 10.1038/nature24285.

[38]B. Bremer, K. Bremer, M. Chase, M. Fay, J. Reveal, D. Soltis, P. Soltis, and P. Stevens, "An update of the Angiosperm Phylogeny Group classification for the orders and families of flowering plants: APG III", Bot. J. Linnean Soc. **161**, 105–121 (2009).

[39]D. Grimaldi, "The co-radiations of pollinating insects and angiosperms in the cretaceous", Annals Missouri Bot. G. **86**, 373–406 (1999).

[40]D. Grimaldi and M. S. Engel, *Evolution of the insects* (Cambridge University Press, 2005).

[41]C. C. Labandeira, "The pollination of mid mesozoic seed plants and the early history of long-proboscid insects", Annals of the Missouri Botanical Garden **97**, 469–513 (2010).

[42]D. Shin and R. Magnusson, "Diffraction by surface-relief gratings with conic cross-sectional grating shapes", J. Opt. Soc. Am. **6**, 1249–1253 (1989).

[43]E. Bradshaw, P. J. Rudall, D. S. Devey, M. M. Thomas, B. J. Glover, and R. M. Bateman, "Comparative labellum micromorphology of the sexually deceptive temperate orchid genus Ophrys: diverse epidermal cell types and multiple origins of structural colour", Bot. J. Linnean Soc. **162**, 504–540 (2010).

[44]K. Yee, "Numerical solution of initial boundary value problems involving Maxwell's equations in isotropic media", IEEE Trans. Ant. Propag. **14**, 302–307 (1966).

[45]D. G. Stavenga, H. L. Leertouwer, and B. D. Wilts, "Quantifying the refractive index dispersion of a pigmented biological tissue using jamin-lebedeff interference microscopy", English, Light Sci. Appl. **2**, 6 (2013).

[46]B. D. Wilts, B. Wijnen, H. L. Leertouwer, U. Steiner, and D. G. Stavenga, "Extreme refractive index wing scale beads containing dense pterin pigments cause the bright colors of pierid butterflies", Advanced Optical Materials **5**, 1600879–n/a (2017).

[47]C. J. van der Kooi, B. D. Wilts, H. L. Leertouwer, M. Staal, J. T. M. Elzenga, and D. G. Stavenga, "Iridescent flowers? contribution of surface structures to optical signaling", New Phytol. **203**, 667–673 (2014).

[48]V. E. Johansen, L. H. Thamdrup, K. Smistrup, T. Nielsen, O. Sigmund, and P. Vukusic, "Designing visual appearance using a structured surface", Optica **2**, 239–245 (2015).

[49]M. Mrksich and G. M. Whitesides, "Patterning self-assembled monolayers using microcontact printing: A new technology for biosensors?", Trends Biotechnol. **13**, 228–235 (1995).

[50]D. Qin, Y. Xia, and G. M. Whitesides, "Soft lithography for micro- and nanoscale patterning", Nat. Protoc. **5**, 491–502 (2010).

[51]R. E. Fontana, J. Katine, M. Rooks, R. Viswanathan, J. Lille, S. MacDonald, E. Kratschmer, C. Tsang, S. Nguyen, N. Robertson, and P. Kasiraj, "E-beam writing: a next-generation lithography approach for thin-film head critical features", IEEE Trans. Magn. **38**, 95–100 (2002).

[52]S. Yasin, D. G. Hasko, and H. Ahmed, "Fabrication of <5 nm width lines in poly(methylmethacrylate) resist using a water isopropyl alcohol developer and ultrasonically-assisted development", Appl. Phys. Lett. **78**, 2760 (2001).

[53]P. J. L. B. Williams and L. M. L. Laurens, "Microalgae as biodiesel & biomass feedstocks: Review & analysis of the biochemistry, energetics & economics", Energy Environ. Sci. **3**, 554 (2010).

[54]J. P. Rolland, E. C. Hagberg, G. M. Denison, K. R. Carter, and J. M. De Simone, "High-Resolution Soft Lithography: Enabling Materials for Nanotechnologies", Angew. Chemie **116**, 5920–5923 (2004).

[55]S.-H. Kang, T.-Y. Tai, and T.-H. Fang, "Replication of butterfly wing microstructures using molding lithography", Curr. Appl. Phys. **10**, 625–630 (2010).

[56]T. W. Odom, J. C. Love, D. B. Wolfe, K. E. Paul, and G. M. Whitesides, "Improved Pattern Transfer in Soft Lithography Using Composite Stamps", Langmuir **18**, 5314–5320 (2002).

[57]H. Bodiguel and C. Fretigny, "Viscoelastic properties of ultrathin polystyrene films", Macromolecules **40**, 7291–7298 (2007).

[58]K. Zhang, S. Zhou, Y. Tang, G. Wang, H. Zhou, T. Fan, and D. Zhang, "Polarization-sensitive color in iridescent scales of butterfly *Ornithoptera*", RSC Advances **4**, 51865–51871 (2014).

[59]K. D. Feller, T. M. Jordan, D. Wilby, and N. W. Roberts, "Selection of the intrinsic polarization properties of animal optical materials creates enhanced structural reflectivity and camouflage", Philos. Trans. R. Soc. London, Ser. B **372** (2017) 10.1098/rstb.2016.0336.

[60]S. Rossel and R. Wehner, "Polarization vision in bees", Nature **323**, 128–131 (1986).

[61]G. Horváth and D. Varjú, *Polarized light in animal vision: polarization patterns in nature* (Springer, 2013).

[62]H. Ichikawa, "Subwavelength triangular random gratings", J. Mod. Opt. **49**, 1893–1906 (2002).

[63]I. J. Buss, G. R. Nash, J. G. Rarity, and M. J. Cryan, "Finite-Difference Time-Domain Modeling of Periodic and Disordered Surface Gratings in AlInSb Light Emitting Diodes With Metallic Back-Reflectors", J. Lightw. Tech. **28**, 1190–1200 (2010).

[64] J. M. Rico-García and L. M. Sanchez-Brea, "Binary gratings with random heights", Applied Optics **48**, 3062 (2009).

[65] Y. Fujii and J. Minowa, "Optical demultiplexer using a silicon concave diffraction grating", Applied Optics **22**, 974–8 (1983).

[66] N. Schneider, C. Zeiger, A. Kolew, M. Schneider, J. Leuthold, H. Hölscher, and M. Worgull, "Nanothermoforming of hierarchical optical components utilizing shape memory polymers as active molds", Opt. Mater. Express **4**, 1895–1902 (2014).

[67] S. Schauer, M. Worgull, and H. Holscher, "Bio-inspired hierarchical micro- and nano-wrinkles obtained via mechanically directed self-assembly on shape-memory polymers", Soft Matter **13**, 4328–4334 (2017).

[68] P. B. Green and P. Linstead, "A procedure for sem of complex shoot structures applied to the inflorescence of snapdragon (*Antirrhinum*)", Protoplasma **158**, 33–38 (1990).

[69] D. Peitsch, a. Fietz, H. Hertel, J. de Souza, D. F. Ventura, and R. Menzel, "The spectral input systems of hymenopteran insects and their receptor-based colour vision", J. Comp. Physiol. **170**, 23–40 (1992).

[70] L. Chittka, "The colour hexagon: a chromaticity diagram based on photoreceptor excitations as a generalized representation of colour opponency", J. Comp. Physiol. **170**, 533–543 (1992).

[71] Z. Bukovac, M. Shrestha, J. E. Garcia, M. Burd, A. Dorin, and A. G. Dyer, "Why background colour matters to bees and flowers", J. Comp. Physiol. **203**, 369–380 (2017).

[72] M. Vorobyev, J. Marshall, D. Osorio, N. Hempel de Ibarra, and R. Menzel, "Colourful objects through animal eyes", Color Res. Appl. **26**, S214–S217 (2001).

[73] A. G. Dyer and L. Chittka, "Biological significance of distinguishing between similar colours in spectrally variable illumination: bumblebees (bombus terrestris) as a case study", J. Comp. Physiol. **190**, 105–114 (2004).

[74] C. J. van der Kooi, J. T. M. Elzenga, M. Staal, and D. G. Stavenga, "How to colour a flower: on the optical principles of flower coloration", Proc. Royal Soc. B **283** (2016) 10.1098/rspb.2016.0429.

[75] K.-i. Noda, B. J. Glover, P. Linstead, and C. Martin, "Flower colour intensity depends on specialized cell shape controlled by a myb-related transcription factor", Nature **369**, 661–664 (1994).

[76] H. L. Gorton and T. C. Vogelmann, "Effects of epidermal cell shape and pigmentation on optical properties of *Antirrhinum* petals at visible and ultraviolet wavelengths", Plant Physiol. **112**, 879–888 (1996).

[77]H. M. Whitney, A. Reed, S. A. Rands, L. Chittka, and B. J. Glover, "Flower iridescence increases object detection in the insect visual system without compromising object identity", Current Biology **26**, 802–808 (2016).

[78]K. Yoshida, T. Kondo, Y. Okazaki, and K. Katou, "Cause of blue petal color", English, Nature **373**, 291 (1995).

[79]K. Yoshida, M. Mori, and T. Kondo, "Blue flower color development by anthocyanins: from chemical structure to cell physiology", Nat. Prod. Rep. **26**, 884–915 (2009).

[80]T. A. Holton and Y. Tanaka, "Blue roses - a pigment of our imagination?", Trends Biotechnol. **12**, 40–42 (1994).

[81]T. Hondo, K. Yoshida, A. Nakagawa, T. Kawai, H. Tamura, and T. Goto, "Structural basis of blue-colour development in flower petals from commelina communis", Nature **358**, 515–518 (1992).

[82]Y. Katsumoto, M. Fukuchi-Mizutani, Y. Fukui, F. Brugliera, T. A. Holton, M. Karan, N. Nakamura, K. Yonekura-Sakakibara, J. Togami, A. Pigeaire, G.-Q. Tao, N. S. Nehra, C.-Y. Lu, B. K. Dyson, S. Tsuda, T. Ashikari, T. Kusumi, J. G. Mason, and Y. Tanaka, "Engineering of the rose flavonoid biosynthetic pathway successfully generated blue-hued flowers accumulating delphinidin", Plant Cell Physiol. **48**, 1589–1600 (2007).

[83]M. Shiono, N. Matsugaki, and K. Takeda, "Phytochemistry: structure of the blue cornflower pigment", Nature **436**, 791–791 (2005).

[84]N. Sasaki and T. Nakayama, "Achievements and perspectives in biochemistry concerning anthocyanin modification for blue flower coloration", Plant Cell Physiol. **56**, 28–40 (2015).

[85]S. S. Williams, S. Retterer, R. Lopez, R. Ruiz, E. T. Samulski, and J. M. DeSimone, "High-resolution PFPE-based molding techniques for nanofabrication of high-pattern density, sub-20 nm features: a fundamental materials approach", Nano letters **10**, 1421–8 (2010).

[86]N. E. Raine and L. Chittka, "Nectar production rates of 75 bumblebee-visited flower species in a german flora (hymenoptera: apidae: bombus terrestris).", Entom. Gen. **30**, 191–192 (2007).

[87]N. E. Raine and L. Chittka, "The adaptive significance of sensory bias in a foraging context: floral colour preferences in the bumblebee bombus terrestris", PLOS ONE **2**, 1–8 (2007).

[88]M. Giurfa, J. Núñez, L. Chittka, and R. Menzel, "Colour preferences of flower-naive honeybees", J. Comp. Physiol. **177**, 247–259 (1995).

[89]R. W. Scotland, "What is parallelism?", Evol. Dev. **13**, 214–227 (2011).